



University of Kentucky  
UKnowledge

---

Theses and Dissertations--Mechanical  
Engineering

Mechanical Engineering

---

2012

## CRYOGENIC BURNISHING OF Co-Cr-Mo BIOMEDICAL ALLOY FOR ENHANCED SURFACE INTEGRITY AND IMPROVED WEAR PERFORMANCE

Shu Yang

University of Kentucky, shuyang1031@gmail.com

[Right click to open a feedback form in a new tab to let us know how this document benefits you.](#)

---

### Recommended Citation

Yang, Shu, "CRYOGENIC BURNISHING OF Co-Cr-Mo BIOMEDICAL ALLOY FOR ENHANCED SURFACE INTEGRITY AND IMPROVED WEAR PERFORMANCE" (2012). *Theses and Dissertations--Mechanical Engineering*. 10.

[https://uknowledge.uky.edu/me\\_etds/10](https://uknowledge.uky.edu/me_etds/10)

This Doctoral Dissertation is brought to you for free and open access by the Mechanical Engineering at UKnowledge. It has been accepted for inclusion in Theses and Dissertations--Mechanical Engineering by an authorized administrator of UKnowledge. For more information, please contact [UKnowledge@lsv.uky.edu](mailto:UKnowledge@lsv.uky.edu).

## **STUDENT AGREEMENT:**

I represent that my thesis or dissertation and abstract are my original work. Proper attribution has been given to all outside sources. I understand that I am solely responsible for obtaining any needed copyright permissions. I have obtained and attached hereto needed written permission statements(s) from the owner(s) of each third-party copyrighted matter to be included in my work, allowing electronic distribution (if such use is not permitted by the fair use doctrine).

I hereby grant to The University of Kentucky and its agents the non-exclusive license to archive and make accessible my work in whole or in part in all forms of media, now or hereafter known. I agree that the document mentioned above may be made available immediately for worldwide access unless a preapproved embargo applies.

I retain all other ownership rights to the copyright of my work. I also retain the right to use in future works (such as articles or books) all or part of my work. I understand that I am free to register the copyright to my work.

## **REVIEW, APPROVAL AND ACCEPTANCE**

The document mentioned above has been reviewed and accepted by the student's advisor, on behalf of the advisory committee, and by the Director of Graduate Studies (DGS), on behalf of the program; we verify that this is the final, approved version of the student's dissertation including all changes required by the advisory committee. The undersigned agree to abide by the statements above.

Shu Yang, Student

Dr. I.S. Jawahir, Major Professor

Dr. J.M. McDonough, Director of Graduate Studies

CRYOGENIC BURNISHING OF *Co-Cr-Mo* BIOMEDICAL ALLOY  
FOR ENHANCED SURFACE INTEGRITY AND  
IMPROVED WEAR PERFORMANCE

---

DISSERTATION

---

A dissertation submitted in partial fulfillment of the  
requirements for the degree of Doctor of Philosophy in the  
College of Engineering  
at the University of Kentucky

By  
Shu Yang

Lexington, Kentucky

Director: Dr. I.S. Jawahir, Professor of University of Kentucky

Lexington, Kentucky

2012

Copyright © Shu Yang 2012

## ABSTRACT OF DISSERTATION

### CRYOGENIC BURNISHING OF *Co-Cr-Mo* BIOMEDICAL ALLOY FOR ENHANCED SURFACE INTEGRITY AND IMPROVED WEAR PERFORMANCE

The functional performance of joint implants is largely determined by the surface layer properties in contact. Wear/debris-induced osteolysis and aseptic loosening has been identified as the major cause of failure of metal-on-metal joint implants. A crucial requirement for the long-term stability of the artificial joint is to minimize the release of debris particles.

Severe plastic deformation (SPD) processes have been used to modify the surface integrity properties by generating ultrafine, or even nano-sized grains and grain size gradients in the surface region of many materials. These fine grained materials often exhibit enhanced surface integrity properties and improved functional performance (wear resistance, corrosion resistance, fatigue life, etc.) compared with their conventional coarse grained counterparts.

The aim of the present work is to investigate the effect of a SPD process, cryogenic burnishing, on the surface integrity modifications of a *Co-Cr-Mo* alloy, and the resulting wear performance of this alloy due to the burnishing-induced surface integrity properties. A systematic experimental study was conducted to investigate the influence of different burnishing parameters on distribution of grain size, phase structure and residual stresses of the processed material. The wear performance of the processed *Co-Cr-Mo* alloy was tested via pin-on-disk wear tests. The results from this work show that the cryogenic burnishing can significantly improve the surface integrity of the *Co-Cr-Mo* alloy which would finally lead to advanced wear performance due to refined microstructure, high hardness, compressive residual stresses and favorable phase structure on the surface layer. A finite element model (FEM) was developed for predicting the grain size changes during burnishing of *Co-Cr-Mo* alloy under both dry and cryogenic conditions. A new material model was used for incorporating flow stress softening and associated grain size refinement caused by the dynamic recrystallization (DRX). The new material model was implemented in a commercial FEM software as a customized user subroutine. Good agreement between predictions and experimental observations was achieved. Encouraging trends are revealed with great potential for application in industry.

**KEYWORDS:** Cryogenic Burnishing, *Co-Cr-Mo* Alloys,  
Surface Integrity, Wear, FEM Simulation

---

Shu Yang

---

September, 24<sup>th</sup>, 2012

CRYOGENIC BURNISHING OF *Co-Cr-Mo* BIOMEDICAL ALLOY  
FOR ENHANCED SURFACE INTEGRITY AND  
IMPROVED WEAR PERFORMANCE

By

Shu Yang

Dr. I.S. Jawahir

---

Director of Dissertation

Dr. J.M. McDonough

---

Director of Graduate Studies

September, 24<sup>th</sup>, 2012

---

I dedicate my dissertation to my parents, my friends and my family.

## ACKNOWLEDGEMENTS

I would first like to sincerely thank my advisor Professor I.S. Jawahir for his continuous guidance and support throughout my graduate study. It is because of his motivation and encouragement that I could successfully complete my dissertation. I would also like to express my sincere gratitude to Emeritus Professor O.W. Dillon Jr., for all the guidance, inspiration and the valuable time he has spent in helping me successfully complete my research work. Special thanks are extended to Professor D.A. Puleo for his long-time support and help during my study, especially the valuable advice associated with biomedical field. Additional thanks to Professor F. Badurdeen for agreeing to be on my committee and take time to help me with my dissertation progress. I would like to thank all of you for your time and advice during the defense process.

I am also grateful to Professor D. Umbrello from Department of Mechanical Engineering, University of Calabria (Italy) for his help on starting my research on numerical modeling by using DEFORM-2D, and Professor J.C. Outerio from the Catholic University of Portugal for providing the opportunity to conduct residual stress analysis. In addition, I would like to thank all the Faculty members and the staff of the Department of Mechanical Engineering and the Institute for Sustainable Manufacturing for their continued support and cooperation. I would like to thank my research team members for their continued support. Last but not the least, I want to express my thanks to my parents, my family and my friends for their love, affection and support without which I would not have accomplished my goals in life.



## TABLE OF CONTENTS

ACKNOWLEDGEMENTS .....	iii
LIST OF TABLES .....	vii
LIST OF FIGURES .....	viii
CHAPTER 1: INTRODUCTION .....	1
1.1 Introduction .....	1
1.2 Overview of the dissertation.....	4
CHAPTER 2: LITERATURE REVIEW .....	6
2.1 Hip implant.....	6
2.2 <i>Co-Cr-Mo</i> biomedical alloy .....	15
2.3 Investigations on process, surface integrity and functional performance ..	22
2.4 Surface integrity in burnishing .....	30
2.5 Effect of cryogenic cooling in manufacturing processes .....	38
2.6 Significant process and product sustainability factors .....	43
2.7 Modeling of burnishing process .....	47
CHAPTER 3: SURFACE INTEGRITY MODIFICATIONS OF <i>Co-Cr-Mo</i> BIOMEDICAL ALLOY THROUGH CRYOGENIC BURNISHING.....	53
3.1. Introduction .....	53
3.2. Experimental work .....	54
3.2.1. Work material .....	54
3.2.2. Burnishing experiments .....	56
3.2.3. Infrared thermal-camera setup and calibration .....	60
3.2.4. Characterization of surface integrity.....	62
3.3. Results and discussion.....	65
3.3.1. Burnishing force.....	65
3.3.2. Temperature analysis .....	67
3.3.3. Microstructure.....	73
3.4. Chapter concluding remarks.....	91

CHAPTER 4: EFFECT OF BURNISHING CONDITIONS IN TERMS OF COOLING METHOD, DEPTH OF PENETRATION AND BURNISHING SPEED ON SURFACE INTEGRITY MODIFICATIONS OF <i>Co-Cr-Mo</i> ALLOY.....	94
4.1 Introduction .....	94
4.2 Experimental work .....	95
4.3 Effects of cooling method and depth of penetration .....	97
4.3.1 Temperature .....	98
4.3.2 Burnishing force.....	100
4.3.3 Tool-wear .....	102
4.3.4 Microstructure.....	106
4.3.5 Phase change .....	110
4.3.6 Residual stresses .....	115
4.3.7 Microhardness.....	121
4.4 Effect of burnishing speed.....	123
4.4.1. Microstructure.....	124
4.4.2. Phase change.....	125
4.5 Chapter concluding remarks.....	127
CHAPTER 5: ENHANCED WEAR PERFORMANCE OF <i>Co-Cr-Mo</i> BIOMATERIAL THROUGH CRYOGENIC BURNISHING INDUCED SURFACE INTEGRITY MODIFICATIONS.....	130
5.1 Introduction .....	130
5.2 Experimental work .....	131
5.2.1 Work material .....	131
5.2.2 Burnishing experiments .....	133
5.2.3 Characterization of surface integrity.....	135
5.2.4 Pin-on-disk wear test.....	135
5.3 Results and discussions .....	137
5.3.1. Burnishing force.....	137
5.3.2. Wear volume.....	138
5.3.3. Wear appearance.....	139
5.3.4. Wear surface and wear debris analysis .....	148
5.3.5. Microstructure before wear test .....	154

5.3.6.	Microstructure after wear test .....	158
5.3.7.	Surface and subsurface microhardness .....	161
5.3.8.	Phase change .....	166
5.3.9.	Residual stresses before wear tests .....	175
5.4	Chapter concluding remarks.....	182
<b>CHAPTER 6: FINITE ELEMENT MODELING OF SURFACE INTEGRITY IN BURNISHING.....</b>		<b>185</b>
6.1	Introduction .....	185
6.2	Numerical setup in DEFORM 2D .....	185
6.3	Boundary conditions.....	187
6.4	Material properties .....	190
6.5	Material flow stress development incorporating DRX effects.....	192
6.6	User subroutine for predicting grain size .....	201
6.7	Variable friction modeling .....	204
6.8	Calibration and validation of burnishing model for force and temperature .....	205
6.9	Calibration and validation of user subroutine for grain size prediction ...	217
6.10	Chapter concluding remarks.....	231
<b>CHAPTER 7: CONCLUSIONS AND FUTURE WORK.....</b>		<b>233</b>
7.1	Conclusions .....	233
7.2	Future Research Directions .....	238
<b>REFERENCES.....</b>		<b>241</b>
<b>VITA.....</b>		<b>261</b>

## LIST OF TABLES

Table 2.1: Mechanical properties of implant metals (Ratner et al. 1996).....	16
Table 2.2: Different Levels of Surface Integrity (SI) Data Set (M'Saoubi et al. 2008)....	23
Table 3.1: Chemical composition in wt.% of BioDur CCM alloy .....	55
Table 3.2: Matrix for the burnishing experimental conditions .....	59
Table 3.3: Procedure for polishing the specimens for analysis of microstructure .....	63
Table 3.4: FWHMs of measured plane ( $III_{\gamma}$ ) peaks .....	91
Table 4.1: XRD parameters for residual stress measurement of the <i>Co-Cr-Mo</i> alloy .....	97
Table 4.2: Burnishing experimental conditions for studying the effects of cooling method and depth of penetration.....	98
Table 4.3: Burnishing experimental conditions for studying the effect of burnishing speed .....	124
Table 5.1: Polishing procedure for pins and disks prior to wear testing.....	133
Table 5.2: Matrix for the pin burnishing experimental conditions .....	134
Table 6.1: Thermal and mechanical properties of uncoated carbide and BioDur CCM alloy (CRS Holdings Inc. 2007).....	191
Table 6.2: Typical room temperature mechanical properties (CRS Holdings Inc. 2007) .....	192
Table 6.3: Important used material parameters for the FE model .....	214

## LIST OF FIGURES

Figure 2.1: Human hip joint illustration (Medina 2012).....	6
Figure 2.2: Metal-on-metal total hip replacement (NIAMS 2011).....	7
Figure 2.3: Effect of heating and cooling rates on the onset temperatures of $A_s$ (hcp to fcc) and $M_s$ (fcc to hcp) transformations (Ray et al. 1991). ....	21
Figure 2.4: Effect of strain-rate on microstructure evolution of <i>Co-29Cr-6Mo</i> alloy deformed to true strain of 0.92 at 1150 degree C at (a) $10^{-3} \text{ s}^{-1}$ , (b) $10^{-2} \text{ s}^{-1}$ , (c) $0.1 \text{ s}^{-1}$ , (d) 1.0, and (e) $10 \text{ s}^{-1}$ (Yamanaka et al. 2009).....	24
Figure 2.5: (a) A bright-field TEM image and a corresponding selected area diffraction pattern; (b) grain size distribution of the top surface layer of the SMAT <i>Cu</i> for 30 minutes; (c) variations of wear rate with the applied load for the 30 minutes SMAT <i>Cu</i> and the coarse-grained <i>Cu</i> at a sliding velocity of 0.01 m/s; (d) variation of the wear volume with the applied load for the SMAT <i>Cu</i> and the coarse-grained <i>Cu</i> samples against a <i>WC-Co</i> ball in mineral oil (Shi and Han 2008).....	26
Figure 2.6: Fatigue strength of some common implant alloys (Teoh 2000).....	28
Figure 2.7: Interaction of axial residual stress and hardness on fatigue life (Sasahara 2005) .....	29
Figure 2.8: (a) Residual stress distribution in surface region due to machining and burnishing, and the influence of burnishing time on residual stress; (b) the influence of burnishing force on residual stress (Fattouh and Elkhabeery 1989).....	31
Figure 2.9: Changes in residual stress values (a) $\sigma_x$ and (b) $\sigma_y$ in function of distance from surface in vicinity of the sample after multiple-path alloying (line 2) and alloying combined with cold (line 3) and hot burnishing (line 1) .....	33
Figure 2.10: (a) Cross-sectional observation of the <i>Cu</i> sample processed by means of SMGT; TEM observations and grain size distributions of the top surface layer: (b) bright field image, (c) transverse axis grain size ( $d_t$ ), (d) longitudinal axis grain size ( $d_l$ ).....	40
Figure 2.11: (a) Schematic illustration of the main steps of microstructural evolution in 1100 <i>Al</i> subjected to orthogonal cutting. (b) The sequence of grain refinement events shown on the cross-section of the material ahead of the tool tip (Ni et al. 2004) .....	41
Figure 2.12: Product sustainability wheel (Jawahir et al. 2006).....	47
Figure 2.13: Model of sliding burnishing and pressure force calculated from the model (Korzynski 2009).....	49
Figure 3.1: Experimental setup for cryogenic burnishing of <i>Co-Cr-Mo</i> discs: (a) Mazak CNC machine equipped with ICEFLY <sup>®</sup> cryogenic equipment, (b) setup details.....	58

Figure 3.2: Schematic of the cryogenic burnishing process .....	60
Figure 3.3: Thermo-camera setup illustration for burnishing process .....	61
Figure 3.4: The temperature relationship of the investigated <i>Co-Cr-Mo</i> disc between the infrared camera and the thermocouple measurement values .....	62
Figure 3.5: Metallurgical sample illustration .....	63
Figure 3.6: X-ray equipment for phase structure analysis .....	65
Figure 3.7: Force measurement results under different burnishing conditions .....	67
Figure 3.8: Simplified cryogenic burnishing illustration .....	68
Figure 3.9: Infrared camera images of temperature field during (a) dry and (b) cryogenic burnishing .....	71
Figure 3.10: (a) Depth profile of temperature from point O, and (b) perimeter profile of temperature from point O .....	72
Figure 3.11: Measured temperature at point O from different burnishing conditions .....	73
Figure 3.12: Microstructure near the surface before burnishing .....	73
Figure 3.13: Microstructure of the surface after burnishing under different conditons: (a) dry burnishing, DoP = 0.127 mm; (b) cryogenic burnishing, DoP = 0.127 mm, (c) dry burnishing, DoP = 0.254 mm and (d) cryogenic burnishing, DoP = 0.254 mm. ....	76
Figure 3.14: Transitional lines show the gradual changes from the burnishing influenced microstructure to the bulk microstructure (0.254 mm DoP): (a) cryogenic, (b) dry .....	79
Figure 3.15: SEM micrographs of <i>Co-Cr-Mo</i> disc near the topmost surfaces after burnishing with 0.254 mm DoP: (a) dry, (b) cryogenic .....	81
Figure 3.16: Comparison of longitudinal axis grain size distribution of the grains shown in Figure 3.15 after dry and cryogenic burnishing with 0.254 mm DoP .....	83
Figure 3.17: Hardness variation with depth below the burnished surface .....	85
Figure 3.18: EDS results of <i>Co-Cr-Mo</i> disc from cryogenic burnishing: (a) bulk, (b) surface .....	86
Figure 3.19: Surface roughness ( $R_a$ ) created using different burnishing conditions .....	88
Figure 3.20: (a) XRD patterns on the burnished surface before and after cryogenic burnishing with 0.254 mm DoP; (b) XRD patterns on the burnished surface when using different burnishing conditions .....	90
Figure 4.1: PROTO iXRD machine used in the residual stress measurement (X-ray Diffraction Center for Materials Research, University of Coimbra, Portugal) .....	96
Figure 4.2: Effects of cooling method and DoP on temperature along the depth profile: .....	99
Figure 4.3: Burnishing forces illustration .....	100
Figure 4.4: (a) Measured burnishing forces, (b) ratio of tangential/radial forces (T/R ratio) vs. DoP (14.3 mm tool diameter) .....	102

Figure 4.5: 3-D topographic profiles of the tool-wear zone: (a) dry, 0.15 mm DoP, (b) cryogenic, 0.15 mm DoP; (c) dry, 0.21 mm DoP, (d) cryogenic, 0.21 mm DoP (14.3 mm tool diameter, 100 m/min burnishing speed) .....	105
Figure 4.6: The effect of the cooling method on microstructure (14.3 mm tool diameter, 0.21 mm DoP, 200 m/min burnishing speed): (a) dry, (b) cryogenic .....	107
Figure 4.7: The effect of the DoP on microstructure (cryogenic, 14.3 mm diameter tool, 200 m/min burnishing speed): (a) 0.08 mm DoP, (b) 0.15 mm DoP, (c) 0.21 mm DoP .....	109
Figure 4.8: The effect of the DoP on burnishing-influenced layer thickness .....	110
Figure 4.9: The effect of the cooling method on surface phase change .....	113
Figure 4.10: The effect of the DoP on surface phase change (14.3 mm tool diameter): (a) cryogenic, 100 m/min burnishing speed, (b) dry, 100 m/min burnishing speed, (c) cryogenic, 200 m/min burnishing speed .....	115
Figure 4.11: Diffraction of X-rays by a crystalline material (Umbrello 2004) .....	116
Figure 4.12: The effect of the cooling methods on residual stresses: (a) tangential and (b) axial directions .....	118
Figure 4.13: The effect of the DoP on residual stresses: (a) tangential and (b) axial directions .....	120
Figure 4.14: Material side flow after burnishing (cryogenic, 0.15 mm DoP, 100 m/min burnishing speed) .....	121
Figure 4.15: (a) The effect of the cooling method on hardness below the surface; the effect of the DoP on hardness below the surface: (b) cryogenic, (c) dry (14.3 mm tool diameter, 100 m/min burnishing speed) .....	123
Figure 4.16: The effect of the burnishing speed on burnishing-influenced layer thickness .....	125
Figure 4.17: The effect of the burnishing speed on surface phase change .....	127
Figure 5.1: Pin burnishing illustration with liquid nitrogen delivery .....	132
Figure 5.2: Experimental setup for pin-on-disk wear tester .....	136
Figure 5.3: Measured radial force comparisons under different burnishing conditions. 138	
Figure 5.4: Wear volume losses of <i>Co-Cr-Mo</i> pins as a function of sliding distance. Velocity 50 mm/s, contact stress 3.54 MPa, new born calf solutions (pin-on-disk). .....	139
Figure 5.5: Topographic maps of worn pin surfaces: (a) initial, (b) dry, 0.127 mm DoP, (c) cryogenic, 0.127 mm DoP, (d) dry, 0.254 mm DoP, (e) cryogenic, 0.254 mm DoP. ....	142
Figure 5.6: Wear depth profiles along line AB, (a) dry vs. cryogenic (0.127 mm DoP), (b) dry vs. cryogenic (0.254 mm DoP), (c) cryogenic, 0.127 mm DoP vs. cryogenic, 0.254 mm DoP .....	144
Figure 5.7: Measured surface roughness ( $R_a$ ) of worn pins and disk .....	146

Figure 5.8: (a) Worn pin surface areas comparison, (b) worn pin surface wear depth distribution.....	148
Figure 5.9: SEM micrographs of typical surface wear tracks.....	149
Figure 5.10: EDS results of wear debris from pin-on-disk wear tests: (a) initial, (b) cryogenic, 0.127 mm DoP, (c) dry, 0.254 mm DoP .....	150
Figure 5.11: SEM micrographs of wear debris: (a) cryogenic, 0.127 mm DoP, (b) dry, 0.254 mm DoP.....	151
Figure 5.12: Microstructure near the surface: (a) initial, (b) cryogenic burnishing, 0.127 mm DoP, (c) cryogenic burnishing, 0.254 mm DoP (note that the square marks on Figure 5.12 (b) were from the Vickers hardness measurements) .....	155
Figure 5.13: Typical microstructures after cryogenic burnishing (0.254 mm DoP): (a) layer A in Figure 5.12 (c) (0 ~ 100 $\mu\text{m}$ ), (b) layer B in Figure 5.12 (c) (100 ~ 200 $\mu\text{m}$ ).....	157
Figure 5.14: Microstructure of the surface after wear tests: (a) dry burnishing, 0.254 mm DoP, (b) cryogenic burnishing, 0.127 mm DoP, (c) cryogenic burnishing, 0.254 mm DoP, (d) initial. Other conditions are given in Table 5.1.....	160
Figure 5.15: Hardness variation before wear test: (a) and (b) subsurface hardness profiles for selected burnishing conditions, (c) $HV_{\text{surface}} / HV_{\text{initial}}$ values... ..	164
Figure 5.16: Hardness variation before and after wear test: (a) initial, (b) cryogenic, 0.127 mm DoP, (c) dry, 0.127 mm DoP.....	166
Figure 5.17: XRD spectra on the burnished surface from different burnishing conditions .....	168
Figure 5.18: XRD spectra on the pin surface before and after wear tests .....	172
Figure 5.19: (a) Relative volume fraction of hcp phase after burnishing; (b) relative volume fraction of hcp phase before and after wear test for initial and cryogenically burnished pins.....	173
Figure 5.20: Relative volume fractions of hcp phase vs. wear volume losses.....	174
Figure 5.21: Surface residual stresses before wear tests.....	175
Figure 5.22: Measured residual stresses after dry and cryogenic burnishing with 0.127 mm DoP: (a) measurement illustration, (b) tangential direction, (c) axial direction.....	177
Figure 5.23: Measured residual stresses after dry and cryogenic burnishing with 0.254 mm DoP: (a) tangential direction, (b) axial direction. ....	178
Figure 5.24: Measured residual stresses after cryogenic burnishing with 0.127 mm DoP and 0.254 mm DoP: (a) tangential direction, (b) axial direction.....	179
Figure 5.25: Compressive areas of the residual stress profiles from dry and cryogenic burnishing with 0.127 mm DoP .....	180
Figure 5.26: Residual stresses after wear tests for all the burnished pins: (a) tangential direction, (b) axial direction. ....	182



Figure 6.1: Computational domain of interest for the 2-D burnishing process and boundary conditions applied .....	188
Figure 6.2: Steps for the proposed 2-D burnishing simulation: (a) roller tool starts to penetrate into workpiece, (b) roller tool reaches the predetermined DoP, (c) roller tool slides against the surface under the predetermined burnishing speed.....	190
Figure 6.3: Burnishing simulation flow .....	192
Figure 6.4: Schematic representation of flow curves during DRV and DRX defining various stress and strain parameters (Sarkar et al. 2011) .....	194
Figure 6.5: True stress-true strain curves of <i>Co-28Cr-6Mo-0.16N</i> (adapted) .....	199
Figure 6.6: Comparison between measured and predicted stress-strain curves for the <i>Co-Cr-Mo</i> alloy, experimental data from (Chiba et al. 2009a; Yamanaka et al. 2009).....	200
Figure 6.7: Critical strain of <i>Co-Cr-Mo</i> alloy as a function of <i>Z</i> values.....	202
Figure 6.8: Variable friction model due to DRX .....	205
Figure 6.9: Calibration procedure for burnishing model .....	206
Figure 6.10: Examples of the effect of J-C constants <i>A</i> and <i>B</i> on radial force predictions (Dry, DoP = 0.254 mm, burnishing speed = 100 m/min, tool diameter = 14.3 mm) .....	207
Figure 6.11: The effect of friction coefficient $\mu$ on the calculated radial force predictions (Dry, DoP = 0.254 mm, burnishing speed = 100 m/min, tool diameter = 14.3 mm) .....	208
Figure 6.12: Tool-workpiece interface and the exit temperature position (Dry, DoP = 0.08 mm, burnishing speed = 100 m/min, tool diameter = 14.3 mm).....	209
Figure 6.13: The effect of tool-workpiece heat transfer coefficient $h_l$ on workpiece exit temperature predictions (Dry, DoP = 0.254 mm, burnishing speed = 100 m/min, tool diameter = 14.3 mm).....	210
Figure 6.14: Equilibrium phase diagram of the binary <i>Co-Cr</i> system (ASM 1986) .....	211
Figure 6.15: (a) The exit temperature for cryogenic conditions (Cryogenic, DoP = 0.254 mm, burnishing speed = 100 m/min, tool diameter = 14.3 mm); (b) predicted exit temperature from different burnishing conditions (burnishing speed = 100 m/min, tool diameter = 14.3 mm).....	213
Figure 6.16: Comparison of measured and predicted radial forces under different burnishing conditions (14.3 mm tool diameter) .....	215
Figure 6.17: Distribution of effective stresses: (a) dry burnishing, (b) cryogenic burnishing. (0.254 mm DoP, 100 m/min speed, 14.3 mm tool).....	216
Figure 6.18: Calibration procedure for grain size prediction.....	217
Figure 6.19: (a) Tool-workpiece interface; (b) strain, (c) strain-rate and (d) temperature distributions along the tool-workpiece interface; (e) strain distribution along the distance below the surface.....	221

Figure 6.20: The effect of Zener-Hollomon constants $\alpha$ and $m'$ on grain size .....	222
Figure 6.21: Predicted grain size distributions after burnishing from different conditions .....	224
Figure 6.22: Predicted grain size variation below the burnished surface: (a) dry and cryogenic burnishing under 0.08 mm DoP, (b) dry and cryogenic burnishing under 0.254 mm DoP; (c) predicted burnishing-influenced layer thicknesses; (d) comparison of the observed and predicted grain size on the burnished surface (burnishing speed = 100 m/min, tool diameter = 14.3 mm) .....	229

## CHAPTER 1: INTRODUCTION

### 1.1 Introduction

Metal-on-metal bearings have a long history in total hip replacement. In the past, total hip replacements (THR) involved the use of metal-metal cast *Co-Cr-Mo* alloys as the implant material, largely due to the relatively high strength, bio-compatibility and corrosion resistance of this alloy. However, limitations in the manufacturing methods adversely affected the performance of these joints. The cast material contained a relatively coarse microstructure, including element segregation leading to the formation of coarse carbide formation in certain areas of the microstructure. As a result, there existed inconsistencies in the mechanical (and wear) properties between various implants produced by the same methods. In addition, high frictional torques between the articulating surfaces resulted in seizing of the implant at the joint equator due to small deformations of the poorly designed and machined acetabular cups and poorly machined femoral heads. It was found that the utilization of ultra-high molecular weight polyethylene as the bearing surface of the acetabular cup reduced the overall friction of the joint. This resolved the problem of high frictional torques, but unfortunately, resulted in the formation of fine polyethylene wear debris between the articulating surfaces, due to metal-plastic abrasion. The accumulation of this wear debris around the joint area was found to cause inflammation of the surrounding tissue and bone osteolysis (i.e. the resorption of bone) at the bone-implant interface, resulting in the subsequent loosening of the implant. The actual number of patients requiring revision surgery (called a bearing exchange) for a worn plastic cup liner has been on the order of 5% at 10 to 15 years. This

means that 95% of hip replacements continue to function well 15 years after surgery. The risk of wearing out a plastic liner is higher in younger (less than 60 years old) and more active patients. Because of this potential for wear, doctors and implant manufacturers have looked for different types of bearings beyond polyethylene which may be more resistant to wear. The search for a longer wearing bearing has led to the development of metal on metal hip implants. These devices are commonly used today in patients less than 60 years of age (Fisher 2011). Retrievals of cast *Co-Cr-Mo* metal-on-metal hip implants which did not experience seizing (some serviced in patients over 25 years) revealed little to no wear of the articulating surfaces. As a result, there is renewed interest on the optimization of the wear performance of *Co-Cr-Mo* metal-on-metal implants used in THR. Currently, more and more hip implants are machined from wrought *Co-Cr-Mo* alloys. The wrought state of these alloys is achieved through thermo-mechanical processing of the cast material in order to improve the mechanical properties by altering the microstructure (i.e., through grain refinement and the elimination of macrodefects).

Improved manufacturing methods led to the reintroduction of metal-on-metal bearings and increased the interest in these implants, especially for young and active patients (Heisel et al. 2003). Volumetric wear rates and osteolytic potential of metal-on-metal bearings are lower than those of metal-on-polyethylene bearings (Greenwald et al. 2001). However, metallic particles have a greater potential for cytotoxicity, and their number is greater (Germain et al. 2003). A reduction in metal-on-metal wear will reduce biological reactivity and thus increase the long-term implant survivorship (Ingham and Fisher 2000).

Among the options available for evaluating the performance of a biomaterial, the enhancement of the surface integrity holds the key. In practical applications, the surface of a material is subjected to the influence of various external stimuli. Corrosion, oxidation, wear and fatigue are a few such material degradation phenomena, which all initiate at the surface. Every year, a large number of revision operations are performed to restore the implant material into the system (Park and Kim 2003). As the population ages, this problem becomes a matter of greater importance. Implant loosening due to poor adhesion wear over a period of time, leakage of ions, and corrosion are some of the reasons attributed to the failure of implants inside the biological environment (Heisel et al. 2003). Often the revision operations are complex and costly. Thus, it has been a constant need by engineers and scientists to improve the surface properties of biomaterial components. Surface modifications seem to offer solutions for improved functionality and biocompatibility of implants.

Severe plastic deformation (SPD) processes have been extensively reported for modifying surface region properties of many materials (Sato et al. 2004; Valiev et al. 2010). Much evidence has shown that SPD induced fine-grained materials possess unusually appealing surface integrity properties and functional performance compared with their coarse-grained counterparts (Qi et al. 2009; Shi and Han 2008; Wang et al. 2003a). However, there is still a large gap between SPD processes on the laboratory scale for fundamental research and its application in large scale production. The possibility of using SPD processes as a surface enhancement tool to improve the functional performance of materials through enhanced surface integrity while avoiding expensive and time-consuming post-treatment processes has not yet been well investigated.

A literature survey suggests that traditional manufacturing processes involving SPD such as burnishing may be used to improve the wear performance of *Co-Cr-Mo* alloys by tailoring the surface integrity properties, such as grain refinement, compressive residual stresses, high hardness, etc.. The major objectives of the research are: a) Investigating the influence of processing conditions, especially the use of cryogenic cooling during processing, on surface integrity changes such as microstructure, phase transformation, residual stresses, etc., generated by burnishing; b) Evaluating the resulting pin-on-disk wear performance of burnished samples in terms of wear volume, wear appearance and wear debris, as well as the surface integrity changes of the *Co-Cr-Mo* samples before and after wear tests in order to identify the major wear mechanism(s) of this *Co-Cr-Mo* alloy and the key influencing surface integrity factors for wear performance; and 3) Developing a finite element (FE) model to predict the surface and sub-surface grain size changes of the *Co-Cr-Mo* alloy due to the burnishing-induced dynamic recrystallization (DRX).

## **1.2 Overview of the dissertation**

In Chapter two, a literature review is presented. It covers the current problems in metal-on-metal joint implants and recent findings from studies on *Co-Cr-Mo* biomedical alloys. The major experimental and numerical studies on surface integrity in burnishing and the influence on components functional performance are discussed. The significant process and product sustainability factors in cryogenic burnishing are also presented.

The experimental results on the surface integrity resulting from burnishing experiments under different conditions including cooling method (dry and cryogenic),

depth of penetration and burnishing speed are reported in Chapters three and four. The surface integrity factors investigated are microstructure (grain size and processing influenced layer), phase transformation, residual stresses, hardness and surface roughness. The use of the liquid nitrogen cooling while burnishing of biomedical alloys is believed to be novel and new.

In Chapter five, the effect of burnishing-induced surface integrity modifications on the wear performance of this *Co-Cr-Mo* alloy is investigated via pin-on-disk wear testing experiments. The wear volume, wear appearance and wear debris, as well as the surface integrity changes of the *Co-Cr-Mo* samples before and after wear tests were studied. The major wear mechanism of this material was identified and the key influencing surface integrity factors were found. The results from this study provide valuable information for establishing the relationships among burnishing conditions, surface integrity properties and the wear performance of this *Co-Cr-Mo* alloy.

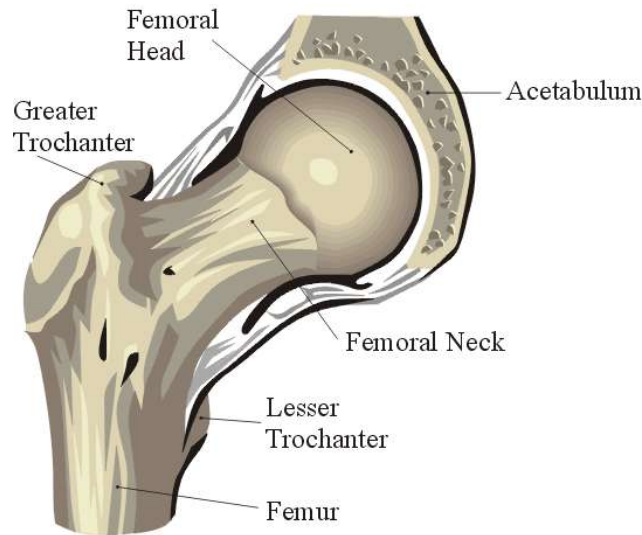
Chapter six presents a numerical study for simulating and predicting the grain size changes of *Co-Cr-Mo* alloys induced by burnishing. A new material model was developed for incorporating flow stress softening and associated grain size refinement caused by DRX. Good agreement between predictions and experimental observations was achieved by using a customized user subroutine built in commercial FEM software.

In Chapter seven, the findings and results of the current work are summarized with final remarks and conclusions. The directions and recommendations of the future work are discussed briefly based on the results and observations presented in this dissertation.

## CHAPTER 2: LITERATURE REVIEW

### 2.1 Hip implant

The human hip joint is composed of two main parts: the femoral head and the acetabular cup (see Figure 2.1). These two parts are naturally composed of bone, separated by a thin layer of cartilage; the cartilage acts as a lubricating film between the two surfaces. If this layer deteriorates due to disease, such as osteoarthritis and rheumatoid arthritis, the friction between the articulating surfaces increases, causing severe pain to the individual. Total hip replacement involves the surgical replacement of damaged or diseased hip joints with that of an artificial hip.



*Adapted from Corel Draw 9 Library*

Figure 2.1: Human hip joint illustration (Medina 2012)

Mimicking the natural ball-in-socket hip joint, metal-on-metal hip replacement systems consist of a metal ball (femoral head), a metal femoral stem in the thighbone, and a metal cup in the hip bone (acetabular component) (Figure 2.2). Metal-on-metal hip



implants are usually recommended for younger and more active patients, mainly because they are more durable and last longer than other materials, i.e., plastic or ceramic. Most of the current metal-on-metal hip implants are made from cobalt-chromium alloys. A hip implant must fulfill certain physical requirements in order to function successfully within the human body. Development of such a device involves careful structural design of the joint components and appropriate materials selection having the required properties. The goal of hip replacement is to minimize pain, while providing full range of motion and ease of mobility for the patient.



Figure 2.2: Metal-on-metal total hip replacement (NIAMS 2011)

Over 600,000 total joint replacements are performed in the United States each year. Due to improved quality, the current generation of metal-on-metal joints has been increasingly accepted by orthopedic surgeons; about one-third of the joint replacements performed annually in this country are metal-on-metal implants. Although factors such as structural design, biocompatibility, strength and even friction have been addressed in the

overall design of hip implants due to the improved manufacturing techniques, one important issue which has not been solved is wear. The debris/particles emitted from a metal-on-metal articulation (with an average size far below 1  $\mu\text{m}$ ) is up to  $10^{14}$  each year, and these particles subsequently migrate into the surrounding tissue (Doorn et al. 1998). The activity of certain cells in the body, in particular macrophage cells, is increased in response to the accumulation of wear debris in the surrounding tissue. These cells envelope the particulate debris and generate biochemical factors such as prostaglandins and interleukins that, when released into surrounding tissues, stimulate osteoclast cell activity that results in peri-implant bone destruction (Wright and Goodman 1996). This can affect implant fixation leading to implant loosening, or necessitate a revision procedure to exchange the bearing surfaces and repair the bone damage. Debris-induced immune reactivity, aseptic inflammation, and subsequent early failure have been reported as high as 4% to 5% at 6 to 7 years post-implantation for current generation metal-on-metal total hip replacements (Hallab and Jacobs 2009). The generation of wear debris at the articulating surfaces and resulting macrophage mediated peri-implant osteolysis and aseptic loosening are the major complications in total hip replacements (Chan and Villar 1996). According to 2005 data from the Nationwide Inpatient Sample, in which approximately 1,000 hospitals evaluating the causes for revision of total hip replacements, up to 50% of revisions are consequences of wear-induced osteolysis and aseptic loosening (Marshall et al. 2008). Thus, methods of reducing wear debris formation have become increasingly important. The need of minimizing wear is essentially a materials issue, which is largely determined by the properties of the material.

A detailed review of key publications which emphasizes on studying the wear characteristics of *Co-Cr-Mo* hip implants based on laboratory as well as clinical experiences is carried out below.

Campbell et al. (1999) described the cellular response observed for clinically retrieved metal-on-metal hip components with *Co-Cr-Mo* bearing surfaces. *Co-Cr* particles that originated from the wear-in phase were responsible for tissue darkening (metallosis) reactions and included macrophages filled with black metallic particles in the nanometer size range. The wear debris was not associated with granuloma formation or necrotic tissue, but the authors stated that the long-term biological effects of *in vivo* wear products are not well defined.

Hallab et al. (1999) analyzed serum protein fractions from patients with cobalt-base total joint arthroplasty components. The distribution of serum *Cr* and *Co* concentrations implied that specific metal-protein complexes were formed from the implant degradation products. The physiological and clinical significance of high metal serum content is unknown according to the researchers.

Buscher et al. (2005) studied the relationship between the subsurface microstructure of metal-on-metal hip joints and wear particle generation in cobalt based alloys. These authors investigated the wear mechanisms on the surface using scanning electron microscopy (SEM) while the microstructure of the subsurface was observed using a transmission electron microscope (TEM). The authors observed a network of stacking faults at some distance from the surface with a change of nanocrystalline microstructure. The wear particles still adhered to the surfaces, and the globular debris

was found in grooves on the articulating surfaces of the cups. The authors then compared the in vivo debris size with the grain size of the surface of the alloy and concluded that the globular wear results from torn nanocrystals while the needle shaped wear is being formed by broken martensite. The crack formation through the nanocrystalline layer led the authors to conclude that the dominating mechanism of debris generation in metal-on-metal joints is surface fatigue within the nanocrystalline layer formed close to the surface during use.

In another study, Buscher and Fischer (2005) investigated the metal-on-metal McKee-Farrar prostheses of the first generation using TEM. The authors used specimens from a conventional disk-on-pin wear test for comparison in order to investigate the impact of mechanically dominated wear mechanisms on the subsurface microstructure. The authors conducted microstructural investigations on laboratory wear specimens and on retrievals. The authors conclude that a gradual decrease in grain size due to the applied tribological loads occurs in the near-surface microstructure of cobalt alloys, which the authors attribute to dynamic recrystallization. The dynamic recrystallization is achieved by two mechanisms, one acting at the top surface by rotating clusters of atoms within a “mechanically mixed” zone and the second acting within the bulk by shearing of cells generated by stacking faults and martensite needles moving towards the surface with increasing strain gradient. The authors also observe, near the surface at a depth of less than about 1  $\mu\text{m}$ , a distinct microstructure of very fine granular crystals in the nm range. This microstructure is very different than the virgin one. The authors attribute the low clinical wear rates to the low stacking fault energy of *Co-Cr-Mo* alloys along with the bio-tribo-chemical reactions on the worn surfaces.

Wimmer et al. (2001) investigated the acting wear mechanism in metal-on-metal hip bearings in *vitro* using commercially available *Co-Cr-Mo* balls under reciprocating sliding wear. The authors observed the wear appearances to define the active wear mechanisms and evaluate their contributions to the wear behavior occurring in metal-on-metal hip bearings. The authors observed initial surface fatigue in the bearings which they attribute to the high local contact stresses. This led to the fracture of *Cr*- and *Mo*-carbides which are torn off from the surfaces resulting in additional surface fatigue by indentations and abrasion. The authors claim that the lack of adhesion wear is due to the formation of oxide layers or other features which have a beneficial influence on wear due to their strong influence on contact chemistry. Oxidized metal matrix wear debris is found after in *vivo* as well as *in vitro* tests. Hence the authors conclude that the wear behavior is mainly influenced by the alternating balance between surface fatigue and abrasion on the one side and by tribochemical reactions on the other side.

In their later work, Wimmer et al. (2003) studied the tribochemical reaction on metal-on-metal hip joint bearings in-vitro and in-vivo. They studied forty two retrieved metal-on-metal prostheses from 13 male and 29 female patients. The authors found indications for abrasion, surface fatigue, and tribochemical reactions in an in-vitro set-up of reciprocating sliding wear with metal-on-metal components. However no signs of adhesion were observed in the metal-on-metal contact system which was attributed to no direct metal-metal contact due to the tribochemical reactions in the oxide layers on the metal surfaces. Tribochemical layers for retrieved metal-on-metal hip bearings and in-vitro test samples were characterized optically using SEM, and chemically using XPS which showed the layers to be predominantly made of organic proteins and constituents

of salts. The authors' findings are in agreement with previous findings of wear due to abrasion because of particle being torn off from the surface due to surface fatigue.

St. John et al. (1999) investigated the wear properties of hip heads and cups fabricated from high and low carbon-wrought *Co-26Cr-6Mo* alloy. It was found from pin-on-disk testing that the alloy with the higher (0.25%) carbon content was more wear resistant. The authors also compared the results of metal-on-polyethylene samples to metal-on-metal samples after 5,000,000 cycles, and found that the wear in metal-on-polyethylene was 110-180 times that for the all metal bearing couple. The authors characterized polyethylene and metal particles retrieved from either the lubricant for pin-on-disk testing or hip simulator testing and compared them with particles retrieved from periprosthetic tissues by other researchers and found them to be of a similar nature. The authors suggest based on these results that metal-on-metal hip prostheses manufactured from the high carbon cobalt/chromium alloy can be used for low wear applications as compared to conventional metal-on-polyethylene implants.

Dowson et al. (2004) investigated the role of materials in metal-on-metal hip implants through the testing of twenty-six pairs of low- and high-carbon components in wrought or cast form over a 5 million test cycles in a 10-station hip joint simulator. The authors observed that low-carbon cast material exhibited higher wear than the high-carbon wrought material at similar diametric clearances. The authors also observed no significant differences between the wear volumes of the wrought and cast high carbon materials. The observations led the authors to conclude that implants of similar geometrical form when tested in a hip joint simulator, but having alternative combinations of the currently adopted high carbon *Co-Cr-Mo* alloys do not exert a major

influence on the magnitude of the running in wear volume. The authors however believed that design characteristics can optimize the load relief offered by lubrication to the articulating surfaces.

Howie et al. (2005) investigated twenty-four cobalt-chrome alloy McKee-Farrar matching acetabular and femoral components after 16 years in situ for wear and loss of sphericity. They classified the wear on the components into four parts: polishing wear which resulted in a surface roughness almost the same as that of an unworn implant; fine abrasive wear resulting in fine surface scratches which were randomly oriented and resulted in a loss of original surface finish; multidirectional dull abrasive wear which resulted in slight increase in surface roughness and many multidirectional shallow wear tracks consistent with abrasive wear; and unidirectional dull abrasive wear, with an obvious loss of the reflective surface and approximately 10-fold increase in surface roughness. The wear tracks in this type of wear were deep and oriented in a common direction. The authors conclude that there is no association between the duration and the type or distribution of wear, and no single pattern of wear.

Nevelos et al. (2004) tried to address the main metallurgical design issues in metal-on-metal bearing design. These authors also show that the difference in wear performance when bi-axial motion was used for pin-on-disk test is much less pronounced than uniaxial tests, which introduces a degree of polishing into the wear mechanism as compared to a hip simulator. Processing methods used for the manufacture of both the femoral head and acetabular cups included casting and forging. The authors conclude that with the exception of low carbon wrought couples against themselves, wear of metal-on-

metal bearings is not dependant on carbide morphology which is influenced by processing method when making the components.

Wang et al. (1999) characterized metallurgical and tribological events occurring at the articulating surfaces of metal-on-metal implants which were tested in a hip simulator, to understand the wear characteristics of *Co-Cr-Mo* alloys. Three of the heads were examined as manufactured, three heads after three million cycles and six heads after six million cycles in the hip simulator which subjected the articulating surfaces to a biaxial rocking motion. The authors found that the wear tracks were caused on the articulating surfaces by full or partial carbide pull-out due to surface fatigue. The authors conclude that carbides in the intermetallics structure are instrumental in maintaining the structural integrity of the matrix. As these carbides fracture or wear away during surface fatigue the matrix support may be reduced resulting in additional material loss by delamination. The authors however do not offer evidence of matrix wear through delamination, after examination of the wear surface.

Affatato et al. (2006) investigated the effect of surface profile parameters on amount of wear in metal artificial hip joints. Twelve *Co-Cr-Mo* ball heads were intentionally damaged in order to reproduce a wide spectrum of surface conditioning and were then subjected to a wear test against a polyethylene cup using a hip joint wear simulator. The surface roughness of the metallic ball heads was qualified in terms of average surface roughness  $R_a$ , total surface roughness  $R_t$  and skewness  $R_{sk}$ . The authors used a linear regression analysis to correlate the wear and the surface profile parameters. The authors observed that all three parameters  $R_a$ ,  $R_t$  and  $R_{sk}$  were capable of predicting the observed variability of the weight loss in a statistically significant way ( $p < 0.01$ ). The



authors conclude that that the surface roughness of retrieved specimens and of components tested *in vitro* under severe conditions such as third-body wear should be qualified by reporting not only the average roughness  $R_a$  but also the skewness  $R_{sk}$  based on the strong correlation coefficient with  $R_{sk}$  of with wear. However the correlation coefficient obtained by the authors uses a linear regression analysis which is a simplistic assumption and fails to account for the interaction among the parameters.

Buford and Goswami (2004) conducted a review of the various wear mechanisms occurring in hip implants (metal-on-polyethylene and metal-on-metal). The primary wear mechanisms in hip implants were found to be abrasion, adhesion and fatigue. The authors classified the wear mechanism into four modes: articulation between the primary contact areas of the prosthesis bearing, surface abrasion resulting from excessive wear and penetration of primary contact areas, particulate or third body wear caused by suspended wear particles in the articulating zone and surface rubbing of not bearing surfaces such as fixation devices causing fretting. The authors also attribute increased wear to increased surface roughness. The authors correlate the wear generation in the hip implants to be a function of type of materials, contact stresses, lubricants and clearance, surface hardness, roughness, type of articulating motion, number of cycles and solution particle count.

## **2.2 Co-Cr-Mo biomedical alloy**

Cobalt alloys are widely used in many heat resistant and wear resistant applications. The heat resistant alloys are used in the fabrication of turbochargers, gas turbines and aircraft jet engines, while the wear resistant alloys are used for cutting tools

in machinery and for medical applications, such as knee and hip prosthetics. This section of review concentrates on the latter application area.

A fully functional total hip replacement involves materials selection according to the required mechanical properties. In the case of metals, alloy design is the initial step in producing a material with all the desired properties. *Co-Cr-Mo* alloys which are used in total hip replacement can be fabricated by various methods. The ASTM F75-87 alloy is a cast *Co-Cr-Mo* alloy. However, limitations in the casting process impose some microstructural features that may alter the mechanical properties. The material specification ASTM F1537-94 is a wrought version of this alloy and the forging process used in its fabrication aids in eliminating void defects and in refining the microstructure, thus improving the mechanical properties (see Table 2.1). A comparison of the properties of the cast and forged *Co-Cr-Mo* alloys shows a definite increase in both the yield and fatigue strengths of the material as a result of the processing methods.

Table 2.1: Mechanical properties of implant metals (Ratner et al. 1996)

Material	Young's Modulus (GPa)	Yield Strength (MPa)	Fatigue Strength (MPa)
Cast <i>Co-Cr-Mo</i> Alloy	210	448-517	207-310
Forged <i>Co-Cr-Mo</i> Alloy	210	896-1200	600-896

Cobalt can be alloyed with significant quantities of elements to create useful engineering materials. Cobalt imparts to its alloys some extremely important properties, such as resistance to several forms of wear, creep and fatigue at high temperatures. The resistance to wear of cobalt alloys derives partly from the fact that they undergo structural

transformation during mechanical deformation. Cobalt alloys also benefit from mechanical twinning and planar slip propensities (Martin 2006).

The corrosion and high temperature oxidation of the metal are improved through the addition of *Cr* (Fontana and Greene 1978). Chromium is also a carbide former and usually forms  $M_{23}C_6$  type carbides (Sims 1968). This is beneficial for strengthening but detrimental because the formation of carbides removes valuable amounts of *Cr* required in solid solution. Since these carbides have a high *Cr* to *C* ratio, high *Cr* contents in the alloy (of up to 30 wt%) are required to establish enough *Cr* in solid-solution to attain good corrosion resistance. In addition, *Cr* acts as a solid solution strengthener and hcp stabilizer.

Molybdenum is added because of its carbide forming tendency and its solid-solution strengthening effect. When *Mo* is added in quantities of 3-4 wt% in stainless steels (e.g., 316L stainless steel), the alloy exhibits better resistance to pitting, sulfuric acid and hot organic acids (Fontana and Greene 1978). The same features can be applied to *Co* alloys, making it a more attractive material for biomedical applications. Similar to *Cr*, *Mo* is also a solid solution strengthener and an hcp stabilizing element.

The addition of *C* strengthens the alloy by forming a solid solution with *Co* and through carbide precipitation. In fact, the effect of *C* as a solid solution strengthener is 100 times that of *Ni* when used in stainless steels. However, the solubility is low. Carbon is also an fcc stabilizer (like *Ni*), but is 30 times more effective than *Ni* in austenitic stainless steels (Pickering 1978).

Modified *Co-Cr-Mo* compositions and processing methods for enhanced thermal and mechanical properties brought significant advantages for medical device manufacturers. The influence of grain size, secondary phases, and interstitial levels on mechanical properties has been better defined for wrought low- and high-carbon alloys. Numerous studies have evaluated the effect of surface modifications that influence wear resistance, and test protocols have been established to characterize the corresponding tribological properties. Berry et al. (1999) provided important manufacturing information related to the production of a wrought high carbon analysis. Thermo-mechanical processing studies were aimed at optimizing the metallurgical structure in order to provide well-defined mechanical properties and improved wear resistance. The work by Berlin et al. (1999) highlighted the importance of post processing on the mechanical properties of investment cast and wrought alloy versions. Post processing operations such as abrasive blasting had no effect on fatigue, but sintering of porous coatings and laser marking reduced the fatigue strength of investment cast and wrought alloys. The post sinter fatigue strength of low carbon wrought alloy was dramatically reduced and was lower than the hot isostatically pressed ASTM F75 castings. Another study by Mishra et al. (1999) included extensive metallographic examination, tensile testing, and axial tension-tension fatigue testing to compare investment grade cast versus high-carbon-wrought compositions with porous coatings. They concluded that the decreased chemical segregation and finer grain size may have been responsible for the improved fatigue strength observed for the wrought high-carbon analysis. Lippard and Kennedy (1999) reviewed the manufacturing operations for the production of wrought bar product intended for a variety of biomedical applications. Important technical information was

documented for primary melting, remelting, hot rolling, annealing, and cold-working processes utilized for commercially available *Co-Cr-Mo* compositions. The effects of thermo-mechanical processing on the microstructure and tensile properties were presented for wrought low-carbon and high-carbon *Co-Cr-Mo* material.

One of the causes of friction in metals is deformation process, where the metal surfaces are deformed both elastically and plastically. In general, when metals are plastically deformed, atomic planes are sheared in response to an external force. This shearing of atoms is referred to as slip, which is an anisotropic process; it only occurs on specific atom planes or close packed planes in a crystal. Therefore, the response to deformation will depend on the crystal structure of the material and crystal orientation. For example, hexagonal close packed (hcp) metals exhibit a lower friction (about 30%) than face centered cubic (fcc) metals (Rabinowicz 1995). If the crystal lattice of the contact surfaces are oriented in such a way that slip may easily occur, then one should also expect the coefficient of friction to drop (Sarkar 1976).

The tribological behavior of *Co-Cr-Mo* alloys used as hip implant materials was examined through the pin-on-disk wear test by Saldivar-Garcia and Lopez (2005). Fully fcc and hcp *Co*-based alloys were tested versus alloys with various volume fractions of hcp phase (0.05 to 1.0 volume fractions). It is found that the set composed by both disks and pins having hcp (hcp-hcp) microstructures exhibited the lowest volume losses, whereas the one corresponding to both having fcc microstructures (fcc-fcc) gave the highest volume losses. The set with intermediate wear performance consisted of an hcp disk and biphasic pins. The results indicated that the hcp structure contributed to improve the wear performance of *Co-Cr-Mo* alloys in metal-on-metal wear tests, and the pairs

both possessing an hcp microstructure tend to exhibit outstanding wear properties. The study by Chiba et al. (2007) demonstrated that the forged no-carbon *Co-Cr* alloy which is more prone to strain-induced fcc-hcp transformation exhibited excellent like-on-like wear performance, mostly against surface fatigue wear, compared to the carbide-hardened cast *Co-Cr* alloy.

Fundamental research into cobalt-based phase transformations has provided the opportunity to improve the thermo-mechanical processing response. Due to the sluggish fcc-hcp transformation of the cobalt alloys made by pure thermal processing methods, the easiest way to generate the hcp structure (at least partially) is by cold working (Martin 2006). The formation of so-called “hcp platelets” is believed to progress through stacking fault coalescence. Salinas-Rodriguez (1999) described fundamental research on the role of fcc to hcp phase transformation during plastic deformation of *Co-Cr-Mo* compositions containing low- and high-carbon content. High-carbon content and slow cooling after thermal treatment inhibited the metastable fcc-hcp phase transformation. In contrast, a fast cooling rate after solution annealing and a controlled grain size range promoted phase transformation during deformation. The strain-induced phase transformation predominated when the carbon content was <0.05%, while the size, morphology, and distribution of secondary carbide particles controlled the ductility and fracture behavior at higher carbon levels. Another study on the allotropic transformation of cobalt also found that, as shown in Figure 2.3, the onset temperature for fcc to hcp transformation ( $M_s$ ) decreased significantly with increasing cooling rate (Ray et al. 1991), which indicated that the application of different cooling methods during processing would play an important role on this fcc to hcp transformation.

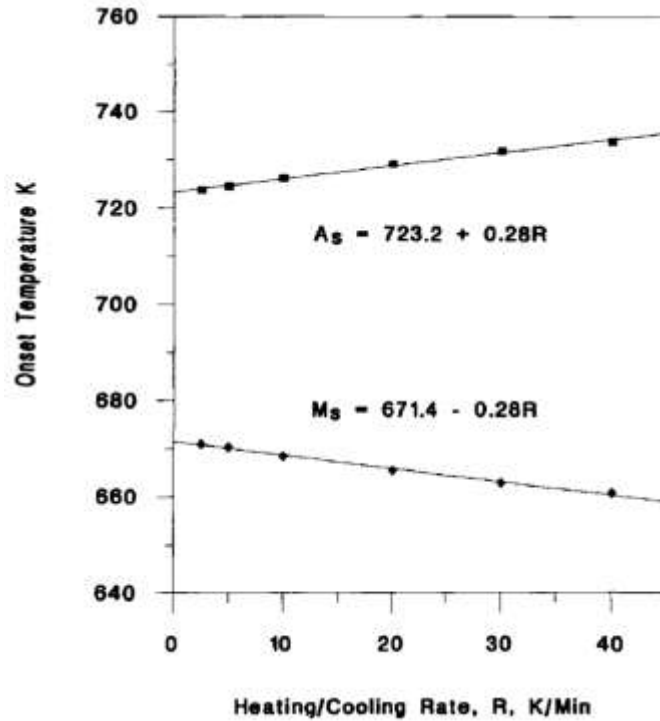


Figure 2.3: Effect of heating and cooling rates on the onset temperatures of  $A_s$  (hcp to fcc) and  $M_s$  (fcc to hcp) transformations (Ray et al. 1991).

Our prior research on machining of *Co-Cr-Mo* alloys for improved wear performance proved that controlled machining processes could greatly improve wear resistance. Pin-on-disk wear tests were conducted for evaluating the wear performance of machined *Co-Cr-Mo* pins. The influence of different machining conditions used in making the pin specimens including cutting speed, depth of cut, feed and nose radius of the tool, on the wear rate of *Co-Cr-Mo* was investigated. A genetic algorithm-based procedure was developed and used to determine the optimal cutting parameters for minimized wear/debris generation while satisfying the optimization constraints of surface roughness, surface microhardness and surface residual stress. The results from this study can help researchers select the right cutting parameters for achieving the most desired process characteristics (Deshpande et al. 2012).

### **2.3 Investigations on process, surface integrity and functional performance**

Most of the biological activities are happening on implant surface regions, especially for joint implants, the bearing surfaces moving relative to each other is a phenomenon that mainly concerns the surface region structure and properties, particularly respect to wear and fatigue performance of the material.

Surface integrity is a measure of the quality of a machined surface and is interpreted as elements which describe the actual structure of both surface and subsurface (Jang et al. 1996). Surface integrity is generally defined by its mechanical, metallurgical and chemical states of surface properties such as surface roughness, hardness variation, structural changes and residual stress, etc. (Table 2.2). Among those elements, residual stresses and microstructure in the surface layers as well as surface roughness play critical roles in determining the performance of biomaterials due to the rigorous requirements on the biomedical devices. Improving the surface integrity properties of materials has long been the objective of many researchers, and a thorough review of surface integrity property impacts on material functional performances can be found in a recent study by M'Saoubi et al. (2008).



Table 2.2: Different Levels of Surface Integrity (SI) Data Set (M'Saoubi et al. 2008)

Minimum SI data set	Standard SI data set	Extended SI data set
1. Surface finish	1. Minimum SI data set	1. Standard SI data set
2. Macrostructure (10X or less)	2. Fatigue tests (screening)	2. Fatigue tests (extended to obtain design data)
<ul style="list-style-type: none"> <li>• Macrocracks</li> <li>• Macroetch indications</li> </ul>	3. Stress corrosion tests	3. Additional mechanical tests
3. Microstructure	4. Residual stress and distortion	<ul style="list-style-type: none"> <li>• Tensile</li> <li>• Stress rupture</li> <li>• Creep</li> <li>• Other specific tests (e.g., bearing performance, sliding friction evaluation, sealing properties of surfaces)</li> </ul>
<ul style="list-style-type: none"> <li>• Grain size</li> <li>• Microcracks</li> <li>• Plastic deformation</li> <li>• Phase transformation</li> <li>• Intergranular attack</li> <li>• Pits, tears, laps, protrusions</li> <li>• Built-up edge</li> <li>• Melted and redeposited layers</li> <li>• Selective etching</li> </ul>		
4. Microhardness		

Severe plastic deformation (SPD) processes have been extensively reported for modifying surface region properties by introducing refined grains and grain size gradients into the surface region of many materials. Langford and Cohen (1969) imposed large plastic strains in iron by repeated passes of wire drawing and found the microstructure of the deformed iron wire to be composed of grains with sizes in the sub-micrometer range.

Yamanaka et al. (2009) conducted hot-compression processing on *Co-29Cr-6Mo* alloy under different temperatures, strains and strain-rates conditions, their results showed that an ultrafine-grained microstructure with a grain size of approximately 0.6  $\mu\text{m}$  was obtained from an initial grain size of 40  $\mu\text{m}$ , and grain refinement due to dynamic recrystallization (DRX) was identified under all deformation conditions. Figure 2.4 shows the effects of strain-rate on microstructure evolution of *Co-29Cr-6Mo* alloy; microstructure refinement was clearly visible with increasing strain-rates. The results from this work indicated that temperature, strain and strain-rate have substantial influence on the microstructure evolution of the material during processing.

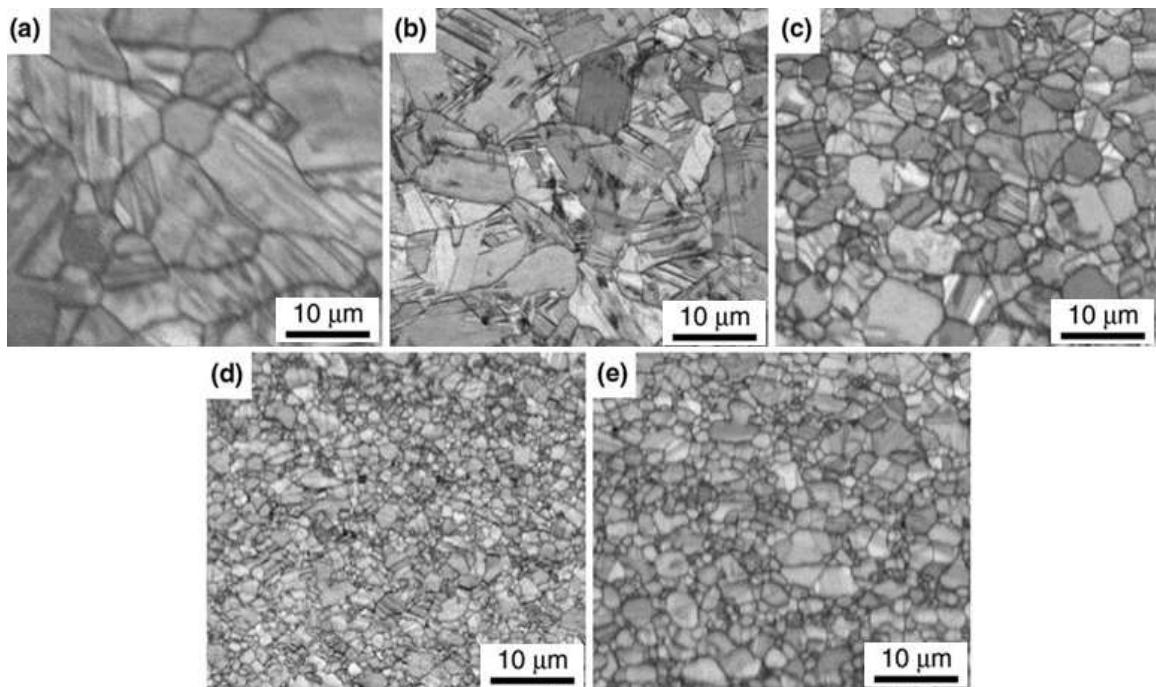


Figure 2.4: Effect of strain-rate on microstructure evolution of *Co-29Cr-6Mo* alloy deformed to true strain of 0.92 at 1150 degree C at (a)  $10^{-3} \text{ s}^{-1}$ , (b)  $10^{-2} \text{ s}^{-1}$ , (c)  $0.1 \text{ s}^{-1}$ , (d) 1.0, and (e)  $10 \text{ s}^{-1}$  (Yamanaka et al. 2009)

The group of machining researchers led by Chandrasekar at Purdue University, in a series of their publications, showed that severe plastic deformation involving large

strains of 3-15 imposed on the chips can strongly influence the refinement of grains in the chip and the machined work surface and subsurface (Brown et al. 2002; Swaminathan et al. 2007a; Swaminathan et al. 2007b). Their work showed that for materials such as copper and its alloys, precipitation-hardenable aluminium alloys, high temperature/high strength materials such as titanium, *Inconel 718*, *AISI 52100* hardened steel and amorphous alloys, average grain sizes in the range of 60 nm~1  $\mu\text{m}$  can be created by just varying the parameters of the machining process.

The use of similar SPD approaches to achieve microstructure refinement has received an impetus in recent years. More and more evidences show that SPD induced nano-sized/ultrafine grained materials possess appealing properties compared with their coarse-grained counterparts. Wang et al. (2003b) fabricated a nanocrystalline surface layer on a low carbon steel plate via SPD process; improvements of wear resistance with the nanocrystalline surface layer were demonstrated. A study by Iglesias et al. (2007) also showed that wear rates of nanostructured copper and titanium created by large strain extrusion machining were significantly lower than that of their coarse-grained counterparts. Karimpoor et al. (2003) also found that nanocrystalline cobalt exhibited unusual mechanical properties such as remarkable work hardening and ductility comparable to those in coarse-grained cobalt.

Nanocrystalline surface layers were generated by SPD process on *Cu*, steels and *Mg* alloy with emphasis on reciprocating sliding wear behaviors (Shi and Han 2008). The wear resistances of the treated alloys were improved compared to the untreated alloys. Figure 2.5 gives the representative results of microstructure and wear performance of SMAT treated copper sample. As shown in Figure 2.5 (a) and (b), the grain size

distribution of the top surface layer was in the range of 5~30 nm. The corresponding sliding wear results (Figure 2.5 (c)) and fretting wear (Figure 2.5 (d)) showed significant improvements comparing to the coarse-grained copper sample.

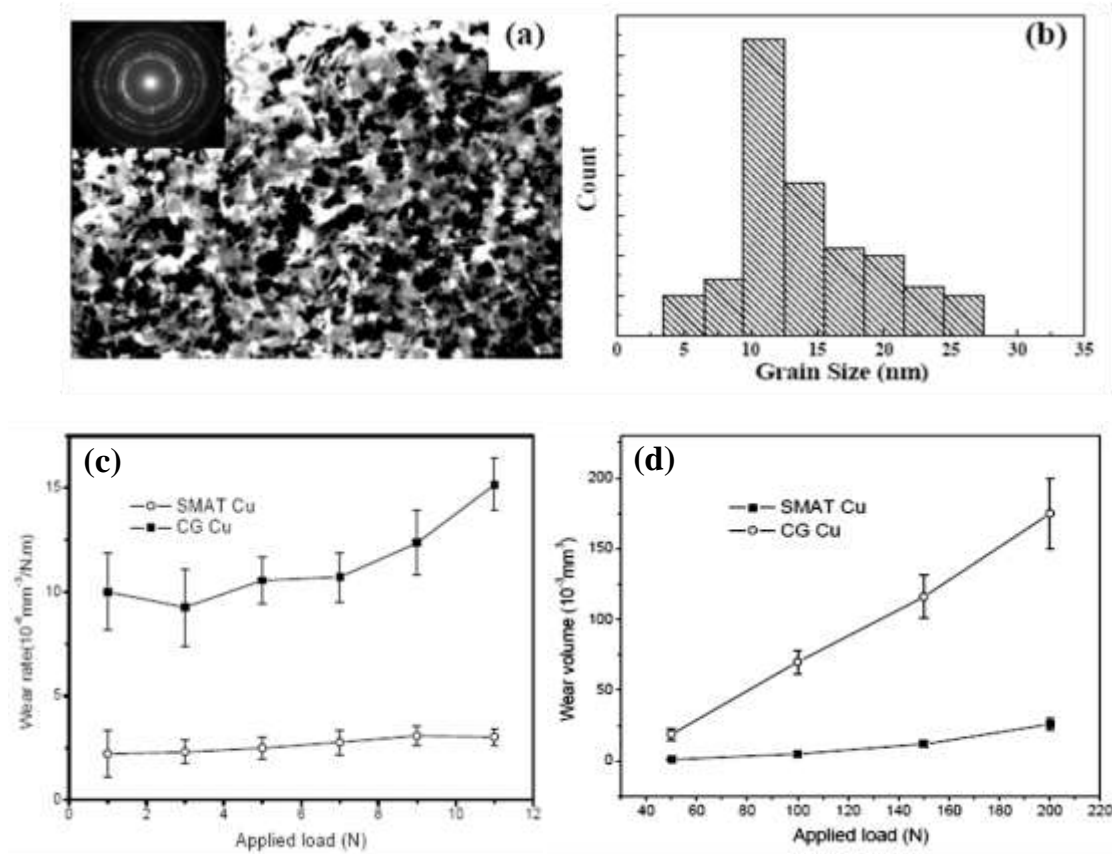


Figure 2.5: (a) A bright-field TEM image and a corresponding selected area diffraction pattern; (b) grain size distribution of the top surface layer of the SMAT *Cu* for 30 minutes; (c) variations of wear rate with the applied load for the 30 minutes SMAT *Cu* and the coarse-grained *Cu* at a sliding velocity of 0.01 m/s; (d) variation of the wear volume with the applied load for the SMAT *Cu* and the coarse-grained *Cu* samples against a *WC-Co* ball in mineral oil (Shi and Han 2008)

In an earlier work, Han et al. (2006) also compared the dry sliding tribological behavior of an electrodeposited nanocrystalline *Cu* and a conventional microcrystalline

*Cu*. Experimental results showed that the wear resistance of nanocrystalline *Cu* was enhanced. The steady-state friction coefficient of the nanocrystalline *Cu* was obviously lower than that of the microcrystalline *Cu* when the load was below 20 N. The wear volume of the nanocrystalline *Cu* was always lower than that of the microcrystalline *Cu* for the applied load ranging from 5 to 40 N. The difference in wear resistance between the nanocrystalline and the microcrystalline *Cu* decreased with increasing load. The enhancement of the wear properties of the nanocrystalline *Cu* was associated with the high hardness and the low work-hardening rate of the nanocrystalline structure, and easy oxidation of wear debris, which are all related to grain refinement.

Dao et al. (2007) conducted a complete review on the tribological properties of nanocrystalline materials. It is claimed that the best choice for wear resistance is to synthesize a nanocomposite material where nanocrystalline hard-metallic or nonmetallic particles are embedded in a relatively compliant metallic matrix; this is due to the fact that a nanocomposite material contains a high density of interphase interfaces which may assist in crack deflection and termination of crack growth (Cavaleiro and De Hosson 2006; Galvan et al. 2005). Moreover, other mechanisms, like interface diffusion (Karch et al. 1987) and sliding (Nieh et al. 1991; Sherby and Wadsworth 1989), are also suggested to further improve ductility in nanocrystalline multiphase structures. These findings could be expanded to the field of hard wear resistant coatings to introduce ductility and prevent fracture under a high contact load, leading to super toughness (Voevodin and Zabinski 2000).

In addition to the microstructure refinement, the mechanical properties are significantly influenced by the process induced residual stresses at the surface region as

well. It is reported that residual stresses in the machined surface considerably affect the service quality of the component including fatigue life and tribological properties, plus, compressive residual stresses were more favorable for improving rolling contact fatigue life than tensile ones (Thiele et al. 2000). As shown in Figure 2.6, the fatigue strength of *Co-Cr* alloys manufactured by hot isostatic pressing (HIP) was more than 50% larger than that of the cast alloys, which was attributed to the compressive residual stresses generated from processing. Compressive residual stresses induced by forging almost doubled the fatigue strengths of cast 316L stainless steel and cast *Co-Cr* alloys (Teoh 2000).

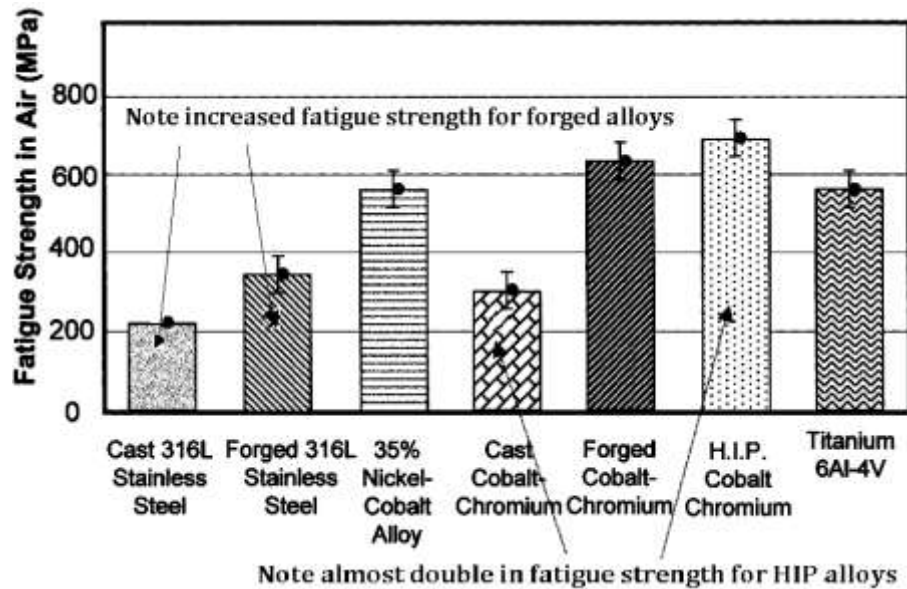


Figure 2.6: Fatigue strength of some common implant alloys (Teoh 2000).

Sasahara (2005) also showed that surface hardness and residual stress had substantial influence on fatigue life (Figure 2.7). As a general trend, it was obvious that the fatigue life around the region A in Figure 2.7, where the axial residual stress was tensile, was short. On the other hand, the fatigue life around the region B and C in the

same figure was very long, where the axial residual stress was from neutral to compressive. In fact, the residual stress distributions along the surface as well as subsurface region were considered to be decisive in determining fatigue life. However, it can be seen that the surface residual stresses alone were enough to affect the fatigue life of the machined parts. In addition, the impacts of tool nose radius, feed rate and shape of cutting edge on residual stresses and hardness changes indicated the essential significances of processing conditions.

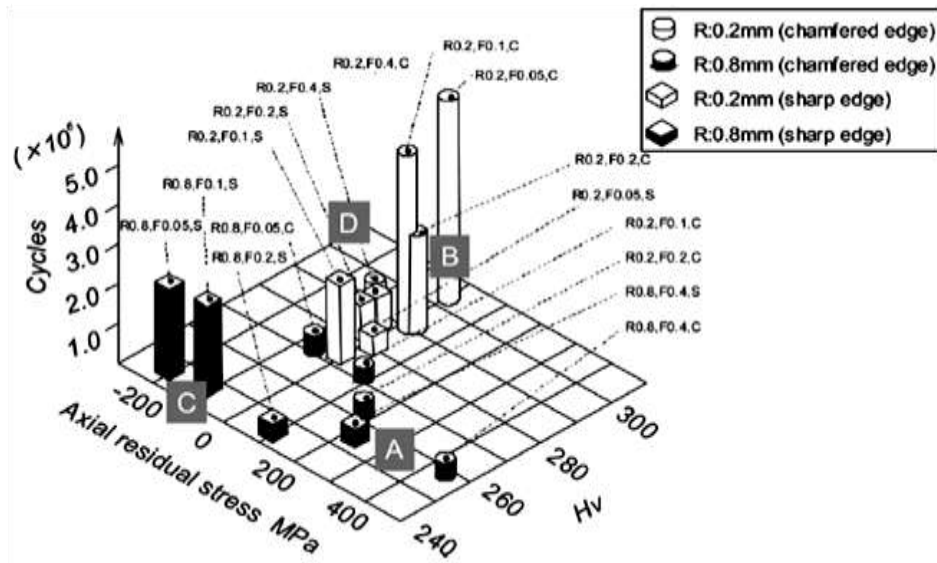


Figure 2.7: Interaction of axial residual stress and hardness on fatigue life (Sasahara 2005)

A large number of studies have been undertaken to evaluate the machining condition effects on surface integrity properties. However, their results show that the residual stresses from machining tend to be tensile by nature; compressive residual stresses can be generated only under certain processing ranges. Leskovar and Peklenik (1981) investigated the influence of cutting process parameters on surface and subsurface conditions in turning, and showed that tensile stresses are dominant after turning and that higher speed tends to produce higher residual stresses. Jang et al. (1996) found that hoop

residual stresses in the cutting direction were predominantly tensile in the machined 304 stainless steel components. Fattouh and Elkhabeery (1989) also showed that machining induces tensile residual stresses to the surface layers in general (Figure 2.8 (a)).

#### **2.4 Surface integrity in burnishing**

Many studies have shown that burnishing is an effective and economic way of improving the fatigue life of components in terms of inducing large amount of compressive residual stresses to the surface region along with refined microstructure and excellent surface quality. Using burnishing in medical device manufacturing applications is new and there are not many research results available in the literature, however, its applications in automotive and aerospace fields have been initiated for a much longer time with more published research results.

Fattouh and Elkhabeery (1989) studied the residual stress distribution in the surface region of solution treated and aged 7075 aluminum alloy workpieces that were orthogonally burnished under lubricated conditions. Their results showed that machined surfaces having tensile residual stresses became compressive after burnishing. Moreover, the maximum residual stress and depth of the stressed region increased with an increase in burnishing speed, force and burnishing time, as shown in Figure 2.8.



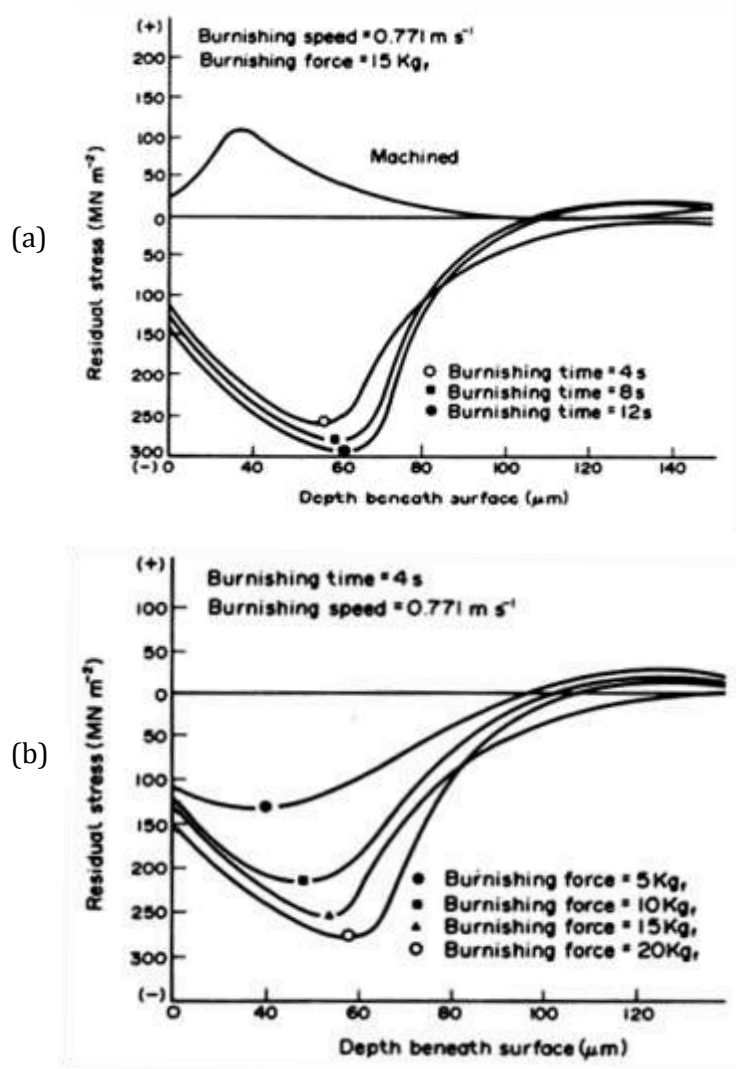


Figure 2.8: (a) Residual stress distribution in surface region due to machining and burnishing, and the influence of burnishing time on residual stress; (b) the influence of burnishing force on residual stress (Fattouh and Elkhabeery 1989)

Studies by Hassan and AlBsharat (1996) and Zhuang and Halford (2001) also reveal that burnishing process imparted compressive residual stresses in the surface region that could mitigate fatigue cracks that usually initiate at the surface. Zhang and Lindemann (2005) have shown that the roller burnishing improved the high cycle fatigue strength of AZ80 alloy by about 110% and an increase of 60% was demonstrated by

Maximov et al. (2009). Compressive residual stresses and hardened surface layer were generated on aluminum *7075-T651* alloy by using a machining-burnishing tool (Segawa et al. 2004). Majzoobia et al. (2009) also found that an increase of about 700% was achieved on fretting fatigue resistance of Aluminum *7075-T6* alloy by deep rolling.

Radziejewska and Skrzypek (2009) conducted hot and cold burnishing processes on carbon steels alloyed with cobalt stellite. Their results showed that the burnishing process had caused deformation of grains up to 20-30  $\mu\text{m}$  thick zone and increased microhardness of the surface zone material. Generation of compressive stresses in surface layer of the alloyed material was also achieved from burnishing. As shown in Figure 2.9, tensile stresses were recognized only in the case of the laser alloyed sample (line 2); compressive residual stresses were generated in surface layer after burnishing (line 1 and 3); especially for the sample which was cold burnished, high compressive stresses were recognized in the analyzed region (line 3), which indicated that processing temperature has a substantial effect on residual stress generation as well.

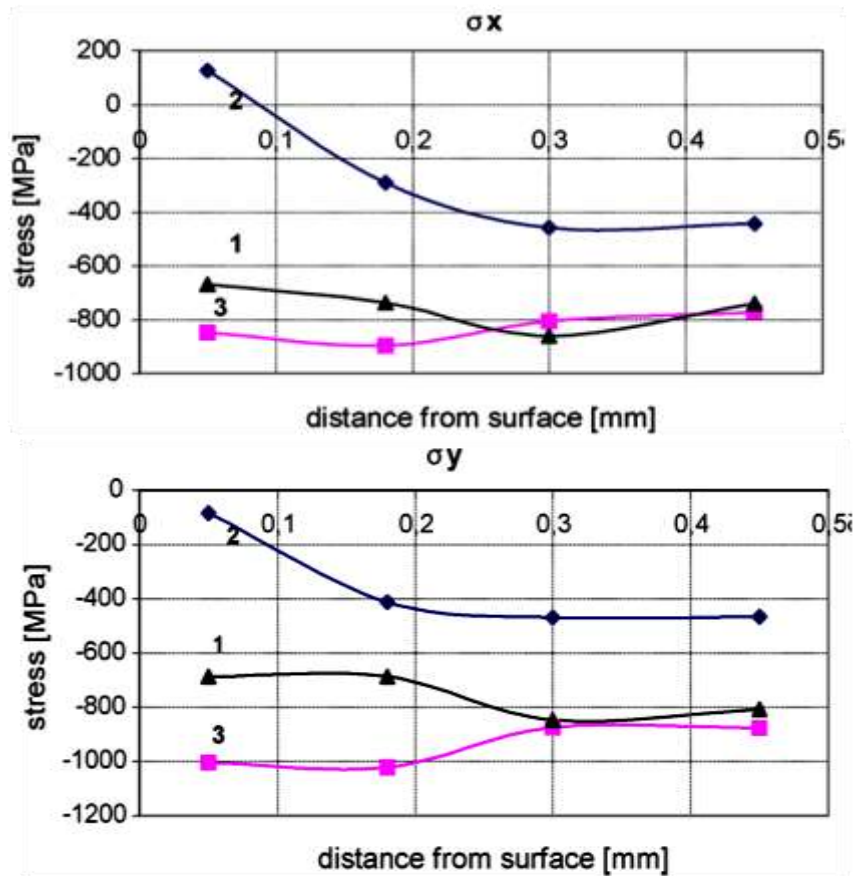


Figure 2.9: Changes in residual stress values (a)  $\sigma_x$  and (b)  $\sigma_y$  in function of distance from surface in vicinity of the sample after multiple-path alloying (line 2) and alloying combined with cold (line 3) and hot burnishing (line 1) (Radziejewska and Skrzypek 2009).

In a recent work (Rodriguez et al. 2012), a deep ball-burnishing process was conducted on *AISI 1045* turned parts for improving productivity and quality of rotating shafts. When this technique was combined with and applied after conventional turning, the resulting process was rapid, simple and cost-effective, directly applicable in lathes and turning centers of production lines. Good surface finish, high compressive residual stresses, and hardness increment of the surface layer were achieved after this process. These characteristics are the key for the fatigue life improvement of the component, and

for wear resistance due to the higher hardness. Prevéy and his co-workers (Prevéy 2000; Prevéy et al. 2001; Prevéy et al. 2000) have shown that by using low plasticity burnishing, a compressive residual stress surface layer with sufficient depth can be created on many materials. These finally led to significant enhancements to the fatigue life of the components. By using a similar low plasticity burnishing method, surfaces with high hardness and large compressive residual stresses were generated on *MgCa* alloys (Salahshoor and Guo 2011). Findings from literature survey indicate that burnishing process tends to introduce compressive residual stresses to the surface region. Moreover, the substantial influences of burnishing conditions on residual stress distribution suggest that an optimal residual stress distribution could be generated under proper burnishing conditions.

In addition to residual stresses, burnishing induced microstructure refinement is demonstrated by many investigators. Altenberger et al. (1999) created nanocrystalline surface layers with compressive residual stresses on *AISI 304* stainless steel from deep rolling. Their results showed that this nanocrystalline surface region remain stable against cyclic loading, even at high stress amplitudes, and impede dislocation movement and slip band formation. Nalla et al. (2003) conducted deep rolling on *Ti-6Al-4V* alloy; it was found that deep rolling is quite effective in improving the fatigue properties at elevated temperatures up to  $\sim 450$  °C, they also observed that the near-surface microstructures consisted of a layer of work hardened nanoscale grains, which were believed to play a critical role in the enhancement of fatigue life. Later on, (Palka et al. (2006) found that burnishing of *X5CrNi 18-9* stainless steel led to an increase in number of slip bands, density of dislocations and twinning deformations in the burnished surfaces, resulting in

an increase in the yield stress from 230 to 450 MPa. These surface properties are generally advantageous. The effect of ball burnishing process on *AISI 1010* steel was investigated by Gharbi et al. (2011), it is found that good surface quality with refined microstructure on the surface layer can be created when proper burnishing conditions were selected. However, they also found that excessive burnishing can lead to subsurface cracks which cause flaking of the burnished surfaces. An ultrafine-grained surface layer was produced on *Mg-Al-Zn* alloy by cryogenic burnishing (Pu et al. 2011b). The total burnishing-influenced zone was found to be over 3.4 mm thick. A large increase in hardness from 0.86 to 1.35 GPa was obtained near the topmost surface, where grains were refined from 12  $\mu\text{m}$  down to 260 nm. The corrosion resistance of the burnished material was significantly enhanced, which was attributed to the combined effects of grain refinement and strong basal texture appearing in the surface.

Moreover, many researchers have pointed out that the burnished surface quality has many advantages over machined ones, which directly or indirectly lead to advanced functional performance of these components. It was revealed that burnishing process helps to reduce friction up to a critical depth due to better surface finish (El-Tayeb 1994). In another study by El-Tayeb (1993), burnishing process was found to reduce wear rate by 38% for copper and 44% for *St-37* steel under proper processing conditions. After roller burnishing of structural *Rb40* steel, Hamadache et al. (2006) observed 89% wear improvement and up to 9% hardness improvement compared to the sample from turning. El-Tayeb et al. (2008) also found that the roller burnishing is capable of decreasing the surface roughness up to 40% in comparison with turning. A 40% reduction of surface

roughness was presented from burnishing after laser alloying of carbon steels with cobalt stellite (Radziejewska et al. 2005).

Compared with grinding, significant improvements in surface roughness, surface microhardness and compressive residual stresses were achieved after sliding burnishing of *42CrMo4* alloy steel shafts with a diamond cylindrical-ended tool (Korzynski et al. 2011). The effect of burnishing parameters on surface roughness and oscillatory bending strength was investigated. Fatigue strength was increased by 18% compared to that of the ground workpiece.

The ease of implementation in standard CNC machining centers offers the possibility of employing burnishing as an effective means of mitigating corrosion fatigue and pitting fatigue initiated failures in aircraft components without altering either material or design (Jayaraman et al. 2007). Applied locally to high stress fatigue prone locations in aging aircraft, burnishing could extend the service life of aircraft structural components, reduce the total cost of fleet ownership, and improve fleet readiness.

Tsuji et al. (2008) used deep rolling to induce compressive residual stress in plasma-carburized *Ti-6Al-4V* alloy sample. The fatigue properties and wear resistance of *Ti-6Al-4V* alloy modified by a combination of low temperature plasma-carburizing and deep rolling were significantly improved in comparison with those of the unmodified *Ti-6Al-4V* alloy. Knowing that fatigue fracture is normally affected by stress concentrators such as holes, grooves and fillets, and also the fact that most engineering designs have notch-like features, in another study, Tsuji et al. conducted plasma-carburizing and subsequently deep-rolling processes on *Ti-6Al-4V* alloys (Tsuji et al. 2009). It was found

that the notch fatigue property of the *Ti-6Al-4V* alloy was remarkably enhanced by after deep rolling process.

Denkena and Lucas (2007) developed combined tools which could cut material and do surface modification simultaneously. The ultimate goal was a selective surface enhancement of structural components through controlled manipulation of subsurface properties. They targeted several millimeters as an in-depth affected zone. Deep rolling was one of the main processes they used to combine with machining processes such as turning and milling to achieve these improvements.

More recently, Grzesik and Zak (2012) compared the surface roughness of *41Cr4* low-alloy steel from conventional cutting, Wiper tool cutting and multipass burnishing operations, the results showed that the improvement of the surface roughness through the burnishing process is about 94% over the one from conventional cutting and 40% over Wiper tool cutting. It is also reported that after burnishing of a hardened steel component (64 HRC) with a ball of 6.35 mm diameter, a target roughness  $R_a = 0.5 \mu\text{m}$  was obtained. In particular, when the surface which was turned with a tool of 0.8 mm nose and feed rate of 0.1 mm/rev and subsequently burnished with a pressure of 38 MPa, surface roughness  $R_a$  reduced to about 0.2  $\mu\text{m}$  (Luca et al. 2005). The roughness improvement ranged between 40% and 90% was obtained after burnishing processes (Shiou and Hsu 2008). Burnishing is also reported to be a cost effective method to prevent corrosion and stress corrosion cracking, and to enhance the wear resistance and fatigue life of the workpiece (Hassan and AlBsharat 1996; Hassan and Momani 2000).

## 2.5 Effect of cryogenic cooling in manufacturing processes

Excessive heat and consequently tool-wear and sometimes poor surface quality are the most important factors affecting performance and productivity of metal processing operations. The cooling applications in machining operations play a very important role and many operations cannot be carried out efficiently without some cooling. Application of a coolant in a cutting process can increase tool-life and dimensional accuracy, decrease cutting temperatures, surface roughness and the amount of power consumed in a process and thus improve the productivity.

The major roles cryogenic cooling plays in machining were defined by Hong and Zhao (1999) as removing heat effectively from the cutting zone, lowering cutting temperatures, modifying the frictional characteristics at the tool/workpiece interfaces, and changing the properties of the workpiece and the tool material.

Exceptional tool-life and surface roughness improvements were achieved with cryogenic cooling over those obtained from using dry and emulsion cooling. In machining of some materials, reductions in tool flank wears up to five fold were obtained with cryogenic cooling (Wang and Rajurkar 1997). Similarly, in machining of *AISI 304* stainless steel using cryogenic cooling, tool-life was increased more than four times (Khan and Ahmed 2008). Another study showed similar results that the  $Al_2O_3$  ceramic inserts cooled by cryogenic cooling method significantly outperformed conventional dry PCBN operations (Ghosh 2005). Wang et al. (2003) employed a hybrid cryogenic machining method with plasma heating enhanced during machining of Inconel 718 and their results indicated an improvement of 156% in tool-life and a 250% improvement in



surface roughness when compared with conventional machining. Zurecki et al. (2003) made a tool-life comparison between cryogenic nitrogen cooled  $Al_2O_3$ -based cutting tools and conventionally cooled CBN tools in machining of hardened steel. They applied cryogenic coolant by spraying with a nozzle to the rake surface of the tool and found that cryogenic cooled  $Al_2O_3$ -based cutting tools endured longer than the conventionally cooled CBN tools. Kumar and Choudhury (2008) investigated dry cutting conditions and cryogenic liquid nitrogen spraying by a nozzle in machining of stainless steel 202 with a carbide insert in terms of tool-wear. They observed about 37.39% advantage in the flank wear with cryogenic machining over the dry cutting. In application of indirect cryogenic cooling, the surface roughness of materials machined with liquid nitrogen cooling was found to be much better than the surface roughness of materials machined without liquid nitrogen cooling. The large differences were attributed to the variation in the tool-wear. Since, the tool-wear increased with the length of cut and the surface roughness increased with tool-wear (Wang and Rajurkar 2000). In the study by Bhattacharyya et al. (1993), better surface finish was obtained with continual flooding of liquid nitrogen onto the workpiece.

In addition to the beneficial contributions of cryogenic cooling on tool-wear and surface finish, the effect of cryogenic cooling process on the resulting workpiece properties (e.g. microstructure, residual stresses, etc.) are of more critical significance to the interests of the current work. Due to the large amount of heat generated during processing, refined grains from SPD are often subjected to growth under high temperature. The cryogenic process has been reported to successfully introduce thicker surface layers consisting of ultrafine/nano-grain structures. By using surface mechanical

grinding treatment at cryogenic temperatures, Li et al. (2008) synthesized a gradient nano-micro-structure in the surface layer of bulk pure copper. The average grain size varied from about 22 nm in the topmost surface to sub-micrometers at about 200  $\mu\text{m}$  deep (Figure 2.10), corresponding to a gradient change in hardness from 2.1 to 1.1 GPa in the coarse-grained matrix. The results proved that severe plastic deformation under cryogenic conditions can successfully introduce nanocrystalline grain structures to the surface and sub-surface layers.

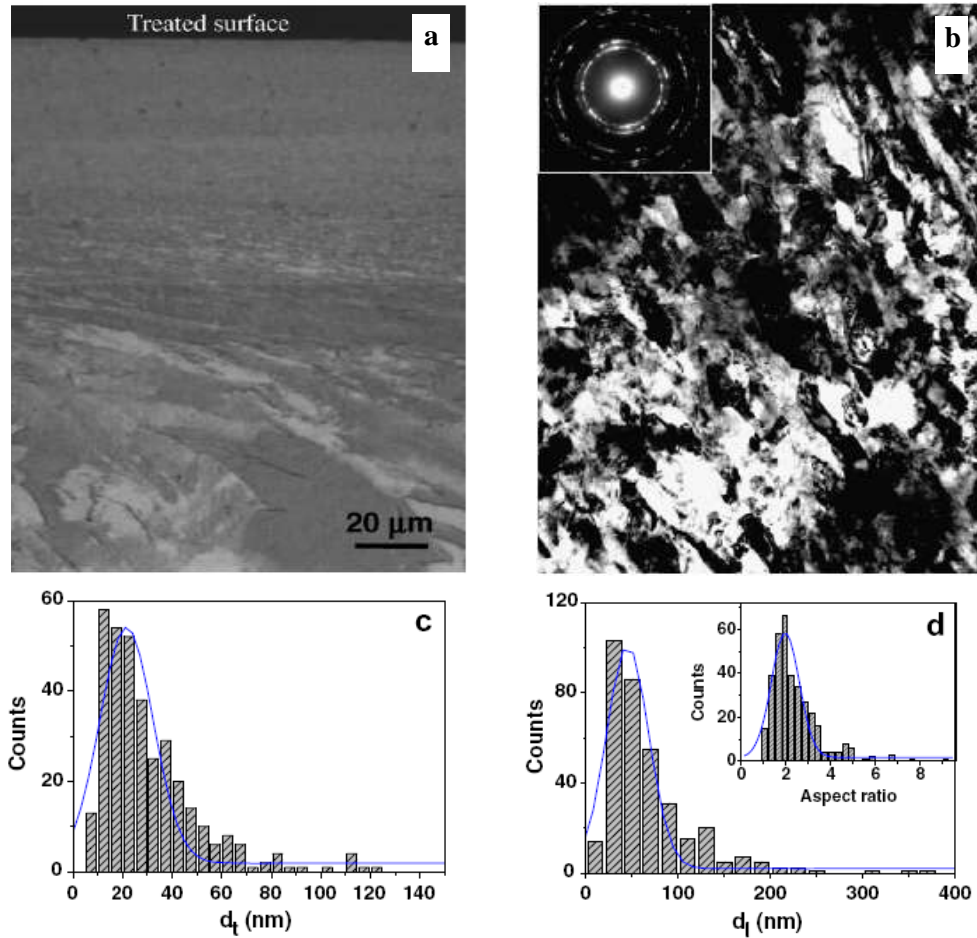


Figure 2.10: (a) Cross-sectional observation of the *Cu* sample processed by means of SMGT; TEM observations and grain size distributions of the top surface layer: (b) bright field image, (c) transverse axis grain size ( $d_t$ ), (d) longitudinal axis grain size ( $d_l$ ).

(Li et al. 2008)

Ni et al. (2004) also reported that by use of cooling fluid during machining, grain growth occurred in the secondary deformation zone (SDZ) resulting in large equiaxed grains of 1.2  $\mu\text{m}$  in diameter was effectively restricted by limiting the grain size to 360 nm (Figure 2.11). More recently, it is found that with the application of liquid nitrogen during burnishing of *AZ31 Mg* alloy, an average grain size of  $523 \pm 131$  nm was achieved, in comparison with the 1.4  $\mu\text{m}$  grain size from dry burnishing, the grain size was reduced by a factor of 3 by using cryogenic cooling (Pu et al. 2012b).

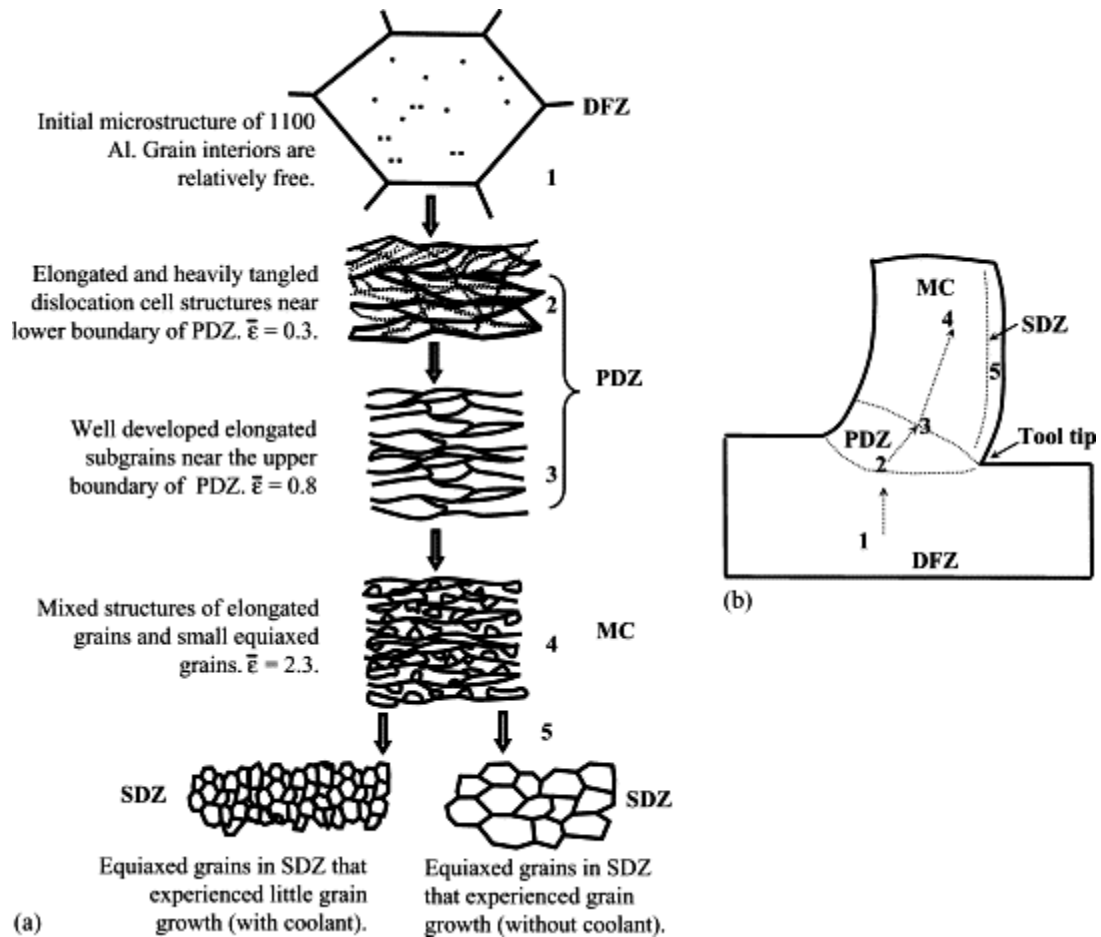


Figure 2.11: (a) Schematic illustration of the main steps of microstructural evolution in 1100 Al subjected to orthogonal cutting. (b) The sequence of grain refinement events shown on the cross-section of the material ahead of the tool tip (Ni et al. 2004)

Along with the benefits on grain refinement, cryogenic SPD is also expected to introduce compressive residual stresses on the surface and sub-surface layers. Few studies have examined effect of cryogenic cooling on residual stresses. It has been reported that the residual stress distribution in *AISI 52100* steel was improved under cryogenic machining conditions (Zurecki et al. 2003). Another study on machining of Inconel 718 showed that the cryogenic machining generated larger compressive residual stresses, and prevailed at deeper levels beneath the machined surface (Kenda et al. 2011). In a recent work, the effect of cryogenic treatment on the residual stresses of *4140* steel was studied by Senthilkumar et al. (2011). Two kinds of cryogenic treatment, shallow ( $-80\text{ }^{\circ}\text{C} \times 5\text{ h}$ ) and deep cryogenic treatment ( $-196\text{ }^{\circ}\text{C} \times 24\text{ h}$ ) were carried out between quenching and tempering in conventional heat treatment process. The results showed that the increases in the compressive residual stress in steel were subjected to cryogenic treatment before tempering. In addition, conventional heat treatment and shallow cryogenic treatment promoted a tensile state of residual stress, while deep cryogenic treatment generated a compressive residual stress.

In summary, the processing-induced surface integrity modifications in terms of fine microstructure, compressive residual stresses, desirable crystal structure and low surface roughness together collectively contribute to the improvements in the mechanical properties of the material (Jawahir et al. 2011), which finally lead to improvement in wear performance of the processed material (Abbas and West 1991; Jawahir et al. 2011). However, very few studies have been devoted to quantify these simultaneous changes in surface integrity during processing, especially under cryogenic conditions.

The major purpose of this project is to study and better understand the surface integrity changes that occur during the burnishing of *Co-Cr-Mo* biomaterial, especially when cryogenic cooling is applied in conjunction with appropriate burnishing conditions to obtain implants with excellent mechanical properties, and the resulting enhanced wear performance during service.

## **2.6 Significant process and product sustainability factors**

"Sustainable Manufacturing" is defined as the creation of manufactured products that use processes that minimize negative environmental impacts, conserve energy and natural resources, are safe for employees, communities, and consumers and are economically sound (US Department of Commerce 2009). It is also stated that sustainable manufacturing includes both the manufacturing of sustainable products as well as the sustainable manufacturing of all products (National Council for Advanced Manufacturing 2009).

Machining is a major manufacturing process in the industry which constitutes the largest among all manufacturing processes, in terms of volume of production and the economic returns. Numerous attempts have been made over the last several decades to develop quantitative understandings of the effects of the process parameters on the resulting machining performance such as the machining power consumption, tool-wear rates, surface integrity, chip-forms/chip breakability, etc. Among these, the way the machining processes use coolant/lubricant applications has always been an area of significant research interest because it is critical to surface and sub-surface integrity of the machined components and to the environmental and personnel health impacts. It is also a major production cost. Analysis carried out by German Automotive industry show

that workpiece related manufacturing costs, incurred with the deployment of cutting fluids, range from 7-17% of the total machined workpiece cost (Weinert et al. 2004). In comparison to this, the tooling costs can account for approximately 2-4% (Byrne et al. 2003).

Conventional cutting fluid is an environmental contaminant and the government has issued strict regulations limiting the dumping of cutting fluid waste. Although the cutting fluid can be recycled, recycling services in the United States charge twice the purchasing price for disposal and the cost is four times as much in Europe. Conventional cutting fluids are considered as one of the top five health hazards in the workplace (Dudzinski et al. 2004). In addition to the growing environmental/health concerns, the machining industry continues to investigate methods to enhance the machining process performance and decrease production costs. Although dry machining eliminates the use of cutting fluid, it has negative impact on tool-life, tends to reduce material removal rates and increase power consumption, and often leads to unfavorable machined product quality (Klocke and Krieg 1999; Kustas et al. 1997). To identify ways to simultaneously improve machining technology and address environmental and health risks requires technological innovation.

Cryogenic machining with liquid nitrogen as the coolant is an environmentally safe alternative to conventional machining. Nitrogen fluid is liquefied by cooling to -196 °C, which is a safe, noncombustible, and noncorrosive gas. It is the most abundant gas, composes about four-fifths (78.03%) by volume of the atmosphere. Colorless, odorless, and tasteless, nitrogen is often used as an “inert” gas due to its nonreactive nature with many materials. The liquid nitrogen in cryogenic machining system quickly

evaporates and goes back into the atmosphere, leaving no residue to contaminate the workpiece, chips, machine tool, or operator, and eliminating disposal costs.

Some major benefits of cryogenic processing are summarized below (Pusavec et al.):

- Sustainable processing methods (cleaner, safer, environmentally-friendly, more health acceptable method, etc.) aiming to eliminate numerous costs associated with conventional cutting fluids and clean-up operations.
- Increased material removal rate with no increase in tool-wear and with reduced tool change over costs resulting in higher productivity.
- Increase of tool-life due to lower abrasion and chemical wear.
- Possibility of hard to machine alloys processing, which in the past, could have been produced only via expensive grinding operations.

In addition to the benefits drawn from the process point of view, improved functional performance and longer service life of products offer great societal and environmental benefits. Surface integrity plays a crucial role in the functional performance of products; enhanced product performance through process-induced surface integrity modifications demonstrates significant sustainability contributions. Due to the numerous types of existing products, this concept is focused here on biomedical joint-implants.

Increasingly, patients are receiving more hip and knee replacement surgeries, with about 600,000 hip replacement procedures alone performed in the US annually. Combined with a growing and worrisome number of hip and knee replacements in younger people, both medical and legal experts predict that the amount of hip and knee

failures may cost US taxpayers, insurers and employers billions of dollars in the coming years, according to The International Herald Tribune (Lawsuits & Legal News 2012). Because hip and knee replacements represent an entire class of products rather than simply one device or one manufacturer, the financial repercussions stemming from hip and knee implants that are alleged to be defective will likely be enormous, especially when revision surgery is taken into account. Thus, reducing wear debris generation has become increasingly a significant sustainability issue.

The major product sustainability sub-elements identified, and shown in Figure 2.12, consider the innovation based 6R (reduce, reuse, recycle, recover, redesign, and remanufacture) approach which allows for a significant transformation from a cradle-to-grave concept to multiple life-cycle consideration for a specific product (Jawahir et al. 2006). Based on the well-recognized sub-elements of the product sustainability wheel, key product sustainability contributions of current study to the joint-implant field can be summarized as:

- Energy Efficiency/Power Consumption: Cost effective manufacturing methods compared to traditional post-processing treatments.
- Purchase/Market Value: Reduced cost for making implants through eliminating post-processing treatments.
- Manufacturing Methods: More economic and effective methods for manufacturing implants.
- Health and Wellness Effect: Increased implants lifetime and functionality; reduced burden of revision or resurgery.
- Service Life/Durability: Increased lifetime of implants.



- Ease of Use: Better functionality due to improved surface integrity; reduced revision due to reduced wear debris generation.
- Functional Effectiveness: Reduced pain and better functionality; longer lifetime of implants.
- Recyclability/reusability: Replacing additional surface coatings with enhanced natural surface layers, reduced cost for coating-separation process.



Figure 2.12: Product sustainability wheel (Jawahir et al. 2006)

## 2.7 Modeling of burnishing process

In the last decade, there have been no remarkable achievements or novelties within the scope of the theoretical burnishing process modeling. Most research on burnishing in the past focused on experimental studies and used simplified analytical


approaches. Only a few analytical and numerical models for burnishing processes were presented. As mentioned earlier, burnishing is commonly used as a finishing process for the purpose of achieving desired surface finish, and more importantly, introducing compressive residual stresses in the material surface. Due to this reason, most of the burnishing models developed in the past were focused on investigating the interactions between the burnishing conditions and the resulting surface finish and/or residual stresses of the workpiece. Very few studies incorporated the microstructural changes into the burnishing model.

Black et al. (1997) studied the process mechanics of burnishing using slip-line field theory. They proposed a simplified 2-D plane-strain model by assuming a rigid-perfectly plastic workpiece and considering a wedge-shaped tool sliding over the surface. Physically their model represents the pushing of a wave of a plastically deformed material ahead of the wedge. Through their model, the equations for estimating the burnishing force, depth of the burnished layer, and surface plastic strain were derived. However, the effect of strain rate and temperature were not taken into account.

The model of material deformation with a ball rolling on the machined surface is assumed as the initial model for deriving the formulae used to select the burnishing force. Due to its similarities with sliding burnishing, it can also be used to calculate the tool force in the sliding burnishing process (Torbilo 1974). However, the predicted force values for sliding burnishing were often overestimated by this model compared to the experimental data (Papsev 1978; Przybylski 1987).

A model of material deformation with a ball sliding on the machined surface has been discussed extensively and the representative formulas for calculating the radial force

were shown in Figure 2.13 (Korzynski 2007; Torbilo 1974). The predicted results were also different from the data from sliding burnishing experiments. As shown in those formulas, the interrelationships among the plastic strain distribution, the burnishing force and the properties of the processed materials were highly empirical, which also limited the predictability of the models only within the used range of the experimental conditions.

Model	Formula for calculating the force	Calculated force (N)
	$P = (0.008 - 0.0013) \left( \frac{DR}{D+R} \right)^2$	100–250
	$P = 0.0085(HB)R^2$	500
	$P \geq \pi \varepsilon_1 HV \left( \frac{DR}{D+R} \right)^2$	60–370
	$P = 2\pi R h q_N$	140
	$P = 0.64\pi \varepsilon HV R^2$	170–350
	$P = \frac{1}{2}\pi R^2 HB$	>900

$\varepsilon, \varepsilon_1$ , experimental coefficients;  $q_N, HB, HV$ , material constants;  $D, R, h$ , geometrical constants.

Figure 2.13: Model of sliding burnishing and pressure force calculated from the model (Korzynski 2009)

In a follow-up study by Korzynski (2009), the analytical model of sliding burnishing which included the mechanical properties of the workpiece, the geometry of the workpiece-tool contact area as well as the stereometry of the machined surface was further developed. It allowed the determination of the dependence of the tip displacement of the machined surface asperities on the burnishing tool pressure. The predicted results were in good agreement with the experimental results during burnishing of low-hardness steels; however, the applicability of the model on high-hardness materials was unknown.

Bouزيد et al. (2004) established an analytical model to analyze the surface roughness after burnishing. This analytical model depended on the tool geometry, the

initial surface roughness and the burnishing parameters (feed rate and penetration depth). The penetration depth of the burnishing tool was estimated by Hertz theory where the tool and the workpiece were supposed to have purely elastic behavior. These authors studied only the case for which the penetration depth was smaller than the initial surface roughness which was obtained by turning or by grinding after turning.

An analytical model and a finite element model were developed to provide a fundamental understanding on the burnishing of an *AISI 1042* material (Bougharriou et al. 2010). The analytical results were concentrated on the surface roughness and on some burnishing parameter effects. The simulations were devoted to the study of the surface profile, the residual stresses and the influence of burnishing parameters (penetration depth, feed rates, diameter of the ball of burnishing tool and initial surface quality) on surface roughness and the residual stress distribution. However, none of the authors take into account the initial residual stresses generated by the turning or grinding which led to imprecise prediction of the roughness and residual stresses by the 2D FE model.

Skalski et al. (1995) developed a 2-D quasi-static burnishing model to numerically analyze the relations between the tool force, penetration depth, radius of the contact area, and depth of plastic deformation in the burnished surface under different tool radii and workpiece yield strengths. The result from Skalski's study showed that the tool force was more influenced by the tool size than by the material yield strength. In addition, a nearly linear relationship exists between the width and depth of the plastic deformation zone.

Röttger developed a 2-D FEM model for roller burnishing using the commercial FEM software “DEFORM-2D” (Röttger 2002). In his model, a rigid ball is gradually pressed down the rough workpiece surface until the normal force reached a value equal to the applied burnishing force. Then the ball was lifted up from the surface and moved horizontally by the distance equal to the burnishing feed. However, this burnishing force-control model led to an underestimated ball penetration depth due to the line-contact condition assumed by the 2-D plane strain model. In addition, the contact time intervals defined for the loading (i.e., pressing) and unloading (i.e., lifting) stages in the load-control curve were not based on the burnishing speed and an unrealistically large value (2.2 seconds) was used for the contact time. Nevertheless, the predicted surface finish ( $R_z$ ) and residual stresses agreed reasonably with the experiments. However, the comparisons of residual stress were made based on the effective stress and detailed information on the six stress components (3 normal & 3 shear) was incomplete.

Based on the model by Röttger, Yen et al. (2005) further established 2-D and 3-D FEM models of roller burnishing using DEFORM software. Their refined 2-D model predicted the residual stresses better than the 3-D model, in contrast, the 3-D model showed more realistic surface deformation and material flow, whereas the simplified 2-D model represents a series of "indenting" cycles.

However, to date, none of the models have incorporated the microstructural changes that occur during burnishing, which is known to be an important influencing factor to the product quality. Due to the wide application of burnishing operations in industrial fields, there is an emerging need for a reliable predictive model that provides a fundamental understanding of the process mechanics as well as good predictions on the

most critical properties, which can help the industrial users effectively and efficiently select the most suitable burnishing conditions for the specific service environments.

## CHAPTER 3: SURFACE INTEGRITY MODIFICATIONS OF *Co-Cr-Mo* BIOMEDICAL ALLOY THROUGH CRYOGENIC BURNISHING

### 3.1. Introduction

The surface integrity of processed components has a critical impact on their performance. Much research has been done to investigate the influence of different aspects of surface integrity on the functional performance in a wide range of applications (e.g., automotive, aerospace, and biomedical) and materials (Jawahir et al. 2011; M'Saoubi et al. 2008). Severe plastic deformation (SPD) processes have been extensively reported for modifying surface region properties by creating ultrafine or nanometer-sized grains and grain size gradients in the surface layer of many materials (Sato et al. 2004; Valiev et al. 2010). These nano-/ultrafine-grained materials are partially due to the high strain/strain-rate involved in the processing.

Much evidence has shown that SPD induced nano-sized/ultrafine grained materials possess appealing surface integrity properties compared with their coarse-grained counterparts (Qi et al. 2009; Shi and Han 2008; Wang et al. 2003a). However, there is still a large gap between SPD processes on the laboratory scale for fundamental research and its application in large scale production. The possibility of using SPD processes as a surface enhancement tool to improve the functional performance of materials through enhanced surface integrity while avoiding expensive and time-consuming post-treatment processes has not yet been well investigated.

Among different kinds of SPD methods, burnishing has stood out as one of the most practical SPD techniques that can effectively modify the material surface integrity properties. Significant grain refinement has been reported in the processed surface layers

of various metals and alloys (Nikitin et al. 2005; Pu et al. 2012b). Burnishing is also an effective method on introducing beneficial compressive residual stresses to the surface region which subsequently improves the fatigue life of components (Prevey et al. 2001; Prevey et al. 2000). Burnishing is also found to improve the wear performance of many metals and alloys (Hamadache et al. 2006; Radziejewska et al. 2005).

The aim of the present work is to investigate the effect of cryogenic burnishing on the surface integrity changes of *Co-Cr-Mo* alloys. Unlike many other materials for aerospace and automotive applications, there are very few studies on using manufacturing processes to improve the surface integrity as well as the functional performance (especially wear performance) of this alloy. In this study, the influence of cryogenic burnishing on the surface integrity modifications, in terms of surface roughness, microstructure, hardness, etc., of *Co-Cr-Mo* alloy was studied. Better surface finish, high hardness value and significant grain refinement were simultaneously achieved with the application of cryogenic cooling. A further aim of this study is to establish the relationships among burnishing conditions, surface integrity properties and the wear performance of this *Co-Cr-Mo* alloy.

## **3.2. Experimental work**

### **3.2.1. Work material**

The material used in the present investigation was BioDur CCM alloy, which is a low carbon wrought version of ASTM F75 Cast *Co-Cr-Mo* Alloy. In order to fully investigate the effects of burnishing, the as-received material was annealed at 1100 °C for 1 hour followed by air cooling. The basic chemical composition of this *Co-Cr-Mo* alloy



is shown in Table 3.1. A *Co-Cr-Mo* alloy bar (50.8 mm diameter) was used to prepare disc samples which have a diameter of 50.8 mm and a thickness of 3 mm.

Table 3.1: Chemical composition in wt.% of BioDur CCM alloy

<i>C</i>	<i>Mn</i>	<i>Si</i>	<i>Cr</i>	<i>Mo</i>	<i>Ni</i>	<i>N</i>	<i>Fe</i>	<i>Co</i>
<0.1 %	<1 %	<1 %	26- 30 %	5-7 %	<1 %	<0.2 5 %	<0.7 5 %	balance

Many metal orthopedic bearings are made from either high carbon wrought alloy (Alghamdi et al. 2012) or cast alloy (Table 3.1). The presence of carbides throughout the matrix increases the difficulty of dislocation motion through the crystallattice (during plastic deformation), thus increasing the strength but reducing the ductility. In addition, it is reported that hard phases like carbides protrude from the surfaces under sliding wear, the real area of contact changes steadily during the wear process. The local carbide/carbide contact stress can be up to 22 GPa theoretically, which will cause *Cr*- and *Mo*-carbides fracture and tear off from the surfaces bringing about additional surface fatigue by indentations and initiating abrasion (Wimmer et al. 2001). It is generally recognized that wrought alloys are better than cast material because of their superior mechanical properties (Sury and Semlitsch 1978). The forging process promotes plastic deformation (Immarigeon et al. 1984) as a route to generate a structure with finer grains, which relates to the enhancement in the properties (Brown 2001).

In general, alloying elements affect the crystallographic characteristics of *Co*. For example, different alloying elements can serve to lower or raise the fcc and hcp transformation temperature, but the kinetics of the transformation remain relatively unchanged for a given driving force. Certainly, the microstructure, morphology and

volume fraction of carbides strongly influence the wear rate. Thus, this work will not compare the wear performance and generalize the results for the various alloy types but will focus on the basic microstructural changes of low carbon cobalt base alloys induced during burnishing process.

### 3.2.2. Burnishing experiments

Burnishing experiments were conducted on a Mazak Quick Turn-10 Turning Center equipped with an Air Products and Chemicals ICEFLY<sup>®</sup> liquid nitrogen delivery system. Liquid nitrogen as a cryogenic coolant was applied to the workpiece on the flank side of the tool-workpiece contact. The experimental setup and the specially designed and fabricated burnishing tool with a fixed burnishing roller are shown in Figure 3.1. Roller burnishing is a manufacturing process commonly used in industry to reduce surface roughness, increase hardness and introduce beneficial compressive residual stresses (Gardin et al. 2007; Zhang and Lindemann 2005). In this study, the roller used was fixed for the purpose of introducing large shear stress and shear strain into the workpiece surface during burnishing and therefore was slightly different from traditional roller burnishing arrangements where the roller was allowed to rotate. The effect of shear strain on grain refinement has been systematically studied by Lee et al. (2002) and Kamikawa et al. (2007). Their results showed that shear strain can greatly affect the grain refinement during accumulative roll-bonding (ARB) process. The role of shear strain in grain refinement was considered from the viewpoints of equivalent strain, strain gradient and strain path. In addition, equal-channel angular pressing (ECAP) is also a SPD technique whereby very large plastic deformations are developed by forcing a rod through a die

which results in a sudden change in the die axis angle without a change in the cross-sectional area (producing shear deformation) (Furukawa et al. 1996; Valiev et al. 1991). Another technique utilized SPD is high-pressure torsion (HPT) where small disk-shaped samples are subjected to combined high-pressure and severe torsional deformations resulting in very large shear strains in the samples (Zhilyaev and Langdon 2008; Zhilyaev et al. 2003). Recently, it is reported that, after cryogenic burnishing of *AZ31 Mg* alloy by using this process, the grain size near the surface was reduced to about 500 nm from 12  $\mu\text{m}$ . Significant improvement of corrosion performance in *AZ31B Mg* alloy was found on samples after cryogenic burnishing (Pu et al. 2011b).

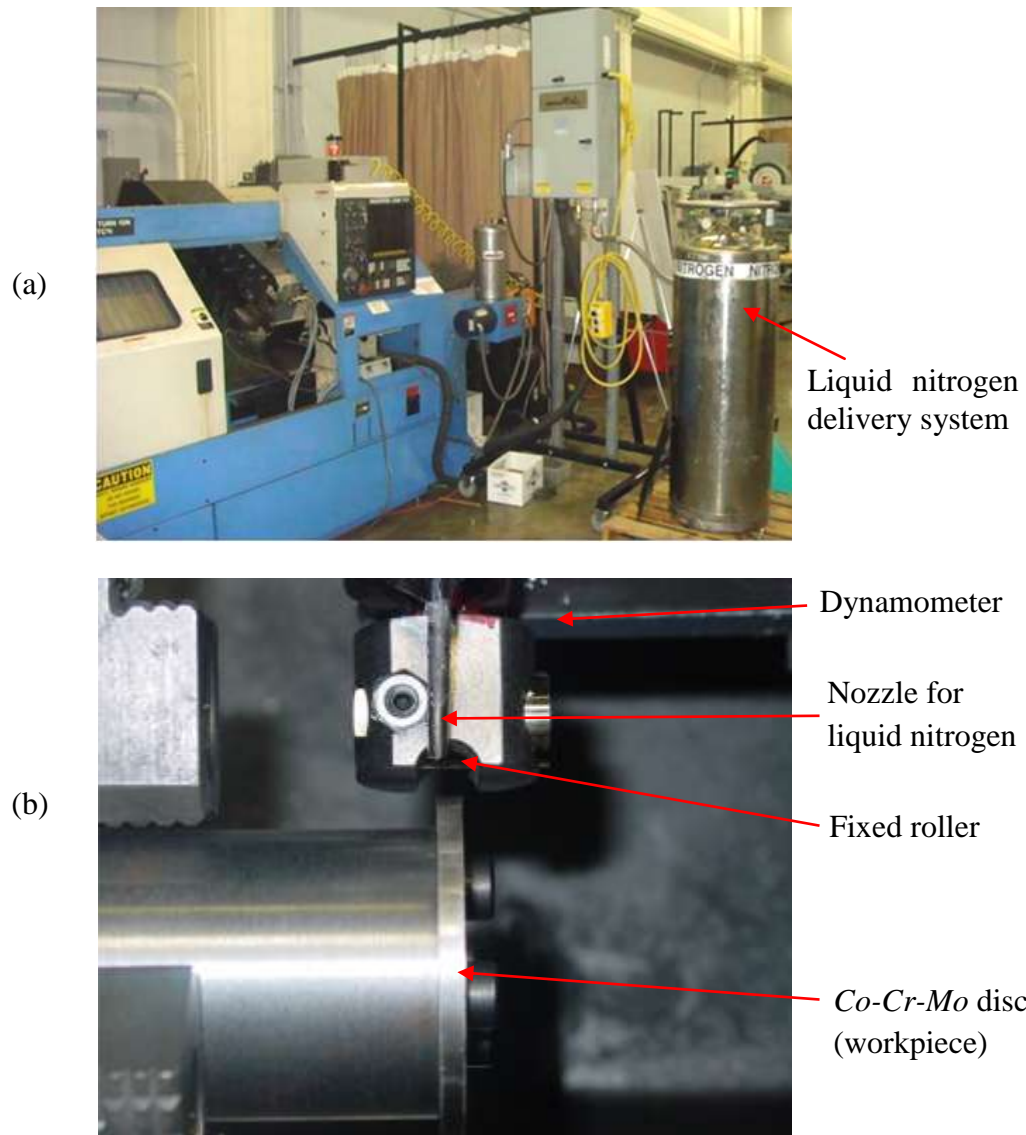


Figure 3.1: Experimental setup for cryogenic burnishing of *Co-Cr-Mo* discs: (a) Mazak CNC machine equipped with ICEFLY<sup>®</sup> cryogenic equipment, (b) setup details.

The burnishing conditions used are listed in Table 3.2. For each condition, one *Co-Cr-Mo* disc sample was used. For dry burnishing, no cooling method was used; for cryogenic burnishing, liquid nitrogen was sprayed to the tool-workpiece interface at 0.6 kg/min. A schematic of the cryogenic burnishing process is shown in Figure 3.2. A machining clearance cut using an uncoated carbide insert was conducted at a feed rate of 0.1 mm/rev and a cutting speed of 100 m/min in order to standardize initial burnishing

conditions. The fixed roller tool was then pressed into the discs at a constant feed rate of 0.025 mm/rev. Simultaneously, the disc was rotating at a burnishing speed (i.e., the linear speed at the contact area between the fixed roller and the disc) of 100 m/min. The feed-in process was stopped when the preselected depth of penetration (DoP) was reached. The burnishing roller then stayed at this position (i.e., for the burnishing dwell time) for 10 seconds. The forces generated during processing were collected by a KISTLER 3-Component Tool Dynamometer which was located just beneath the burnishing tool. An uncoated carbide roller with a diameter of 14.3 mm was chosen as the burnishing tool for the current study. The hardness and surface roughness of the roller was measured to be 1000 HV and 0.01  $\mu\text{m}$  ( $R_a$ ), respectively.

Table 3.2: Matrix for the burnishing experimental conditions

Cooling method	Depth of penetration (mm)	Burnishing speed (m/min)	Burnishing dwell time (sec)
Dry	0.127	100	10
Cryogenic	0.127	100	10
Dry	0.254	100	10
Cryogenic	0.254	100	10

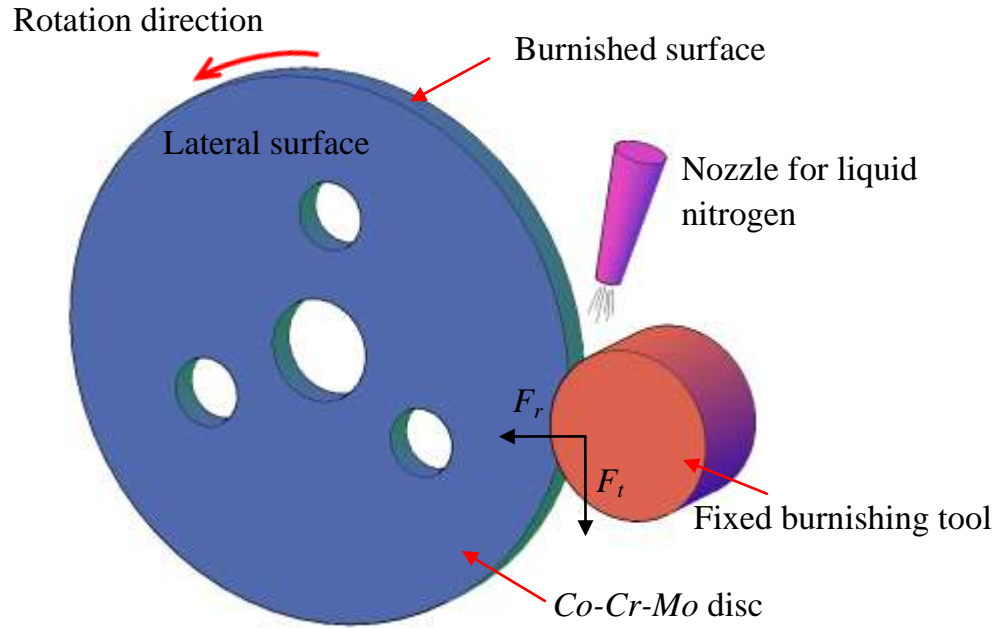


Figure 3.2: Schematic of the cryogenic burnishing process

### 3.2.3. Infrared thermal-camera setup and calibration

A FLIR ThermoCAM PM695 infrared thermo-camera was used during the experiments to record the whole disc thermal field and temperature history during processing. As shown in Figure 3.3, the infrared camera was mounted on the machine and did not move during burnishing. The distance between the workpiece and the camera was 0.4 m.

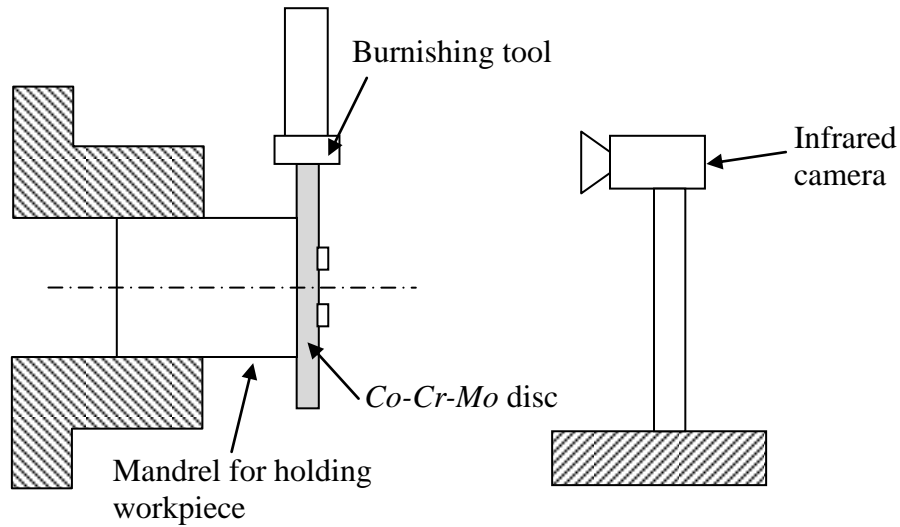


Figure 3.3: Thermo-camera setup illustration for burnishing process

When using the infrared camera, the emissivity of the material is a critical parameter, and its choice will greatly influence the accuracy of the measurements. It was reported that linear relationships between the temperature measured by the infrared camera and the one measured by thermocouple (considered to be the actual temperature) could be found when using the right emissivity (Liang and Yuan 2008). Also, good temperature measurement results were obtained on *Co-Cr-Mo* alloy when the emissivity was set to be 0.27 (Vandamme and Topoleski 2005). Therefore, an emissivity of 0.27 was used for this study. To calibrate the infrared camera, a hotplate was used to heat a *Co-Cr-Mo* disc from room temperature up to 500 °C. The infrared camera and a thermocouple were used to measure the same spot on a *Co-Cr-Mo* disc at the same time. As shown in Figure 3.4, a linear relationship was found between the temperatures measured by infrared camera and thermocouple as:

$$T_{thermal} = 0.5257 T_{infrared} - 3.5046 \text{ (}^{\circ}\text{C)} \quad (3.1)$$

where  $T_{thermal}$  is the temperature measured by thermocouple (actual temperature) and  $T_{infrared}$  is the temperature measured by the infrared camera. This equation can then be used to calculate the actual temperature of the machined surface using the data obtained from the infrared camera.

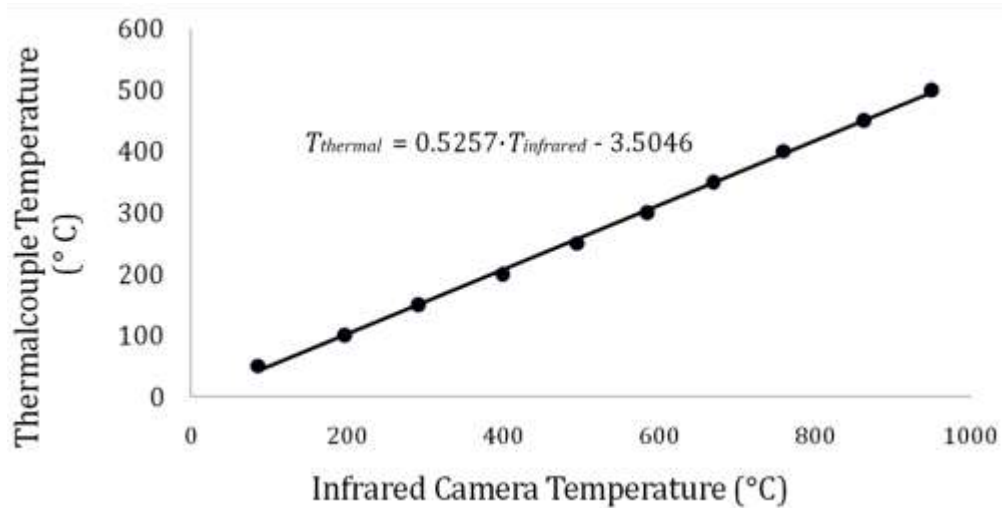


Figure 3.4: The temperature relationship of the investigated *Co-Cr-Mo* disc between the infrared camera and the thermocouple measurement values

#### 3.2.4. Characterization of surface integrity

Surface roughness before and after burnishing under different conditions was measured using a Zygo NewView 7300 white light interferometer system. The hardness variation with depths from the surface was measured using a Vickers indenter on a CSM Micro-Combi Tester. The load used was 100 mN and the duration time was 10s.

Metallurgical *Co-Cr-Mo* discs were cleaned and cut along the cross section using a diamond saw and a very low feed rate to prevent alterations in the microstructure due to heating during the cutting process with the diamond saw (Figure 3.5). The samples were then hot mounted using a Struers Mounting Press (Prontopress-20) machine. Struers



grinding and polishing machine (Rotoforce-3, Multi Doser, Rotopol-25) was then used for polishing and grinding the specimens. Table 3.3 outlines the procedure for polishing and grinding of the specimens for analyzing the microstructure.

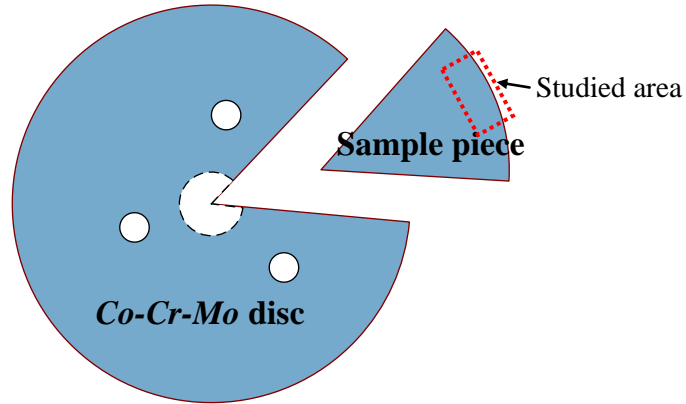


Figure 3.5: Metallurgical sample illustration

Table 3.3: Procedure for polishing the specimens for analysis of microstructure

Step	Surface	Abrasive Type	Speed (rpm)	Force (N)
Planar grinding	SiC-Paper #500		300	150
Fine grinding	MD-Allegro	DiaPro Allegro, water based diamond suspension, diamond grain size 6 $\mu\text{m}$	150	120
Rough polishing	MD-Dac	DiaPro Dac, water based diamond suspension, diamond grain size 3 $\mu\text{m}$	150	110
Final polishing	MD-Nap	DiaPro Nap, water based diamond suspension, diamond grain size 1 $\mu\text{m}$	150	90
Final polishing	MD-Chem	Colloidal Silica suspension for final polishing	150	60

After polishing, the samples were placed on a hot plate for approximately 20 minutes at 130 °C, and then swabbed with a cotton swab dipping with the etchant for approximately 8 seconds. The etchant used for revealing microstructures was a solution made of 120 ml 37% hydrochloric acid, 12 g cupric chloride dehydrate crystalline and 10 ml R.O. Water, which is commonly used for etching implant grade material. The sample specimens were then carefully transferred to the sink and rinsed thoroughly with R.O. water for 1 minute. Compressed air was then used to dry the samples totally. Measurements of the cross-sectional microstructure in the surface region were conducted on the samples before and after burnishing. Metallurgical analysis was conducted by using a Nikon EPIPHOT 300 microscope along with a Leica DFC425 optical microscope and an S-4300 Hitachi scanning electron microscope (SEM). Chemical compositions of the materials were determined from a Princeton Gamma-Tech energy dispersive spectroscopy microanalysis system (EDS).

Phase structures and identification of second phase precipitates on the surfaces were analyzed using a X-ray equipment Bruker AXS D8 Discover (Figure 3.6). The X-ray diffraction (XRD) patterns were measured using  $CuK_{\alpha}$  radiation ( $\lambda = 1.54184 \text{ \AA}$ ,  $K_{\alpha 1}/K_{\alpha 2} = 0.5$ ) from a source operated at 40 kV, and 40 mA. Samples with the same measuring areas were positioned at the center of the plate into the X-ray goniometric in order to ensure a correct beam irradiation.

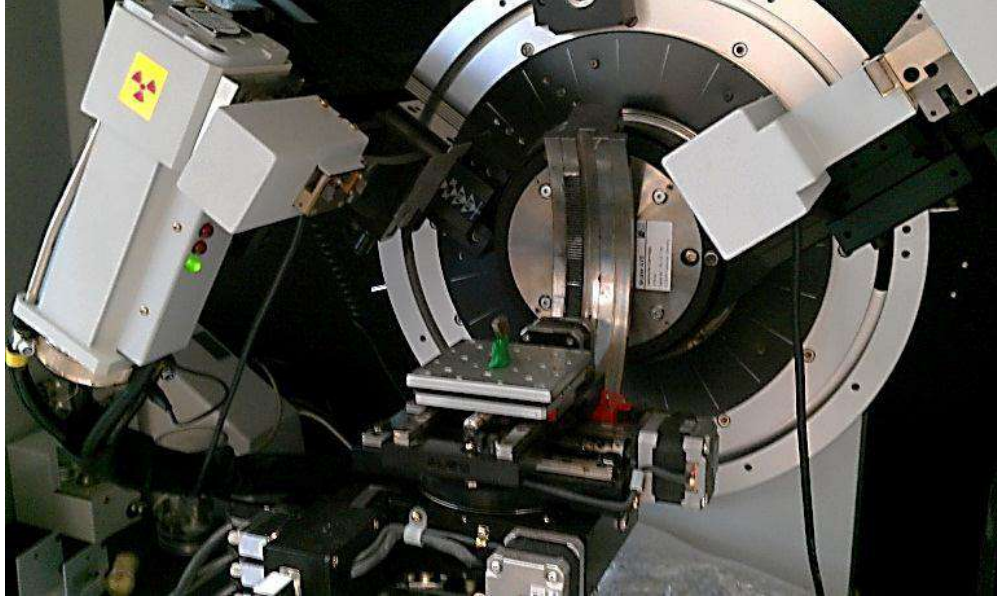


Figure 3.6: X-ray equipment for phase structure analysis

### 3.3. Results and discussion

#### 3.3.1. Burnishing force

Burnishing force components in radial and tangential directions (see Figure 3.2) were measured by using a KISTLER 3-Component Tool Dynamometer, which was attached right beneath the burnishing tool. The measured results are shown in Figure 3.7. Due to the fact that the force during burnishing was not constant; the forces shown were the average values of the last 4 s among the 10 s burnishing dwell time. It can be observed that, with lower DoP (0.127 mm), the cryogenic burnishing approach had higher radial and tangential forces when compared to those generated in dry burnishing. Generally, lowering the temperature results in reduction of wear rate and increase of tool-life (Khan and Ahmed 2008; Wang et al. 2003b). However, a reduction in the temperature of the workpiece can increase its shear stress, thus, the cutting force may be

increased and this may negatively affect the tool-life (Carter 1956). In the current study, liquid nitrogen was applied on the tool flank side towards the workpiece surface; it had a high tendency to precool the workpiece and therefore to increase the hardness and strength of the workpiece material. As described for cryogenic machining, when the temperature was lower, the workpiece material became stronger and harder, and in turn, the burnishing forces increased (Zhao and Hong 1992). The increased ploughing effect (i.e., larger radial and tangential forces) should be desirable for the occurrence of strain-induced grain refinement in *Co-Cr-Mo* alloys (Yamanaka et al. 2009) since more severe plastic deformation will be introduced to the burnished surface and sub-surface. However, when the DoP increased to 0.254 mm, the forces measured during dry burnishing were very close to the ones from cryogenic conditions. It is also noted the burnishing forces under dry condition with 0.254 mm DoP gave larger error values compared to the other three conditions. This is due to an increase of burnishing forces during the later part of the dry burnishing process, which is likely caused by the greater tool-wear under larger DoP. When the DoP increased, a higher processing temperature (will be discussed in the following section) was introduced from the more severe plastic deformation. Compared to the precooling effect which made the material stronger under cryogenic conditions, during dry burnishing, the greater tool-wear resulting from the higher processing temperature led to increased burnishing force, which made the burnishing forces under both dry and cryogenic burnishing with higher DoP similar as shown in Figure 3.7.

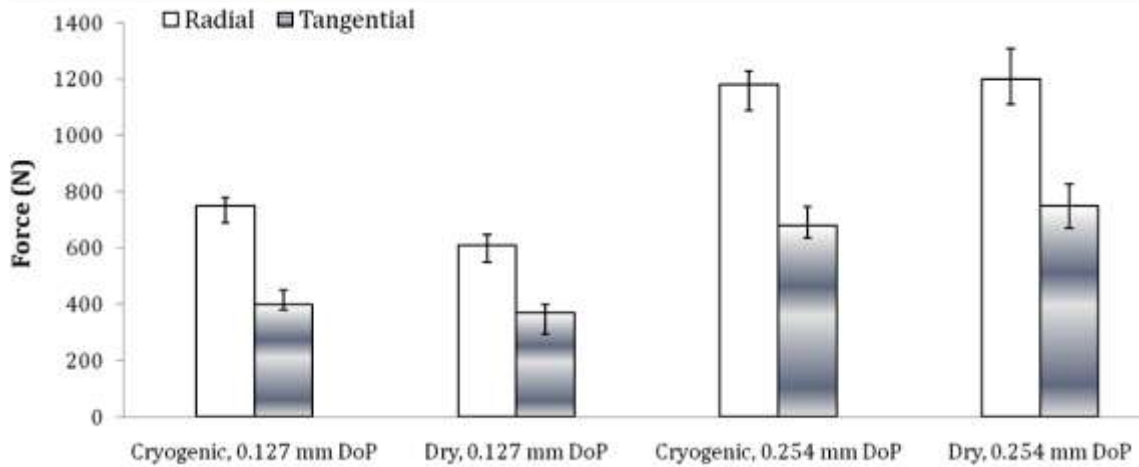


Figure 3.7: Force measurement results under different burnishing conditions

### 3.3.2. Temperature analysis

Grain refinement due to SPD induced DRX is determined by the combined effects of strain, strain rate and temperature during processing (Li et al. 2008; Xiao et al. 2008). In addition to grain size changes, the processing temperature is known to be a critical factor for the residual stress generation (Outeiro et al. 2008; Radziejewska BN and Kalita 2005), and the occurrence of phase transformation of the processed materials (Umbrello et al. 2012).

The most critical temperature for the SPD induced DRX is the temperature within the tool-workpiece contact zone. As illustrated in Figure 3.8, the burnishing roller was pressed into the workpiece as the disc specimen was rotating which resulted in sliding between the tool and the specimen. The mechanism for this process is very similar to machining with large edge radius tool and large negative rake angle (chipless machining). During burnishing, the tool-workpiece contact zone was under the most severe plastic deformation conditions, and the DRX process will be triggered within this zone when the

critical strain for DRX was exceeded (Yanagimoto et al. 1998). Right after the material left this zone, the temperature effect became the dominating factor.

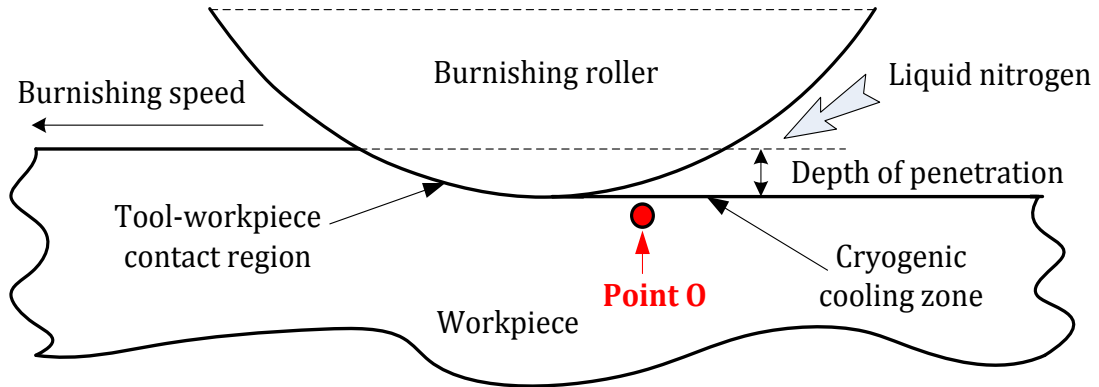


Figure 3.8: Simplified cryogenic burnishing illustration

Figure 3.9 shows overviews of the temperature fields captured by the infrared camera during dry and cryogenic burnishing with 0.254 mm DoP. Due to the design of the burnishing tool, the exact tool-workpiece contact zone temperature cannot be captured. Thus, the first point where the material appeared in the image is defined as the exit point O in Figure 3.9, which was within the cryogenic cooling zone and was considered to be the most representative value for the cooling zone temperature. In this study, in order to have a more complete understanding of the processing temperature, two temperature profiles were taken from this point. As shown in Figure 3.9 (a) and (b), the depth profile was taken from exit point O towards the center of the disc, which provided the information on the process induced temperature changes along the disc radial direction; the perimeter profile was obtained along the burnished surface, which enabled one to study the same spot temperature changes within and outside of the cryogenic cooling zone.

Figure 3.10 (a) shows the data obtained from the two depth profiles. For dry burnishing, the temperature at point O gave the highest value (710 °C), which then decreased with increasing distance toward the center. This behavior is commonly observed in both dry machining and burnishing. The maximum temperature is within the deformation zone where the tool and workpiece make contact (O'Sullivan and Cotterell 2002), which cannot be measured here. Thus, it can be claimed that the actual temperature within the tool and workpiece contact zone was higher than the temperature at point O (710 °C). The depth profile from cryogenic burnishing showed a  $\cap$  shaped curve. The temperature at point O was 290 °C and increased to 450 °C at a distance of 1.8 mm from point O. The lower temperature at point O should be caused by the effective cooling due to the location of the nozzle where liquid nitrogen was sprayed onto the burnished surface within the cooling zone. By using cryogenic cooling, a 510 °C temperature reduction was achieved within the cooling zone located just after the tool-workpiece contact zone. Beyond 1.8 mm, the temperature gradually decreased again. The in-depth temperatures from dry and cryogenic burnishing still showed a 70 °C difference at depth of 15 mm from point O, which indicated that the temperature layer influenced by cryogenic cooling is more than 15 mm thick. This claim was also supported by the data obtained in the perimeter profile (Figure 3.10 (b)). Instead of decreasing with increasing distance from the point O as in the dry burnishing profile, the temperature from cryogenic burnishing increased from 290 °C to 500 °C at about 40 mm away from the point O. The depth and perimeter profiles for cryogenic burnishing both had a  $\cap$  shaped curve (first increasing then decreasing) starting from point O. Studies on machining showed that the maximum temperatures during processing were always in the tool-workpiece contact

zone with and without cryogenic cooling. However, it is also reported that compared to dry machining, the tool-workpiece temperature was largely reduced with the application of cryogenic cooling (Pu et al. 2011a; Umbrello et al. 2012). Since the temperature within the tool-workpiece contact zone was not obtained, it is expected that the tool-workpiece contact temperatures for both dry and cryogenic burnishing should be higher than the measured point O temperatures. Moreover, the tool-workpiece contact temperature for cryogenic burnishing should be lower than the one from dry burnishing.

It should be noticed that for both dry and cryogenic conditions, the temperatures almost stabilized at a distance of 20 mm from point O with a small decreasing slope. It can also be observed from the thermal images shown in Figure 3.9 that the disc surfaces for both conditions showed a very bright color around the whole perimeter; as indicated in the scale bars, the bright color corresponded to the highest temperature range. This is most likely due to the high spindle speed of 730 RPM (i.e., 100 m/min surface speed) used for the burnishing experiments. The heat generated during burnishing was conducted into the cooler disc center and accumulates during multi-passes, which finally led the surface into a nearly static temperature state. Another finding from Figure 3.10 (b) is the temperature difference ( $\sim 200$  °C) between dry and cryogenic burnishing outside of the cooling zone, where the material left the tool-workpiece contact zone and was no longer subjected to plastic deformation. The higher surface temperature prompted the dynamic recovery of the microstructure and compromised the SPD effect within the process-influenced layer. The influence of the perimeter surface temperature difference on the surface integrity, especially on the hardness and grain size changes, will be discussed in later sections.



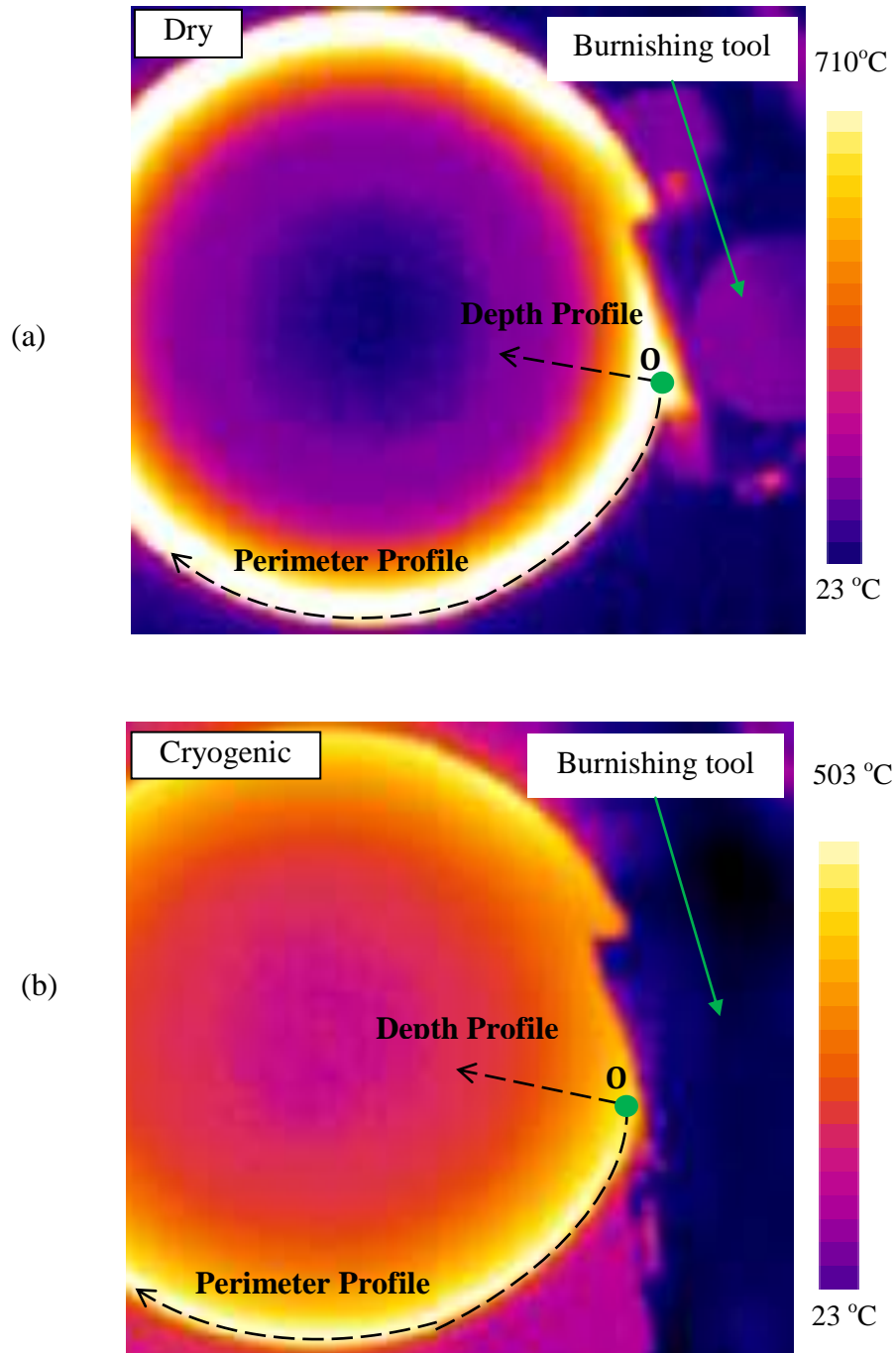


Figure 3.9: Infrared camera images of temperature field during (a) dry and (b) cryogenic burnishing

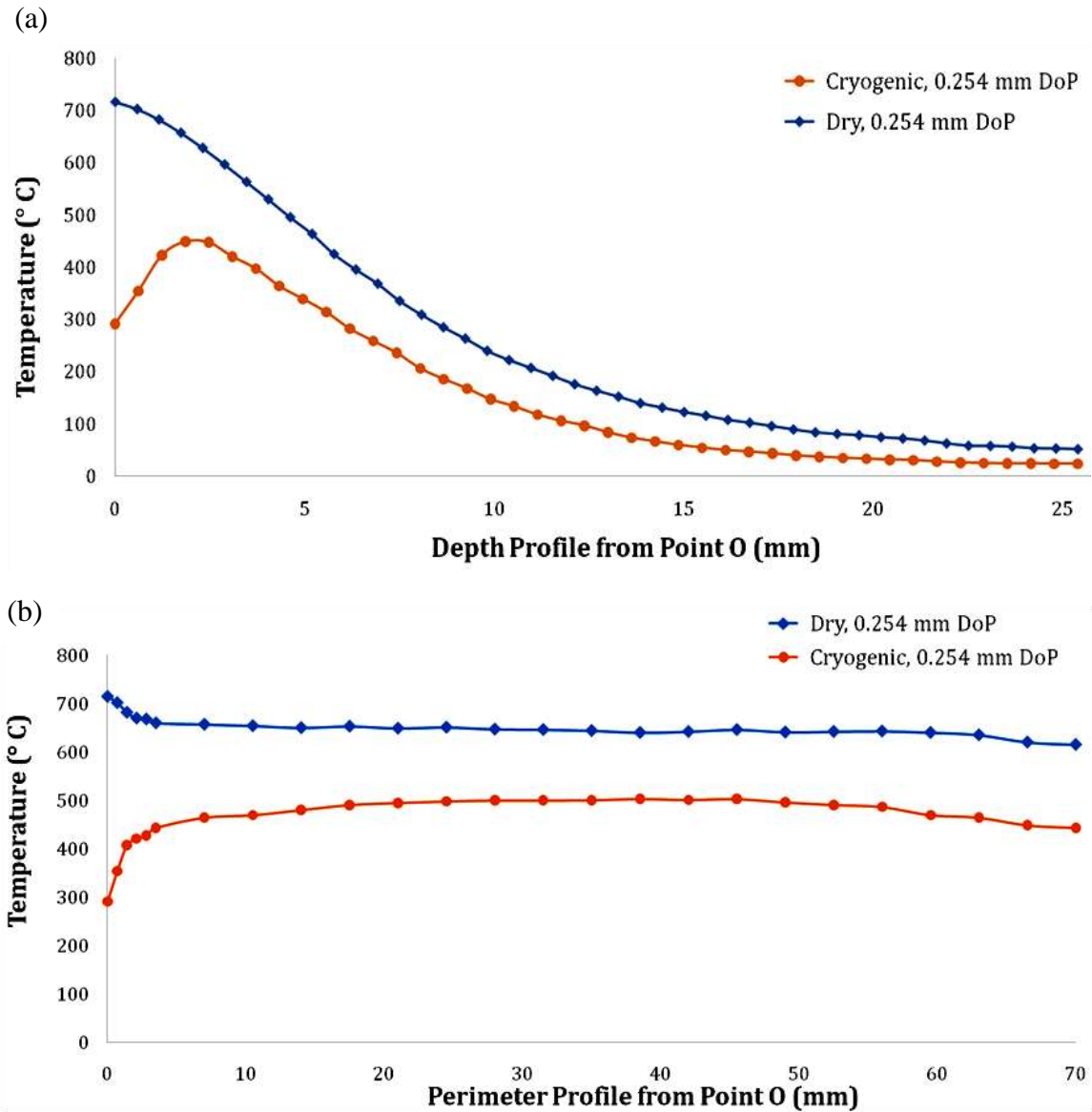


Figure 3.10: (a) Depth profile of temperature from point O, and (b) perimeter profile of temperature from point O

Figure 3.11 summarizes the obtained temperatures at point O (one temperature reading for each condition) for the different burnishing experiments. It is evident that the cryogenic cooling showed a reduction of the temperatures at point O for all conditions.

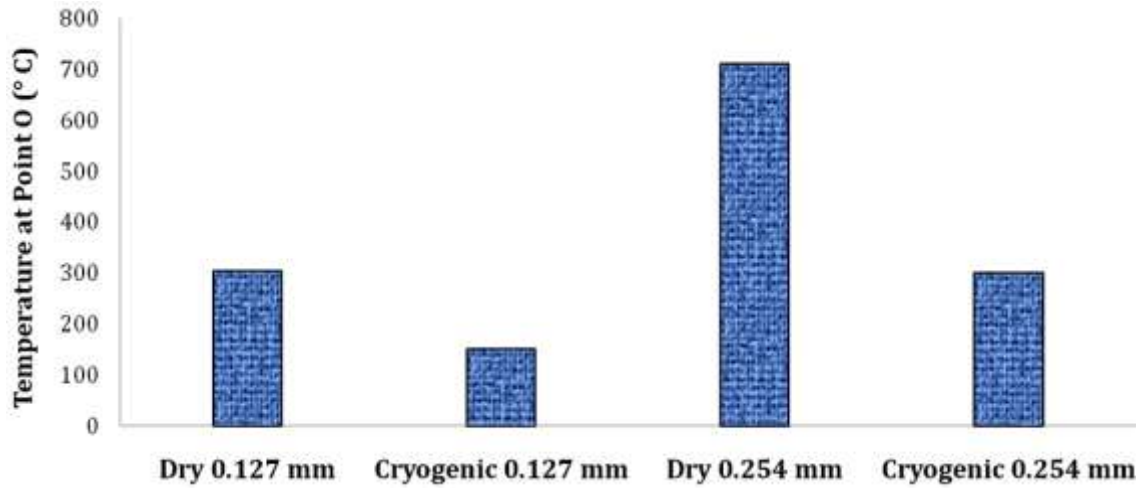


Figure 3.11: Measured temperature at point O from different burnishing conditions

### 3.3.3. Microstructure

The microstructure near the surface before burnishing is shown in Figure 3.12. The grain boundaries were clearly visible near the surface with an average grain size of  $80 \pm 30 \mu\text{m}$ .

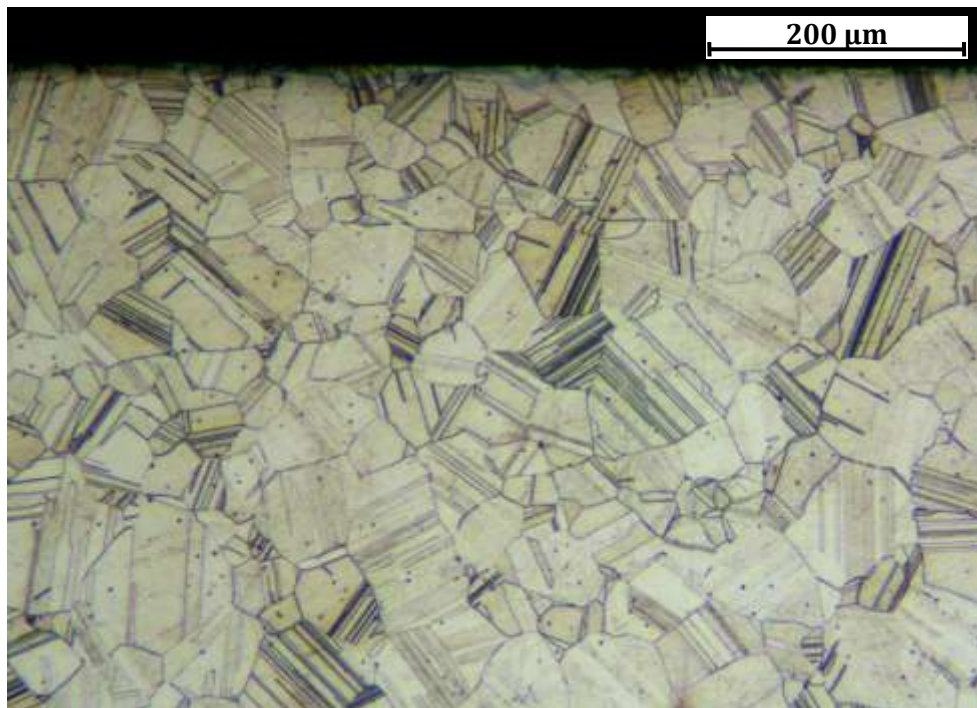
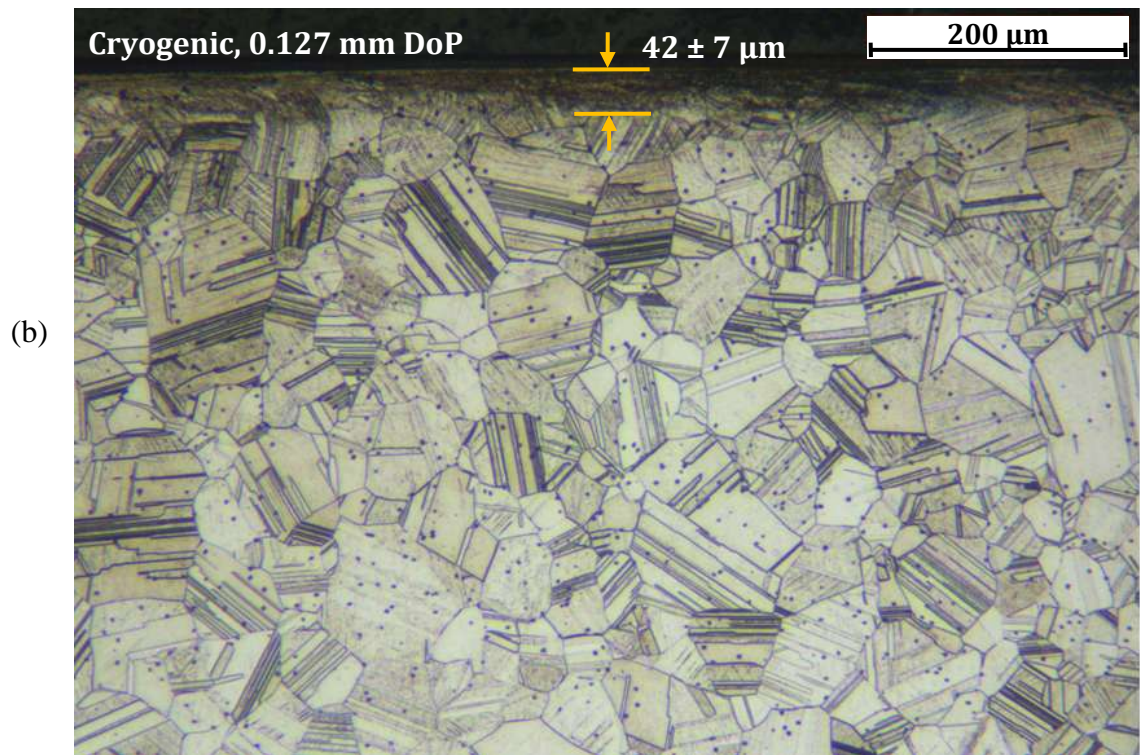
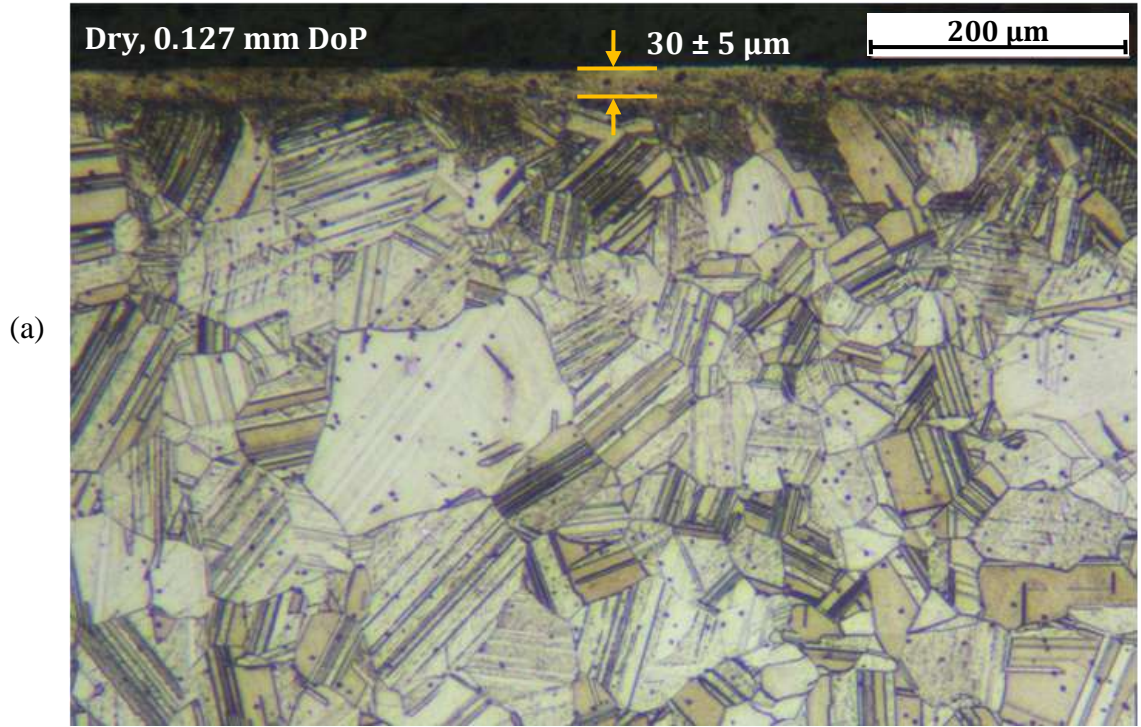


Figure 3.12: Microstructure near the surface before burnishing

Figure 3.13 shows the microstructures of the surface regions produced using different burnishing conditions. It can be observed that adjacent to the burnished surface; a layer existed where the grain boundaries were not discernable under the current observation method. By using similar scales and measuring techniques, this featureless layer with indiscernible grain boundaries was also reported in other materials after burnishing (Li et al. 2008; Nalla et al. 2003). The burnishing-influenced layer is defined as a layer where the microstructure shows the features of recrystallized grains, elongated subgrains, and/or grains with heavy twinings and stacking-faults (Wu et al. 2005). The line where those features end and the bulk microstructure appears is considered as the end of the burnishing-influenced layer. The measured burnishing-influenced layer thicknesses were marked on Figure 3.13. Two specimens were cut from each disc sample for microstructure analysis. On each specimen, five thickness measurements at different locations were taken and the total 10 readings were averaged to yield the layer thickness values shown in Figure 3.13. As a general trend, cryogenic burnished samples (Figure 3.13 (b) and (d)) had thicker burnishing-influenced layers than those burnished using dry conditions (Figure 3.13 (a) and (c)). Comparing Figure 3.13 (c) and (d), it is clearly visible that the depth of the process-influenced layer from cryogenic burnishing ( $138 \pm 47 \mu\text{m}$ ) was much greater than the one from dry burnishing ( $43 \pm 9 \mu\text{m}$ ). Moreover, the results also indicate that increasing the DoP from 0.127 mm to 0.254 mm under dry conditions did not lead to a significantly thicker process-influenced layer (compared to the equivalent comparison for cryogenic burnishing); this is likely due to the accelerated dynamic recovery of the microstructure and the compromised SPD effect within the process-influenced layer from the higher surface temperature.



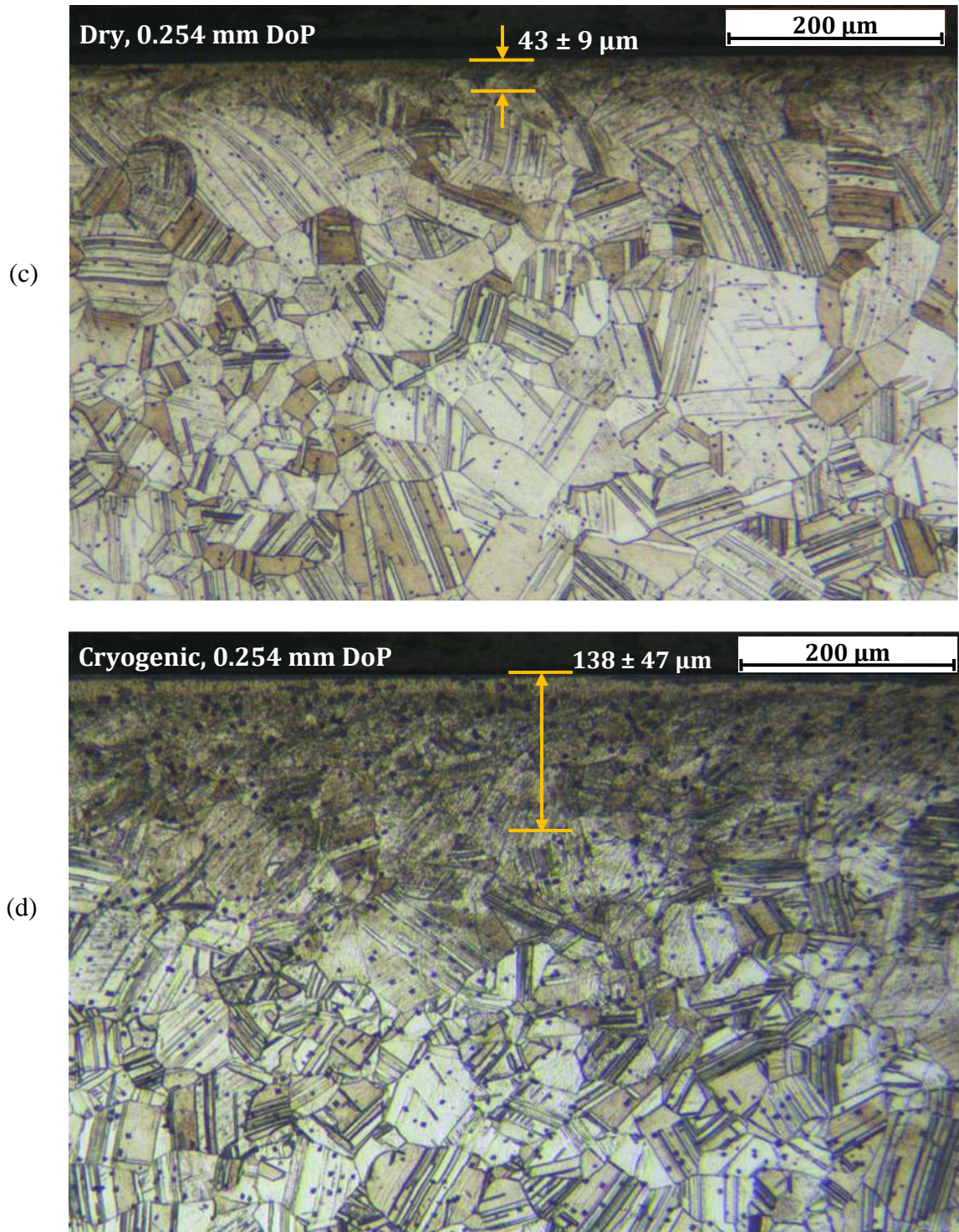


Figure 3.13: Microstructure of the surface after burnishing under different conditons: (a) dry burnishing, DoP = 0.127 mm; (b) cryogenic burnishing, DoP = 0.127 mm, (c) dry burnishing, DoP = 0.254 mm and (d) cryogenic burnishing, DoP = 0.254 mm.

Other conditions are given in Table 3.2

Similar fine-grained surface layers were reported during processing of different materials. Significant grain refinement to the nanocrystalline level was found in machined *AISI 52100* steel due to SPD induced DRX (Jayal et al. 2010). Surface mechanical attrition treatment (SMAT) was also reported to create such surface layers on pure *Ti* and *Cu*, with grain sizes in the range of 50-250 nm (Li et al. 2008; Zhu et al. 2004). The microstructural evolution of this *Co-Cr-Mo* alloy after burnishing with 0.254 mm DoP was further studied. As shown in Figure 3.14 (a), a clear transition from the initial microstructure to the featureless layer on the top can be observed; the microstructure from cryogenic burnishing can be categorized into three layers. Above the transitional line 1, there was a featureless layer where no grain structure and grain boundaries can be identified under the current observation method. This disappearance of grain boundaries was likely caused by the formation of nano/ultrafine grains through DRX. Nano/ultrafine grain structures have been reported frequently on *Co-Cr-Mo* alloys through SPD induced DRX in various processes, such as hot compression deformation (Kurosu et al. 2010a) and combustion synthesis (Li et al. 2003). Between transitional line 1 and 2, grain boundaries gradually became visible as the depth increased. The grains in this layer also showed heavy twinings and stacking-faults. It was reported that the volume fraction of dynamically recrystallized grains increased with strain in a sigmoidal scheme (Fatemi-Varzaneh et al. 2007). Since the strain induced by burnishing decreases with distance from the surface to the bulk material, it is expected that the amount of ultrafine grains decreases with increasing depth. Below transitional line 2, the grain boundaries were clearly visible; this layer already showed the same microstructure as the bulk material. Similar findings were reported by Wu et al. (2005). After SMAT

processing of cobalt, a microstructural evolution in the deformed surface layer was observed. Recrystallized nano-grains, elongated subgrains, grains with heavy twinings, and equiaxed bulk grains with stacking-faults were observed sequentially, from the depth of 15  $\mu\text{m}$  to 180  $\mu\text{m}$ . This is very similar to the present investigation.

Figure 3.14 (b) gives the detailed microstructural changes for dry burnished sample. The only difference between the two samples in this figure was the cooling method used during burnishing. As shown in Figure 3.10 (b), the surface layer temperature outside the cooling zone was almost constant for both dry and cryogenic burnishing; however, cryogenic cooling during the burnishing process gave a temperature which is 200  $^{\circ}\text{C}$  lower than dry burnishing. It is expected that, except for the very short tool-workpiece contacting time where temperature and SPD effects were both prominent, the microstructural evolution after plastic deformation was heavily influenced by this temperature difference. This claim is proved by the microstructure observation between the two samples shown in Figure 3.14. Compared to the gradual in-depth evolution of microstructure from cryogenic burnishing, dry burnished sample showed a much more rapid microstructure change from surface to the bulk material (Figure 3.14 (b)); the transitional layer in Figure 3.14 (a) showed the microstructural evolution with the appearance of recrystallized featureless layer, while heavy twinings and stacking-faults (an obviously darker microstructure compared to the bulk materials) cannot be observed. The microstructure seemed to be directly changed from recrystallized grains into bulk grains. This is likely caused by the higher temperature within the tool-workpiece contact zone which reduced the SPD effect as well as the higher temperature outside the tool-workpiece contact zone which prompted the dynamic recovery process.



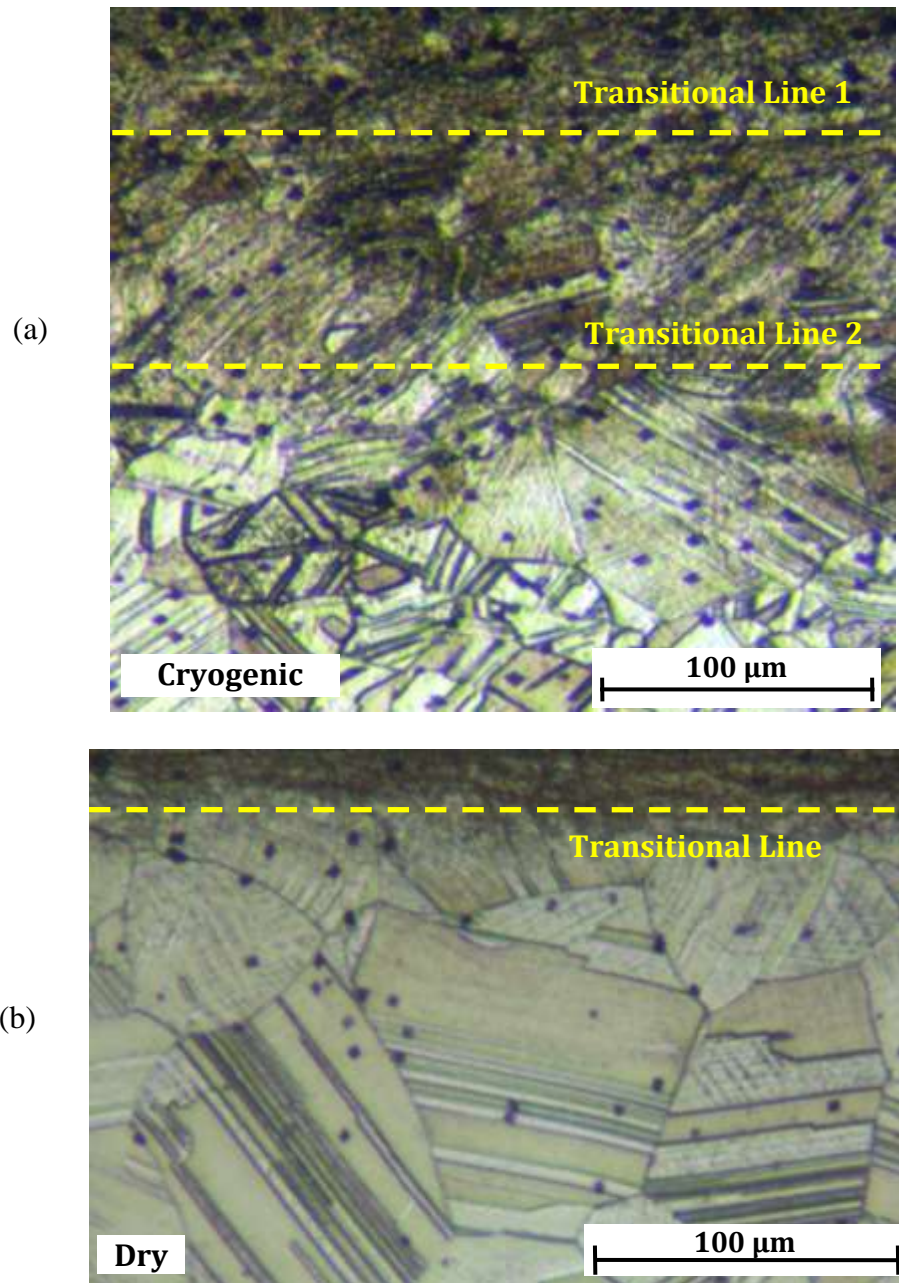


Figure 3.14: Transitional lines show the gradual changes from the burnishing influenced microstructure to the bulk microstructure (0.254 mm DoP): (a) cryogenic, (b) dry

Scanning electron microscopy (SEM) pictures of the typical microstructures near the topmost surface obtained from dry and cryogenic burnishing with 0.254 mm DoP are shown in Figure 3.15. The same samples used for optical microscopy were examined under SEM, the very top surface of the lateral side of the sample showed a white oxide

layer with less than 1  $\mu\text{m}$  thickness, the SEM images were taken just beneath that layer and defined as the “near topmost surface microstructures”. This oxide layer was confirmed by the EDS results. While the average longitudinal axis grain size was  $80 \pm 30$   $\mu\text{m}$  for the initial material, the grain size near the topmost surface (shown in Figure 3.15 (b)) was reduced to submicron scale after cryogenic burnishing. The smallest grain size measured was 300 nm. As the distance from the surface increased, the amount of ultrafine grains decreased. The grains beneath the burnishing-influenced layer, especially for the cryogenic burnished sample (Figure 3.14 (a)), showed heavy twinings and many stacking-faults compared to the initial sample surface (Figure 3.12).

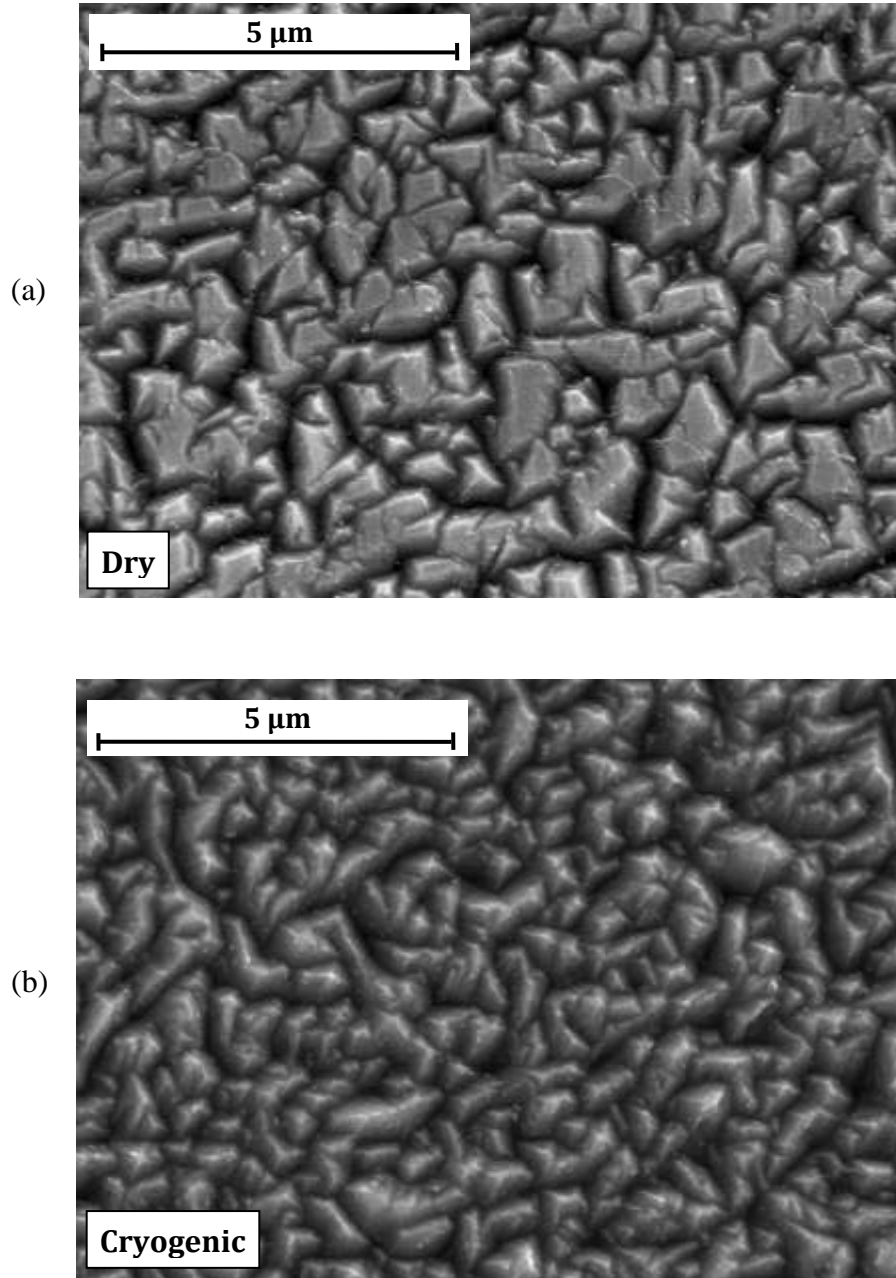


Figure 3.15: SEM micrographs of *Co-Cr-Mo* disc near the topmost surfaces after burnishing with 0.254 mm DoP: (a) dry, (b) cryogenic

The grain refinement mechanism of *Co-Cr-Mo* alloy from DRX was systematically studied by Yamanaka et al. (2009). The grain size after DRX is determined by the Zener-Hollomon ( $Z$ ) parameter (Zener and Hollomon 1946), which is expressed as  $Z = \dot{\epsilon} \cdot \exp(Q/RT)$ , where  $Q$  is the activation energy of lattice diffusion of

the material,  $R$  is the gas constant,  $\dot{\epsilon}$  is the effective strain-rate and  $T$  is the local temperature. It combines the effects of temperature and strain rate into a single parameter that has been shown to be successful in correlating grain size data obtained for different materials under various testing conditions (Yamanaka et al. 2009; Yanagimoto et al. 1998). Once DRX is completed, the recrystallized grain size ( $d$ ) can be calculated as  $d = d_0 \cdot \alpha \cdot Z^m$ . Here  $d_0$  is the initial grain size in microns,  $\alpha$  and  $m$  are material constants. Thus, it is expected that smaller grain size should be observed after DRX when the processing temperature is lower. The cooler temperatures also impede grain growth after the material exits from the tool-workpiece contact. This claim is supported by the current experimental observation. Figure 3.16 shows the longitudinal axis grain size distribution of the grains shown in Figure 3.15 from dry and cryogenic burnishing (0.254 mm DoP). More than 70% of the grains from cryogenic burnishing fell into the range from 300 nm to 600 nm, while about 80% of the grains from dry burnishing were approximately one-micron in size, hence a smaller grain size was achieved by cryogenic burnishing. Therefore, it is evident that the thicker surface layers with grain refinement occurred due to the SPD-induced DRX and effective liquid nitrogen cooling. Moreover, compared to dry burnishing, the larger burnishing force during cryogenic burnishing also led to more severe plastic deformation.

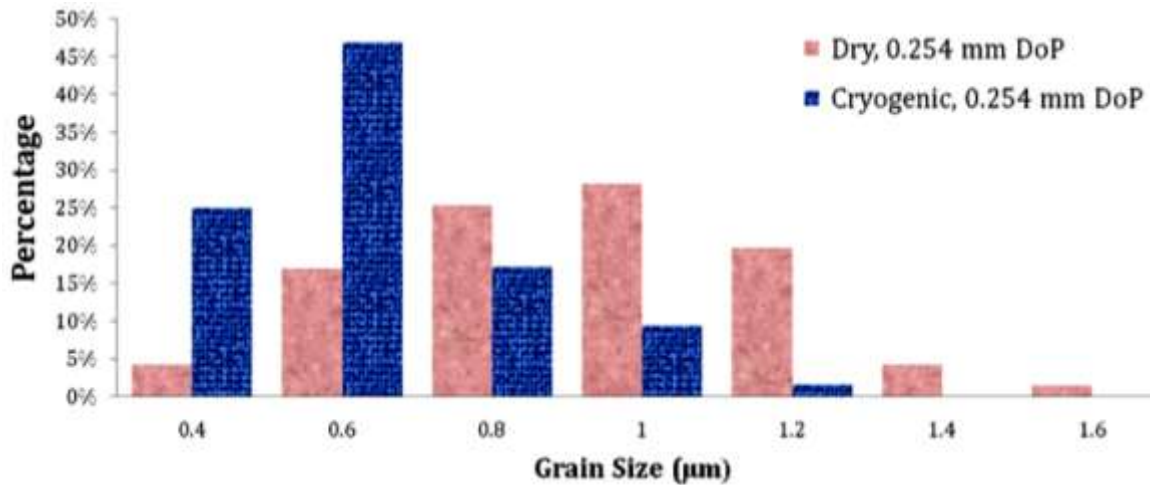


Figure 3.16: Comparison of longitudinal axis grain size distribution of the grains shown in Figure 3.15 after dry and cryogenic burnishing with 0.254 mm DoP

#### 3.3.4. Subsurface microhardness

The subsurface microhardness variations obtained from different conditions are illustrated in Figure 3.17. The average measured microhardness of the virgin disc material was 300 HV. The burnished hardness decreased significantly with increase in depth, which coincided with the microstructure changes observed in these samples. Closer to the surface the hardness might even be higher, but it cannot be measured by such microhardness techniques. Compared to the initial disc, a hardness increase of up to 87% was achieved using cryogenic burnishing. Based on the well-known Hall-Petch relationship between hardness and grain size as well as the close interrelations among hardness, yield stress, and residual stresses, high hardness values often indicate fine grain size and large residual stresses. The Hall-Petch relationship which predicts an increasing hardness with a decreasing grain size ( $\text{Hardness} \sim 1/\text{diameter}^{0.5}$ ) (Hall 1951; Petch 1953) is confirmed for cobalt base alloys when the hardness of fine grained wrought alloys (400-500 HV) is compared to the hardness of coarse grained cast alloys (300-350 HV).

However, nano/ultrafine grained metals do not always follow the Hall-Petch relationship. A significant reduction in grain size might also lead to material softening. This effect, which is often referred to as inverse Hall-Petch relation, is valid for grains which are smaller than dislocation loops and no hardening will take place (Arzt 1998; Nieh and Wadsworth 1991; Takeuchi 2001). In contrast, the Hall-Petch relationship which predicts an increasing hardness with a decreasing grain size ( $\text{Hardness} \sim 1/\text{diameter}^{0.5}$ ) (Hall 1951; Petch 1953) is confirmed for cobalt base alloys when the hardness of fine grained wrought alloys (400-500 HV) is compared to the hardness of coarse grained cast alloys (300-350 HV). It is also reported that for a similar cobalt base alloy investigated, lattice defects were still visible even within the nanocrystals (Buscher and Fischer 2005). Thus, it is assumed that the inverse Hall-Petch relation may not apply to this *Co-Cr-Mo* alloy in very small grains, and the hardness is enhanced towards the surface. Recalling the tribological behavior of a nanocrystalline surface, the increase in hardness should be beneficial for the wear performance (Buscher and Fischer 2005). A high hardness reduces the effect of three body abrasion by increasing the resistance against surface fatigue by indentation.

In the current work, microstructure changes after cryogenic burnishing were observed up to  $138 \pm 47 \mu\text{m}$  distance below the surface. In contrast, microhardness differences were measured to the depth of over  $800 \mu\text{m}$  while burnishing using the cryogenic cooling. It is reasonable to state that the variations in microhardness were at least partially due to the different residual stresses being generated during processing.

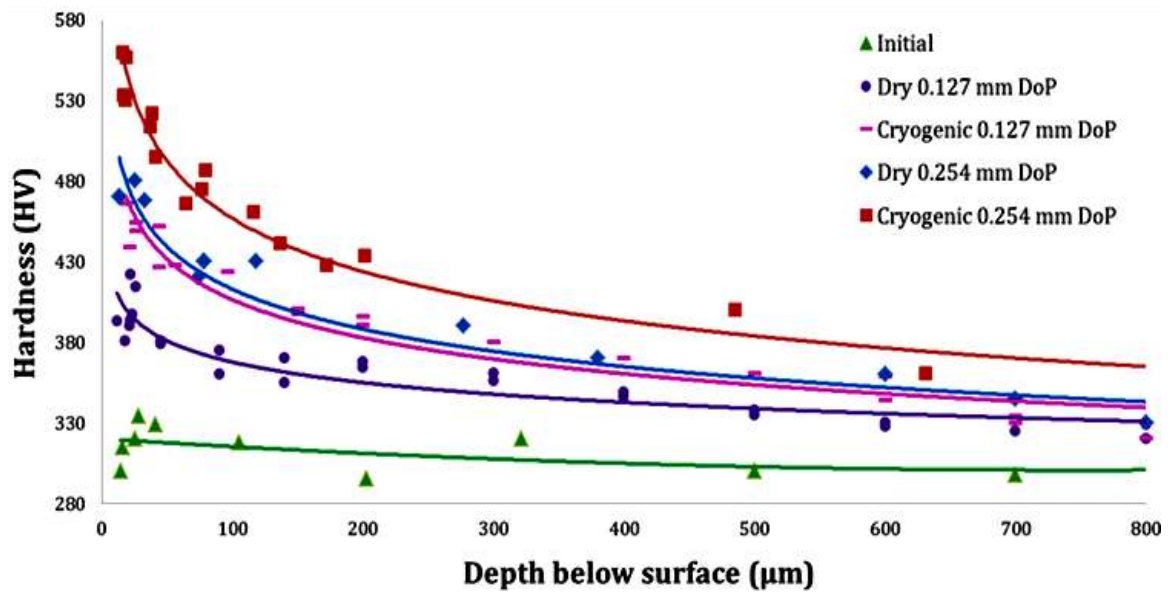


Figure 3.17: Hardness variation with depth below the burnished surface

### 3.3.5. Chemical composition

Figure 3.18 shows the results from the energy-dispersive X-ray spectroscopy (EDS) measurements. Measurements were taken on the processed surface and in the bulk material. No difference on chemical composition was detected before and after cryogenic burnishing by the EDS method.

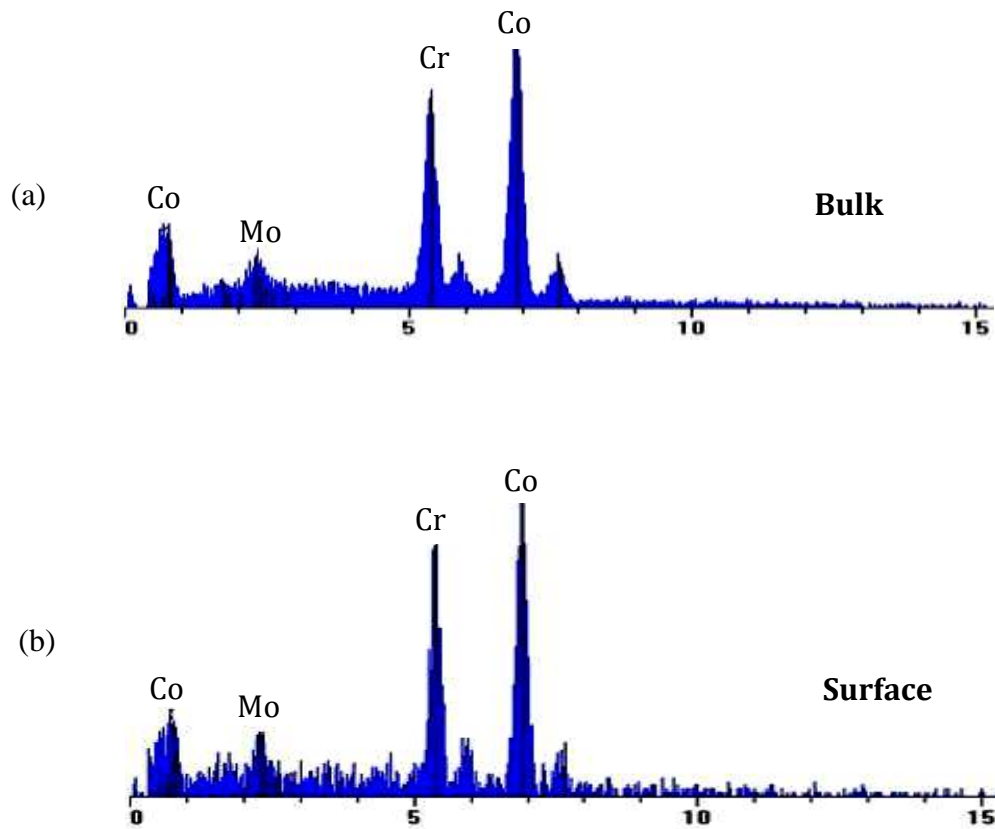


Figure 3.18: EDS results of *Co-Cr-Mo* disc from cryogenic burnishing: (a) bulk, (b) surface

### 3.3.6. Surface roughness

Many SPD processes, such as SMAT (Tao et al. 2002) and surface nanocrystallization & hardening (SNH) (Villegas et al. 2005), are focused on utilizing the process induced severe plastic deformation for grain refinement. Because these processes often need or introduce high temperature during processing, unsatisfactory surface finishes are often reported. Dramatic increases of surface roughness from 0.41  $\mu\text{m}$  of the as-received material to 5.5  $\mu\text{m}$  was reported after SNH of nickel-based Hastelloy *C-2000* (Villegas et al. 2005).



For the purpose of improving the surface finish for different applications, the manufactured components are usually also subjected to a final delicate polishing procedure. For example, the surface roughness for joint implants needs to be lower than  $0.01\ \mu\text{m}$  (ASTM F2033-12). The final polishing, however, will remove more material which will then cause loss of the beneficial surface created during SPD processing. Better surface finish after processing will be favorable for retaining the process-enhanced surface layer. The surface roughness ( $R_a$ ) after burnishing under different conditions is shown in Figure 3.19. On each sample, six roughness readings at different locations of the disc sample were taken and the obtained roughness values were averaged to yield the overall  $R_a$  values shown in Figure 3.19. The application of liquid nitrogen cooling led to about 40% decrease in surface roughness for both 0.127 mm and 0.254 mm DoP compared with dry burnishing. The better surface finish in cryogenic burnishing should be due to the reduced temperature and improved tool-wear through effective cooling by applying liquid nitrogen. The beneficial effect of cryogenic machining on surface roughness was also reported on *AISI 4037* steel (Dhar and Kamruzzaman 2007). For the same cooling conditions, burnishing when using larger DoP led to increased surface roughness which should be caused by the higher temperature (Figure 3.10) and greater tool-wear. It is noted that the surface roughness after burnishing is within  $2\ \mu\text{m}$ , compared with the about  $140\ \mu\text{m}$  burnishing-influenced layer thickness from cryogenic burnishing with 0.254 mm DoP. By avoiding/minimizing polishing, the process-influenced layer with beneficial properties will be largely retained, thus improving the functional performance of the processed components.

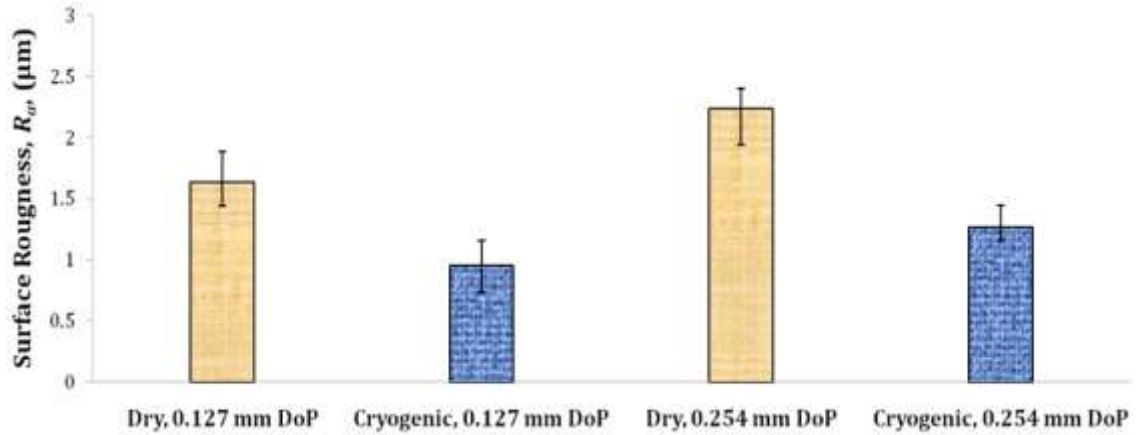


Figure 3.19: Surface roughness ( $R_a$ ) created using different burnishing conditions

### 3.3.7. Phase analysis by XRD method

Grain refinement due to SPD induced DRX is often studied as an independent topic from phase transformation. However, more attention has been paid to combined phase transformation and SPD for fabricating nano/ultrafine-structured metals (Tsuji and Maki 2009). Phase transformation of *Co-Cr-Mo* alloy during processing (Chiba et al. 2009b; Shingo Kurosu 2010) and wear (Chiba et al. 2007; Fischer 2009) has been extensively reported. Such a transformation will influence the mechanical and the tribological behavior of the alloys.

An attempt was made to compare the effect of different burnishing conditions on phase transformation of the *Co-Cr-Mo* alloy using XRD technique. Detailed XRD  $2\theta$  scans were carried out from  $39^\circ$  to  $100^\circ$ . Figure 3.20 shows the relative intensity profiles of the detailed XRD  $2\theta$  scan from  $39.5^\circ$  to  $54^\circ$ . Phases of the annealed *Co-Cr-Mo* specimen before burnishing were analyzed. The absolute intensity of the diffracted X-rays detected by the detector was different in each XRD pattern. This is due to the differences in the count time or the heights of the workpieces during measurement. (Han

et al. 2008) has showed that this did not make the peaks of each phase more intense because the relative intensities of each constituent phase remain constant. Therefore, the difference in the absolute intensity in each burnished surface does not affect the presence/absence of or the relative amount of the specific phase structure in interest. It was found that the initial specimen had both fcc- $\gamma$  and hcp- $\epsilon$  phases in the surface layer. However, the XRD patterns obtained from the dry and cryogenic burnished surfaces consist mainly of fcc- $\gamma$  phase. It is postulated that the original  $\epsilon$  phase had transformed into the  $\gamma$  phase during burnishing. The formation of the hcp- $\epsilon$  phase is totally suppressed by the burnishing process (both dry and cryogenic). The suppression of martensitic- $\epsilon$  transformation is conjectured to be a result of grain refinement when they are smaller than 10  $\mu\text{m}$  (Huang and Lopez 1999). Moreover, no peaks indicating the precipitation of the  $\sigma$  phase were observed.

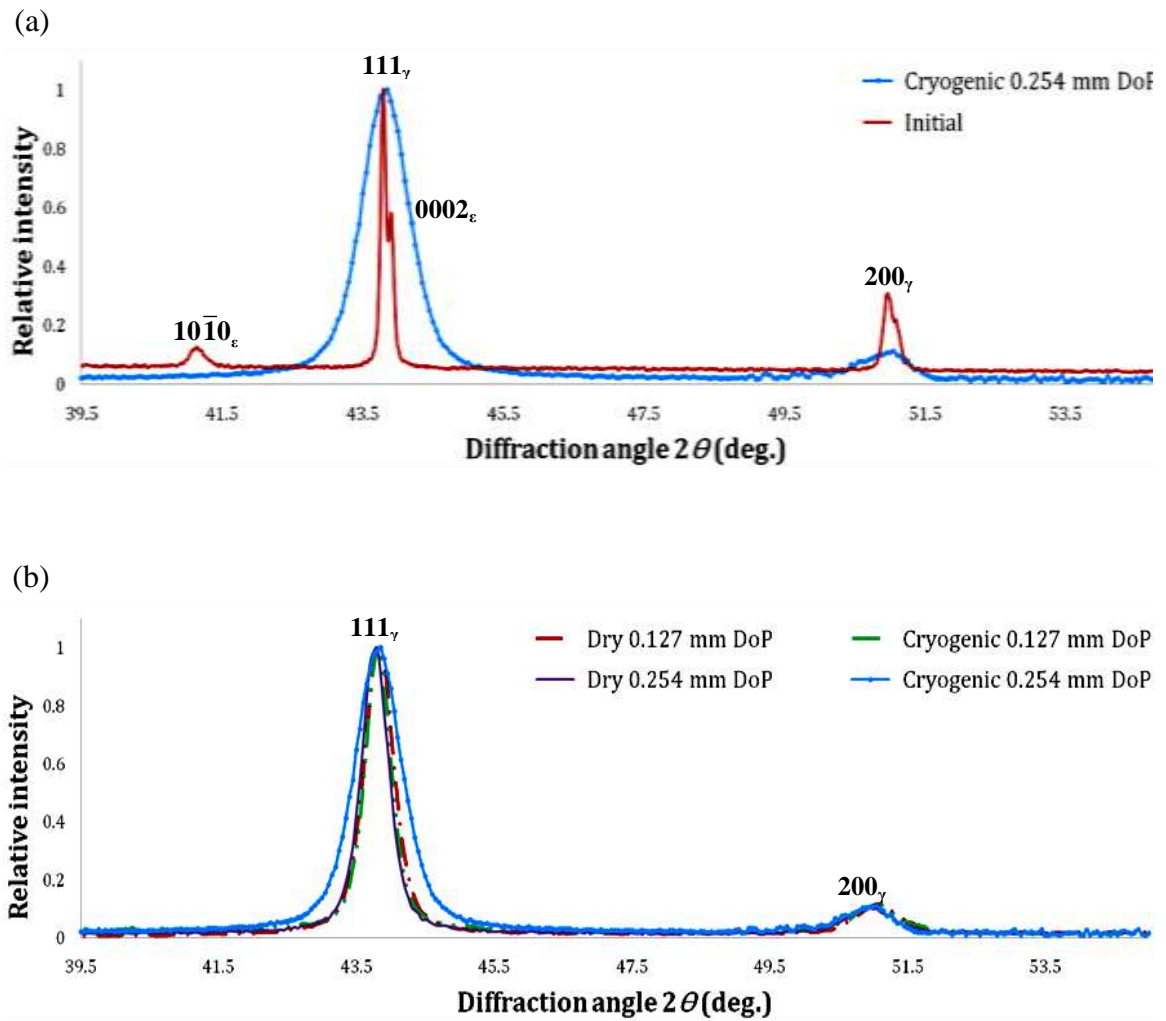


Figure 3.20: (a) XRD patterns on the burnished surface before and after cryogenic burnishing with 0.254 mm DoP; (b) XRD patterns on the burnished surface when using different burnishing conditions

Table 3.4 shows the full width at half maximum (FWHM) results of burnished and initial samples. The FWHMs of burnished samples were all significantly larger than that of the initial sample. It is reported that the peak broadening occurs both by decreasing grain size and increasing dislocation density (Jiang et al. 2006), however, it is very difficult to separate these two factors. The FWHM of the cryogenic burnished

sample with 0.254 mm DoP is much larger than the dry burnished sample under otherwise the same conditions. SEM results (Figure 3.16) have shown that the grain size from cryogenic burnishing is slightly smaller than the one from dry burnishing. Therefore, the difference in FWHM values is probably caused by the more severe stress state induced dislocation density increase from cryogenic burnishing compared to dry burnishing. This finding is consistent with the temperature measurement results shown Figure 3.10 (b). The higher temperature during dry burnishing compromised the SPD effect and reduced the process-influenced layer thickness. Moreover, the FWHM results also indicate that increasing the DoP from 0.127 mm to 0.254 mm under dry conditions did not lead to much thicker process-influenced layer due to the higher temperature.

Table 3.4: FWHMs of measured plane ( $111_\gamma$ ) peaks

Peak	Samples	FWHM (°)
$111_\gamma$	Initial	0.087
	Dry burnishing, 0.127 mm	0.447
	Cryogenic burnishing, 0.127 mm	0.485
	Dry burnishing, 0.254 mm	0.453
	Cryogenic burnishing, 0.254 mm	0.781

### 3.4. Chapter concluding remarks

Burnishing experiments with the application of liquid nitrogen were conducted on an annealed *Co-Cr-Mo* alloy using a custom-made burnishing tool. Surface integrity modifications on this *Co-Cr-Mo* alloy were achieved from cryogenic burnishing processing. The major findings from this study are summarized below:

- (a) The temperature analysis by using the infrared-thermal camera showed that the application of liquid nitrogen during burnishing significantly suppresses the temperature rise within and outside the tool-workpiece contact zone, which can largely sustain the effect of SPD during burnishing as well as keeping the DRX refined grains from growing.
- (b) The microstructure of *Co-Cr-Mo* alloy can be greatly improved by changing the cooling conditions. With the application of liquid nitrogen, the created burnishing-influenced layer thickness can be increased by up to a factor of 3 compared to the one from dry conditions.
- (c) Increasing the burnishing DoP under dry conditions from 0.127 mm to 0.254mm slightly increased the thickness of the process-influenced surface layer ( $30 \pm 5 \mu\text{m}$  to  $43 \pm 9 \mu\text{m}$ ), which was likely due to the higher temperature effect. In contrast, with the application of liquid nitrogen, the burnishing-influenced layer was significantly increased ( $42 \pm 7 \mu\text{m}$  to  $138 \pm 47 \mu\text{m}$ ) by increasing the burnishing DoP from 0.127 mm to 0.254mm. The effects of cryogenic cooling on studied surface integrity parameters (microstructure, hardness, surface roughness, chemical and phase compositions) were presented.
- (d) Microstructure refinement in the surface layer was observed under both dry and cryogenic conditions. Close to the topmost surface, more than 70% of the grains from cryogenic burnishing with 0.254 mm DoP fell into the range from 300 nm to 600 nm, while about 80% of the grains from dry burnishing with 0.254 mm DoP were approximately one-micron in size. Cryogenic burnishing with 0.254 mm

DoP reduced surface grain size by a factor of approximately 270 times through SPD-induced DRX (original grain size is 80  $\mu\text{m}$  in average).

- (e) Compared to dry burnishing, the application of liquid nitrogen reduced the surface roughness by about 40% for both burnishing conditions with 0.127 mm and 0.254 mm DoP. However, burnishing with larger DoP increased the surface roughness due to more severe plastic deformation and higher processing temperature. Due to the severe plastic deformation involved in the process, it should be noted that the application of cryogenic burnishing is limited for creating super-smooth bearing surfaces as the final finishing process. However, better surface finish under cryogenic conditions will be favorable for retaining the process-enhanced surface layer by minimizing the material loss during the final polishing, thus improving the functional performance of the processed components.
- (f) Microhardness measurements indicated that the hardness close to the surface in the burnishing-influenced layer was increased to different extents, among which, the most significant hardness increase was achieved from cryogenic burnishing with 0.254 mm DoP, an increase of up to 87% relative to the bulk value was detected.

Overall, the results suggest that cryogenic burnishing can significantly modify the surface/subsurface properties of *Co-Cr-Mo* alloy, leading to potential performance improvement of critical components in various applications, including biomedical implants.

## **CHAPTER 4: EFFECT OF BURNISHING CONDITIONS IN TERMS OF COOLING METHOD, DEPTH OF PENETRATION AND BURNISHING SPEED ON SURFACE INTEGRITY MODIFICATIONS OF *Co-Cr-Mo* ALLOY**

### **4.1 Introduction**

Burnishing is a cold-forming process which improves the surface characteristics by plastic deformation of the surface layers (Loh et al. 1989b). A literature survey has showed that work on the burnishing process has been conducted by many researchers and the process also improves the properties of the parts, e.g. higher wear resistance (Hamadache et al. 2006; Niberg 1987), increased hardness (Loh et al. 1989a), surface quality (El-Tayeb et al. 2008; Radziejewska et al. 2005), refined microstructure (Altenberger et al. 1999; Palka et al. 2006) and increased maximum residual stress in compression (Fattouh and Elkhabeery 1989; Zhang and Lindemann 2005). Thus, control of the burnishing process conditions in such a way as to introduce desired properties in the surface region could lead to considerable improvement in component life.

Seemikeri et al. (2008) studied the effect of burnishing on surface integrity and fatigue life of *AISI 1045* material in terms of evaluating the combined effects of burnishing process parameters, identifying the predominant parameter, establishing their order of significance, and setting the levels of different parameters to minimize surface roughness and/or maximize surface hardness and fatigue life. Lopez et al. (2007) applied burnishing to reduce the roughness of surfaces obtained by ball-end milling of two materials, *P20* low carbon steel (32 HRC) and the nickel alloy *Inconel 718* (42 HRC, precipitation hardened). They concluded that using a large radial width of cut in end-milling followed by small step over during burnishing can produce the acceptable final roughness. For some process parameters compressive cold work is greater and deeper in



the Inconel 718 than in the steel. Rao et al. (2008) did a similar experimental parametric study on HSLA dual-phase steel. Their result also indicated that burnishing parameters have significant effect on the surface hardness and wear resistance. Salahshoor and Guo (2011) investigated the effect of various combinations of burnishing parameters on surface integrity characteristics of a potential biomaterial *MgCa* alloy. Their results showed that the *MgCa* alloy can be safely burnished at suitable burnishing conditions with no cracks produced at the surface and in the subsurface. It is also found that the microstructure including grain size did not show a noticeable change after burnishing. Residual stresses were highly compressive especially at low burnishing pressure.

In surveying the literature on the influence of the process parameters, it can be found that the major process parameters affecting the resulting surface conditions are: depth of penetration/burnishing force, burnishing speed, feed-rate, tool size, tool material, number of passes, and coolant/lubrication. In this chapter, the effects of three burnishing parameters, namely: cooling method, depth of penetration (DoP) and burnishing speed on processing temperature, force, tool-wear and the workpiece surface integrity properties in terms of microstructure, microhardness, phase change and residual stresses were investigated.

## **4.2 Experimental work**

The work material, the burnishing process method and the surface integrity characterization methods in terms of microstructure, microhardness, and phase change analysis used in this chapter are the same as described in Chapter 3.

The residual stresses in the *Co-Cr-Mo* samples before and after wear tests were obtained by XRD using the  $\sin^2\psi$  method (Noyan and Cohen 1987). The equipment used was a PROTO machine (model iXRD) (Figure 4.1) available at the X-ray Diffraction Center for Materials Research, University of Coimbra, Portugal. The parameters used in the X-ray analysis are shown in Table 4.1. To determine the in-depth residual stress profiles, layers of material were successively removed by electropolishing method to minimize the modification of stresses. Further corrections to the residual stress data were made due to the volume of material removed. It is noted that in the present study, the total penetration depth of the X-ray beam for this *Co-Cr-Mo* alloy is about 10  $\mu\text{m}$ . Since the strength of the X-ray beam decreases exponentially with the distance from the surface, it is estimated that the measurement for the nominal depth is an average value of a layer about 5  $\mu\text{m}$  thick below that depth.



Figure 4.1: PROTO iXRD machine used in the residual stress measurement (X-ray Diffraction Center for Materials Research, University of Coimbra, Portugal)

Table 4.1: XRD parameters for residual stress measurement of the *Co-Cr-Mo* alloy

Young modulus	241 GPa
Poisson ratio	0.3
Radiation	<i>Mn-K<math>\alpha</math></i>
Voltage and current	18 kV, 4 mA
Collimator diameter	3 mm
Bragg angle $2\theta$ (°)	156.50 (hkl) = (311)
Number of $\psi$ angles	15

### 4.3 Effects of cooling method and depth of penetration

The preliminary results drawn from Chapter 3 have shown that the application of liquid nitrogen cooling can significantly influence the burnished surface integrity. However, due to the varying thermal softening and mechanical hardening effects under different burnishing conditions, the effectiveness of liquid nitrogen cooling on surface integrity enhancements varies as well. Thus, there is a need to establish better relationships among liquid nitrogen cooling, burnishing conditions and the resulting surface integrity for the purpose of finding the optimal combination of conditions for achieving the most desirable processing /product functional performance.

Continuing the investigations in Chapter 3, a new set of burnishing experiments with varying burnishing speed, depth of penetration and cooling method were conducted to further study the effect of different burnishing conditions on surface integrity modifications of *Co-Cr-Mo* alloy to a greater depth. The burnishing experimental

conditions for studying the effects of cooling method and depth of penetration are shown in Table 4.2.

Table 4.2: Burnishing experimental conditions for studying the effects of cooling method and depth of penetration

Exp. No	Tool Diameter (mm)	Depth of Penetration (mm)	Surface Speed (m/min)	Cooling
1	14.3	0.08	100	Dry
2	14.3	0.08	100	Cryogenic
3	14.3	0.08	200	Dry
4	14.3	0.08	200	Cryogenic
5	14.3	0.15	100	Dry
6	14.3	0.15	100	Cryogenic
7	14.3	0.15	200	Dry
8	14.3	0.15	200	Cryogenic
9	14.3	0.21	100	Dry
10	14.3	0.21	100	Cryogenic
11	14.3	0.21	200	Dry
12	14.3	0.21	200	Cryogenic
13	14.3	0.254	100	Dry
14	14.3	0.254	100	Cryogenic

#### 4.3.1 Temperature

The temperature was measured by following the procedure described in Chapter 3. The temperature profile along the distance below the surface shown in Figure 4.2 is equivalent to the depth profile taken from exit point O towards the center of the disc as

shown in Figure 3.9. The results agree with the findings in Chapter 3, significant temperature reductions were achieved by cryogenic cooling. Especially on the workpiece surface, a temperature drop of 380 °C was observed between dry and cryogenic conditions at 0.21 mm DoP, 100 m/min burnishing speed (Figure 4.2 (a)). It can also be observed here that increasing DoP and burnishing speed also led to an increase of temperature but to different extents.

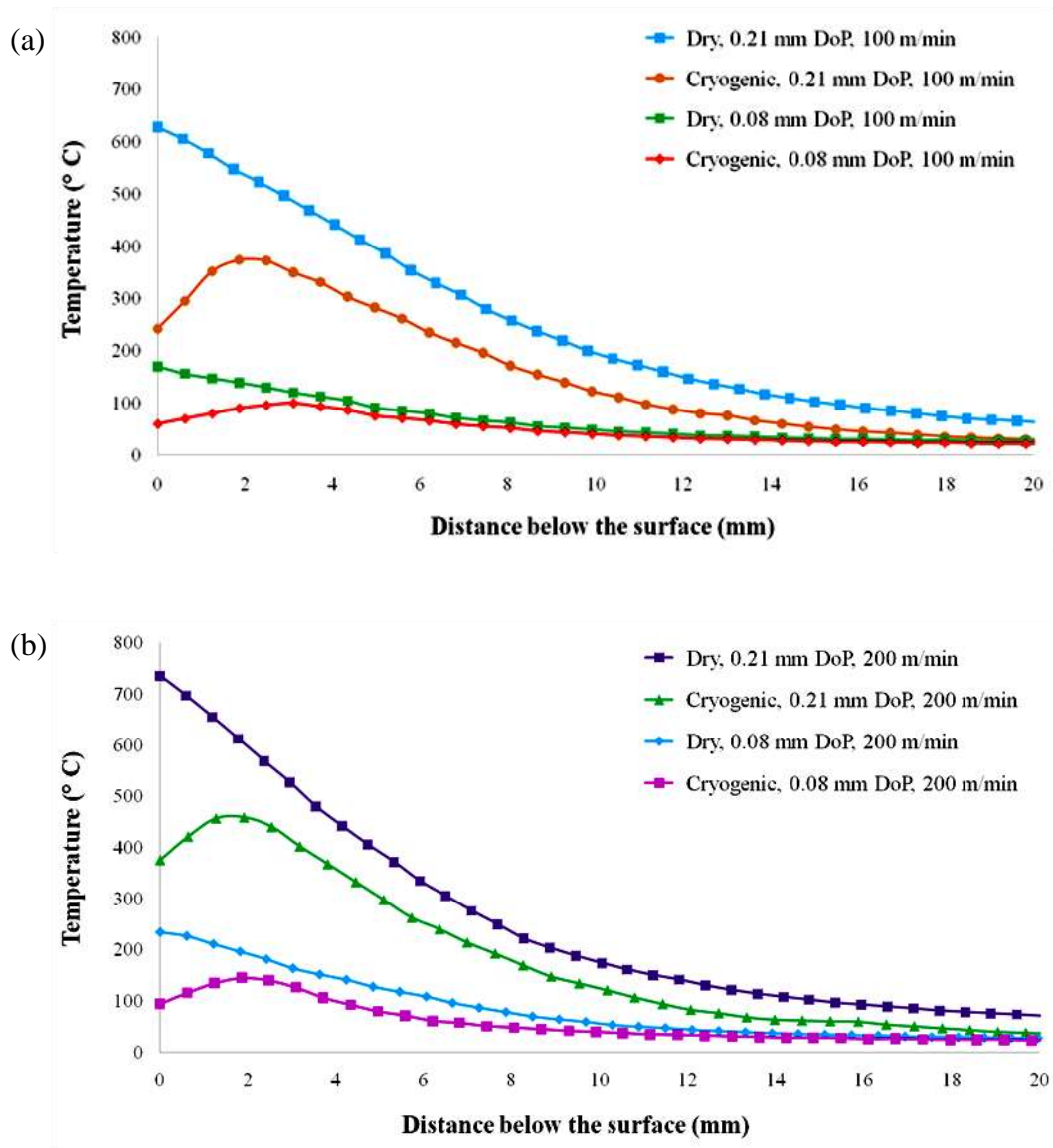


Figure 4.2: Effects of cooling method and DoP on temperature along the depth profile: (a) 100 m/min burnishing speed, (b) 200 m/min burnishing speed

### 4.3.2 Burnishing force

During the cutting process, stress varies in the tool-workpiece contact area. When the cutting depth is small enough, no chip will form; this is thus called a burnishing process. The forces during burnishing process should be analyzed firstly due to an arc-shaped cutting edge, as shown in Figure 4.3. It can be seen that the burnishing force at the arc cutting edge is the resultant force at edge  $F_T$  and  $F_R$ . The tangential force  $F_T$  makes the metal move ahead; while the radial force  $F_R$  presses the metal to the surface. When the conditions reach a certain threshold, chips form. According to Luo et al. (2006), when  $F_T > F_R$ , chips will form; when  $F_T < F_R$ , the metal is pressed to the basal body and no chips are formed. This distinguishes the burnishing process from the cutting process.

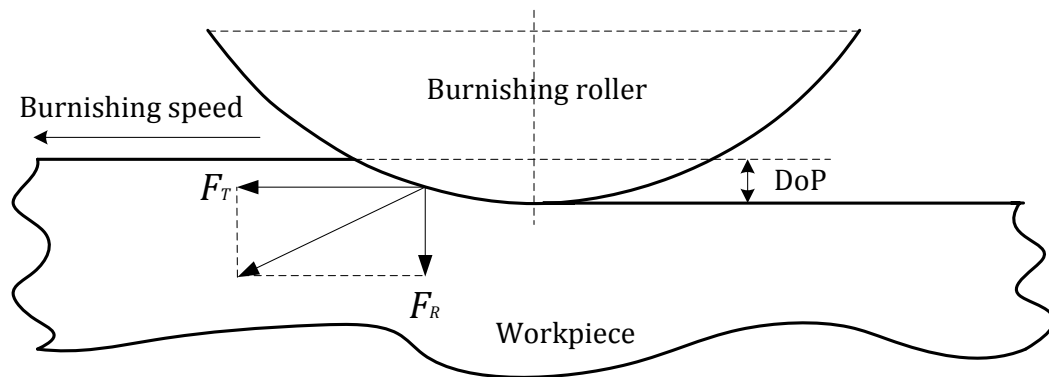


Figure 4.3: Burnishing forces illustration

The measured burnishing forces in both radial and tangential directions are shown in Figure 4.4 (a). The forces shown were the average values of the last 4 s of the experiment obtained from the 10 s of used burnishing dwell time. The results agree with the findings in Chapter 3, i.e., with increasing DoPs, the burnishing forces increased accordingly. However, the burnishing forces were not linearly increasing against DoP values, which is likely due to the nonlinearly increase of the thermal softening effect

when using increased DoPs. Moreover, with lower DoPs (0.08 mm and 0.15 mm), the cryogenic burnishing test had slightly higher radial and tangential forces when compared to those generated in dry burnishing. Presumably the precooling effect made the material stronger when using cryogenic conditions. However, when the DoP increased (0.21 mm), the force differences between dry and cryogenic conditions became insignificant, which is attributed to the greater tool-wear resulting from the higher processing temperature under larger DoPs. This claim is supported by the changes of the ratio of tangential force and radial force against DoP (Figure 4.4 (b)) as well as the 3-D topographic profiles of the tool-wear zone under different conditions (Figure 4.5). It can be observed in Figure 4.4 (b) that, by increasing the DoP from 0.08 mm to 0.21 mm, the ratio of tangential/radial forces (T/R ratio) increased also, which indicated the increase of friction force with increasing DoP values. However, the increasing rate of the T/R ratio under dry conditions is higher than the one with cryogenic cooling, which is likely due to the beneficial effect of cryogenic cooling on tool-wear.

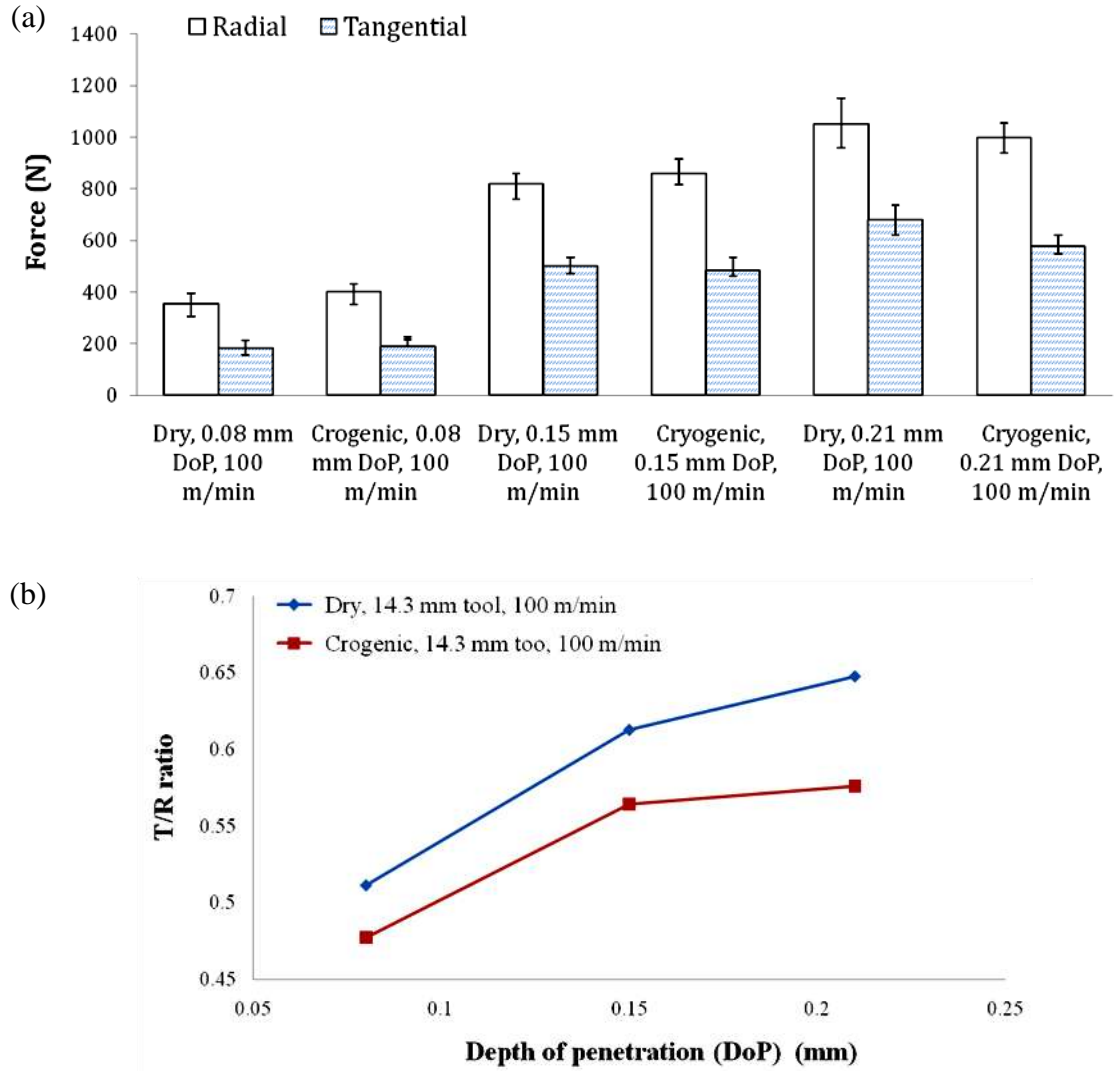


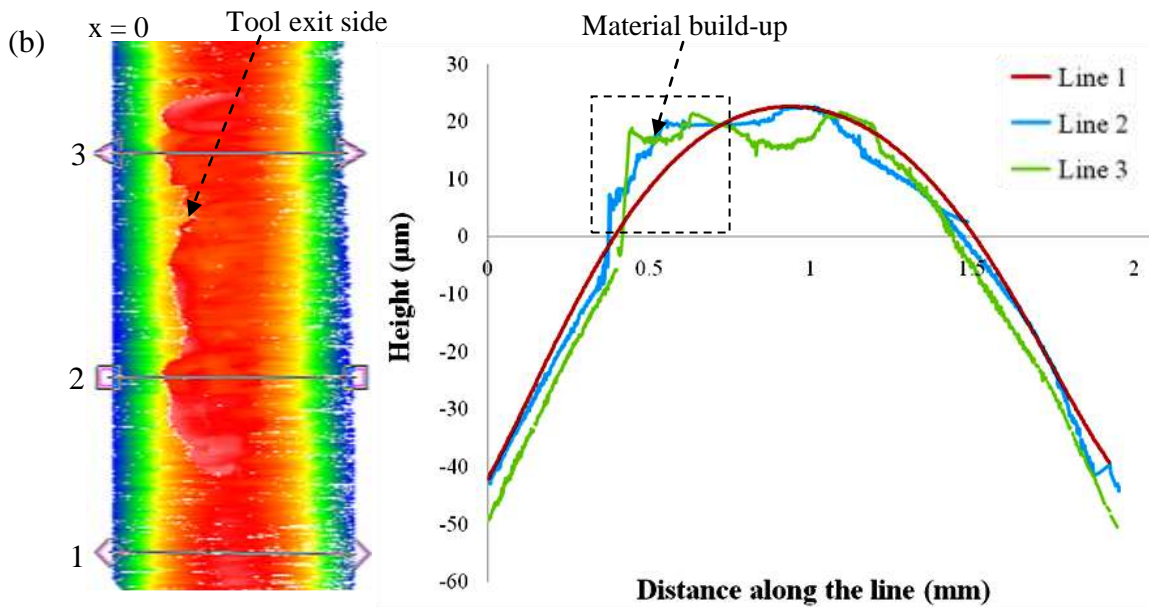
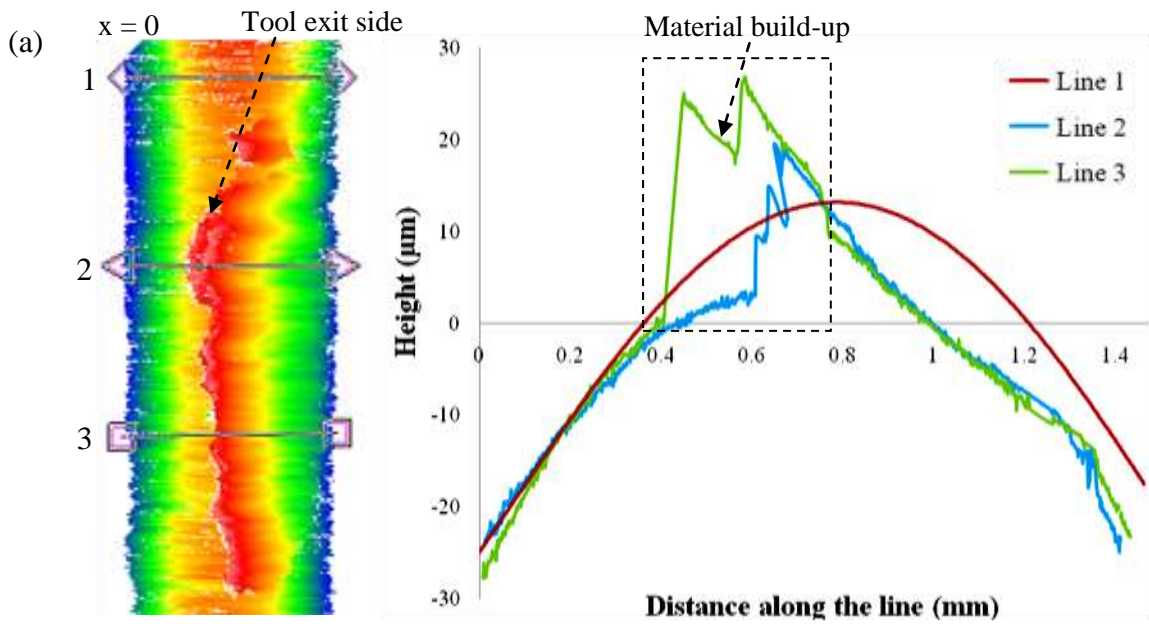
Figure 4.4: (a) Measured burnishing forces, (b) ratio of tangential/radial forces (T/R ratio) vs. DoP (14.3 mm tool diameter)

#### 4.3.3 Tool-wear

In addition, profiling of the tool-wear zone three dimensionally under different conditions were conducted by using the white light interferometer system. In Figure 4.5, the surface topographic images are presented on the left side, the corresponding profile plots of the three lines (marked as 1, 2 and 3 on the topographic images) are given on the right side. Line 1 always shows the profile of the original tool without any signs of wear,



in contrast, lines 2 and 3 are drawn across the wear zone for the purpose of comparing the level of tool-wear under different conditions. The tool-wear from 0.08 mm DoP for both dry and cryogenic conditions was very minor and the difference was indistinguishable, thus, Figure 4.5 only shows the results from 0.15 mm and 0.21 mm DoPs which gave clear comparisons between dry and cryogenic conditions. It is evident from Figure 4.5 (a) and (b) that, with 0.15 mm DoP, the tool when using dry conditions had more material build-up at the tool exit side as well as slightly more tool-wear compared to cryogenic conditions. When a larger DoP was used (0.21 mm), the effect of cooling method (dry and cryogenic) on tool-wear became obvious. As shown in Figure 4.5 (c) and (d), the tools after dry and cryogenic burnishing with 0.21 mm DoP both have obvious tool material loss. The maximum wear depth which represents the maximum difference between the worn tool profile and the original tool profile without any wear is marked on Figure 4.5 (c) and (d). It can be clearly observed that, with the same DoP value used (0.21 mm), the maximum wear depth from cryogenic burnishing ( $\sim 20 \mu\text{m}$ ) was 13% of that of the one from dry burnishing ( $\sim 150 \mu\text{m}$ ). The discrepancy of the effect of cryogenic cooling on tool-wear under different DoPs is attributed to the higher processing temperature when larger DoP was used.



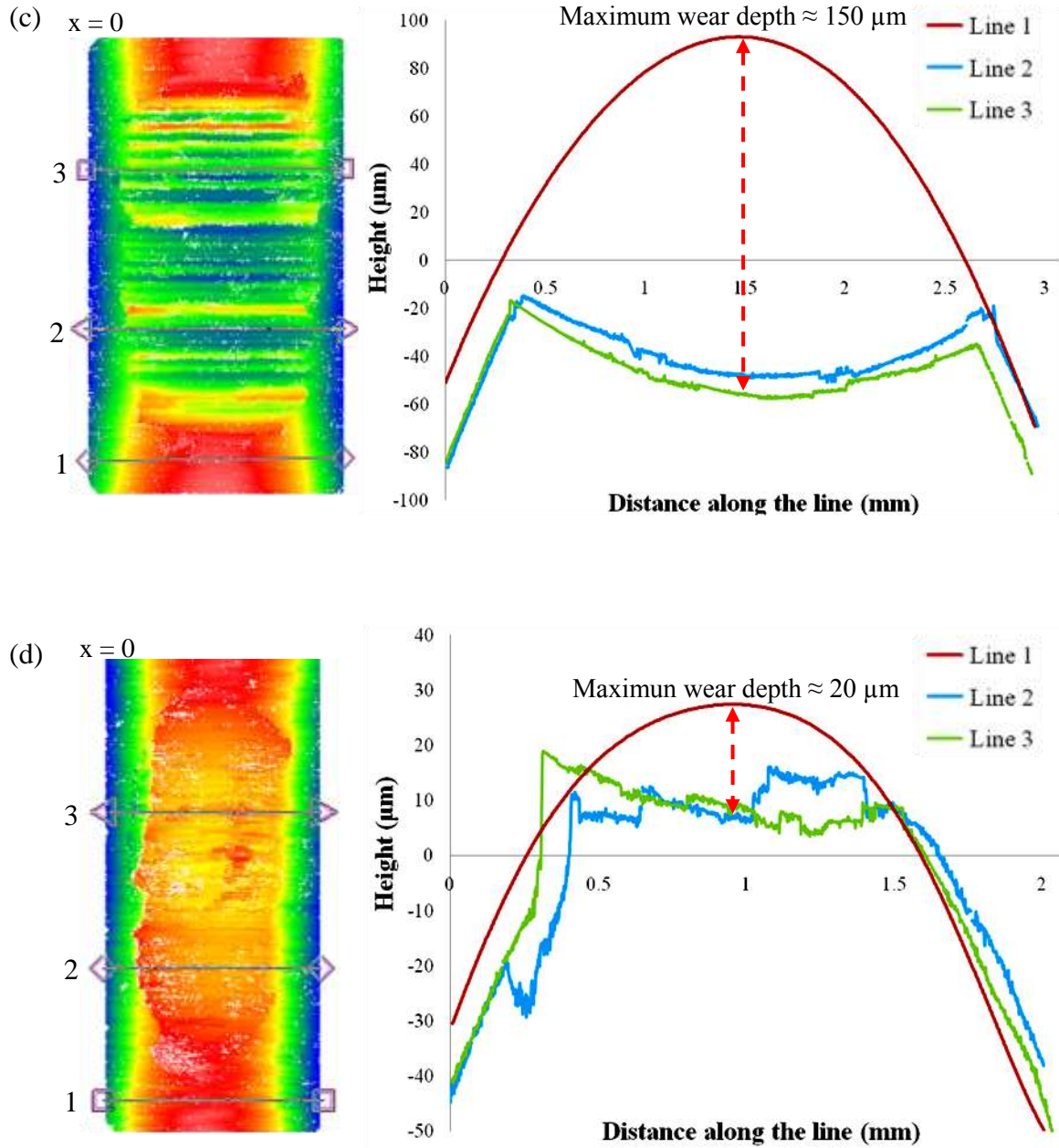


Figure 4.5: 3-D topographic profiles of the tool-wear zone: (a) dry, 0.15 mm DoP, (b) cryogenic, 0.15 mm DoP; (c) dry, 0.21 mm DoP, (d) cryogenic, 0.21 mm DoP (14.3 mm tool diameter, 100 m/min burnishing speed)

#### 4.3.4 Microstructure

Figure 4.6 shows the microstructures of representative burnished surface microstructures using 14.3 mm tool diameter, 0.21 mm DoP, 200 m/min burnishing speed. A burnishing-influenced layer in which grain boundaries were no longer clearly visible at this magnification was formed. Consistent with the findings in Chapter 3, the thickness of the burnishing-influenced layer with refined grains obtained when using cryogenic conditions ( $57 \pm 10 \mu\text{m}$ ) was 3.6 times larger than the one from dry conditions ( $16 \pm 6 \mu\text{m}$ ), which is attributed to the more SPD effect due to the application of cryogenic cooling which results in lower processing temperature.

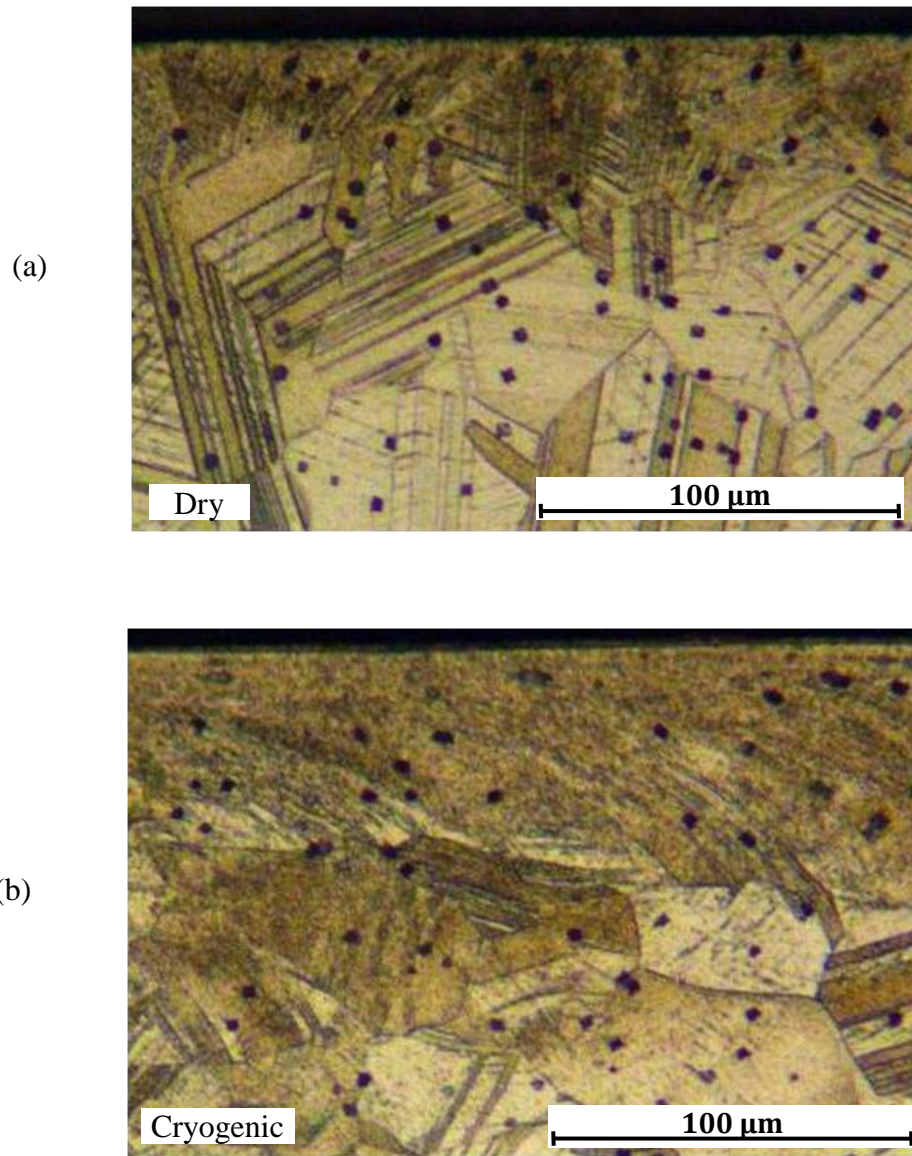
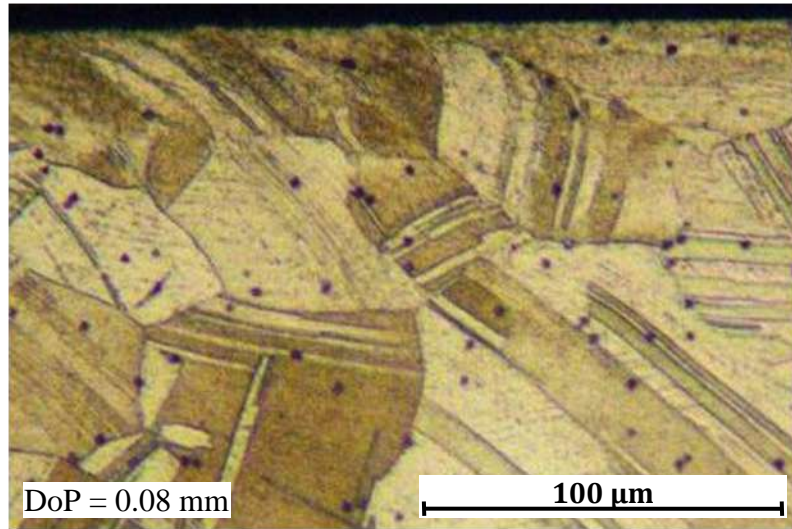


Figure 4.6: The effect of the cooling method on microstructure (14.3 mm tool diameter, 0.21 mm DoP, 200 m/min burnishing speed): (a) dry, (b) cryogenic

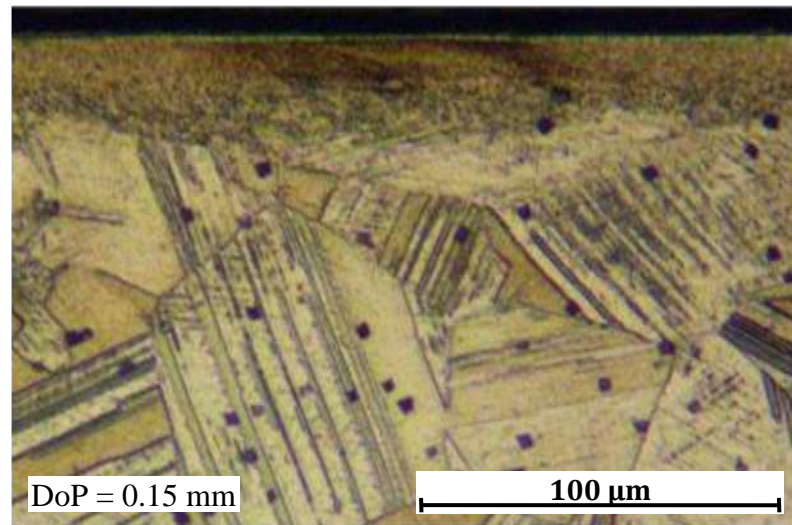
The microstructures of the burnished surfaces under cryogenic conditions, 14.3 mm diameter tool, 200 m/min burnishing speed with changing DoP values are shown in Figure 4.7. The burnishing-influenced layer was about 13  $\mu\text{m}$  thick with 0.08 mm DoP (Figure 4.7 (a)). The thickness of this layer increased to 28  $\mu\text{m}$  with 0.15 mm DoP (Figure 4.7 (b)) and further increased to 57  $\mu\text{m}$  with 0.21 mm DoP under cryogenic

conditions (Figure 4.7 (c)). The increase of the layer thickness with increasing DoP agrees with burnishing force measurements as shown in Figure 4.4 (a).

(a)



(b)



(c)

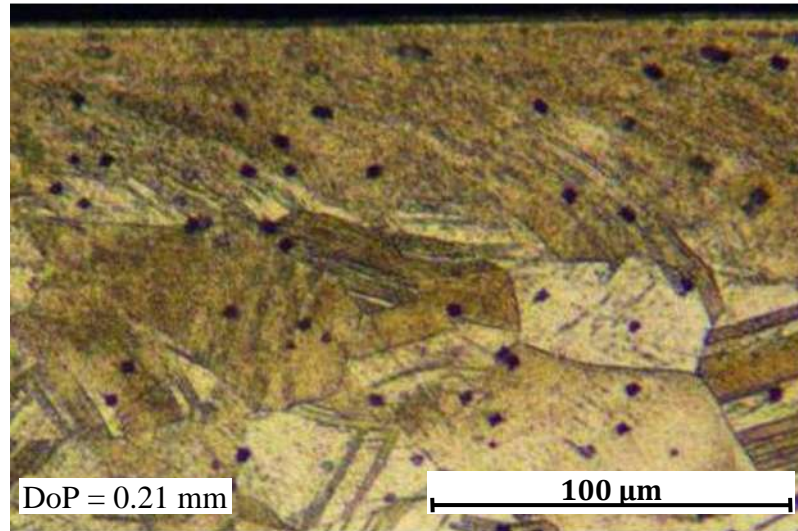


Figure 4.7: The effect of the DoP on microstructure (cryogenic, 14.3 mm diameter tool, 200 m/min burnishing speed): (a) 0.08 mm DoP, (b) 0.15 mm DoP, (c) 0.21 mm DoP

The effect of DoP on the burnishing-influenced layer thickness was affected by the cooling method and the burnishing speed. As shown in Figure 4.8, with the burnishing speed of 100 m/min, the burnishing-influenced layer thickness obtained when using dry conditions also increased with the increase of DoP, however, the layer thickness with cryogenic cooling increased faster than the one from dry conditions. This can be explained by the stronger thermal softening effect due to larger DoP, induced a higher processing temperature. This claim was further supported when the burnishing speed increased from 100 m/min to 200 m/min. It can be observed in Figure 4.8 that, with 200 m/min burnishing speed, the burnishing-influenced layer thickness was almost constant when the DoP was changed from 0.08 mm to 0.21 mm; the work-hardening effect was compromised by the thermal softening effect, which led to almost no change in the layer thickness.

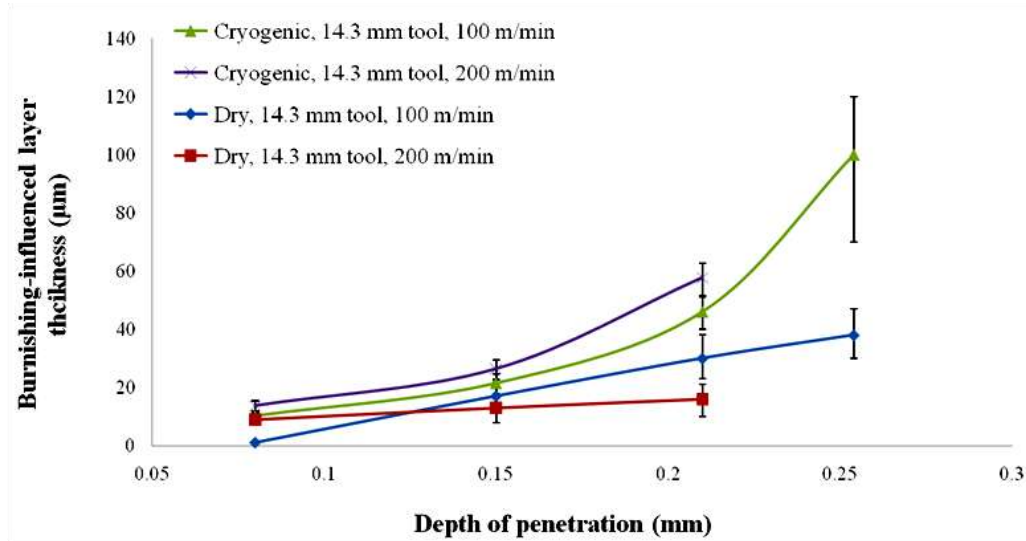


Figure 4.8: The effect of the DoP on burnishing-influenced layer thickness (14.3 mm diameter tool)

#### 4.3.5 Phase change

*Co-Cr-Mo* alloys used in the manufacture of orthopedic prosthetic devices possess very low stacking fault energies. As a result, plastic deformation by dislocation glide in the face centered cubic (fcc) metastable phase is severely restricted (Rajan 1982; Rajan and Vandersande 1982; Vander Sande 1976). This behavior leads to formation of strain-induced crystal defects, such as intrinsic stacking faults, twins and regions of highly localized slip along pre-existing and strain-induced stacking faults, when these alloys are subjected to external stresses exceeding their yield strength. Thus, the ductility of these materials is small compared with other fcc metals. The interactions between dislocations of limited mobility and dissociated dislocations and/or twins lead to very rapid and highly localized hardening. This eventually leads to fracture if no additional strain-producing mechanisms become available to relieve the high stresses required to maintain plastic flow. Large strain plastic deformation of *Co-Cr-Mo* alloys must therefore be



microscopically accommodated by alternative mechanisms. Strain-induced phase transformations have been suggested to play an important role during large strain plastic deformation in *Co-Cr-Mo* alloys (Rajan 1982; Rajan and Vandersande 1982; Vander Sande 1976), this type of dynamically induced transformation during processing (Chiba et al. 2009b; Shingo Kurosu 2010) and wear (Chiba et al. 2007; Fischer 2009) has been extensively reported, which will influence the mechanical and the tribological behavior of the alloys. Graham and Youngblo (1970) demonstrated that the amount of hcp phase formed during cold swaging of *Co-Cr-Mo-Ni* multiphase alloys increased rapidly with the amount of deformation. The tensile yield strength was correlated linearly with the amount of strain-induced hcp phase. Olson and Cohen (1975) have shown that the ability of low stacking fault energy materials to deform uniformly during tensile testing is enhanced by the strain-induced phase transformations.

In addition to the findings from processing of *Co-Cr-Mo* alloys, according to the TEM observations, different appearances of plastic deformation with respect to the distance to the worn surfaces of *in vivo* and *in vitro* hip implant surface were revealed. It is found that the uppermost surface consists of a nanocrystalline microstructure of fcc and strain-induced hcp *Co-Cr-Mo* solid solutions. Moreover, at a depth of about 30  $\mu\text{m}$  from the worn surface, electron diffraction patterns verified the presence of  $\epsilon$ -martensite, which has a hcp lattice structure and form strictly on the discrete (111) $_{\gamma}$  sliding planes. The change in microstructure certainly has a big impact on the wear mechanisms as has been shown by pin-on-disk laboratory tests (Buscher and Fischer 2003).

In the current study, the effect of different burnishing conditions on phase transformations of the *Co-Cr-Mo* alloy was studied. Figure 4.9 shows the detailed XRD

$2\theta$  scan profiles from  $35^\circ$  to  $70^\circ$  of the burnished pins. Phases of the annealed *Co-Cr-Mo* specimen before burnishing were analyzed also (Figure 4.9 (a)); it was found that the initial specimen had both fcc  $(111)_\gamma$  and hcp  $(0002)_\epsilon$  phases initially in the surface. The XRD patterns obtained from dry and cryogenic burnishing experiments with 0.08 mm DoP, 100 m/min burnishing speed show a combination of fcc  $(111)_\gamma$  and hcp  $(10\bar{1}1)_\epsilon$  phases. Also, the relative intensity of the hcp  $(10\bar{1}1)_\epsilon$  peak from cryogenic conditions is 2.7 times greater than the peak intensity from dry burnishing. In contrast, as shown in Figure 4.9 (b), when the burnishing speed increased to 200 m/min, the relative intensity of  $(10\bar{1}1)_\epsilon$  peak reduced under cryogenic conditions, and the dry burnished sample with otherwise the same conditions consisted mainly of fcc  $(111)_\gamma$  phase. It is reported that slow cooling after thermal treatment inhibited the metastable fcc  $\Rightarrow$  hcp phase transformation of *Co-Cr-Mo* alloy. In contrast, a fast cooling rate after solution annealing and a controlled grain size range promoted this phase transformation during SPD processes (Salinas-Rodríguez 1999). As shown in Figure 4.2, with 0.08 mm DoP, the application of cryogenic cooling led to a  $110^\circ\text{C}$  temperature difference between dry and cryogenic burnishing under 100 m/min burnishing speed, and a  $150^\circ\text{C}$  temperature difference when the burnishing speed increased to 200 m/min. From the results above, it can be stated that the lower processing temperature and the faster cooling rate due to the application of liquid nitrogen promote the fcc  $\Rightarrow$  hcp transformation during and after burnishing.

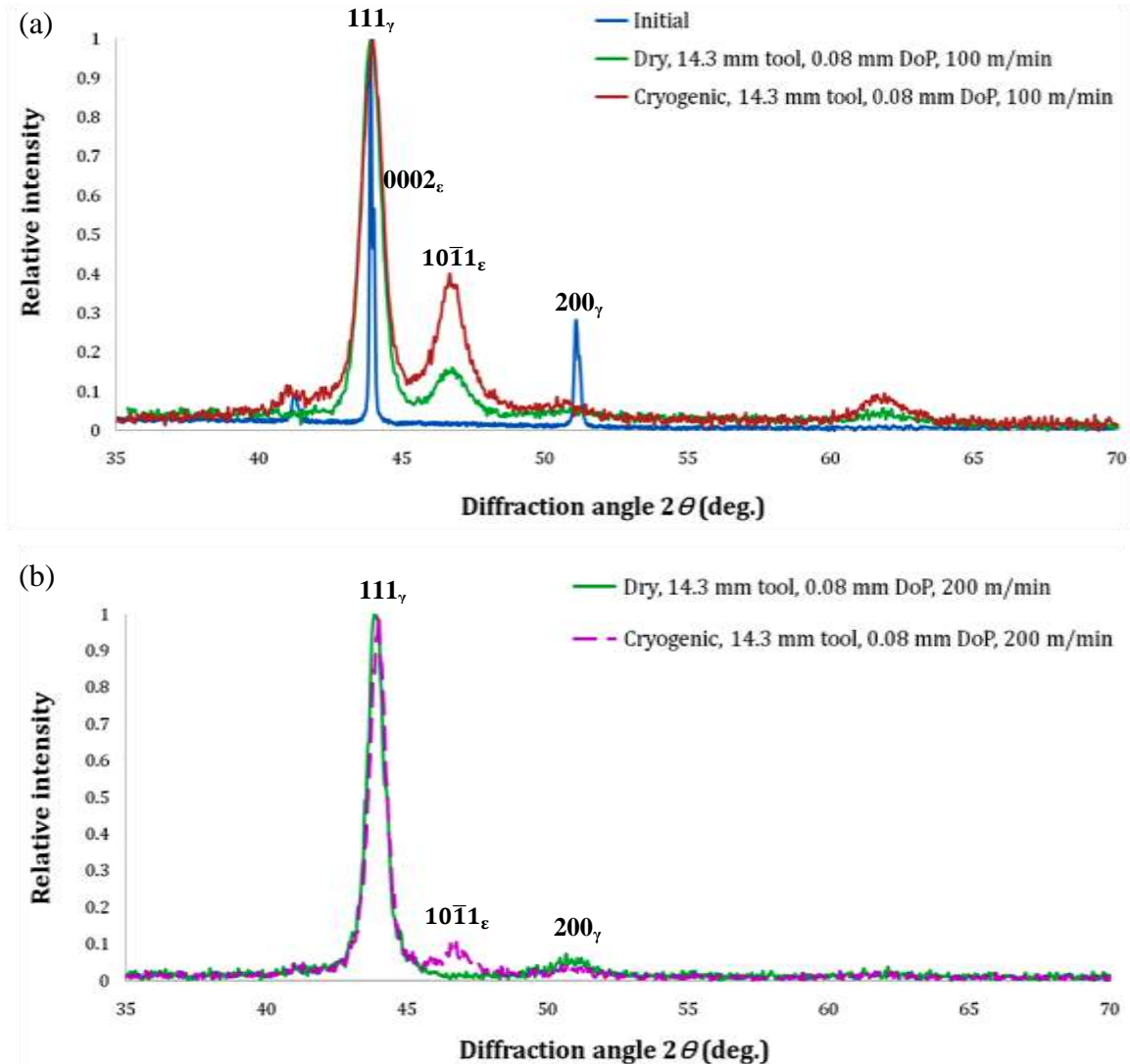
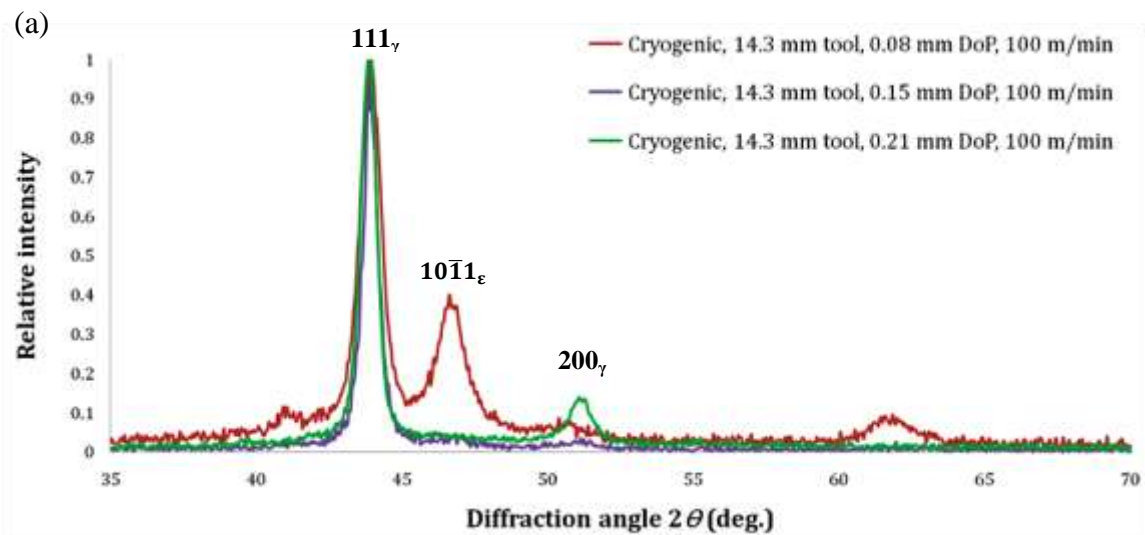


Figure 4.9: The effect of the cooling method on surface phase change

In addition to temperature, the definition of “strain-induced transformation” also suggests that larger DoP could lead to more severe plastic deformation which should promote the fcc  $\Rightarrow$  hcp transformation. However, the findings from the current study gave contradictory results. As shown in Figure 4.10, for both dry and cryogenic conditions, increasing of DoP values all led to the reduction of the hcp ( $10\bar{1}1$ ) $_\epsilon$  peak intensity. One possibility for this discrepancy is that, when larger DoP was used, the

processing temperature was in competition with the work-hardening effect and compromised the happening of the strain-induced phase transformation. Another possibility is due to complicated phase transformation nature of the *Co-Cr-Mo* alloy. It is reported that, by changing the mill intensity and milling duration (equivalent to the amount of plastic deformation), the cobalt alloys can undergo the strain-induced phase transformation following the routes of hcp + fcc => hcp, hcp + fcc => hcp => fcc + hcp, and hcp + fcc => hcp => fcc + hcp => fcc (Huang et al. 1995). It suggests that there is an optimal burnishing force exists beyond which this transformation will be inhibited. In the current study, the reported phase analysis results just represented the final phase state of the burnished sample; the history of the phase transformation during processing cannot be captured.



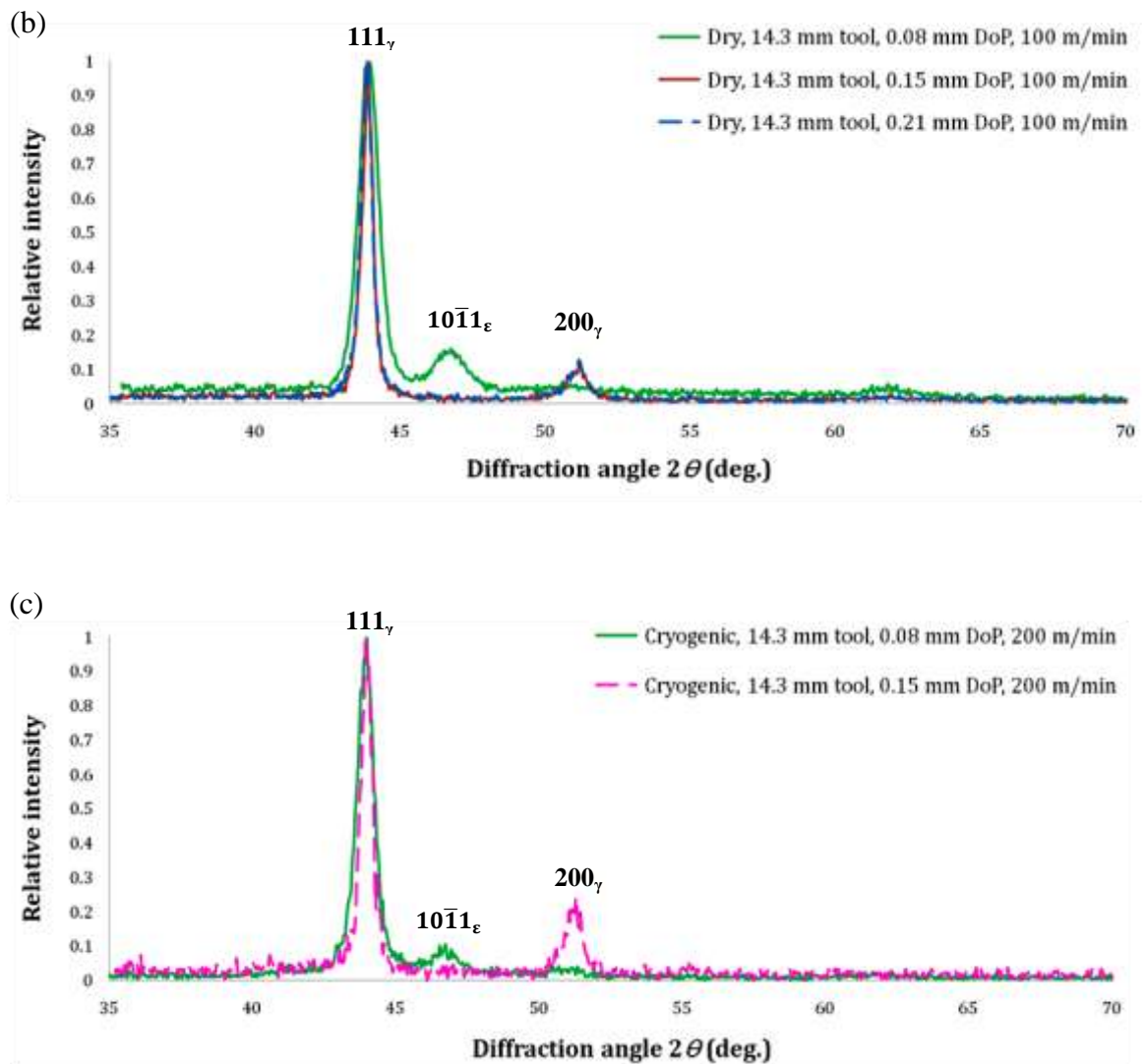


Figure 4.10: The effect of the DoP on surface phase change (14.3 mm tool diameter): (a) cryogenic, 100 m/min burnishing speed, (b) dry, 100 m/min burnishing speed, (c) cryogenic, 200 m/min burnishing speed

#### 4.3.6 Residual stresses

XRD is the most non-destructive way of evaluating surface residual stresses. The basic principle is based on Bragg's law, which states that when a monochromatic X-ray beam with wavelength  $\lambda$  is projected onto a crystalline material at an angle  $\theta$ , diffraction occurs only when the distance traveled by the rays reflected from successive planes

differs by a complete number  $n$  of wavelengths (Figure 4.11). Lines ABC and DEFGH represents X-ray radiation. Initially, lines AB and DE have the same wavelength. These lines will remain in phase if EFG is an integral multiple of this wavelength. This causes reinforcement of the incident X-ray beam, which is known as constructive interference or diffraction. If EFG is not an integral multiple of the incident beam wavelength, then the lines will be out of phase resulting in destructive interference and diffraction will not occur. This can be expressed using  $n\lambda = 2d\sin\theta$ , where  $n$  is an integer,  $\lambda$  is the wavelength of a beam of X-rays incident on a crystal with lattice planes separated by distance  $d$ , and  $\theta$  is the Bragg angle. XRD relies on the elastic deformation of a material to measure internal stresses in a material. The deformation cause changes in the spacing of the lattice planes from their stress free value to a new value that corresponds to the magnitude of the applied stress. Because the wavelength is constant, the unknown parameters in Bragg's equation are the interplanar spacing  $d$  and Bragg angle  $\theta$ . Thus, if  $\theta$  becomes known, the  $d$  value can be obtained using Bragg's law. Complete theories and procedures for residual stress measurements by using XRD method can be found in Umbrello (2004).

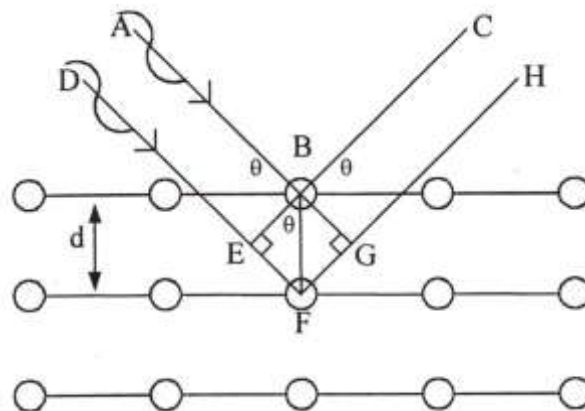


Figure 4.11: Diffraction of X-rays by a crystalline material (Umbrello 2004)

Figure 4.12 shows the in-depth residual stresses of the burnished *Co-Cr-Mo* samples under both dry and cryogenic conditions. The initial surface residual stresses (without any processing) were close to neutral in both tangential and axial directions due to the used stress relief annealing procedure. The axial and tangential residual stresses in the burnished samples became tensile after burnishing when compared to its state before burnishing. This is different from the literature findings on traditional burnishing processes, which reported that burnishing normally induces more compressive residual stresses (Fattouh and Elkhabeery 1989; Zhuang and Halford 2001). The contradictory findings from the results in Figure 4.12 and the literature data may be caused by the different roller settings. The used burnishing tool was fixed in this study, while it was allowed to rotate in most literature examples. The fixed tool setting led to both large radial and tangential forces (Figure 4.2). The latter is normally close to zero when using a conventional rotating roller.

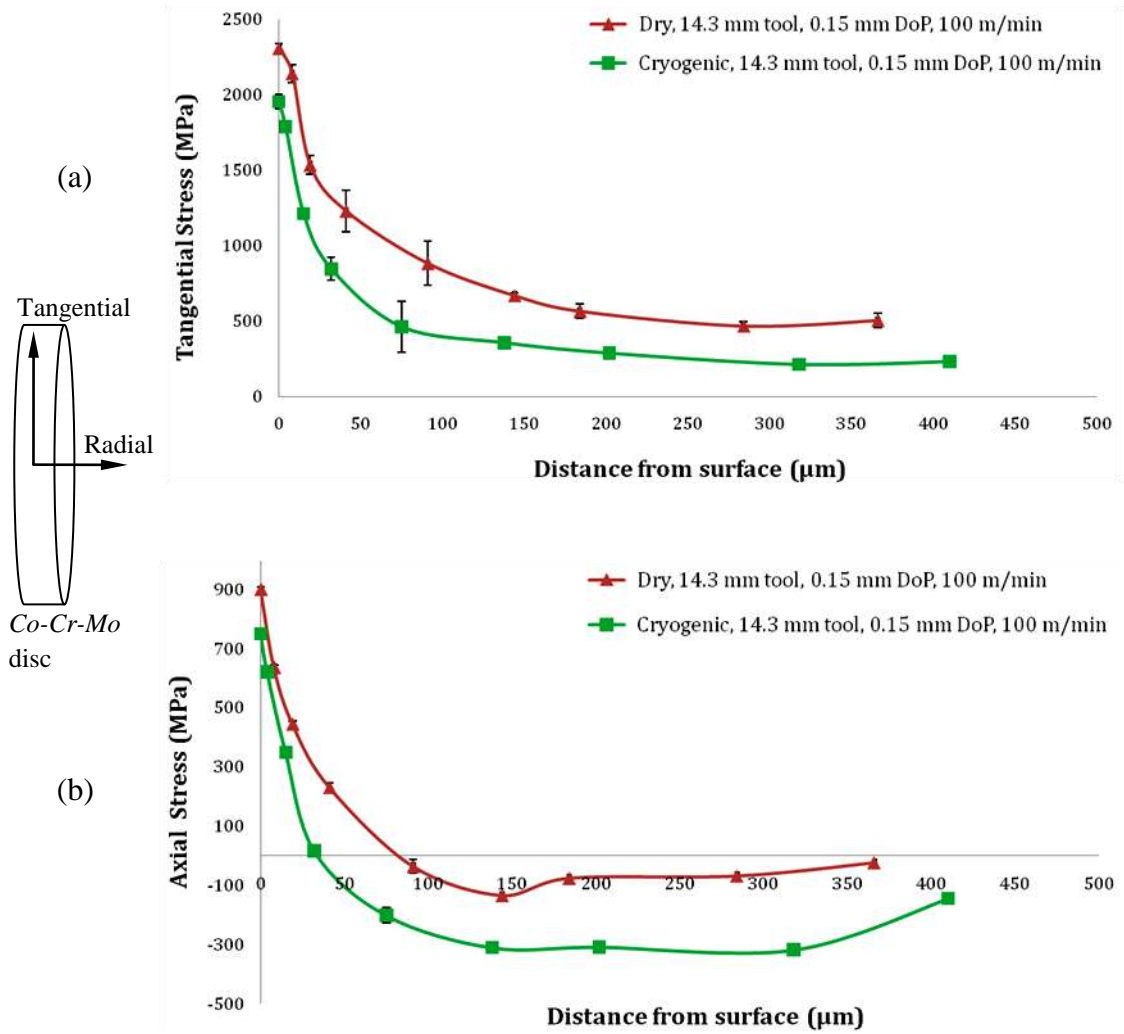


Figure 4.12: The effect of the cooling methods on residual stresses: (a) tangential and (b) axial directions

Another possible reason for this discrepancy is that an optimal burnishing force exists, when the force exceeds this optimal value, the residual stresses will become more tensile. This claim was supported by the residual stress results when a smaller DoP was used. As shown in Figure 4.13, the tangential residual stress close to the surface with 0.08 mm DoP was less tensile than the one with 0.15 mm DoP, which corresponds to larger burnishing forces, and became compressive at a depth of 4  $\mu\text{m}$  below the surface. Moreover, the axial residual stress with 0.08 mm DoP was totally compressive, while the



one with 0.15 mm DoP was still tensile at a depth of 35  $\mu\text{m}$  below the surface. Similar results were found from the literature. The residual stresses after roller burnishing in *AZ80 Mg* alloy became less compressive when the burnishing force was increased from 200 N to 300 N (Zhang et al. 2005). Also, the surface hardness and wear resistance of HSLA dual-phase steels started to decrease after a certain burnishing force (optimum value) was reached, which was claimed to be caused by excessive work hardening and flaking of surface layers (Srinivasa Rao et al. 2008). Salahshoor and Guo (2011) also found that the residual stresses of *MgCa* alloy became less compressive when high burnishing pressures were used. In the current study, burnishing with larger DoP (0.15 mm) gave a 860 N radial force, while the radial force with 0.08 mm DoP was only 400 N (the force values are averaged). Larger DoP (0.15 mm) resulted in more tensile residual stresses compared to the residual stresses from burnishing with smaller DoP (0.08 mm) which corresponded to smaller burnishing forces. Consistent with the results from the literature survey, the current study suggests that a critical DoP (burnishing force) exists beyond which residual stresses will become more tensile.

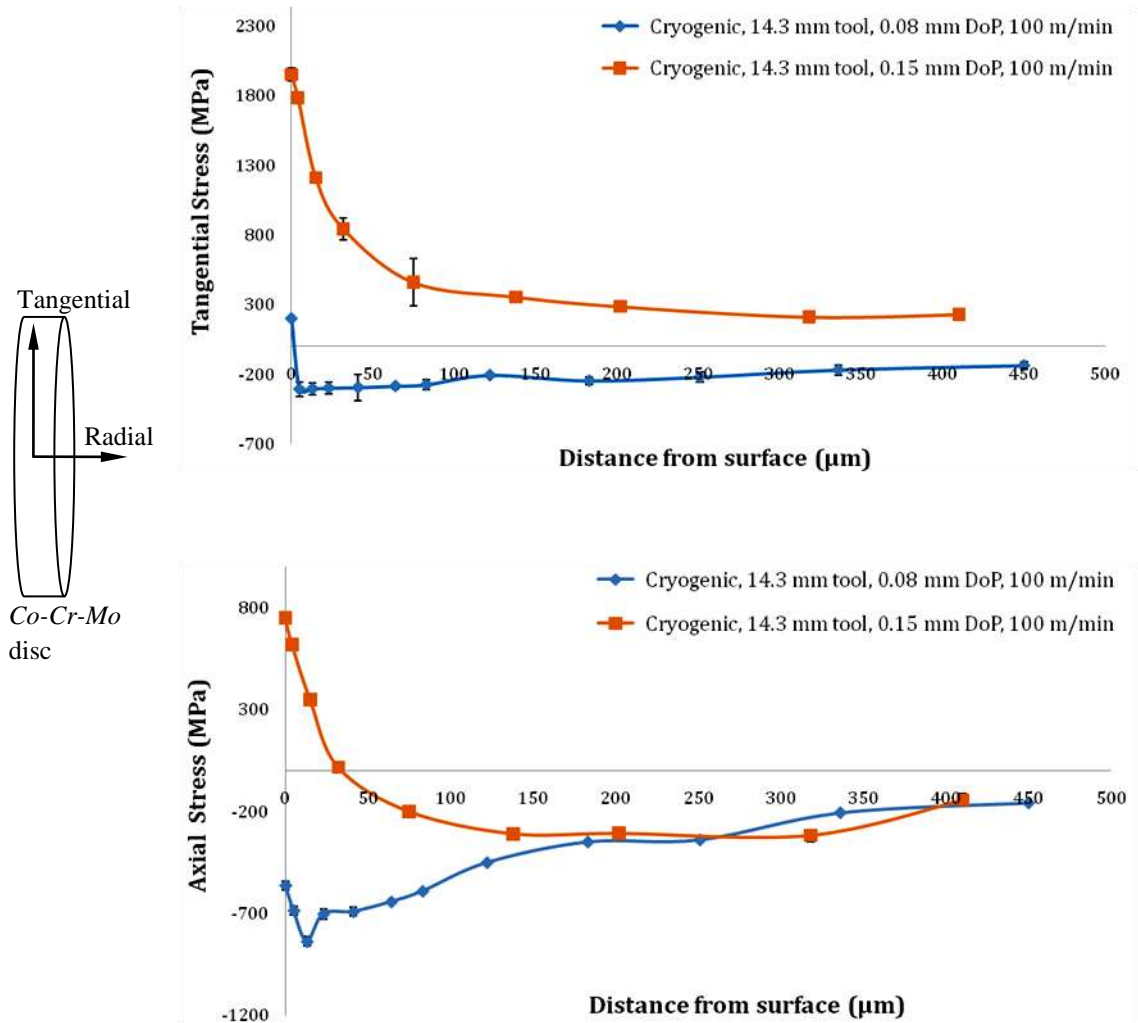


Figure 4.13: The effect of the DoP on residual stresses: (a) tangential and (b) axial directions

It should be noted that, in general, the axial residual stresses were significantly more compressive than the tangential residual stresses. As shown in Figure 4.12, the differences between the axial and tangential surface residual stresses for dry condition are 1400 MPa and 1200 MPa for cryogenic conditions. The large difference in the two directions is a result of the anisotropic plastic deformation induced by the burnishing process in a thin disk specimen (50.8 mm in diameter and 3 mm in width). As shown in

Figure 4.14, clear evidence of material side flow in the axial direction occurred during the burnishing process.



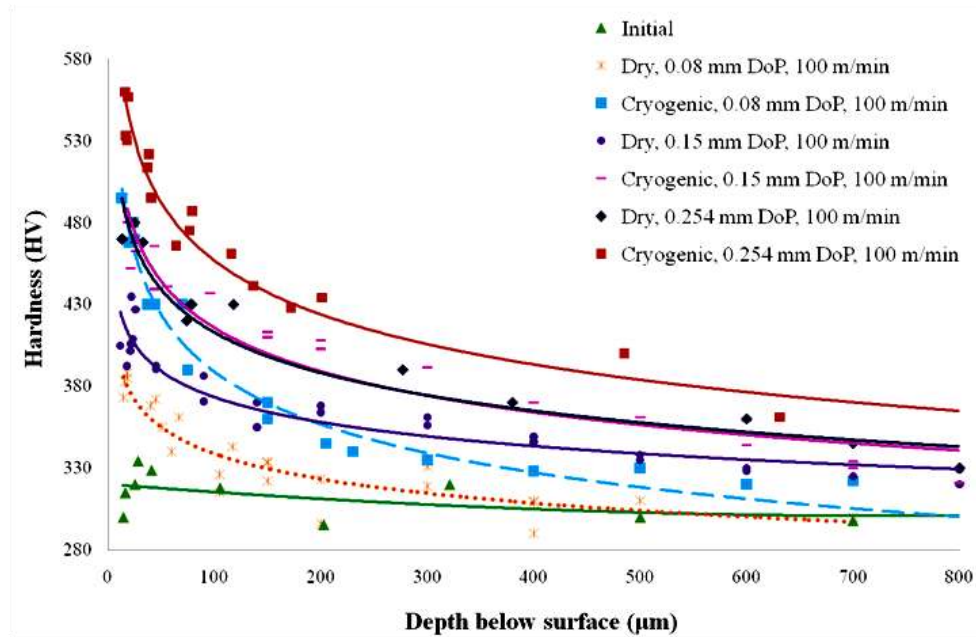
Figure 4.14: Material side flow after burnishing (cryogenic, 0.15 mm DoP, 100 m/min burnishing speed)

#### 4.3.7 Microhardness

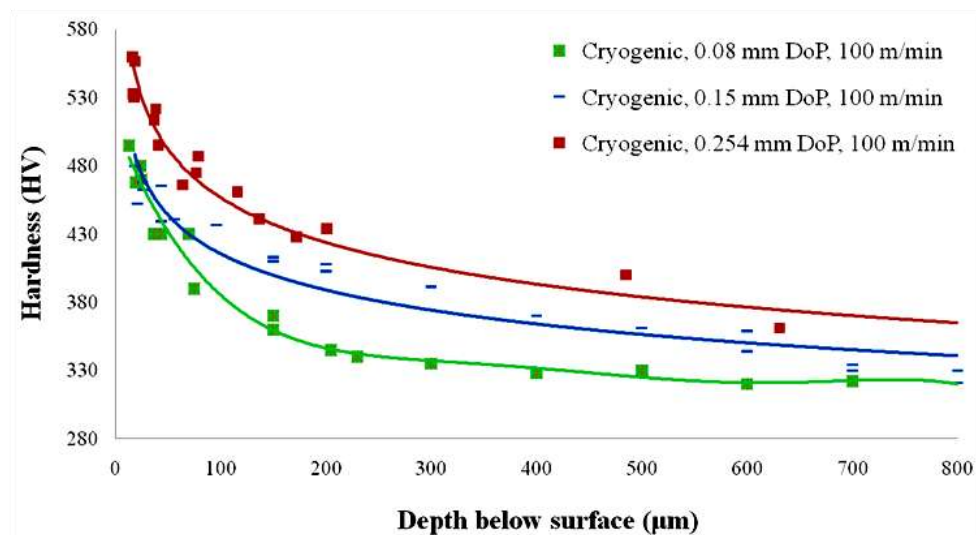
The hardness variation with depth below the burnished surface under different processing conditions is shown in Figure 4.15. The hardness increased 86.7% from  $300 \pm 20$  HV in the bulk material to  $560 \pm 26$  HV at about  $12 \mu\text{m}$  below the burnished surface after cryogenic burnishing using 0.254 mm DoP. Using the same DoP, the hardness increase was smaller under dry conditions ( $480 \pm 10$  HV). Surprisingly, the hardness at this depth from cryogenic burnishing using 0.08 mm DoP was very similar to the one from cryogenic burnishing using 0.15 mm DoP despite the differences in their microstructures. Larger DoP was expected to introduce more plastic deformation to the surface which should result in more work-hardening effect and greater hardness. This discrepancy can be explained by the different phase compositions of the samples from different conditions. As shown in Figure 4.10, the amount of hcp phase in the cryogenically burnished pin with 0.08 mm DoP is significantly higher than the one with 0.254 mm DoP. It has been reported that as the volume fraction of hcp phase in the *Co-*

*Cr-Mo* alloy increases, the hardness also increases (Saldivar-Garcia and Lopez 2005). In contrast, the hardness under dry conditions was increasing with the increase of DoP values.

(a)



(b)



(c)

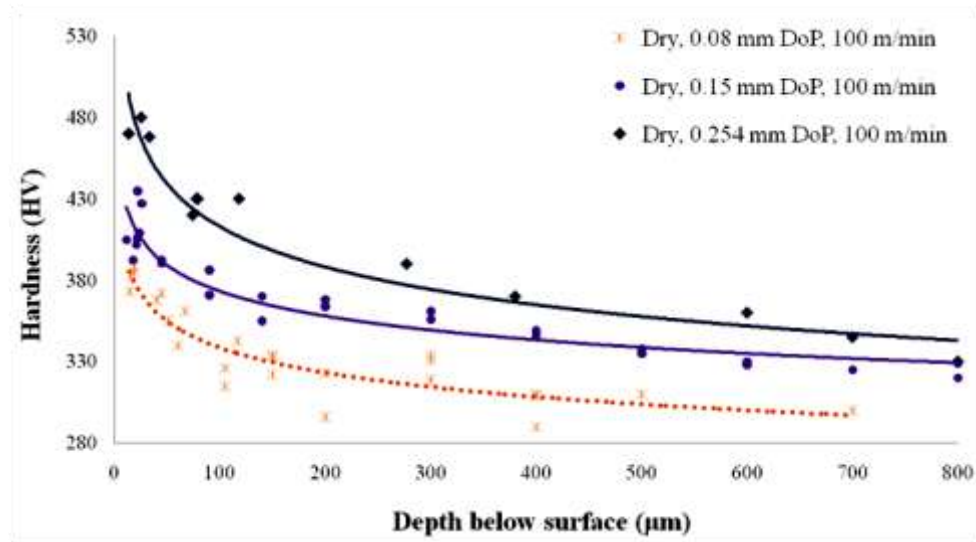


Figure 4.15: (a) The effect of the cooling method on hardness below the surface; the effect of the DoP on hardness below the surface: (b) cryogenic, (c) dry (14.3 mm tool diameter, 100 m/min burnishing speed)

#### 4.4 Effect of burnishing speed

The burnishing experimental conditions used for studying the effect of burnishing speed are shown in Table 4.3.

Table 4.3: Burnishing experimental conditions for studying the effect of burnishing speed

Exp. No	Tool Diameter (mm)	Depth of Penetration (mm)	Surface Speed (m/min)	Cooling
1	14.3	0.08	100	Dry
2	14.3	0.08	100	Cryogenic
3	14.3	0.08	200	Dry
4	14.3	0.08	200	Cryogenic
5	14.3	0.15	100	Dry
6	14.3	0.15	100	Cryogenic
7	14.3	0.15	200	Dry
8	14.3	0.15	200	Cryogenic
9	14.3	0.15	300	Dry
10	14.3	0.15	300	Cryogenic

#### 4.4.1. Microstructure

The effect of burnishing speed on the burnishing-influenced layer thickness is shown in Figure 4.16. The layer thickness did not change much with the cutting speed at 0.15 mm DoP under dry conditions and only slightly increased with cryogenic cooling. Increasing cutting speed normally affects the work-hardening effect in two ways: (a) more heat generation leads to higher temperature and compromises the work-hardening effect; and (b) increased strain-rate leads to stronger work-hardening effect. The slight increase of the layer thickness under cryogenic conditions can be due to the fact that the work-hardening effect outweighed the thermal softening, which also indicated the effective cooling of liquid nitrogen compared to the dry conditions.

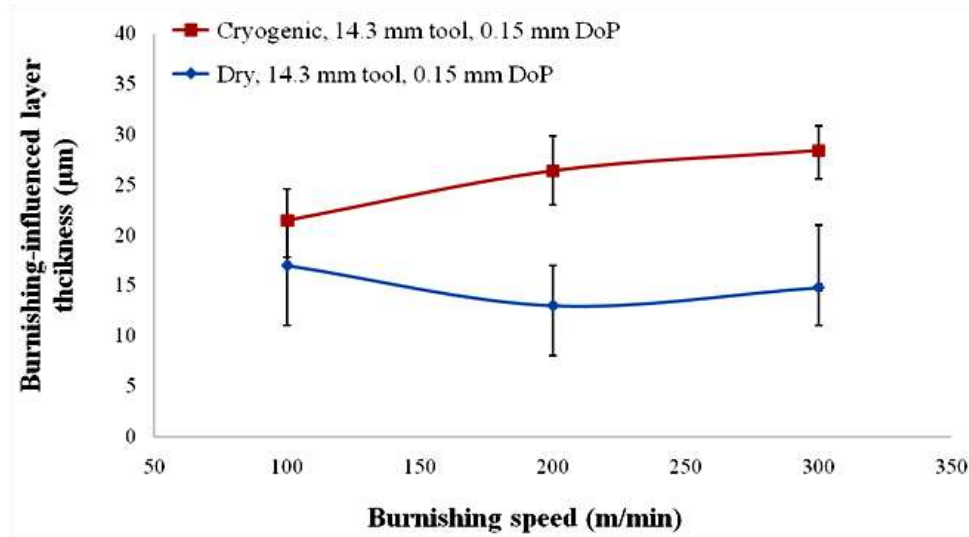
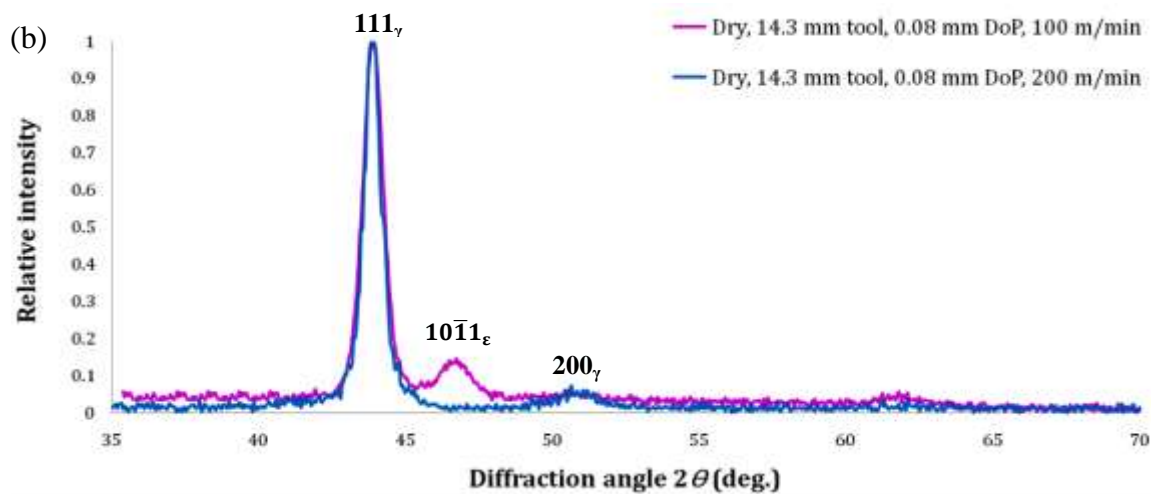
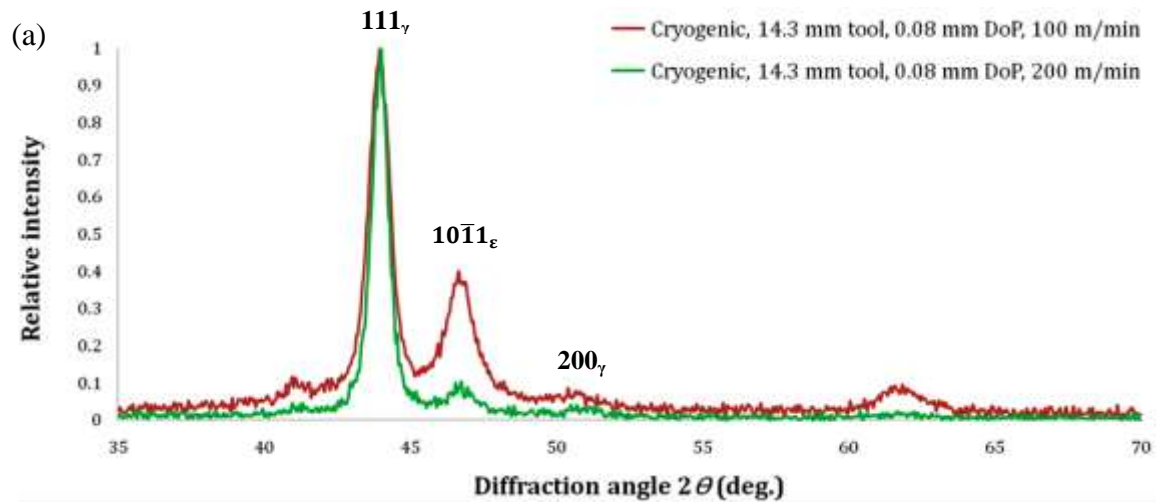


Figure 4.16: The effect of the burnishing speed on burnishing-influenced layer thickness

#### 4.4.2. Phase change

Figure 4.17 shows the phase compositions of the burnished samples from different burnishing speeds. It can be observed that, no matter what kind of cooling method or DoP used, the amount of the hcp phase was always decreasing with the increase of burnishing speed, which can be caused by the greater thermal softening effect when a higher burnishing speed was used as discussed in section 4.3.1. Moreover, it should be noted that, even though this fcc  $\Rightarrow$  hcp transformation is called a “strain-induced transformation”, it is concurrently affected by strain, strain-rate and temperature the three important processing parameters in any process. Yamanaka et al. (2009) studied the phase structures of the *Co-29Cr-6Mo* alloys subjected to hot compression at 1150 °C at various strain rates. Their results indicate that the formation of the hcp  $(10\bar{1}1)_\epsilon$  phase is not linearly increasing with increased strain-rate. Rather, a  $\Lambda$  shaped (first increasing then decreasing) relationship was observed on the amount of the hcp  $(10\bar{1}1)_\epsilon$  phase with

increasing strain-rates. This may also contribute to the reduce hcp peak intensity when larger burnishing speed was used as shown in Figure 4.17. However, the range of the strain-rates used is very low ( $0.001$  to  $10\text{ s}^{-1}$ ) compared to the burnishing process ( $10^3$  to  $10^4\text{ s}^{-1}$ ), so that their results cannot be directly used in the present study. The relationships of the strain, strain-rate and temperature on the strain-induced fcc => hcp transformation of the *Co-Cr-Mo* alloy is still unclear, further very basic studies on this matter are needed for the better control of the process induced property modifications.





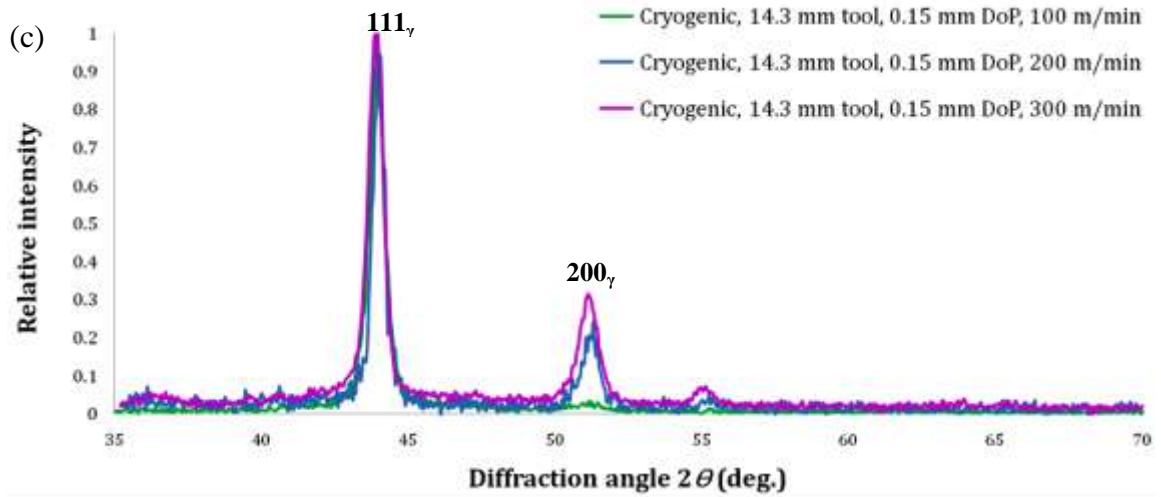


Figure 4.17: The effect of the burnishing speed on surface phase change

#### 4.5 Chapter concluding remarks

An experimental investigation was performed to study the effect of the different burnishing parameters, including cooling method (dry, cryogenic), burnishing speed and depth of penetration (DoP), on the some aspects of the surface integrity of the *Co-Cr-Mo* alloy. The surface integrity factors investigated include microstructure, phase changes, residual stresses and hardness. Major finding from this experimental study can be summarized below:

- (a) Significant reduction of surface temperature was achieved during cryogenic burnishing, where liquid nitrogen was sprayed onto the exit surface from the flank side of the tool.
- (b) Microstructure refinement in the surface layer was observed under both dry and cryogenic conditions. In addition to the cooling method, the thickness of the burnishing-influenced layer with microstructure refinement was also dependent on the used depth of penetration and burnishing speed. The results on

microstructural changes also suggest that optical microscopy may not be adequate to accurately characterize the resulting microstructures from different burnishing conditions. Advanced characterization techniques, such as SEM, TEM or AFM, are needed.

- (c) The residual stresses became more tensile after burnishing at large DoP (0.15 mm), compared with the initial status, and became compressive under smaller DoP (0.08 mm). However, the application of liquid nitrogen during burnishing led to the formation of more compressive residual stresses in both directions. In addition, larger differences up to 1400 MPa were found in residual stresses between tangential and axial directions. The large difference in residual stress values in the two directions could be caused by the different deformation directions. Severe side flow of the material in the axial direction was evident during the burnishing process. Further studies are needed to investigate the possible causes for the different distribution of residual stresses in the two directions. Without the application of liquid nitrogen, the residual stresses became more tensile under all the burnishing conditions used.
- (d) A remarkable increase in the relative intensity of the hcp  $(10\bar{1}1)_\epsilon$  peak was achieved on the cryogenic burnished surface, which should significantly enhance the wear performance of the *Co-Cr-Mo* alloy. However, increasing of DoP and burnishing speed all led to a decrease of the amount of the hcp phase in this region, which can be due to the complicated phase transformation mechanisms of the *Co-Cr-Mo* alloy.

- (e) The hardness of the burnished surface was increased after both dry and cryogenic burnishing compared with the initial value. The largest increase of 87% was observed on the sample with the thickest grain refinement layer (cryogenic burnishing, 0.254 mm DoP, 100 m/min burnishing speed). However, the hardness was not only dependent on the microstructures, but also on the phase composition and possible residual stresses.

## **CHAPTER 5: ENHANCED WEAR PERFORMANCE OF *Co-Cr-Mo* BIOMATERIAL THROUGH CRYOGENIC BURNISHING INDUCED SURFACE INTEGRITY MODIFICATIONS**

### **5.1 Introduction**

Improved manufacturing methods led to reintroduction of metal-on-metal bearings and growing interest in these implants, especially for young and active patients (Heisel et al. 2003). Volumetric wear rates and osteolytic potential of metal-on-metal bearings are lower than those of metal-on-polyethylene bearings (Greenwald et al. 2001). However, metallic particles have a greater potential for cytotoxicity, and their number is greater (Germain et al. 2003). A reduction in metal-on-metal wear will reduce biological reactivity and thus increase long-term implant survivorship (Ingham and Fisher 2000).

Among the options available for evaluating the performance of a biomaterial, the enhancement of the surface integrity holds the key. In practical applications, the surface of a material is subjected to the influence of various external stimuli. Corrosion, oxidation, wear and fatigue are a few such material degradation phenomena, which all initiate at the surface. Thus, it has been a constant need by engineers and scientists to improve the surface properties of biomaterials. Surface modifications seem to offer solutions for improved functionality and biocompatibility of implants.

The aim of the present work is to investigate the effect of burnishing-induced surface integrity modifications on the wear performance of this *Co-Cr-Mo* alloy. The wear volume, wear appearance and wear debris, as well as the surface integrity changes of the *Co-Cr-Mo* samples before and after wear tests were studied. The major wear

mechanism of this material was identified and the key influencing surface integrity factors were found. The results from this study provide valuable information for establishing the relationships among burnishing conditions, surface integrity properties and the wear performance of this *Co-Cr-Mo* alloy.

## 5.2 Experimental work

### 5.2.1 Work material

The material used in the present investigation was the same as used in Chapters 3 and 4. A *Co-Cr-Mo* alloy bar (9.5 mm diameter) is used to prepare pin samples which have a diameter of 9.5 mm and length of 25.4 mm. In order to minimize the possible influences caused by the surface speed differences (zero speed at the center and maximum at the edge) on the pin flat ends during burnishing and wear test, one end of the pin was made into a hollow cylinder with an inner diameter of 5.3 mm (Figure 5.1). The disks used for pin-on-disk wear test were prepared from a 50.8 mm diameter bar stock of the same alloy.

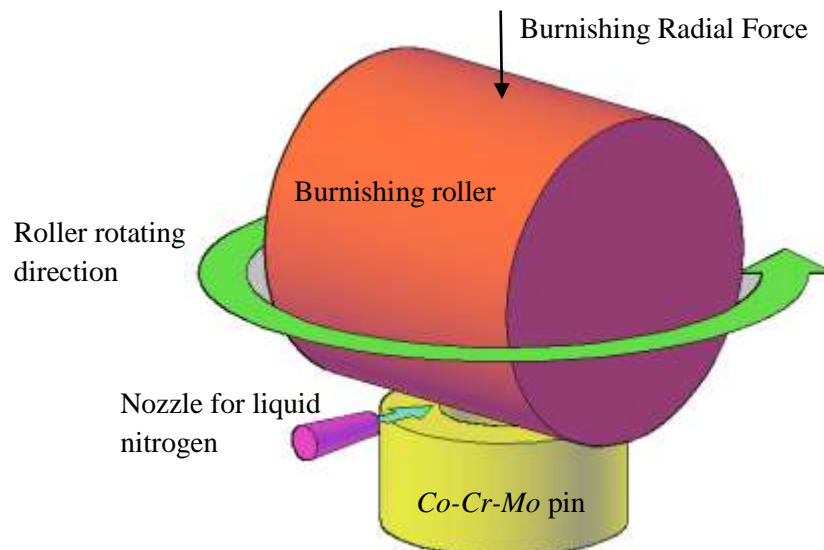


Figure 5.1: Pin burnishing illustration with liquid nitrogen delivery

The surfaces of disk and pin specimens were thoroughly cleaned and then gently polished using a Struers RotoPol-22 polishing machine to achieve a surface roughness  $R_a$  less than 0.05 microns for wear testing in a custom made pin-on-disk tester (ASTM F732). The samples to be mounted were placed firmly in a holder designed to ensure that the surfaces of all the samples were on the same level and then coupled to the spindle of the Struers Rotoforce equipment. The spindle rotated the specimen against various grinding and polishing papers which were held magnetically on the rotating grinding disk. Table 5.1 shows the steps followed in grinding and polishing the samples to achieve the surface roughness of 0.05 microns. At the end of each step, the samples were cleaned with soap and water and dried using laboratory compressed air. At the end of the final polishing step the samples were ultrasonically cleaned in distilled water to ensure that there were no contaminants present from the final polishing stage which could influence the surface roughness measurements as well as affect the results of the pin-on-disk wear tests.

Table 5.1: Polishing procedure for pins and disks prior to wear testing

Step	Surface	Abrasive Type	Speed (rpm)	Force (N)
Fine grinding	MD-Allegro	DiaPro Allegro, water based diamond suspension, diamond grain size 6 $\mu$	150	80
Rough polishing	MD-Dac	DiaPro Dac, water based diamond suspension, diamond grain size 3 $\mu$	150	80
Final polishing	MD-Nap	DiaPro Nap, water based diamond suspension, diamond grain size 1 $\mu$	150	60
Final polishing	MD-Chem	Colloidal Silica suspension for final polishing	150	60

Thereafter, the disks and the pins were subjected to a surface roughness measurement to ensure that the surface roughness ( $R_a$ ) was less than 0.05  $\mu\text{m}$ . The surface roughness was measured with a non-contact, three-dimensional, optical interferometry optical profiler Zygo New View 7000 which uses a white light interferometric technique. Five surface roughness measurements were taken for each polished sample for statistical purposes.

### 5.2.2 Burnishing experiments

Burnishing experiments were conducted on a HASS Machining Center equipped with an Air Products and Chemicals ICEFLY<sup>®</sup> liquid nitrogen delivery system. Liquid nitrogen as a cryogenic coolant was applied to the workpiece on the flank side of the tool-workpiece contact. The experiment setup and the specially designed and fabricated burnishing tool with a fixed burnishing roller are shown in Figure 5.1. In this study, the roller used is fixed for the purpose of introducing large shear stress and shear strain into

the workpiece surface during burnishing and therefore is slightly different from traditional roller burnishing arrangements where the roller is usually allowed to rotate.

The burnishing conditions used are listed in Table 5.2. For dry burnishing, no cooling method was used; for cryogenic burnishing, liquid nitrogen was sprayed to the tool-workpiece interface at 0.6 kg/min. The roller tool was pressed into the pin at a constant feed rate of 0.05 mm/s and, simultaneously, rotating at a burnishing speed (i.e., the average linear speed at the contact area between the roller and the pin) of 42.5 m/min along the longitudinal axis of the pin (see Figure 5.1). The feed-in process was stopped when the preselected depth of penetration (DoP) was reached. The burnishing roller then stayed at this position (i.e., burnishing dwell time) for 20 seconds. The forces generated during processing were collected by a KISTLER 4-Component Tool Dynamometer. An uncoated carbide roller with a diameter of 14.3 mm was chosen as the burnishing tool for the current study. The hardness and surface roughness of the roller was measured to be 1000 HV and 0.01  $\mu\text{m}$  ( $R_a$ ), respectively.

Table 5.2: Matrix for the pin burnishing experimental conditions

Cooling Method	DoP (mm)	Burnishing Speed (m/min)	Burnishing stay duration (sec)
Dry	0.127	42.5	20
Cryogenic	0.127	42.5	20
Dry	0.254	42.5	20
Cryogenic	0.254	42.5	20



### 5.2.3 Characterization of surface integrity

The surface integrity characterization methods used for analyzing the microstructure, microhardness, surface roughness, phase structure and residual stresses in this chapter are the same as the ones used in Chapters 3 and 4.

Chemical compositions of the wear debris were determined from a Princeton Gamma-Tech energy dispersive spectroscopy microanalysis system (EDS) and the typical profile was used for analysis. Topographic morphologies of the worn pin surfaces were measured by using the same Zygo NewView 7000 white light interferometric measurement system as used for surface roughness measurements.

### 5.2.4 Pin-on-disk wear test

Pin-on-disk testing is a commonly used technique for investigating sliding wear. It essentially consists of a "pin" in contact with a rotating disc. Either the pin or the disk can be the test piece of interest. The contact surface of the pin may be flat, spherical, or, indeed, of any convenient geometry, including that of the actual wear components of interest. To conduct wear tests on the pins machined with different burnishing conditions, a suitable tribological testing system (pin-on-disk tester) was built in house using a vertical milling machine. Figure 5.2 shows the setup for the pin-on-disk tester used for wear testing of the pin specimens. The fixture for holding multiple pins (three) was mounted on the machine table, with a regulator to ensure the application of a constant load on the pin as well as to ensure a constant contact stress of 3.54 MPa between the disk and the pin throughout the wear test according to the ASTM-F732 standard for pin-on-disk tests.

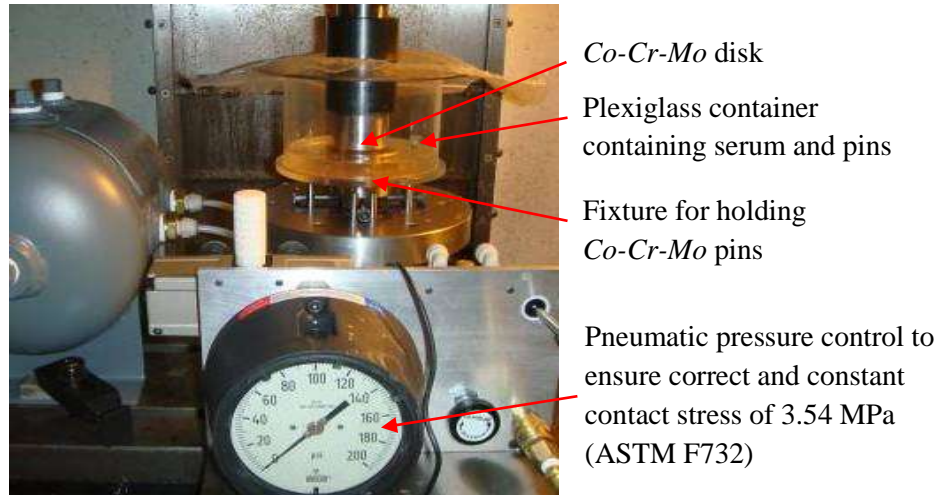


Figure 5.2: Experimental setup for pin-on-disk wear tester

The Plexiglas container maintains a solution of new born calf serum and distilled water (50% concentration) with 0.2% by weight sodium azide and 20 mM EDTA for mimicking the human body conditions during wear tests. A pneumatic cylinder with the controller ensures the application of a constant load on the pins during the entire duration of the test. An average contact stress of  $3.54 \pm 3\%$  MPa (ASTM-F75. 2011) was applied during the entire duration of the wear test. In addition to the rotation of the disc, the pins also traverse a square path which gives a biaxial relative motion between the pin and the disc. The average sliding velocity between the pin and the disc was 50 mm/s. Due to the fact that neither the geometry of the sliding partners nor the direction of motion and the duration of loading correspond to any conditions *in vivo*, no relevant quantitative data is expected from this type of tests. The pins were removed from the wear tester every 100,000 cycles for cleaning and measurement of wear. The wear debris was collected at the end of the wear test, cleaned with 100% acetone for 5 times, and kept in the refrigerator for debris analysis later. Prior to weighing, the pins were cleaned ultrasonically with 100% acetone for ~5 min. The wear volumes of the pins were

determined gravimetrically after each test period. The progressive gravimetric wear of pins tested was converted to volumetric values (using a density of 8.276 mg/mm<sup>3</sup>). The wear volume  $V$  was calculated as:

$$V = \frac{M_{loss}}{\rho} \quad (5.1)$$

where  $M_{loss}$  is the measured weight loss (g) and  $\rho$  is the density of the pin.

### **5.3 Results and discussions**

#### **5.3.1. Burnishing force**

The measured radial direction burnishing force is shown in Figure 5.3. The cryogenic burnishing approach has slightly higher forces when compared to those generated in dry burnishing. In the current study, liquid nitrogen was applied on the tool flank side towards the workpiece surface; it has a tendency to precool the workpiece and increase the hardness of the workpiece material. As the material study on cryogenic machining shows, when the temperature is lower the workpiece material becomes harder, and in turn, the burnishing forces increase (Zhao and Hong 1992). The increased ploughing effect (i.e., larger burnishing forces) should be desirable for the occurrence of strain-induced grain refinement in *Co-Cr-Mo* alloys (Yamanaka et al. 2009) since more SPD effect will be introduced to the burnished surface and sub-surface.

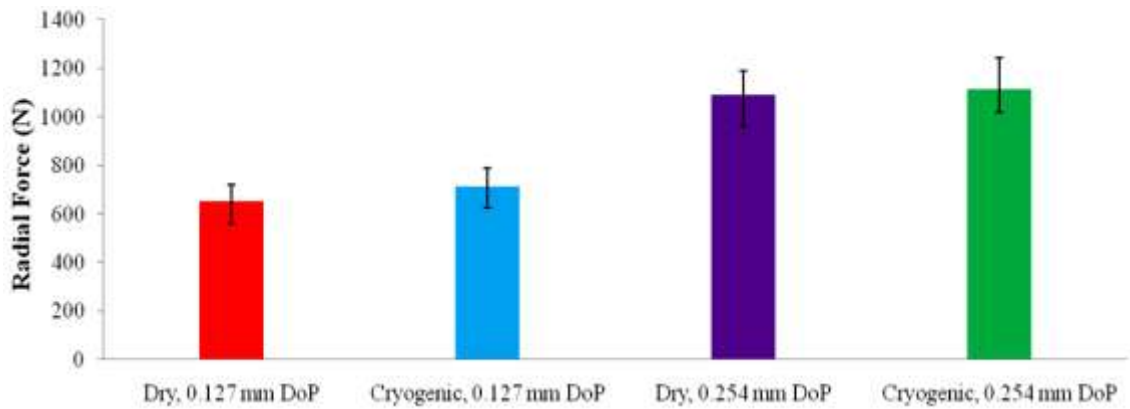


Figure 5.3: Measured radial force comparisons under different burnishing conditions.

### 5.3.2. Wear volume

The nature of the wear phenomenon is extremely complex since it involves many mechanisms and influencing factors. An accurate and thorough understanding and estimation of the results is possible only when all the factors are correctly considered and combined. In this study, worn surfaces were generated under two-dimensional sliding wear by means of a laboratory pin-on-disk method, and therefore, all known major wear mechanisms may act at the same time (DIN50320. 1979). In order to find a close correlation between the surface integrity properties and the wear performance, the acting wear mechanisms and the failure sequence have to be known (Zum Gahr 1987). In doing so, one should distinguish between mechanisms which are predominantly of mechanical nature (surface fatigue, abrasion) and mechanisms which are of combined chemical and mechanical nature (adhesion, tribochemical reactions) (Czichos 1986).

The measured progressive wear volume losses of *Co-Cr-Mo* pins as a function of the sliding distance are shown in Figure 5.4. It can be observed that significant wear volume differences were generated during wear tests for pins that had previously subjected to different burnishing conditions. The pin from cryogenic burnishing with

0.127 mm DoP possessed the least wear volume loss. In contrast, the initial pin without any prior processing showed the most severe wear volume loss, and the remaining pins that had been prepared using other burnishing conditions showed intermediate volume losses. The possible causes for the wear volume differences are discussed in the following sections.

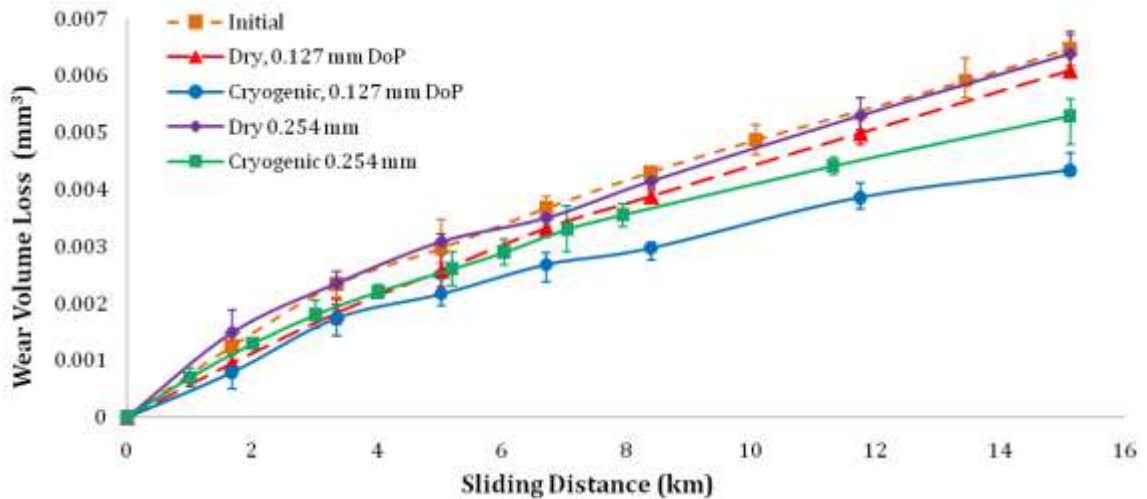
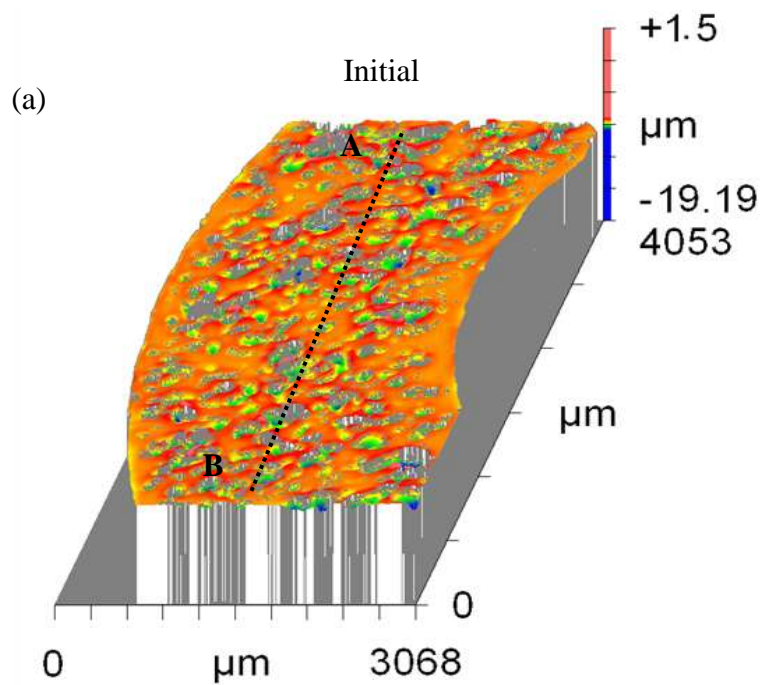


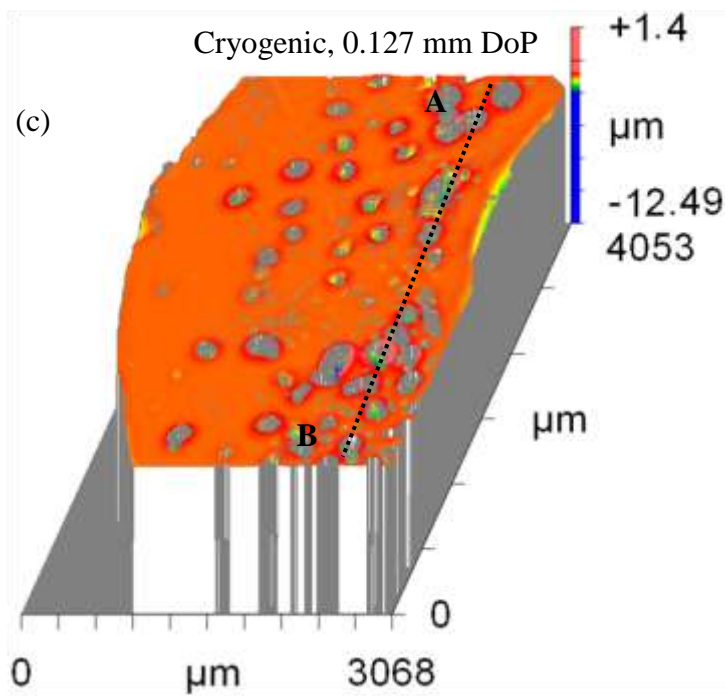
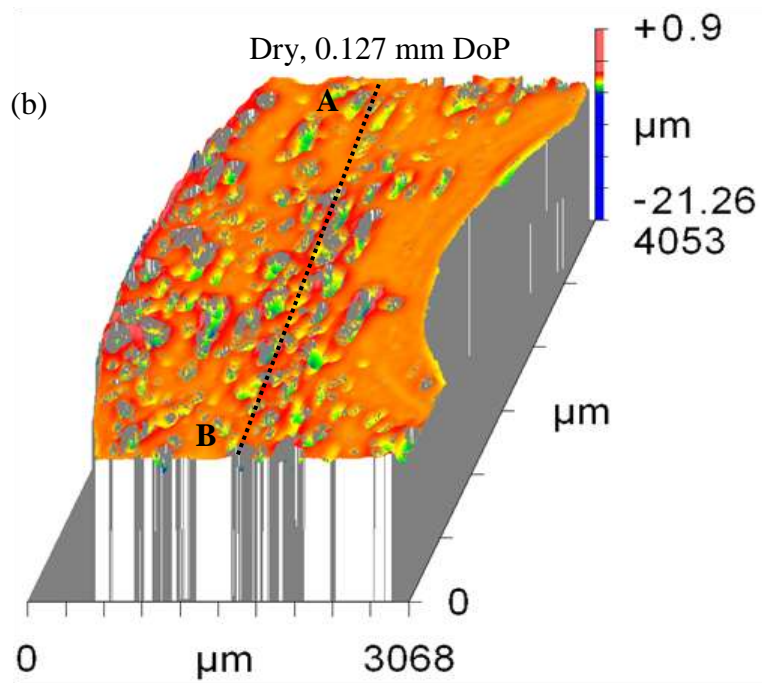
Figure 5.4: Wear volume losses of *Co-Cr-Mo* pins as a function of sliding distance. Velocity 50 mm/s, contact stress 3.54 MPa, new born calf solutions (pin-on-disk).

### 5.3.3. Wear appearance

The acting wear mechanisms are defined by means of their wear appearances. To investigate the topographic morphologies of the worn pin surfaces, topographic maps of each worn pin surface with the same size (3 mm × 4 mm) were obtained using the Zygo NewView 7000 white light interferometric measurement system. Figure 5.5 shows the typical images of the worn pin surfaces. It can be observed that even though wear scars were developed during the wear tests on all the pin surfaces, different burnishing conditions led to very different severities of wear. After wear tests, the initial pin (Figure 5.5 (a)) shows the most severe signs of wear with dense wear scars covered all over the

measured surface area. In contrast, the pin from cryogenic burnishing with 0.127 mm DoP (Figure 5.5 (c)) shows a smoother surface with the fewest amount of wear scars. The observations are consistent with the wear volume losses of the two conditions shown in Figure 5.4. However, it is difficult to compare the wear performance of the pins from the other conditions due to the similar topographic maps shown in Figure 5.5 (b), (d) and (e). Further investigations were conducted to evaluate the wear performance of the pins from all the conditions.





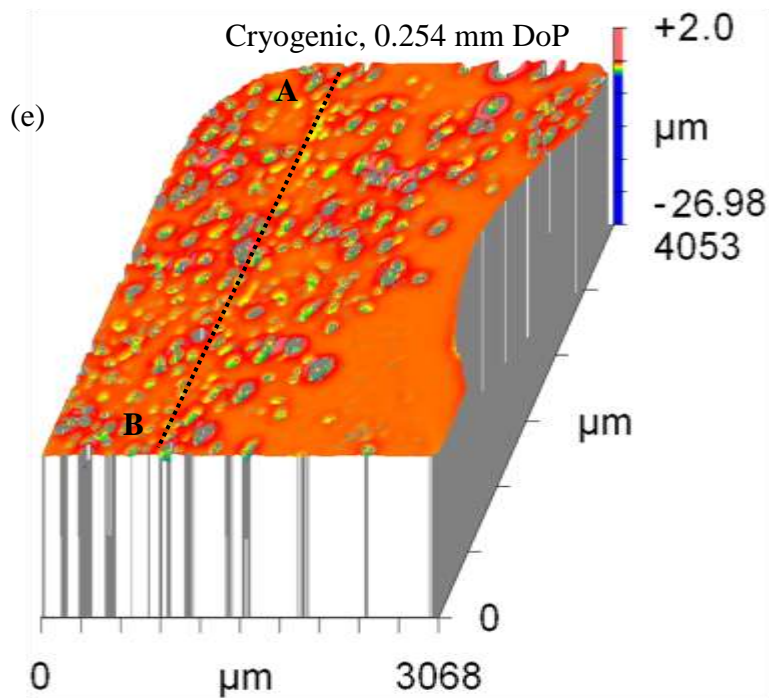
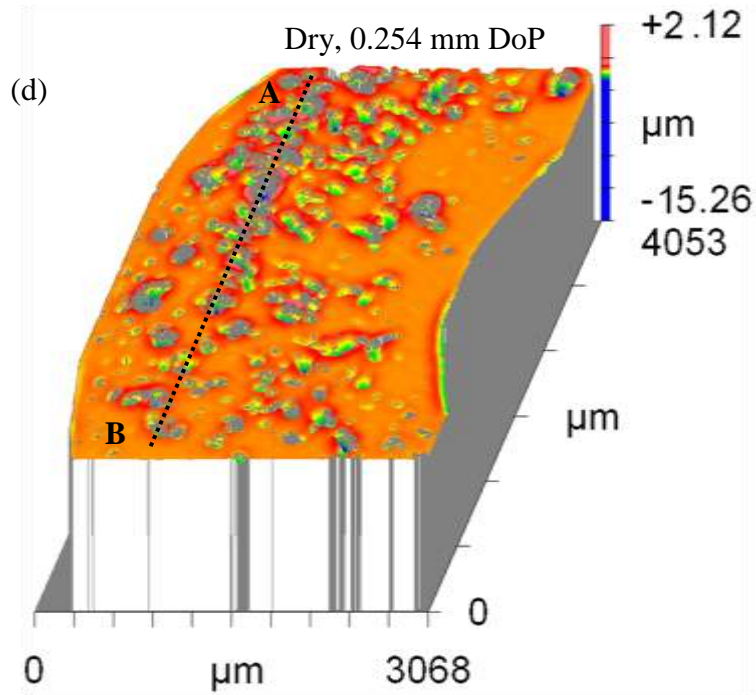
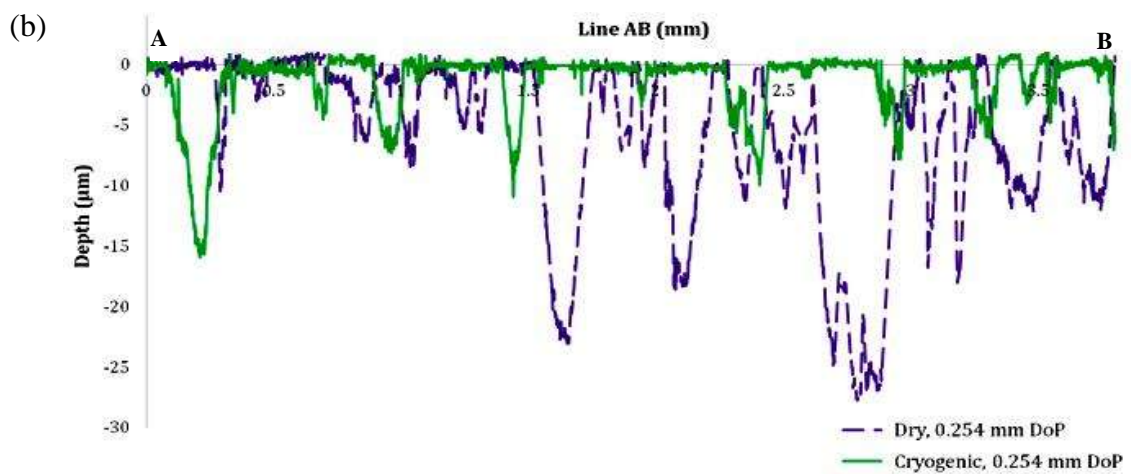
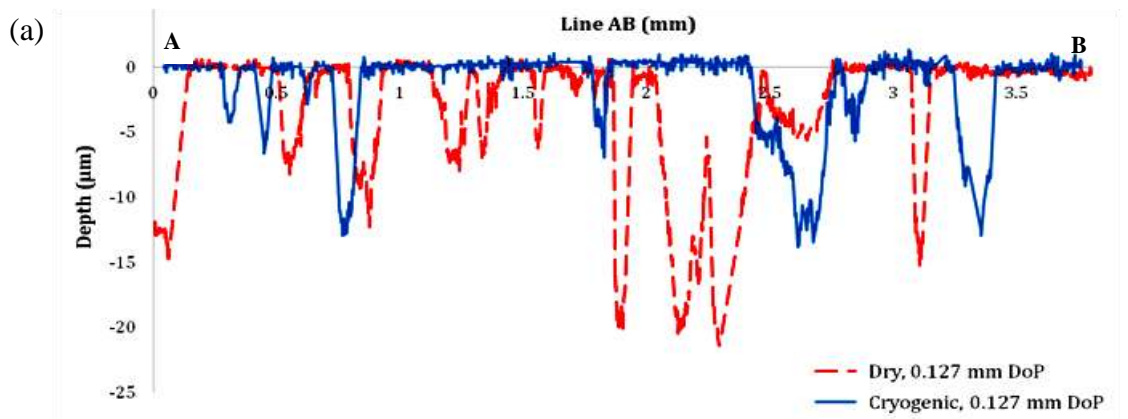


Figure 5.5: Topographic maps of worn pin surfaces: (a) initial, (b) dry, 0.127 mm DoP, (c) cryogenic, 0.127 mm DoP, (d) dry, 0.254 mm DoP, (e) cryogenic, 0.254 mm DoP.



The depth profiles along the line AB shown in Figure 5.5 are presented in Figure 5.6. The profiles were taken along the lines where the most severe wear presented. The profiles in Figure 5.6 (a) and (b) all show that the wear scars on the cryogenically burnished samples are much deeper and more severe than the ones from dry burnishing. However, the profiles in Figure 5.6 (c) shows that surface peaks and valleys due to wear on the two cryogenically burnished samples are very similar to each other. Note the different units used on horizontal (mm) and vertical ( $\mu\text{m}$ ) axes; the profile shapes do not represent the real shapes of the wear tracks.



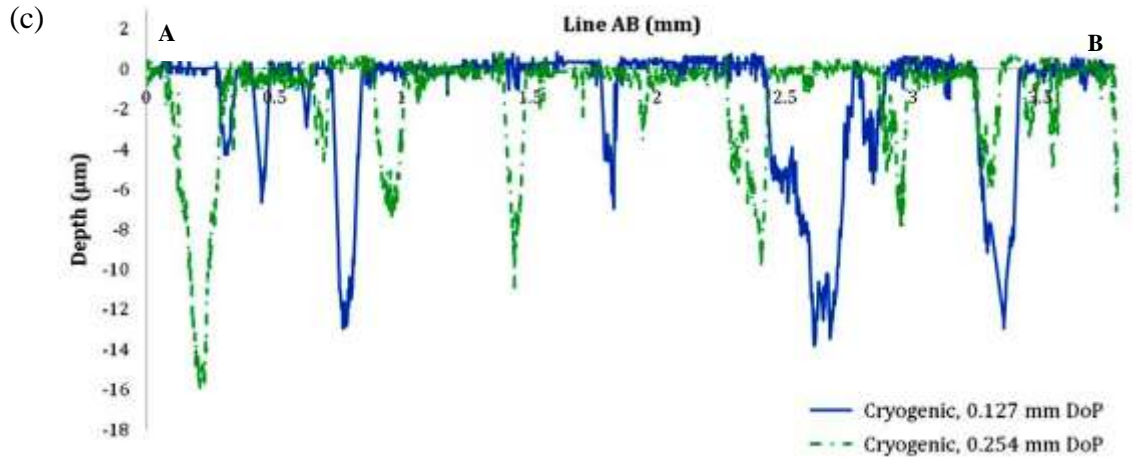


Figure 5.6: Wear depth profiles along line AB, (a) dry vs. cryogenic (0.127 mm DoP), (b) dry vs. cryogenic (0.254 mm DoP), (c) cryogenic, 0.127 mm DoP vs. cryogenic, 0.254 mm DoP

To quantitatively investigate the surface characteristics of the worn pin surfaces, an average surface roughness ( $R_a$ ) value was measured for each pin sample. On each sample surface, six small surfaces with the size of 2 mm  $\times$  2 mm were measured and the obtained roughness values for each small area were averaged to yield the overall  $R_a$  values shown in Figure 5.7. In comparison with the worn pins surfaces, the surface roughness of the worn disk surfaces corresponding to the pins with the highest volume loss (initial) and the lowest volume loss (cryogenic, 0.127 mm) was measured, the results were shown in Figure 5.7. It is apparent that, in general, cryogenically burnished pins gave lower  $R_a$  values compared to the ones from dry burnishing. Consistent with the topographic observations shown in Figure 5.5, cryogenic burnishing with 0.127 mm DoP gives the lowest  $R_a$  value, and the initial pin has the highest surface roughness. Moreover, it can be found that the ranking for the surface roughness values of all the pins studied are: Initial > Dry, 0.254 mm DoP > Dry, 0.127 mm DoP > Cryogenic, 0.254 mm DoP > Cryogenic, 0.127 mm DoP.

In contrast to the  $R_a$  values of the worn pins, the surface roughness of the two disks after wear tests showed an insignificant difference, despite that their corresponding pins had very different  $R_a$  values. This is likely due to the biaxial motion between the pin and the disk during the pin-on-disk wear test. During the test, the pin was beneath the disk and the whole surface of the pin was in contact with the disk throughout the entire testing period; on the other hand, the disk surface is much larger than the pin surface, which makes every single spot on the disk in discontinuous contact with the pin. In addition, the upside-down design of the wear test device makes the wear debris fall off the disk surface easily and reduces the happening of third-body wear. Thus, for each spot of area on the disk surface which equals to the size of the pin head, the wearing time each single spot experienced was much shorter than the pin, which eventually led to the better overall surface roughness of the disk compared to the pins.

Surface profile curve studies have revealed that wear volume loss correlates with surface finish. As mentioned earlier, the surface roughness of all the pins and disk before the wear test were made to have the same values ( $R_a = 0.05 \mu\text{m}$ ) in order to eliminate roughness effect. However, it can be observed that after wear tests, the roughness values were very different. The different wear resistance of the pins is likely due to the burnishing induced surface integrity modifications in the surface layer, which will be carefully studied in the following sections.

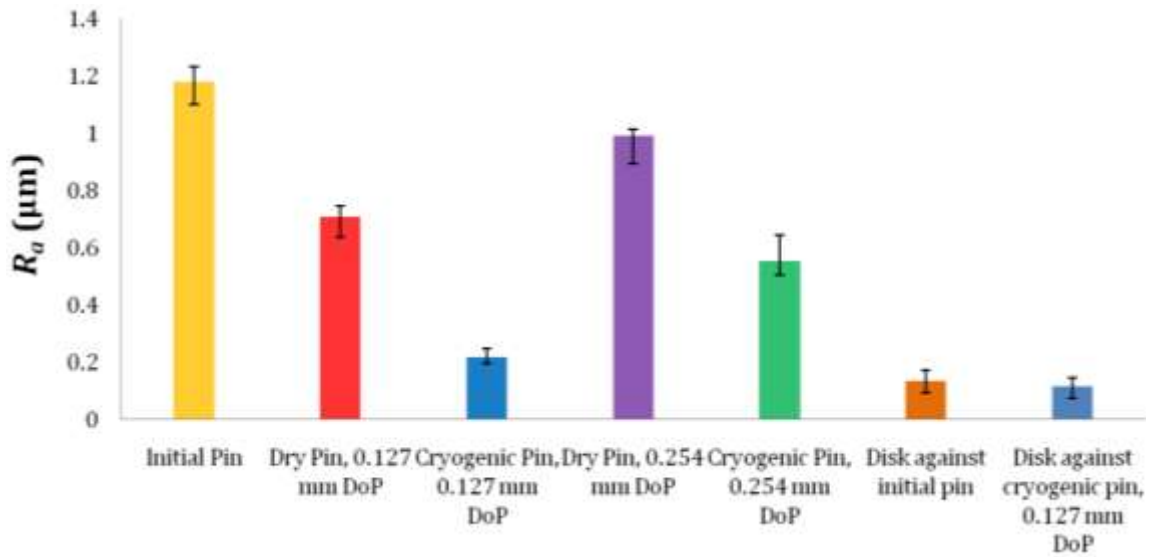
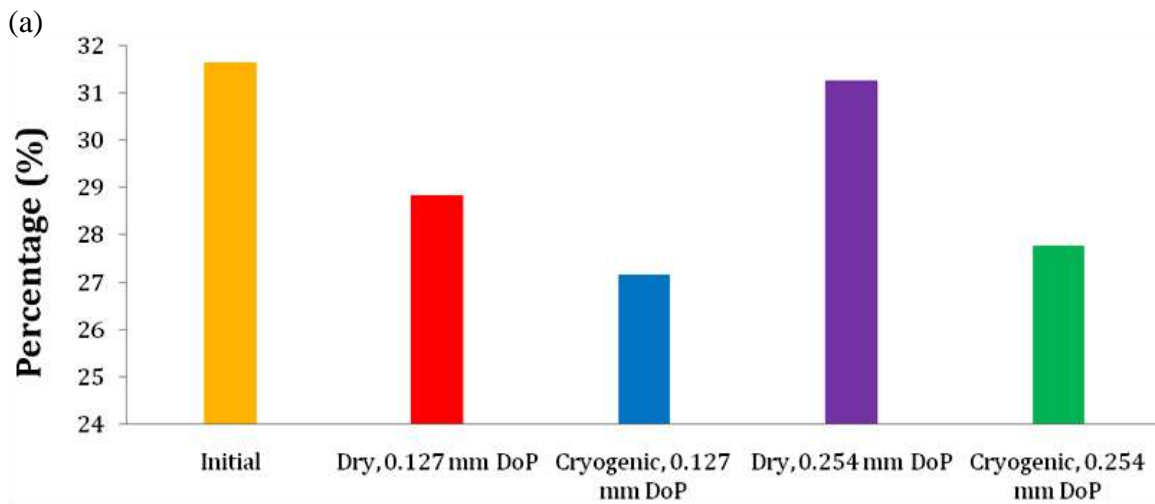


Figure 5.7: Measured surface roughness ( $R_a$ ) of worn pins and disk

In addition to the surface roughness values, the wear-induced surface damage was evaluated in terms of the worn area percentage and the wear depth distribution. As shown in Figure 5.8, the percentages of the worn area and the wear depth distribution on the measured pin surfaces were obtained from the Zygo measurement data. It should be noted that the worn area percentage values were obtained based on the same surface size as shown in Figure 5.5 for each condition; in contrast, the 100% values for the wear depth distributions were different for each pins, the comparison was just for the percentage but not the actual amount. The surface roughness value reflects well the wear amount and can be considered as the denominator of the depth distribution values.

Consistent with the observations from Figure 5.5 and Figure 5.7, the cryogenically burnished pins in general had less wear areas than the dry and initial pins (Figure 5.8 (a)). The pin from cryogenic burnishing with 0.127 mm DoP gave the lowest worn area value which once again confirmed its best wear performance. The wear depth distribution also represents the severity of the surface damage due to wear. Due to the

fact most of the damage starts from the surface in contact, superior surface properties often reduce the surface damage as well as the propagation of the damage in the subsurface region. Thus, the depth distribution of the worn area is a good representative of the surface conditions. As shown in Figure 5.8 (b), the majority of the wear depth for all the pins investigated was within 5  $\mu\text{m}$  deep. More specifically, for the cryogenically burnished pin with 0.127 mm DoP, more than 70% of the wear depth was distributed in the range less than 1  $\mu\text{m}$ . In contrast, large amount of the wear depth for the pin from dry burnishing with 0.254 mm DoP fell into the range from 2 to 7  $\mu\text{m}$ , relating this with its high surface roughness value, suggesting more severe damage occurred in the subsurface region.



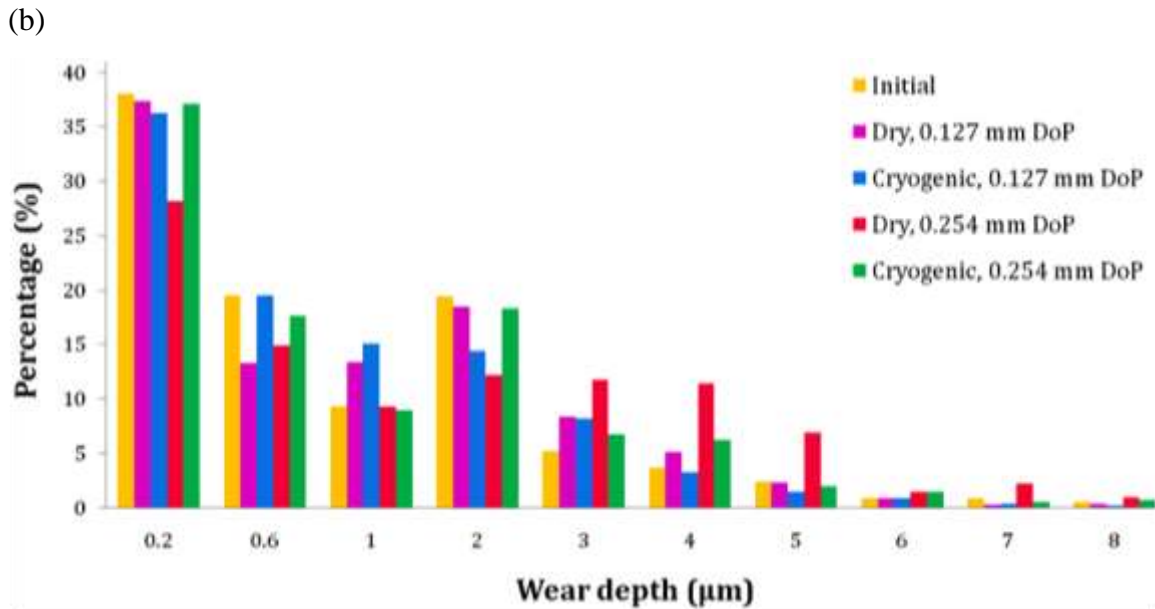


Figure 5.8: (a) Worn pin surface areas comparison, (b) worn pin surface wear depth distribution

#### 5.3.4. Wear surface and wear debris analysis

Based on medical motivations, it is worthwhile to investigate the reasons for these particles which are generated during the wearing process. In doing so, one should attempt to distinguish between mechanisms which are predominantly of a mechanical nature (surface fatigue, abrasion) and mechanisms which are chemical and mechanical nature (adhesion, tribochemical reactions) (Czichos 1986). An analysis of the resultant wear debris by SEM and EDS was made to investigate the tribological response of the pin surfaces. SEM pictures of the typical wear tracks on the worn surfaces are shown in Figure 5.9; with respect to the wear appearances, signs of abrasive wear (Figure 5.9 (a)), adhesive wear (Figure 5.9 (d)) and surface cracks due to fatigue (Figure 5.9 (b) (c)) were detected on all worn pin surfaces, suggesting that the wear mechanisms involved are very similar in all the conditions investigated. In particular, the morphology of the resultant

wear debris indicates that some plastic deformation would be present under the wear conditions employed (metal-metal pin-on-disk).

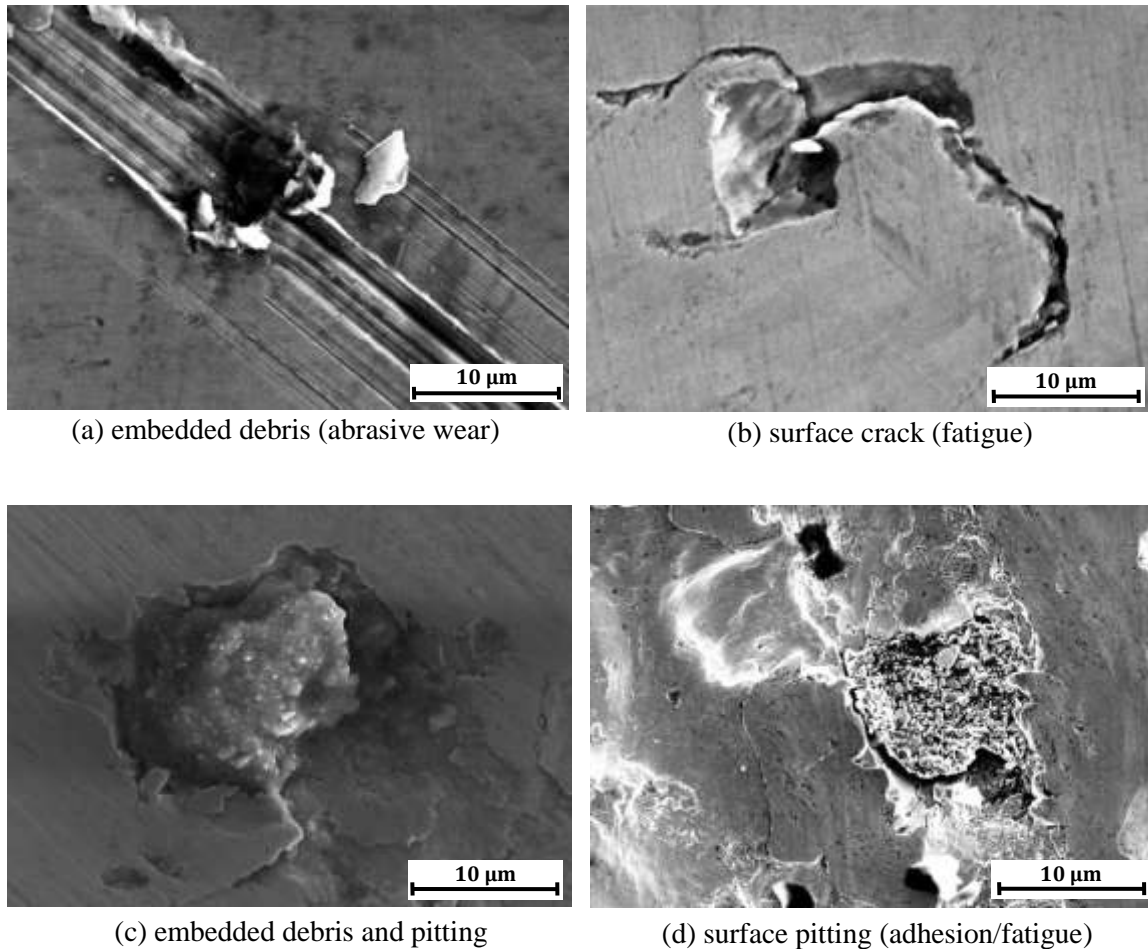


Figure 5.9: SEM micrographs of typical surface wear tracks

Figure 5.10 shows the results from the energy-dispersive X-ray spectroscopy (EDS) measurements on the wear debris from the initial, cryogenically burnished pins with 0.127 mm DoP and dry burnished pins with 0.254 mm DoP respectively. Significant levels of oxide debris were detected amongst the metallic debris. It was found that the wear debris consisted mainly of metallic particles combined with high amount of oxides. The presence of metallic debris (and not only oxides) suggests that during the test, the

metallic surfaces were contacting each other. Moreover, no difference on chemical composition was detected on the three conditions by the EDS method.

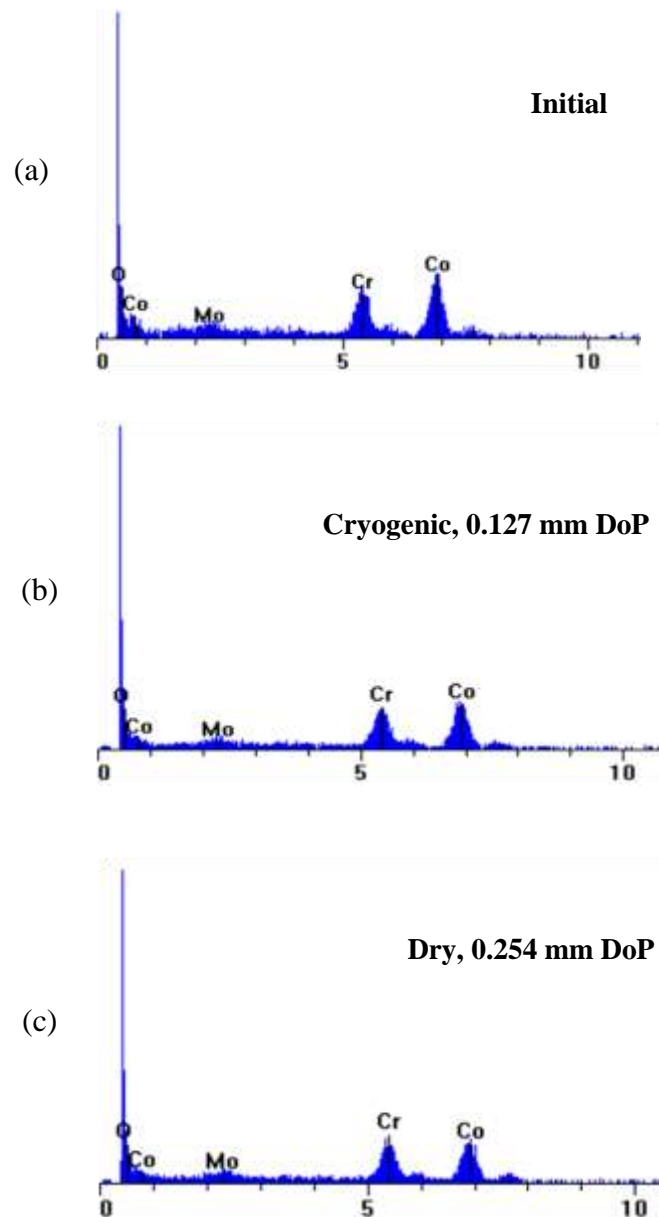


Figure 5.10: EDS results of wear debris from pin-on-disk wear tests: (a) initial, (b) cryogenic, 0.127 mm DoP, (c) dry, 0.254 mm DoP

The metallic debris particles (Figure 5.11) were collected at the end of the wear test – the size range for these particles was anywhere between 20 nm to 30  $\mu\text{m}$ . The



bright appearance around the edge of the debris was caused by the charging of electrons due to the poor conductivity of the metal oxides.

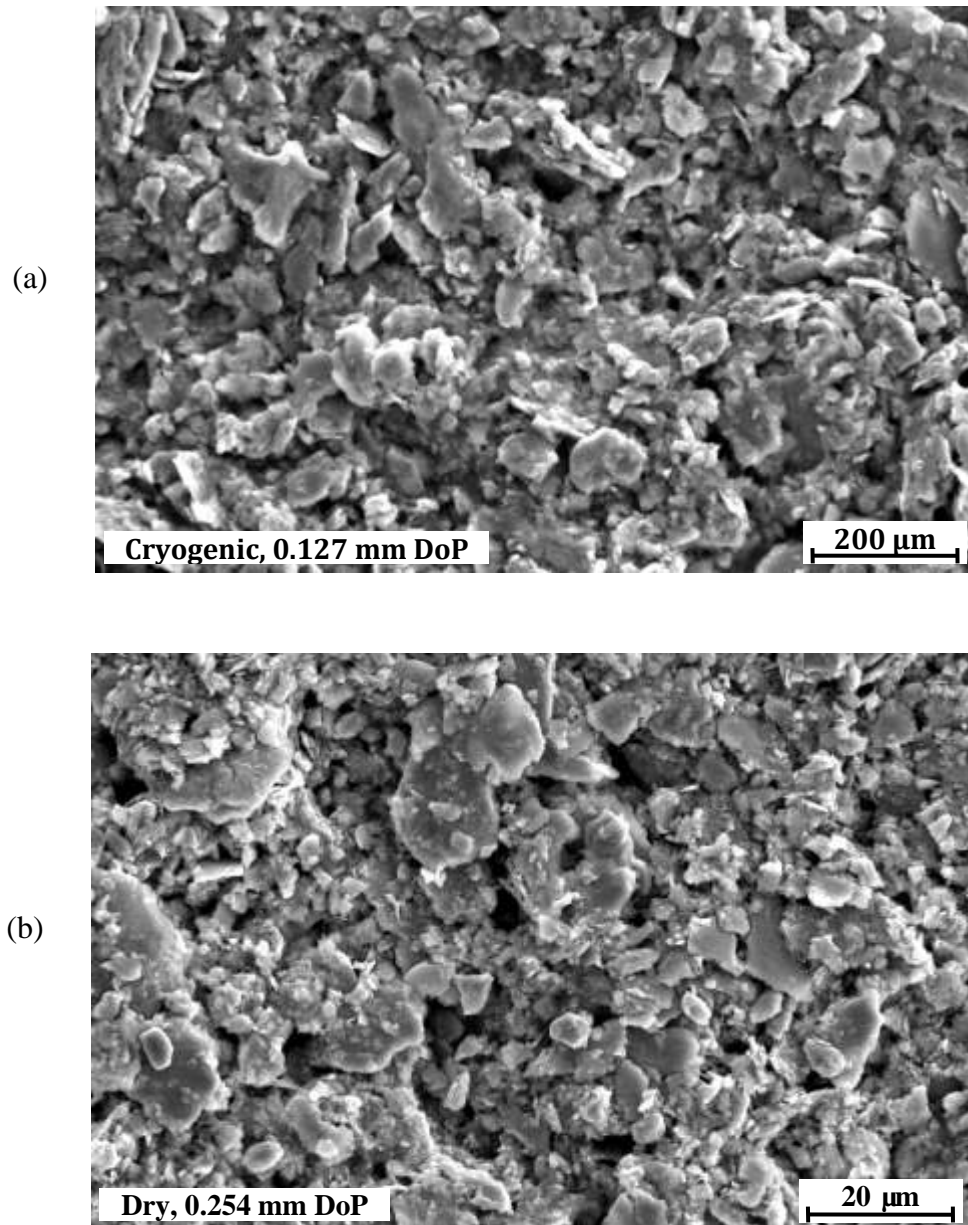


Figure 5.11: SEM micrographs of wear debris: (a) cryogenic, 0.127 mm DoP, (b) dry, 0.254 mm DoP

Starting with smooth polished surfaces, the contact area is governed by cyclic local stresses which scatter theoretically between 3.54 MPa and 11 GPa (Wimmer et al.

2001) depending on the contact of the solid constituents. In the current study, the low carbon alloys provide fairly smooth surfaces, which reduce the probability of high medium or flash temperatures due to the direct carbide/carbide contact. Even with high carbon *Co-Cr-Mo* alloys, where the contact area may be much smaller due to protruding carbides, a mean temperature increase of only  $\Delta T = 60$  K was calculated using an approach by Wimmer et al. (2001). Thus, mainly mechanically dominated effects must lead to the wear/debris generation of the *Co-Cr-Mo* pins.

We consider that the used solution does not bear mechanical contact stresses under this low relative speed and high normal force, if carbides are in contact with themselves or with the matrix. In carbide/carbide contact, the local pressure may become higher than their hardness, which is physically difficult. Thus, the maximum possible local pressure is limited to 11 GPa, above this value protruding carbides are fractured or pressed into the metal matrix to achieve a mechanically balanced situation between the remaining matrix and carbide contact spots. A direct metal-metal contact would be possible in areas of high plastic deformation, and a metal-oxide/metal-oxide contact in areas of low plastic deformation. The oxides might spall off the surfaces by surface fatigue resulting in wear particles of compacted metal-oxides (Saleski et al. 1983; Sullivan 1987). This type of surface fatigue can bring about two different routes of failure. One follows the assumption that an oxide layer is generated by tribochemical reactions and spalls off when reaching a critical thickness (Lee and Eliezer 1984). The other involves a wear particle that is generated by cyclic contact stresses that are so small that the particle oxidizes instantaneously when torn-off from the surface in order to reach a state of reduced free energy (Saleski et al. 1983). In both cases wear particles were

found, which have an oxide layer just at the surface or which are completely oxidized. On a *Co-Cr-Mo* solid solution most likely *Cr*-oxides are generated together with metal-hydroxides. During the time span in which the metal surface is not covered by a repassivation layer shortly after being scratched or torn off all metal ions are dissolved by corrosion. Thus, very often the metal ions in the fluid just represent the chemical composition of the materials tested. These indirect testing methods, therefore, do not bring about a coherent view of what happens in the single contact spots and have to be taken very critically.

Oxidized metal wear debris is found after *in vivo* as well as in *in vitro* tests from literature (Anissian et al. 1999; Doorn et al. 1998), as well as current results. One can assume that metallic or oxide particles are torn off the surfaces and act afterwards as interfacial media. This leads to more abrasion or surface fatigue depending on whether the particles stick to one surface and scratch the other or act as rolling particles bringing about indentations (Fischer 1996). Both mechanisms can act at the same time if the normal loads are predominantly carried by these particles. The effect of the much harder, torn off carbide fragments on the wear behavior is even more distinct. Again, small particles become loose and slide or roll between the contacting surfaces resulting in surface fatigue by indentation. The bigger particles, with a size exceeding the gap between the contacting bodies, become embedded within one of the bodies and scratch the counter-face resulting in abrasion.

The question raised is what the initiating mechanism is? With respect to the wear appearances observed in this tribosystem, one can assume that even if the first particles are generated by tribo-oxidation, the most effective will be those, which are generated by

surface fatigue leading to fractured or torn-off carbides (Figure 5.9 (b) and (d)). The load is then carried by a very small number of contact points under high mechanical stress leading to additional abrasion and surface fatigue. Both bring about loss of material and a steady removal of existing passive layers followed by repassivation. This claim is directly supported by the study by Wimmer et al. (2001) on the acting wear mechanisms on metal-on-metal hip joint bearings. Putting all these observations together, the stationary tribological behavior of this tribosystem can be attributed to a balance between mechanically acting mechanisms (abrasion and surface fatigue) and chemically and mechanically driven tribochemical reactions.

#### 5.3.5. Microstructure before wear test

The material microstructure near the surface before burnishing is shown in Figure 5.12 (a). The grain boundaries are clearly visible near the surface with an average grain size of  $80 \pm 30 \mu\text{m}$ . Figure 5.12 (b) and (c) give the microstructures of the surface regions produced using cryogenic burnishing with 0.127 mm DoP and 0.254 mm DoP respectively. It can be observed that adjacent to the burnished surface, especially for the cryogenically burnished pin with 0.254 mm DoP (Figure 5.12 (c)), a layer exists where the grain boundaries are not optically discernable under the current observation method. By using similar scales and measuring technique, this refined layer with indiscernible grain boundaries was also reported in other materials after burnishing (Li et al. 2008; Nalla et al. 2003). The burnishing-influenced layer is defined as a layer where the microstructure shows the features of recrystallized grains, elongated subgrains, and/or grains with heavy twinings and stacking-faults (Wu et al. 2005). The results also indicate that increasing the DoP from 0.127 mm to 0.254 mm under cryogenic conditions

lead to more severe plastic deformation and a thicker process-influenced layer due to the much higher burnishing force (Figure 5.3) and effective cryogenic cooling.

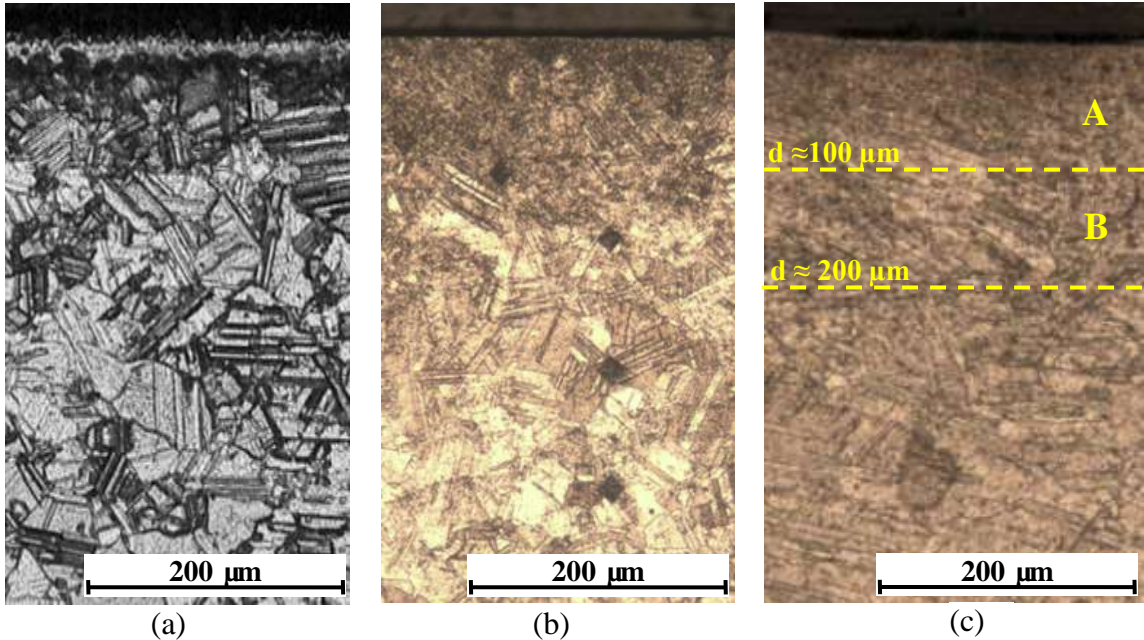


Figure 5.12: Microstructure near the surface: (a) initial, (b) cryogenic burnishing, 0.127 mm DoP, (c) cryogenic burnishing, 0.254 mm DoP (note that the square marks on Figure 5.12 (b) were from the Vickers hardness measurements)

It is reported that on the machined surface of *AISI 52100* steel (Jayal et al. 2010), significant grain refinement to the nanocrystalline level was found due to SPD induced DRX. The formation of the refined layers from burnishing (Figure 5.12 (b) and (c)) was similar to the “white layers” generated during machining. In addition to machining, surface mechanical attrition treatment (SMAT) was also claimed to create such surface layers on pure *Ti* and *Cu*, the grain sizes in the layers were found to be in the range of 50-250 nm (Li et al. 2008; Zhu et al. 2004). Many evidences show that SPD induced nano-sized/ultrafine grained materials possess appealing properties compared with their coarse-grained counterparts. A study from Iglesias et al. showed that wear rates of

nanostructured copper and titanium produced by large strain extrusion machining are significantly lower than that of their coarse-grained counterparts (Iglesias et al. 2007). Nanocrystalline surface layers generated by SPD process on *Cu*, steels and *Mg* alloy showed improved sliding wear behaviors compared to the untreated alloys (Shi and Han 2008). The detailed microstructural evolution of this *Co-Cr-Mo* alloy after burnishing with 0.254 mm DoP was further studied. As shown in Figure 5.13 (a), a featureless layer where no grain structure and grain boundaries can be clearly identified using the current observation method. The disappearance of grain boundaries in Figure 5.13 (a) is likely caused by the formation of nano/ultrafine grains through SPD-burnishing induced DRX. Nano/ultrafine grain structures have been reported frequently on *Co-Cr-Mo* alloys through SPD induced DRX in various processes, such as hot compression deformation (Kurosu et al. 2010a; Yamanaka et al. 2009) and combustion synthesis (Li et al. 2003). They are also reported in hip implants (Buscher and Fischer 2005). They develop as wear progresses in the body. In layer B (Figure 5.13 (b)), grain boundaries gradually became clear as the depth from the burnished surface increases, the grains in this layer also showed elongated subgrains. It was reported that the volume fraction of dynamically recrystallized grains increased with strain in a sigmoidal scheme (Fatemi-Varzaneh et al. 2007). Since the strain induced by burnishing decreases with distance from the surface to the bulk material, it is expected that the density of ultrafine grains decreases with increasing depth. Similar findings were reported by (Wu et al. 2005). After SMAT processing of cobalt, a microstructural evolution in the deformed surface layer was observed. Recrystallized nano-grains, elongated subgrains, grains with heavy twinings,

and equiaxed bulk grains with stacking-faults were observed sequentially, from the depth of 15  $\mu\text{m}$  to 180  $\mu\text{m}$ . This is very similar to the present investigation.

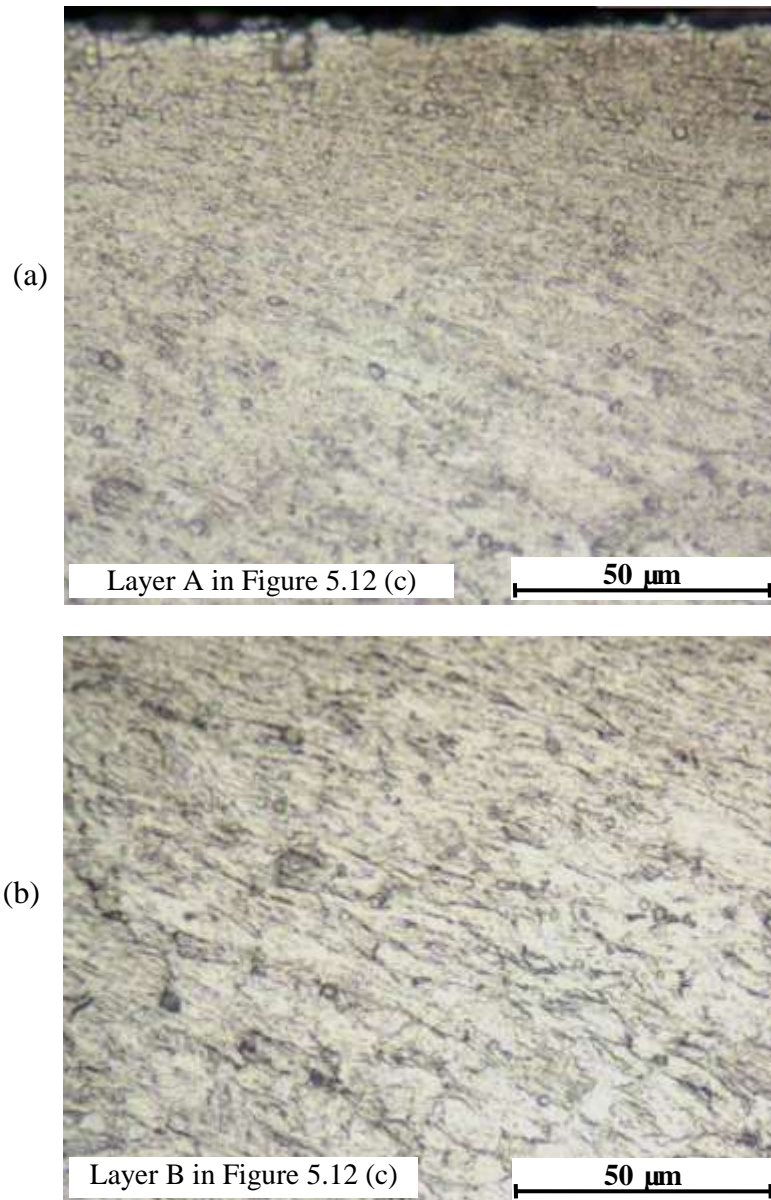


Figure 5.13: Typical microstructures after cryogenic burnishing (0.254 mm DoP): (a) layer A in Figure 5.12 (c) (0 ~ 100  $\mu\text{m}$ ), (b) layer B in Figure 5.12 (c) (100 ~ 200  $\mu\text{m}$ ).

Thus, it is expected that smaller grain size should be the result of DRX when the processing temperature is low. This claim has been proved in a previous study (Yang et

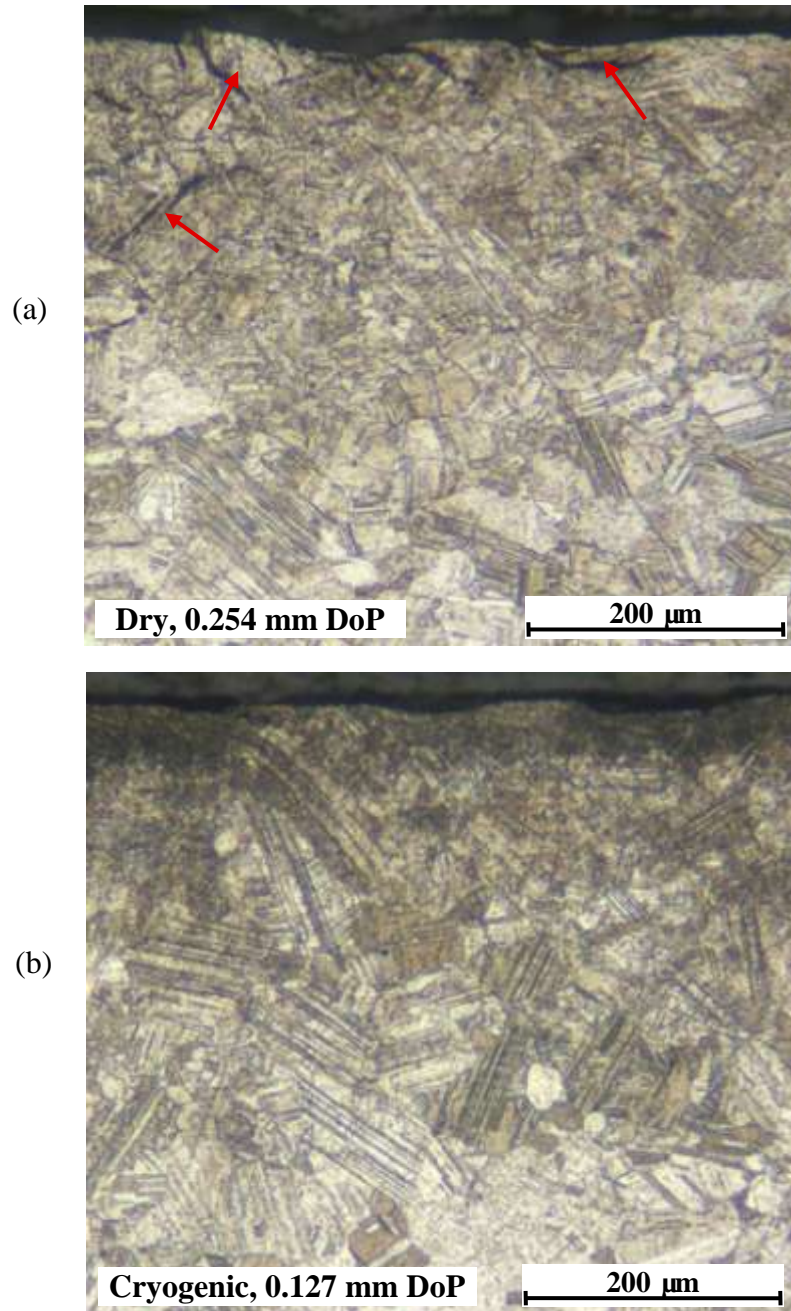
al. 2011), by using the otherwise same conditions, smaller grain size was achieved by cryogenic burnishing, remarkable grain refinement occurred due to the SPD-induced DRX and effective liquid nitrogen cooling.

#### 5.3.6. Microstructure after wear test

Very fine grains in the nm range were reported on cobalt base alloys from the *in vitro* as well as in *in vivo* wear test which is attributed to the DRX-induced grain refinement during wear process (Buscher and Fischer 2005). Due to the fact that wear particles are produced by different ways of crack initiation and propagation depending on the acting wear mechanism, microstructure analysis on the pins after wear tests was performed to investigate the surface and subsurface deformation mechanisms of the pins made using different burnishing conditions. Figure 5.14 gives the typical cross-sectional microstructures of the *Co-Cr-Mo* pins after wear tests respectively; in particular, Figure 5.14 (a) and (b) also correspond to the burnished pins with the most wear loss (dry, 0.254 mm DoP) and the least wear loss (cryogenic, 0.127 mm DoP). It is evident from Figure 5.14 (a) that, within the surface layers of the dry burnished pin, surface and subsurface cracks are developed during wear, which may eventually break away from the surface and become wear debris. In contrast, as shown Figure 5.14 (b) and (c), the cross-sectional microstructures of the cryogenically burnished pin after wear test have fewer cracks compared to the one from dry burnishing (Figure 5.14 (a)), this is likely due to the gradient of the microstructure changes from the surface towards the bulk material, no instabilities occur which would represent eventual sites for crack initiation. Thus tribologically induced fatigue crack initiation and propagation is shifted towards the top surface, which suggests that the cryogenically burnished pins possess stronger resistance



to the adhesion and surface fatigue induced wear debris generation. In addition, a thin layer ( $< 2 \mu\text{m}$ ) at the top surface with indiscernible grain boundaries was observed within the initial pin after wear. More information on the pin microstructure and its changes during wear tests is presented later in this chapter when phase changes are reported.



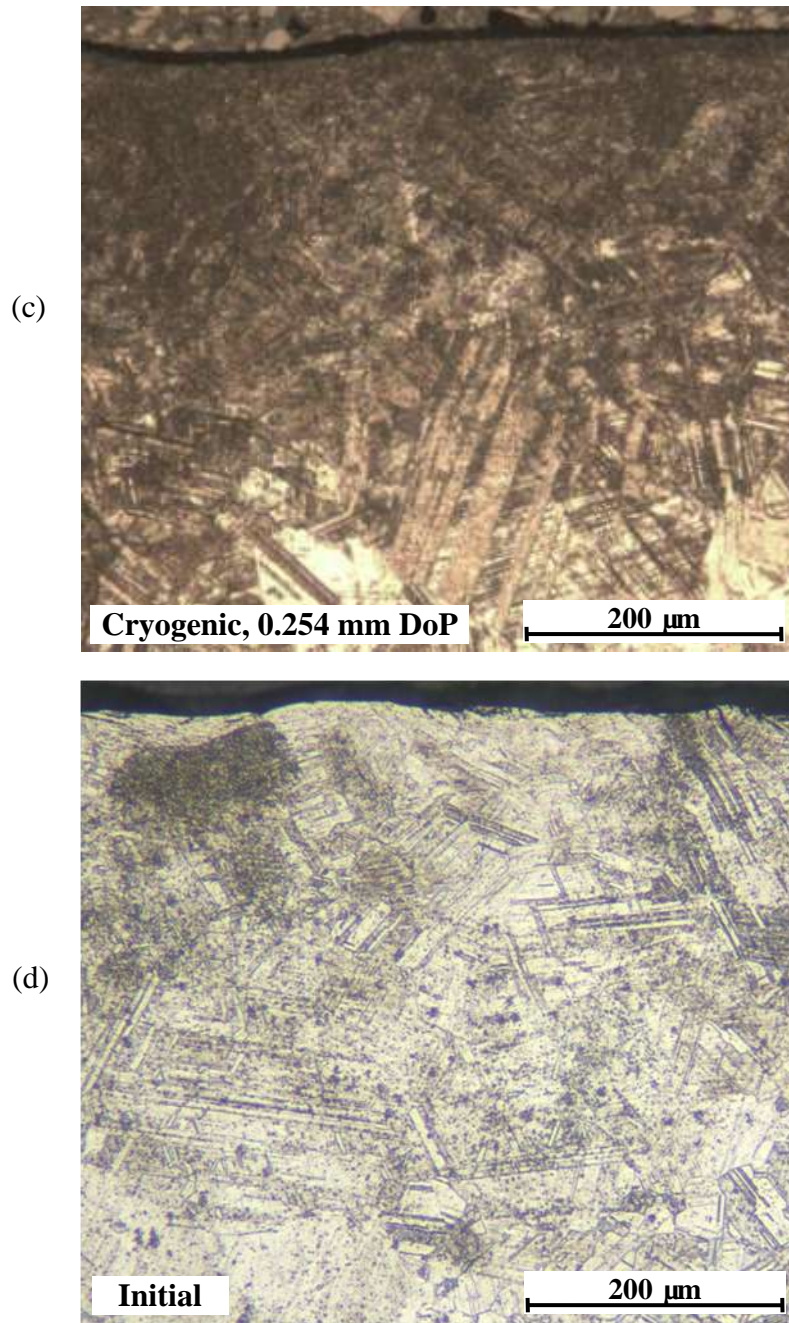


Figure 5.14: Microstructure of the surface after wear tests: (a) dry burnishing, 0.254 mm DoP, (b) cryogenic burnishing, 0.127 mm DoP, (c) cryogenic burnishing, 0.254 mm DoP, (d) initial. Other conditions are given in Table 5.1.

### 5.3.7. Surface and subsurface microhardness

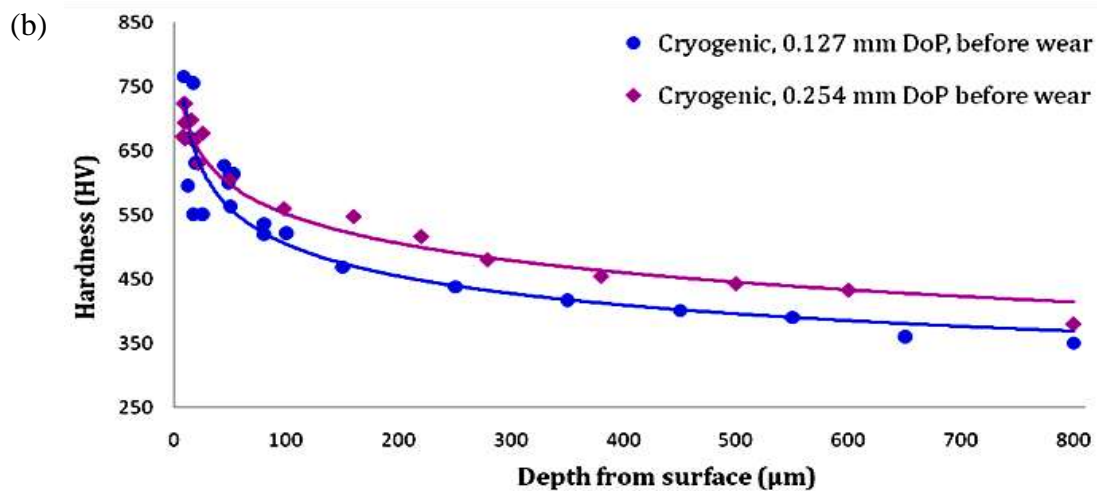
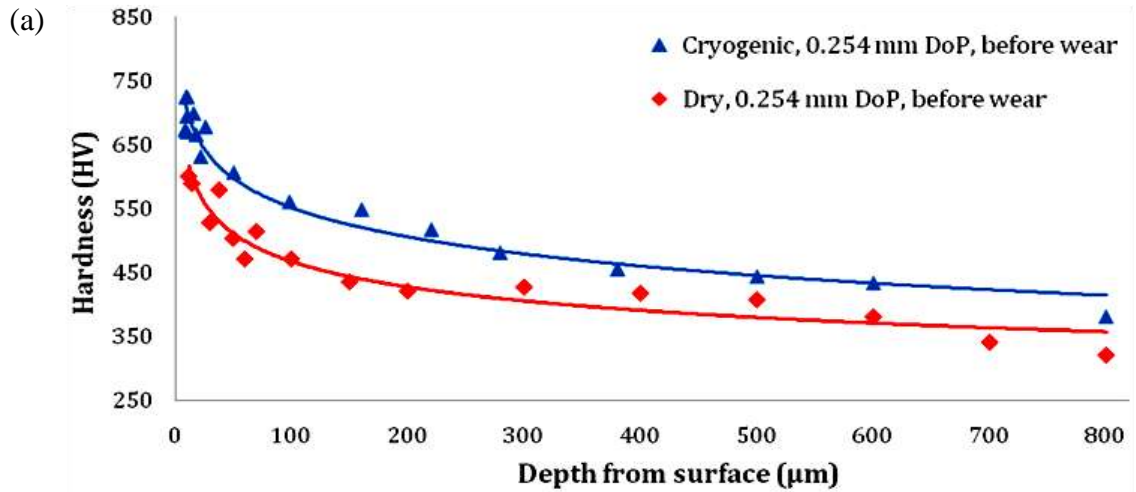
Hardness is a materials resistance to localized plastic deformation and is directly related to the wear resistance. The subsurface hardness profiles of the pins made using selected burnishing conditions are shown in Figure 5.15 (a) and (b). The average value of the measured microhardness of the virgin disk is  $330 \pm 20$  HV. As a general trend, the hardness decreases significantly with the distance below the surface, which coincided with the microstructural changes observed in these samples. Closer to the surface the hardness might even be greater, but this cannot be measured by such microhardness techniques. Based on the well-known Hall-Petch relationship between yield stress and grain size as well as the close interrelations among hardness, yield stress, and residual stresses, high hardness values often indicate fine grain size and large residual stresses. As shown in Figure 5.15 (a), it is clearly visible that cryogenic burnishing led to greater hardness values and a deeper burnishing influenced layer than the ones from dry burnishing, this is likely caused by the higher temperature within the tool-workpiece contact zone which reduces the SPD effect as well as the higher temperature outside the tool-workpiece contact zone which prompts the dynamic recovery process during dry burnishing. The application of liquid nitrogen on the flank side of the tool-workpiece contact region effectively suppressed the temperature rise during and after burnishing and helped retain the SPD effects from processing.

It is also found that cryogenic burnishing with larger DoP did not lead to a higher surface hardness (Figure 5.15 (b)). This is likely due to the higher amount of hexagonal close packed (hcp) phase in the cryogenically burnished pin with 0.127 mm DoP. It has been reported that as the volume fraction of hcp phase in the *Co-Cr-Mo* alloy increases,

the hardness also increases (Saldivar-Garcia and Lopez 2005). The surface hardness values ( $HV_{\text{surface}}/HV_{\text{initial}}$ ) of all the pins before and after wear tests are shown in Figure 5.15 (c). Compared to the initial pin hardness, an increase of up to 140% was achieved using cryogenic burnishing. It should be noticed that the improved pin-on-disk wear behavior in pins with hcp phase structures is not directly related to the hardness differences between contacting surfaces. Relating the results shown in Figure 5.4, Figure 5.15 (c) and Figure 5.17, it can be observed that with similar hardness values, the wear volume losses are lower in pins with higher fraction of the hcp phase.

The strain-induced hardening of the subsurface is achieved by several microstructural effects, which act simultaneously. Generally, blocking and subsequent accumulation of dislocation tangling lead to an increase in hardness. Blocking can be obtained from plastic deformation by either increasing the grain boundary density or creating other lattice defects which also hinder the movement of dislocations. In particular, stacking faults and their intersections are known to distinctly increase the material strength by piling up dislocations (Lu et al. 1997). Mainly at elevated temperatures these intersections may be passed by dislocations to achieve a relaxation of the lattice (Lu et al. 1999). However, this form of work-hardening is even limited at room temperature since the stacking fault density is increased with increased work-hardening which in turn hinders the formation of new stacking faults (Huang and Lopez 1999). In addition to stacking faults, strain-induced phase transformations into hcp structures further contribute to this hardening effect. It should be mentioned that the hardening effect of strain-induced  $\epsilon$ -martensite is similar to that of stacking faults and differs from that of  $\alpha$ -martensite in steels. Referring to the tribological behavior of a nanocrystalline

surface, the increase in hardness due to grain rotation and sliding should be beneficial. A high hardness reduces the effect of three body abrasion by increasing the resistance against surface fatigue by indentation.



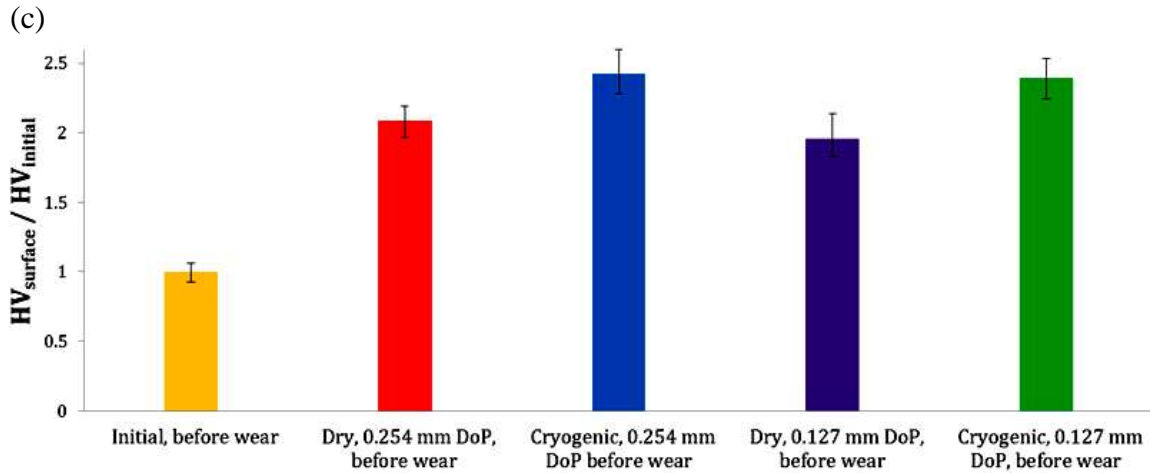
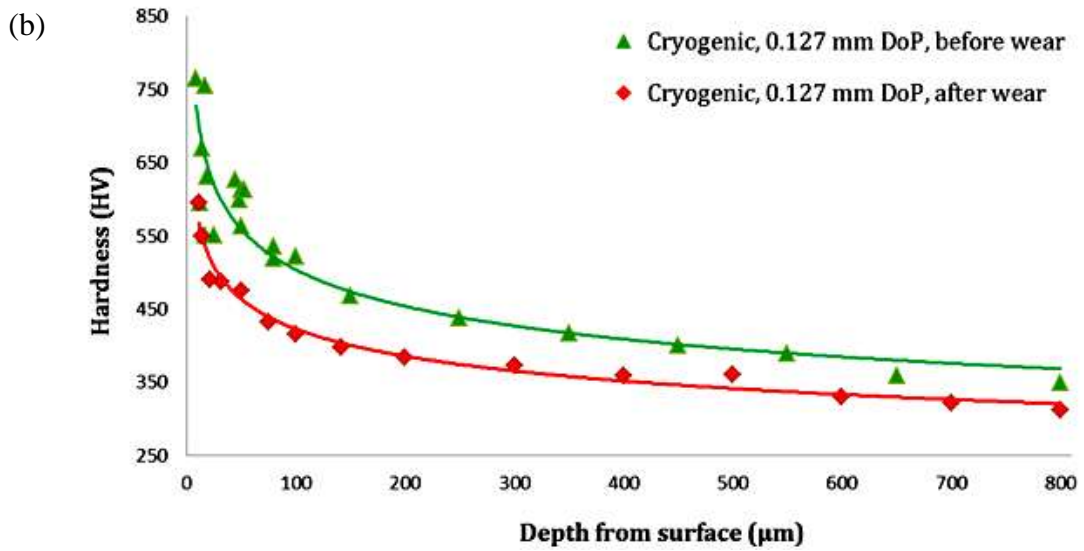
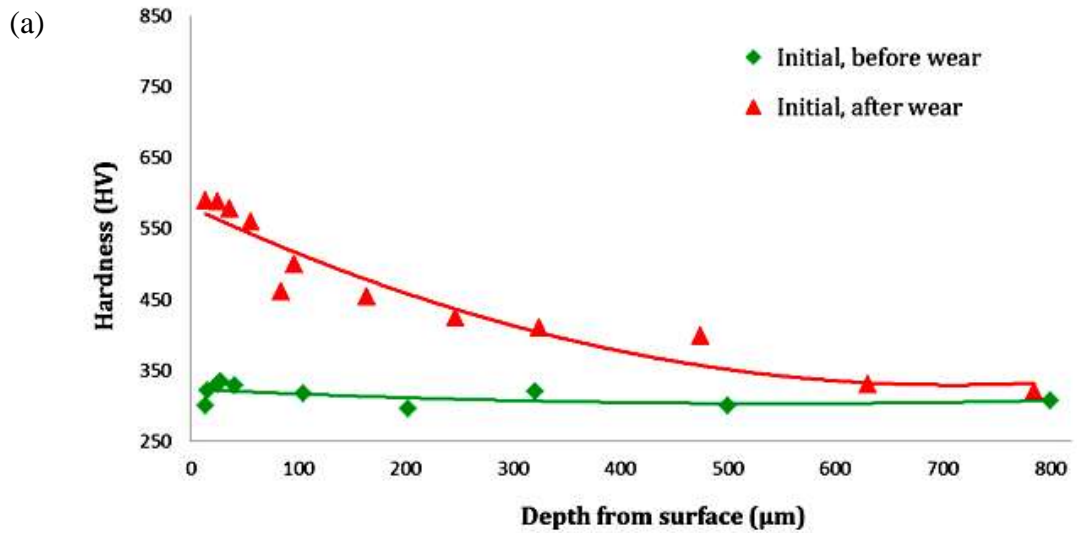


Figure 5.15: Hardness variation before wear test: (a) and (b) subsurface hardness profiles for selected burnishing conditions, (c)  $HV_{\text{surface}} / HV_{\text{initial}}$  values

The subsurface hardness profiles of the selected pins before and after wear tests are shown in Figure 5.16. As shown in Figure 5.16 (a), it can be observed that compared to the initial pin before wear which shows little hardness variation along the depth, a significant hardness increase close to the surface was developed during wear tests, starting from the microhardness of the unworn material of 330 HV the hardness increases up to 590 HV at 11  $\mu\text{m}$ .; the hardness profile of the worn initial pin is very similar to the ones from burnishing, which confirms that plastic deformation was present during wear. Similar results were reported from *in vivo* and *in vitro* wear studies of this *Co-Cr-Mo* alloy by Buscher and Fischer (2005), the changes in hardness were attributed to be a result of the wear-induced changes of the subsurface microstructure. In contrast to the hardness increase observed in the initial pin after the wear test, the pins from burnishing all show reduced hardness along the depth, moreover, the hardness after wear evolves into all having similar values, despite the very different values before wear. Due to the aggressive wear conditions used in current study, it is very likely that the burnishing

induced property modifications have been used up during wear, and the similar resulting hardness profiles for the initial and burnished pins also indicate that the plastic deformation induced work-hardening as well as material loss due to wear are occurring concurrently during the pin-on-disk wear test.



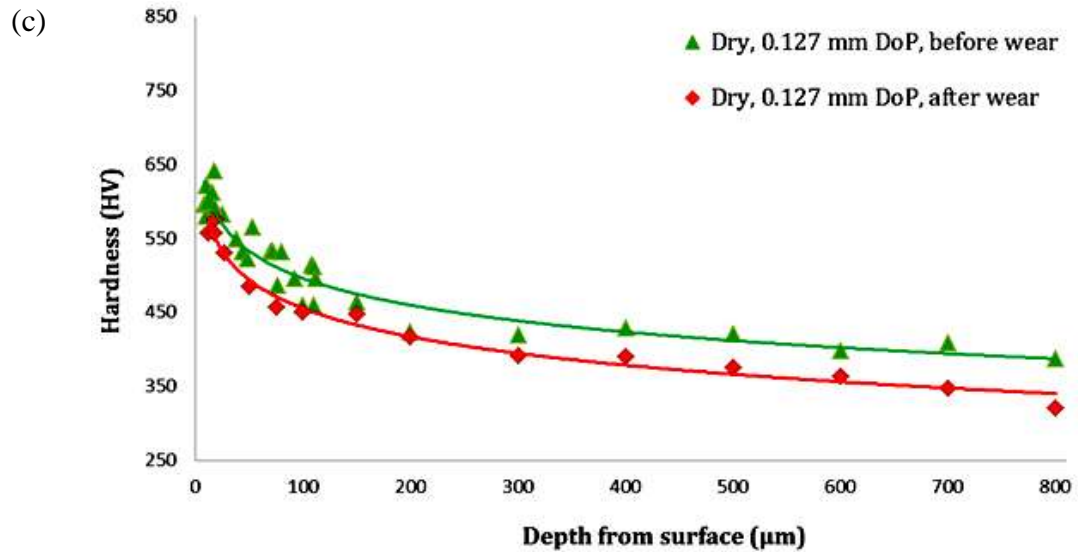


Figure 5.16: Hardness variation before and after wear test: (a) initial, (b) cryogenic, 0.127 mm DoP, (c) dry, 0.127 mm DoP.

### 5.3.8. Phase change

In the current study, the effect of different burnishing conditions on phase transformations of the *Co-Cr-Mo* alloy before and after wear tests was studied. Figure 5.17 shows the detailed XRD  $2\theta$  scan profiles from  $39^\circ$  to  $70^\circ$  of the burnished pins before wear tests. Phases of the annealed *Co-Cr-Mo* specimen before burnishing were analyzed (Figure 5.17 (a)); it was found that the initial specimen (after annealing and without any following processing) had both fcc  $(111)_\gamma$  and hcp  $(0002)_\epsilon$  phases initially in the surface. In contrast, the XRD patterns obtained from dry and cryogenic burnishing with 0.254 mm DoP consist mainly of fcc  $(111)_\gamma$  phase, and the ones from dry and cryogenic burnishing with 0.127 mm DoP show a combination of fcc  $(111)_\gamma$  and hcp  $(10\bar{1}1)_\epsilon$  phases. It is reported that slow cooling after thermal treatment inhibited the metastable fcc  $\Rightarrow$  hcp phase transformation. In contrast, a fast cooling rate after solution annealing and a controlled grain size range promoted phase transformation during



deformation (Salinas-Rodriguez 1999). The strain-induced fcc => hcp phase transformation plays an important role during large strain plastic deformation of low carbon *Co-Cr-Mo* implant alloys. The microstructures and the strain hardening behavior observed indicate that the dynamic formation of the hcp phase acts as a soft strain producing mechanism at low stresses and causes a rapid decrease in the strain hardening rate. As the flow stress increases, the rate of decrease of the strain hardening rate decreases gradually leading to regime of constant hardening rate that starts at a stress that depends on the initial grain size and deformation mode. This behavior implies that the larger strain hardening rate required to maintain uniform flow at high stresses can be attributed to the static hardening contribution of the dynamically formed hcp phase.

From the above, it can be stated that the lower processing temperature and the faster cooling rate due to the application of liquid nitrogen promote the fcc => hcp transformation during and after burnishing, moreover, it also suggests that larger DoP could lead to more severe plastic deformation which should promote the fcc => hcp transformation. However, in competition with this is the effect of the higher processing temperature which would compromise the happening of this transformation. Referring to the findings from Chapter 4, it can be concluded that the strain-induced phase transformation of *Co-Cr-Mo* alloy is concurrently influenced by strain, strain-rate and temperature during processing. The relationships of the strain, strain-rate and temperature on the strain-induced fcc => hcp transformation of the *Co-Cr-Mo* alloy is still unclear, further studies on this matter are needed for the better control of the process induced property modifications.

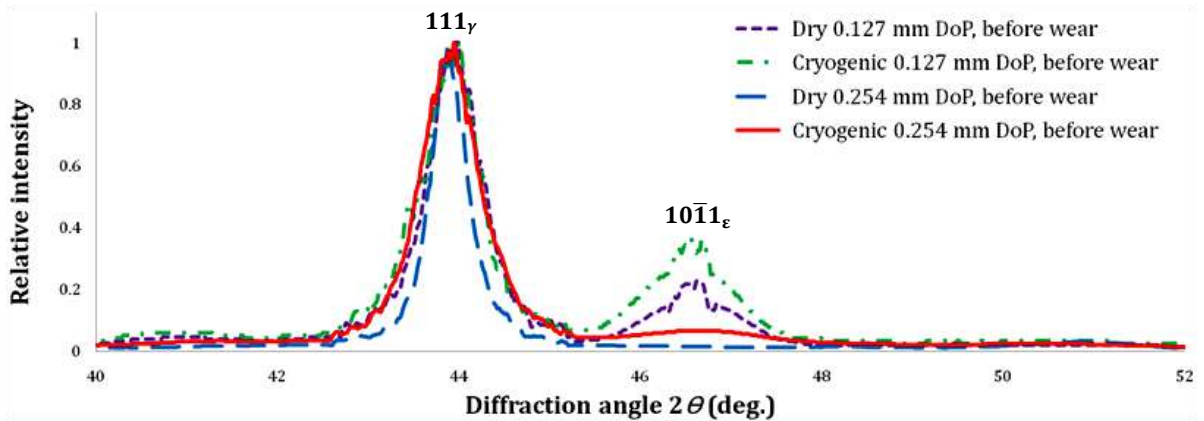


Figure 5.17: XRD spectra on the burnished surface from different burnishing conditions

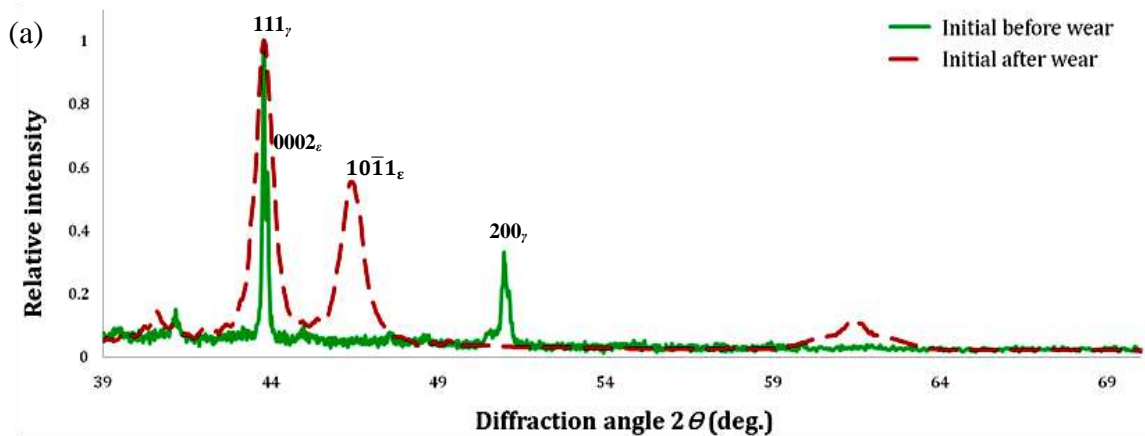
As shown in Figure 5.4 (the wear volume losses in pins as a function of the sliding distance), for burnished pins, the one with highest amount of hcp phase structures exhibited the lowest volume losses (cryogenic, 0.127 mm DoP), and the pins with intermediate wear resistance consisted of a reduced hcp amount. The wear volume losses increase with reducing hcp amount, the highest volume loss corresponds to the pin with pure fcc phase structure (dry, 0.254 mm DoP), which indicates that the hcp structure improves the wear resistance of this *Co-Cr-Mo* alloy in metal-metal wear tests. It should be noticed from Figure 5.18 that the phase structures of the worn pin surfaces all evolved into similar fcc + hcp phase structures during wear tests, regardless of the different original phase structures of the pins. This fcc + hcp phase structure is likely to be a more stable, stronger and more wear resistant crystallographic structure, which is a possible reason for the very different wear rates of the “run-in” and “steady-state” periods which is observed in many of the joint implants. During the first few hundred cycles of loading (the “run-in” period), a significant level of wear is observed. Afterward, a lower yet

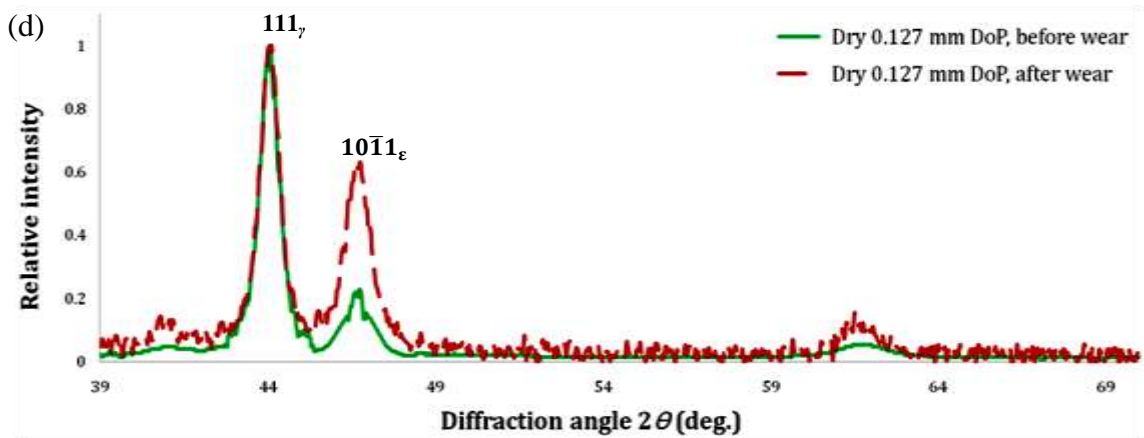
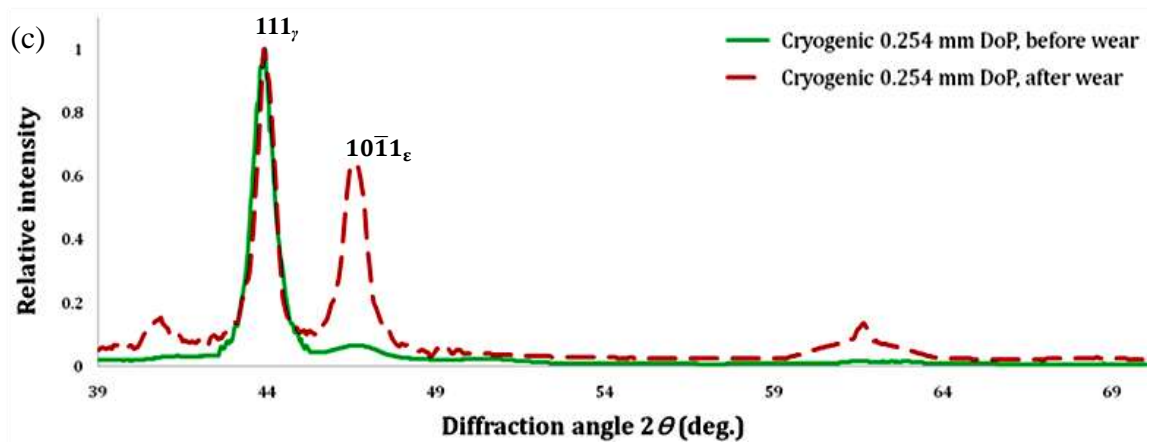
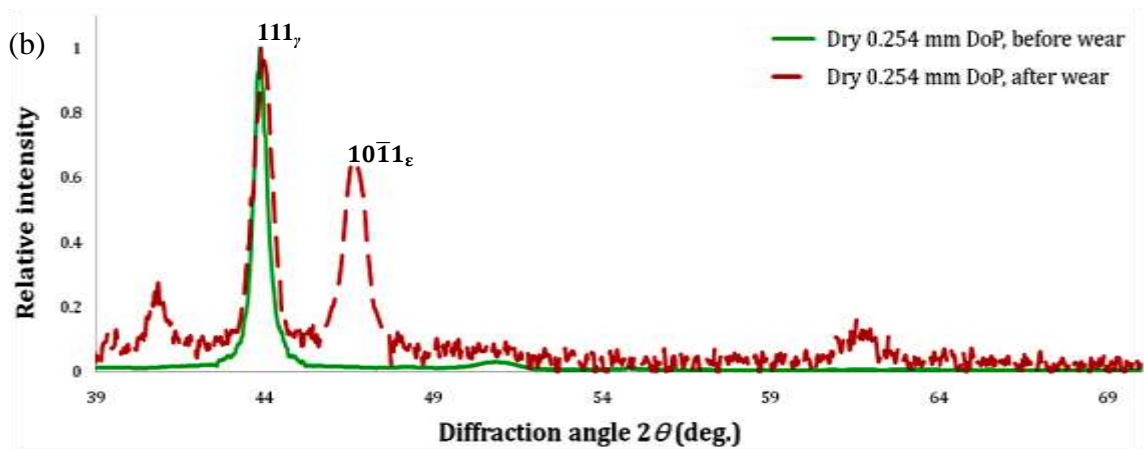
measurable steady-state wear level is observed compared to the run-in period (Cuckler 2005; Silva et al. 2005).

Among the most comprehensive work carried out on the sliding wear of cobalt-base alloys was that by (Buckley 1968), who compared the sliding wear of cobalt with that of copper. Low friction and adhesion levels were noted for the cobalt, which was attributed to its hcp structure, compared to the copper's fcc structure. During sliding, friction with cobalt was noted to remain at a low, steady value, whilst that of copper was observed to rise with increased sliding distance. A similar pattern was observed in the values of adhesion measured before and after testing. The difference between the sliding behavior of metals in hcp phase and fcc phase were attributed to the greater number of active slip systems available in the fcc structure. There are twelve primary slip systems within a typical fcc metal, which are all crystallographically similar. In comparison, there are only three primary slip systems in cobalt, these being based on the planes with greatest atomic density and with greatest distance between planes. Hcp materials are thus less deformable, at a given load, due to the more difficult cross slip between planes. In addition, recrystallization under more extreme conditions (e.g., temperature, strain) and alignment of this plane in grains at the sliding surface allow for regions of extended easy glide and thus lead to reduced shear needed to overcome junction formation during sliding, hence the friction and adhesion values are lower. With fcc metals, strain of adhered or welded junctions will result in increased shear stress due to work hardening. This work hardening is a result of the interaction of slip planes and slip plane dislocations forming barriers to other dislocation slip plane movement and thus a greater stress is needed to overcome these barriers. In another study, it is found that at temperatures

between room temperature and 300 °C, a cobalt-base alloy, Stellite 31, undergoes a much lower level of wear compared to various nickel- and iron-based alloys, which is also attributed to the fewer number of slip planes in the hcp structure of cobalt (Stoot et al. 1977).

In addition, an increase of the interfacial free energy would result in a reduction of the friction coefficient due to the reduction of the work of adhesion at the interface. Moreover, increasing the interfacial free energy would also improve the hydrophilic characteristics of the interface and would also increase its ability to retain a film of liquid lubricant (Buckley 1968). Improved lubrication conditions at the interface decrease the interfacial shear stress and would cause a further reduction of the friction coefficient. However, further experimental work on the wear behavior is needed to substantiate quantitatively the arguments put forward in the present study.





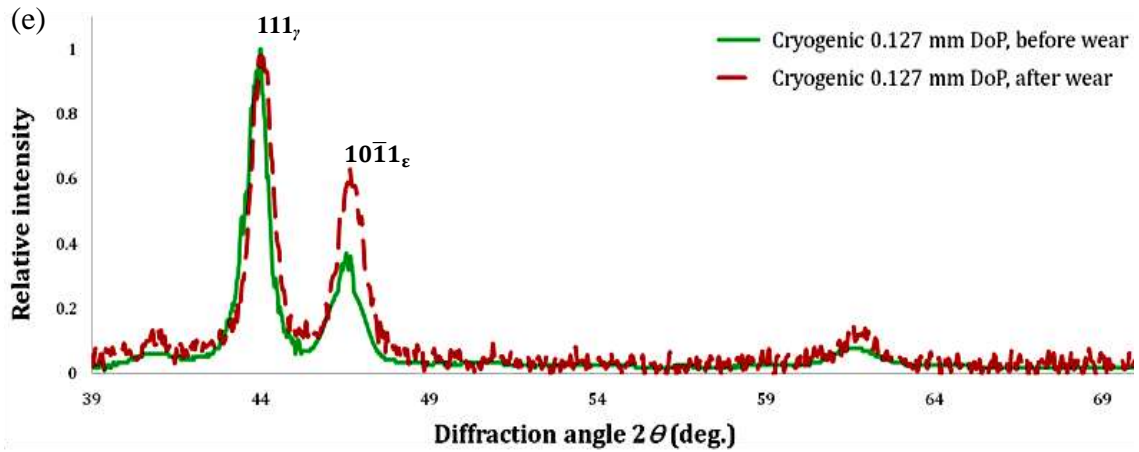


Figure 5.18: XRD spectra on the pin surface before and after wear tests

Quantitative analyses of the relative volume fractions of fcc- $\gamma$  and hcp- $\epsilon$  phases were calculated as (Sage and Guillaud 1950):

$$\frac{x}{1-x} = \frac{I_{(111)\gamma}}{I_{(10\bar{1}1)\epsilon}} \quad (5.2)$$

where  $x$  is the volume fraction of  $\gamma$  phase and  $I_{(111)\gamma}$  and  $I_{(10\bar{1}1)\epsilon}$  are the integrated intensities of the  $(111)\gamma$  and  $(10\bar{1}1)\epsilon$  peaks, respectively. The results are shown in Figure 5.19. The initial pin has almost no  $(10\bar{1}1)\epsilon$  hcp structure on the surface. In contrast, significant amount of  $(10\bar{1}1)\epsilon$  hcp structure was introduced to the pins from dry and cryogenic burnishing with 0.127 mm DoP. The dry and cryogenically burnished pins with 0.254 mm DoP show lower hcp amount.

From the results presented above, it is clear that pins with different amounts of hcp phase have different wear tendencies. As discussed in section 5.3.6, with similar hardness values, the wear volume losses are lower in pins with higher amount of hcp phase. (Crook and Li 1983) also attributed the superior wear performance of the cobalt-

chromium alloys to the tendency of undergoing phase changes from fcc form to the hcp form, which as discussed earlier is less prone to occur due to a smaller number of available slip planes. It is apparent that the wear behavior of hcp structures has a better tribological response than the one corresponding to fcc structures. Accordingly, the wear properties of the fcc alloys can be improved in *Co*-base alloys through the fcc => hcp transformation. This, in turn, can be used for the development of biomedical devices with superior tribological properties.

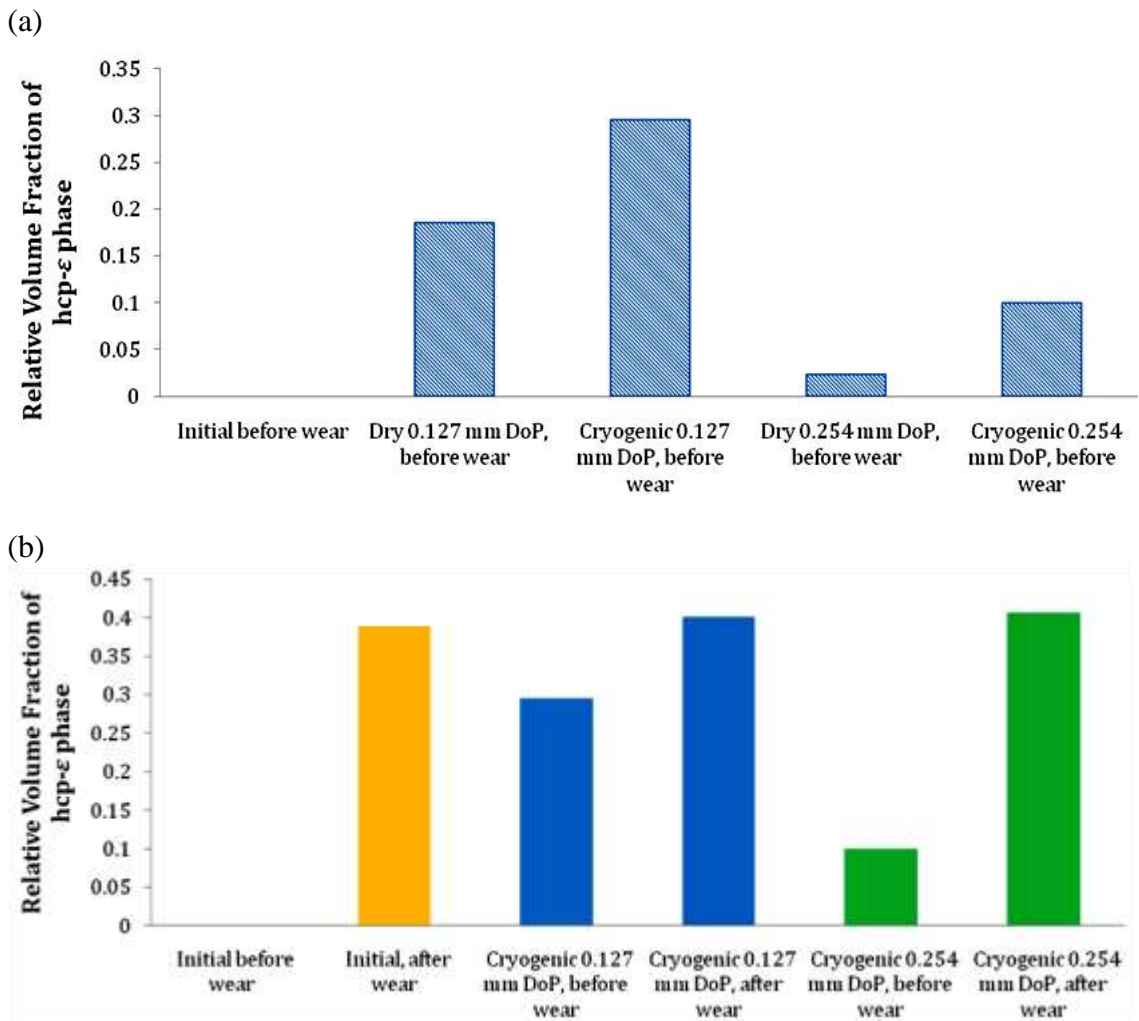


Figure 5.19: (a) Relative volume fraction of hcp phase after burnishing; (b) relative volume fraction of hcp phase before and after wear test for initial and cryogenically burnished pins.

Figure 5.20 shows the effect of the hcp volume fraction on the wear volume loss. It can be observed that if the improved wear performance of the pins was dictated by hcp phase only, the tendency would be linear regardless of the other surface integrity properties investigated. It has been reported that microstructure and residual stresses also have significant influences on the wear resistance and fatigue performance of many metallic materials (Iglesias et al. 2007; Sasahara 2005; Shi and Han 2008). Thus, it can be stated that phase structure is an important influencing, but not the only, factor contributing to the wear performance of the *Co-Cr-Mo* alloy, microstructure and residual stresses are decisive to the performance of this *Co-Cr-Mo* alloy. The effect of residual stresses on the wear performance of this alloy will be discussed later to validate this statement.

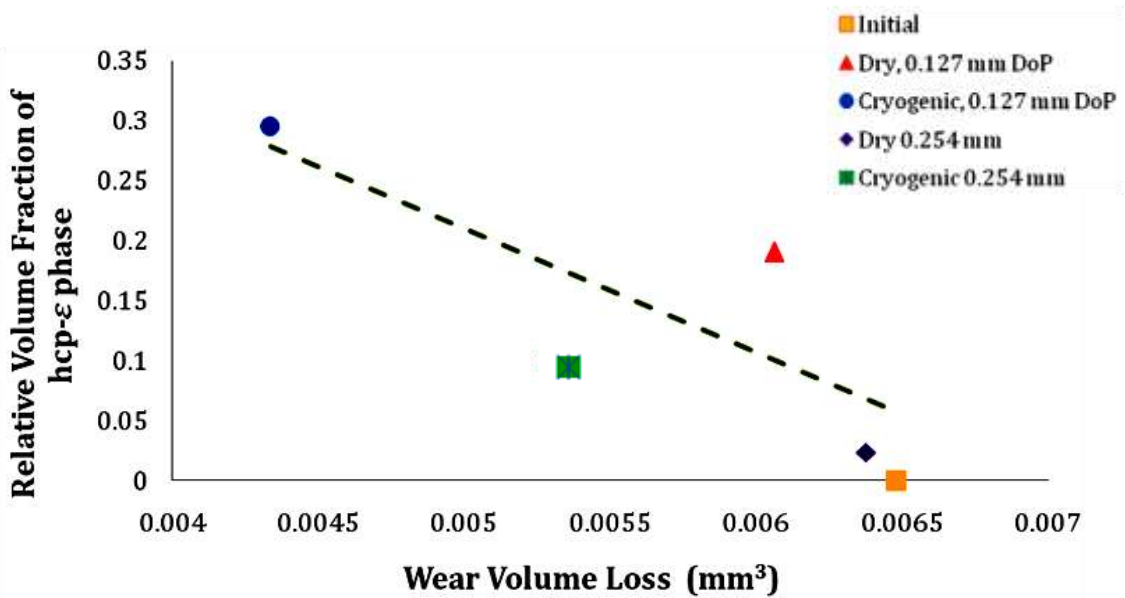


Figure 5.20: Relative volume fractions of hcp phase vs. wear volume losses.



### 5.3.9. Residual stresses before wear tests

The reliability of a mechanical component depends to a large extent on the physical state of its surface layers. This physical state includes the distribution of residual stresses induced in the surface layers during the manufacturing processes. The nature of the residual stresses (compressive or tensile) will enhance or impair the ability of a component to withstand fatigue, creep, stress, corrosion cracking, etc. Residual stresses can have a detrimental effect on structural integrity and are an important consideration in failure assessment of all structures.

Figure 5.21 shows the surface residual stresses for all the pin samples in the tangential and axial directions. As shown in Figure 5.21, the initial surface residual stresses in both directions were very small compared to the other ones measured after burnishing.

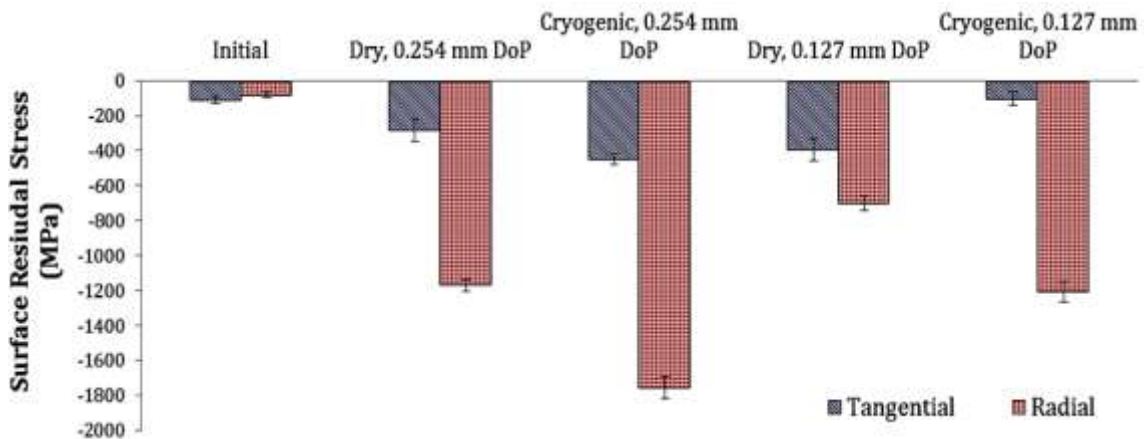


Figure 5.21: Surface residual stresses before wear tests

In addition to the surface residual stresses, the depth distribution of the residual stresses along the sub-surface is sometimes more important to the component performance, high stress gradient along the sub-surface is found to result in heavily worn

surfaces in alumina hip joints (Pezzotti et al. 2012). Greater compressive depth with larger compressive values along the sub-surface is claimed to be desirable to the functional performance of many materials (James et al. 2007; Wilson et al. 2009). Figure 5.22 shows the in-depth residual stresses in the tangential and axial directions (Figure 5.22 (a)) after burnishing using 0.127 mm DoP under both dry and cryogenic conditions. The penetration depth of the compressive residual stresses was extended to greater depth (more than 600  $\mu\text{m}$ ) along with the peak compressive residual stress was increased by a factor of 121% in the tangential direction under cryogenic conditions compared with the ones from dry conditions. The penetration depth of the compressive residual stresses in the axial direction was similar for both dry and cryogenic conditions, but larger compressive values were created along the entire depth during cryogenic burnishing.

It has been reported that the application of liquid nitrogen could introduce a favorable residual stress distribution in the surface layer, which may further improve the functional performance of metallic materials. Compared with conventional oil-based cooling, (Ben Fredj and Sidhom 2006) found that cryogenic cooling led to about 50% reduction of tensile residual stress in the parallel direction of the disc workpiece, and the residual stress in the perpendicular direction was reduced to nearly zero from 200 MPa tensile, which substantially improved the fatigue life of *AISI 304* steel specimens subjected to high cycle fatigue loading. (Zurecki 2003) found that the residual stress distribution in machined *AISI 52100* steel was significantly improved by using cryogenic cooling.

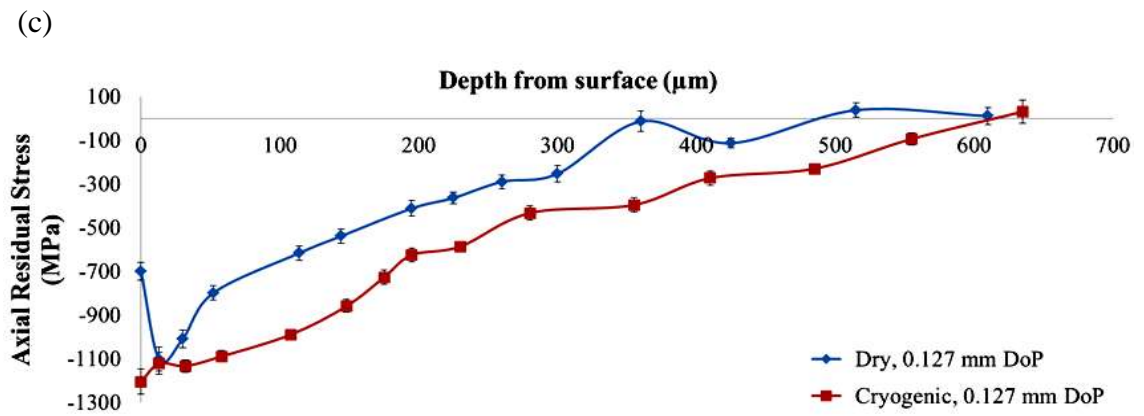
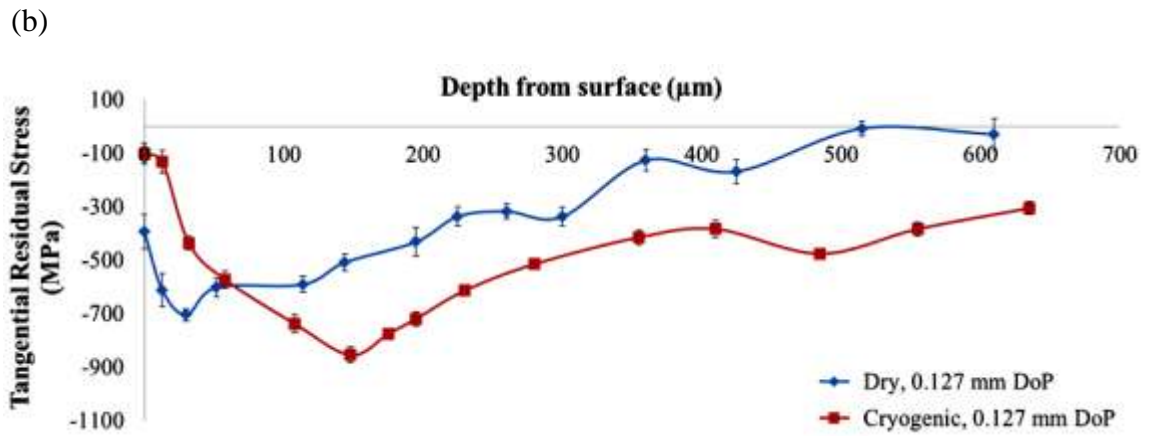
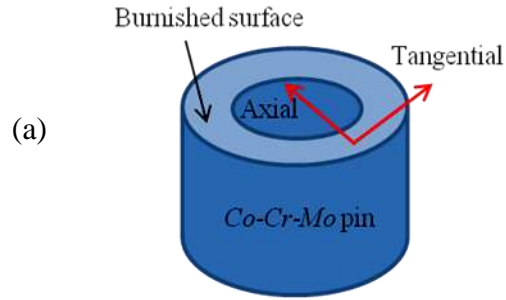


Figure 5.22: Measured residual stresses after dry and cryogenic burnishing with 0.127 mm DoP: (a) measurement illustration, (b) tangential direction, (c) axial direction.

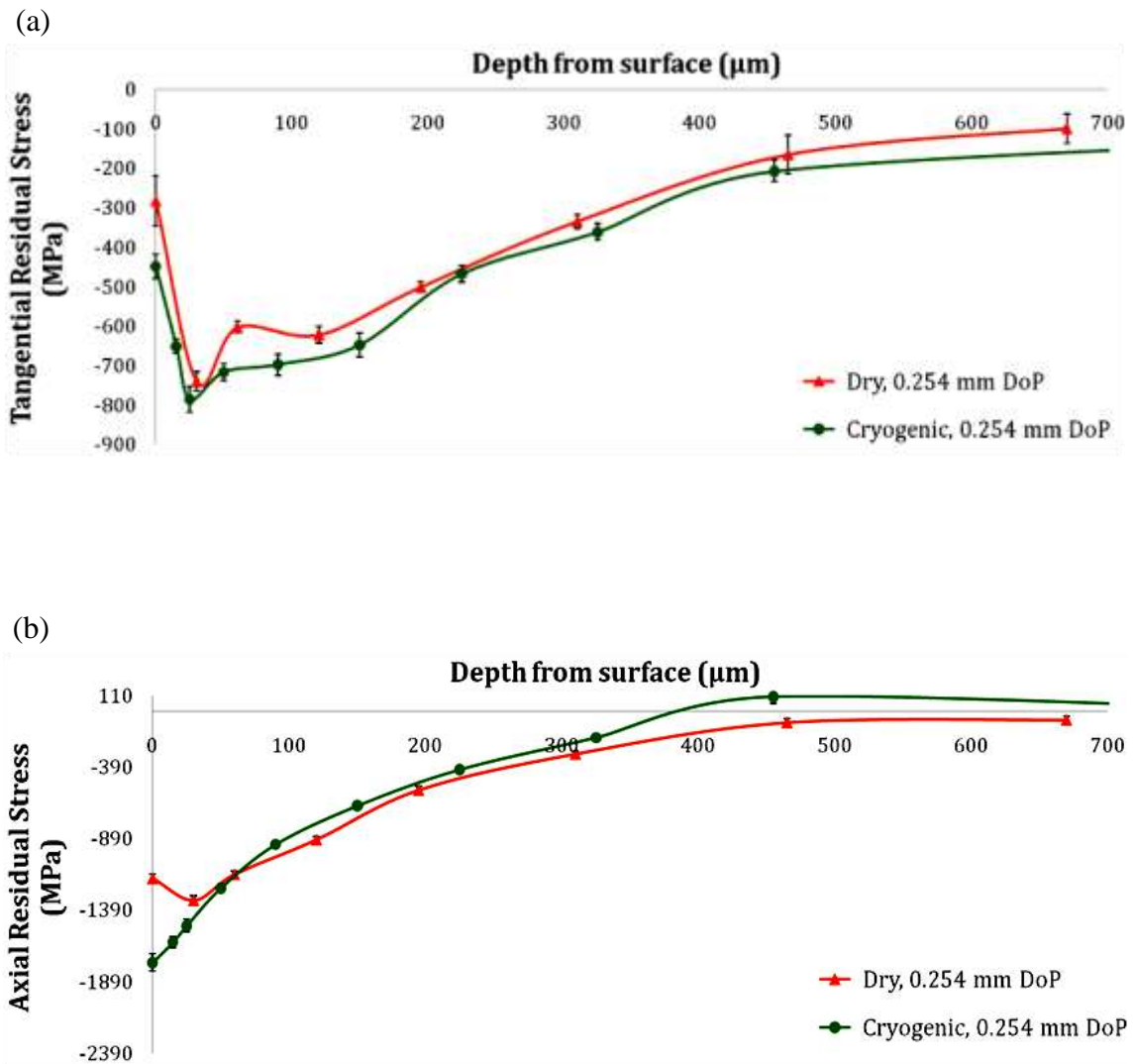


Figure 5.23: Measured residual stresses after dry and cryogenic burnishing with 0.254 mm DoP: (a) tangential direction, (b) axial direction.

Figure 5.24 shows the residual stress distributions after cryogenic burnishing with 0.127 mm DoP and 0.254 mm DoP in both tangential and axial directions. For the case of tangential residual stresses as shown in Figure 5.24 (a), by increasing the DoP from 0.127 mm to 0.254 mm, the maximum compressive value was created at a distance closer to the surface. However, a reduction of 8% on the maximum compressive value and shallower

compressive depth were developed with increased DoP under cryogenic conditions, which is likely caused by the increased temperature due to more severe ploughing effects and more tool-wear compared to the smaller DoP. In contrast, larger maximum compressive residual stress was created in the axial direction from cryogenic burnishing with larger DoP (Figure 5.24 (b)), however, cryogenic burnishing with 0.127 mm DoP led to still deeper penetration depth of the compressive residual stresses.

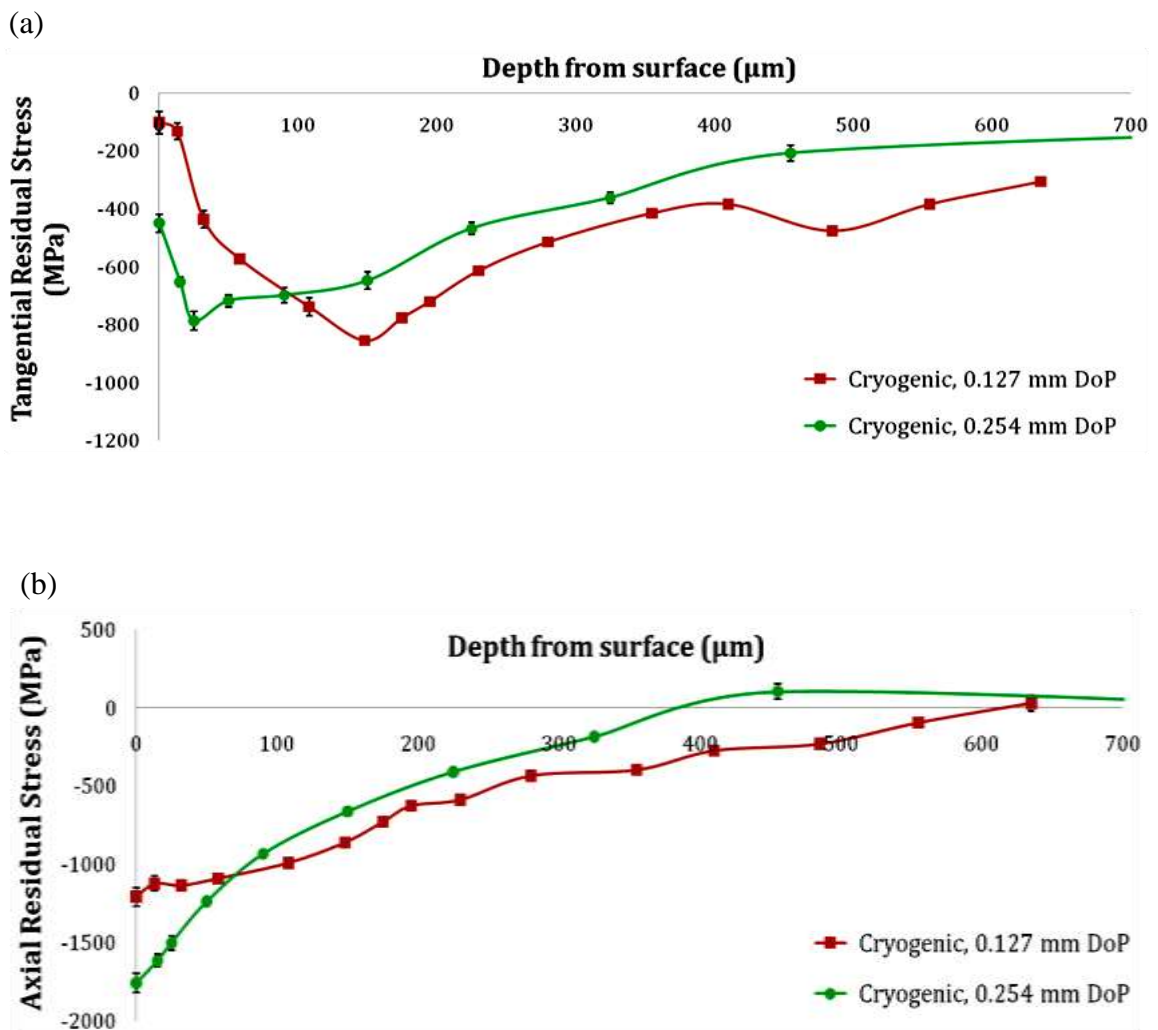


Figure 5.24: Measured residual stresses after cryogenic burnishing with 0.127 mm DoP and 0.254 mm DoP: (a) tangential direction, (b) axial direction.

The compressive area which is the area defined by the compressive portion of the residual stress profile and the depth axis has been reported to be an important influencing factor on the fatigue life and corrosion performance of different materials (Hashimoto et al. 2009; Pu et al. 2012a). Figure 5.25 shows the compressive areas calculated by the integration of the residual stress profiles with respect to depth below the burnished surface up to 600  $\mu\text{m}$  after burnishing using 0.127 mm and 0.254 mm DoPs under dry and cryogenic conditions. It can be observed that, with 0.127 mm DoP, the application of liquid nitrogen increased the compressive areas in both directions by a factor of 2 compared to the ones from dry burnishing. The results suggested that the higher temperature due to the heat generation (dry conditions) tends to make the residual stresses more tensile, if no proper cooling method was used. It is evident from the results reported above that cryogenic cooling could induce large and deep compressive residual stresses on the surface, which should further enhance the functional performance of the components such as fatigue life and wear/corrosion resistance.

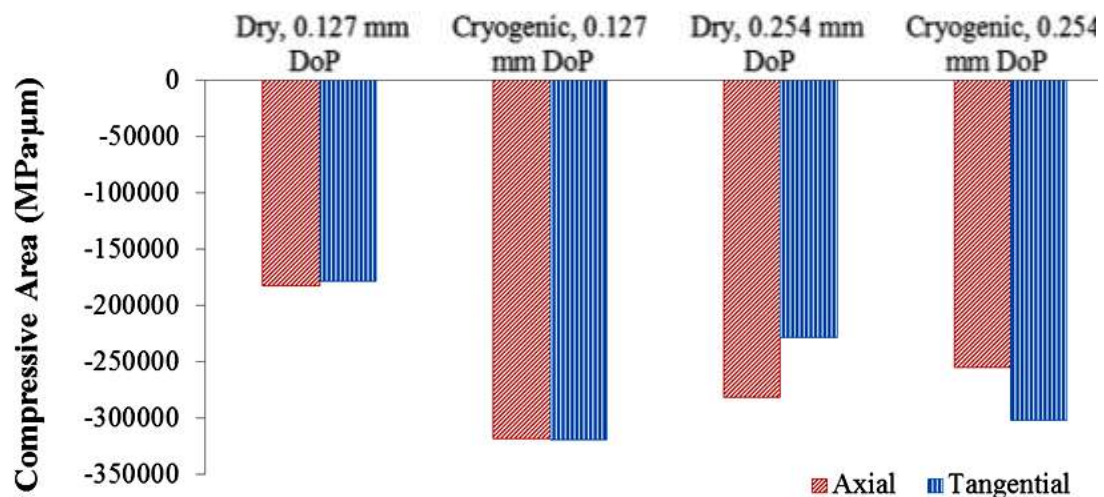


Figure 5.25: Compressive areas of the residual stress profiles from dry and cryogenic burnishing with 0.127 mm DoP

### 5.3.10. Residual stresses after wear tests

Figure 5.26 shows the residual stress distributions of the burnished pins after wear tests. It can be observed that for all the tested pin samples, the residual stresses tended to be similar with little difference in the worn surfaces, independent of their initial distributions before wear, the residual stress build-up in the early stages of wear and the initial stress pattern were destroyed. Due to the fact that the residual stresses all tended to be similar after wear, it is assumed that there is an optimal residual stress state which will be naturally evolved into during wear under certain test conditions. This phenomenon is consistent with the hardness distributions after wear tests discussed in section 5.3.6. Similar results were reported in the study of the residual stresses that developed during the wear of *AISI-SAE 1018* and *4340* steels (Ho et al. 1983). It is found that the wear process alters any initial stress distribution produced by pre-wear processing to such a degree that the wear rate is not affected by these stresses; however, different initial stress states could affect the wear performance of those materials significantly which has been shown by the results presented above.

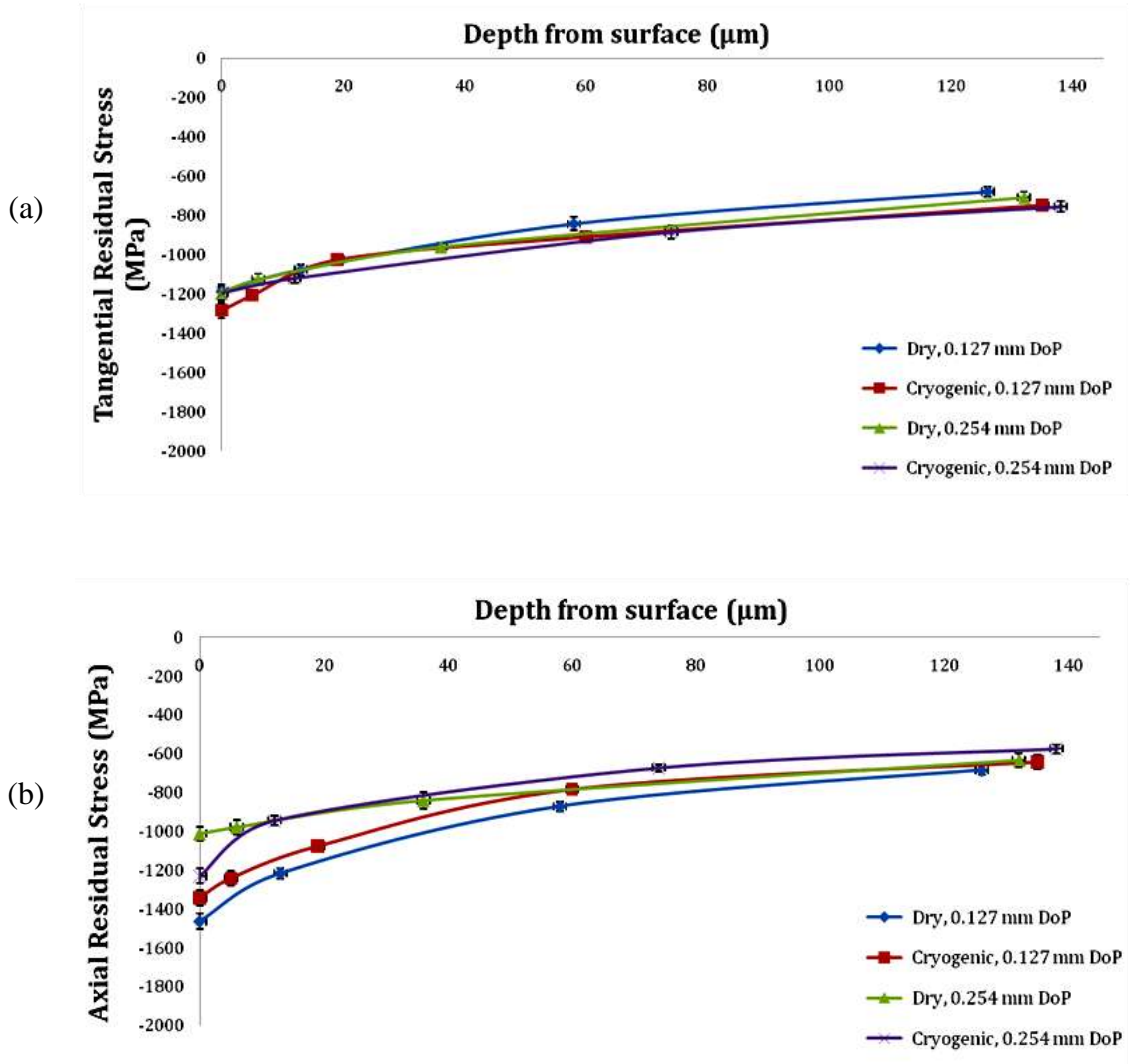


Figure 5.26: Residual stresses after wear tests for all the burnished pins: (a) tangential direction, (b) axial direction.

#### 5.4 Chapter concluding remarks

Dry and cryogenic burnishing experiments were conducted on annealed *Co-Cr-Mo* pins. The burnished pins were later subjected to pin-on-disk wear tests to explore the influence of burnished-induced surface integrity modifications on the wear performance of the studied *Co-Cr-Mo* alloy. These tests are meant to be preliminary ones for



predicting performance as hip implant material. The most important findings from this study are summarized below:

- (a) The major wear mechanism was identified as surface fatigue leading to fractured or tear-off metallic or oxide particles, which act afterwards as interfacial media. This further led to abrasion or surface fatigue depending on whether the particles stick to one surface and scratch the other or sometimes act as rolling particles bringing about indentations.
- (b) Cryogenic burnishing can significantly improve the wear performance of the *Co-Cr-Mo* alloy, which was attributed to the burnishing-induced surface integrity enhancements.
- (c) The microstructure of the *Co-Cr-Mo* alloy can be greatly modified by changing the cooling conditions. Grain refinement in the surface region was achieved through SPD-induced DRX during burnishing. Strain-induced fcc to hcp phase transformation was also observed under certain burnishing and cooling conditions.
- (d) It was found that minimal wear volume losses were achieved in pins with the highest hcp amount. In contrast, the highest values of mass losses corresponded to fcc pins. Intermediate wear values were found in pins with lower hcp amounts for the wear conditions used in this work. Moreover, it was found that the exhibited wear volume losses do not follow a single linear trend with the phase structure differences. Apparently, the changing phase structure features of the contacting surfaces play an important role in the tribological response. Under the wear conditions employed (metal-metal pin-on-disk), the dominant mechanism

involved some plastic deformation on the contacting surfaces, and included some oxidation of the wear debris.

- (e) Cryogenic cooling during burnishing can induce large and deep compressive residual stresses on the surface layer, which should further enhance the functional performance of the components such as fatigue life and wear/corrosion resistance.
- (f) It is also found that the presence of the hcp structure exceeded the effect of grain size on the wear performance of the *Co-Cr-Mo* alloy. However, the comparison between cryogenic and dry burnishing with 0.254 mm DoP showed that when there was no hcp structure present in the crystal matrix, the better wear performance of the cryogenically burnished pin was likely due to the thicker burnishing-induced refinement layer and compressive residual stresses. Thus, it is fair to conclude that the surface layer properties in terms of phase structure, microstructure and residual stresses were concurrently influencing the pin-on-disk wear behavior of this *Co-Cr-Mo* alloy. Further studies are needed for systematically identifying the level of importance of each of these properties on the wear performance of the *Co-Cr-Mo* alloy.
- (g) Finally, based on the above results, it is suggested that future developments in *Co-Cr-Mo* hip implants should consider material prototypes that have high hcp phase structure, fine-grained microstructure as well as thick compressive residual stress layers as these properties tend to exhibit superior wear performance in metal-on-metal contact. Manufacturing these products can benefit from using cryogenic cooling to produce the desired properties.

## CHAPTER 6: FINITE ELEMENT MODELING OF SURFACE INTEGRITY IN BURNISHING

### 6.1 Introduction

In this chapter, a robust FEM-based model for burnishing of *Co-Cr-Mo* alloy was developed and calibrated using the experimental data obtained in Chapters 3 and 4. A new material model was also developed for incorporating flow stress softening, caused by DRX, within the commercial DEFORM program. Since DEFORM contains a warning against using the program for unstable materials ( $\partial\sigma/\partial\varepsilon < 0$ ), this modification also requires coupling with the corresponding DRX models of the metallurgical mechanism (in this case changing grain size). A user subroutine was developed to predict the DRXed grain size and the formation of burnishing-influenced layer based on the DRX mechanism. Good agreements between the predicted and measured grain size were achieved for certain experimental conditions after using data presented earlier for determining several related material parameters.

### 6.2 Numerical setup in DEFORM 2D

The used roller burnishing process is a complex 3-dimensional one. A number of assumptions and simplifications had to be made in order to apply the 2-D plane strain simulations for this process. Therefore, the first task of this study was to evaluate Yen's 2-D basic model (Yen et al. 2005) for burnishing simulations. In doing so, attempts were made to reproduce the simulation results from Yen's model by following the same procedure to build and setting up a 2-D burnishing model using the software DEFORM-2D<sup>TM</sup>. The predictions were verified by comparing with the data provided in Yen et al.

(2005). Based on the results of this evaluation, specific modifications/refinements were then implemented in order to improve the model's applicability to our case.

As mentioned above, the current study was carried out using the commercial FE software DEFORM-2D™ to simulate the burnishing process for *Co-Cr-Mo* alloy. The computational domain of interest for the 2-D burnishing process is shown in Figure 6.1. The model was implemented by developing and using a customized user subroutine which is a Lagrangian implicit code designed for simulating metal forming processes. In addition, an adaptive remeshing technique was utilized during the simulation of the burnishing process. The work material was allowed to flow around the round edge of the roller tool so that the physical process can be simulated more realistically. A thermo-mechanical FEM simulation scheme was created by including tool and workpiece thermal and mechanical properties. Both the workpiece and tool models used four-node bilinear displacement and temperature (CPE4RT) quadrilateral elements for the deformations occurring during the burnishing process. The computational domain of the workpiece was a 20 mm × 4 mm rectangular area and initially meshed with 8000 isoparametric quadrilateral elements. A finer mesh was maintained in the region of large deformations near the tool by defining a high mesh density window to cover the burnished surface (18 mm × 1.5 mm) as shown in Figure 6.1 marked as “detail area”. The smallest element dimension on the workpiece was about 15 μm. The workpiece was assumed to be a rigid visco-plastic material and the elastic portion was neglected. The tool was meshed with 3000 elements and assumed to be rigid but heat conducting. Because there are few FEM simulations of burnishing and not much data on the used alloy in the ranges needed, many of the parameters utilized herein must be evaluated

from the data reported earlier in this dissertation. Our objective in this chapter is to create a model of the entire burnishing process with reasonable values of needed parameters.

### **6.3 Boundary conditions**

The boundary conditions applied on the FE model are also shown in Figure 6.1. The tool was set to be rigid body and fixed in all directions. The tool initially contacted the workpiece at a location of 1 mm from the right edge of the detail area. The bottom of the workpiece was first fixed in the horizontal direction and then allowed to move vertically as the roller tool penetrated into the workpiece (Figure 6.2 (a)). The workpiece stopped moving vertically when the predetermined DoP value was reached (Figure 6.2 (b)), and the bottom of the workpiece was then fixed in the vertical direction and allowed to move horizontally at the velocity that equaled to the burnishing speed (Figure 6.2 (c)). The roller tool started to slide against the workpiece surface, and finally stopped at another location of 1 mm from the left edge of the detail area. The left and right edges of the workpiece were free ( $\sigma_{xx} = 0$ ,  $\sigma_{xy} = 0$ ). The tool's total travel distance was 16 mm within the detail area. The top of the workpiece was free except the tool-workpiece interface area. The inter-object boundary conditions between the workpiece and the tool were set to be shear friction type and heat conducting. The friction coefficient and the heat transfer coefficient values used between the workpiece and the tool will be discussed in the later sections in detail.

For the thermal analysis, the temperatures at the bottom and left sides of the workpiece as well as the top side of the tool were set to 20 °C. The top and right sides of the workpiece, as well as the bottom part of the burnishing tool (shown as red lines in

Figure 6.1) were allowed to exchange heat with the environment; the convection coefficient was  $0.02 \text{ kW}/(\text{m}^2\text{K})$ , which is the value for free air convection in DEFORM-2D. In order to simulate the effect of cryogenic cooling, an environmental window for heat exchange was defined as shown in Figure 6.1 with the size of  $3 \text{ mm} \times 1 \text{ mm}$ . The window was fixed in its position and did not move with the workpiece. It can be considered to be attached to the tool. The local environment temperature was set to be  $-184 \text{ }^\circ\text{C}$  for mimicking the liquid nitrogen temperature. The local convection coefficient within the window domain can be adjusted to simulate the cryogenic cooling effect, the finding of whose value will be discussed in the following sections.

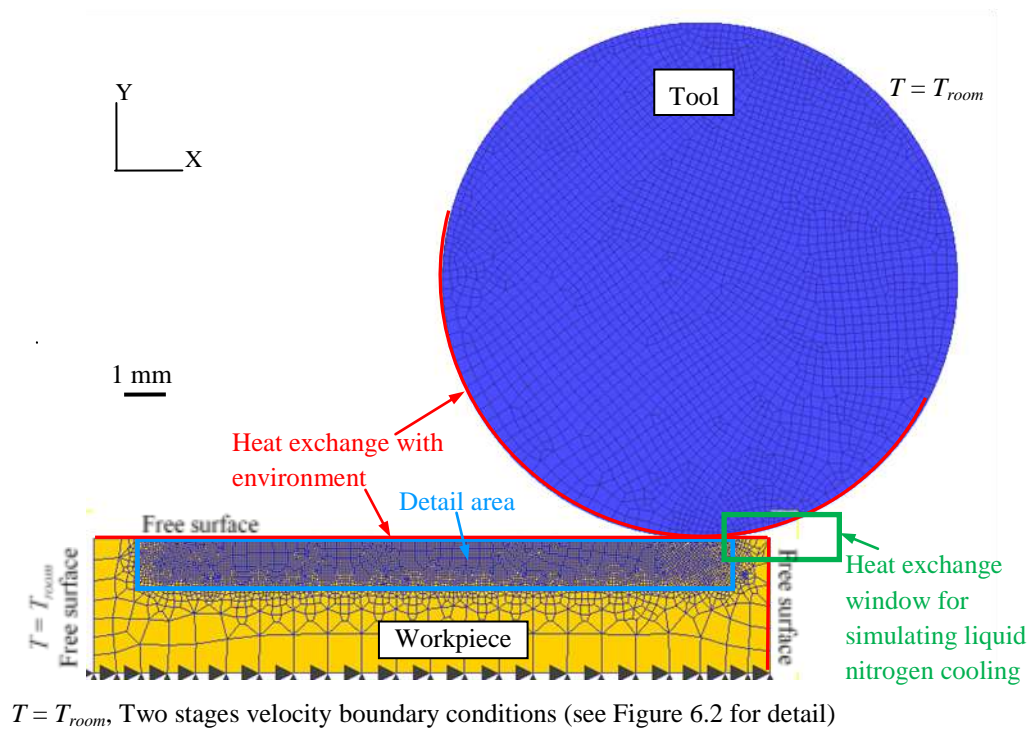
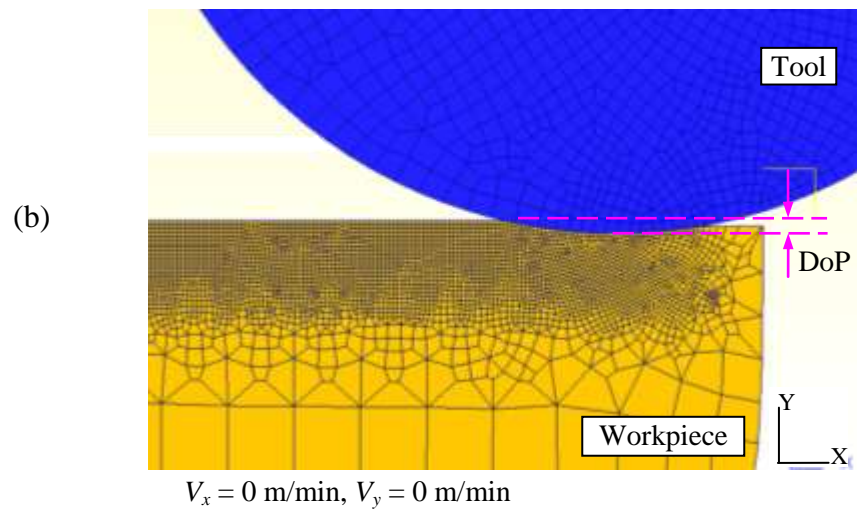
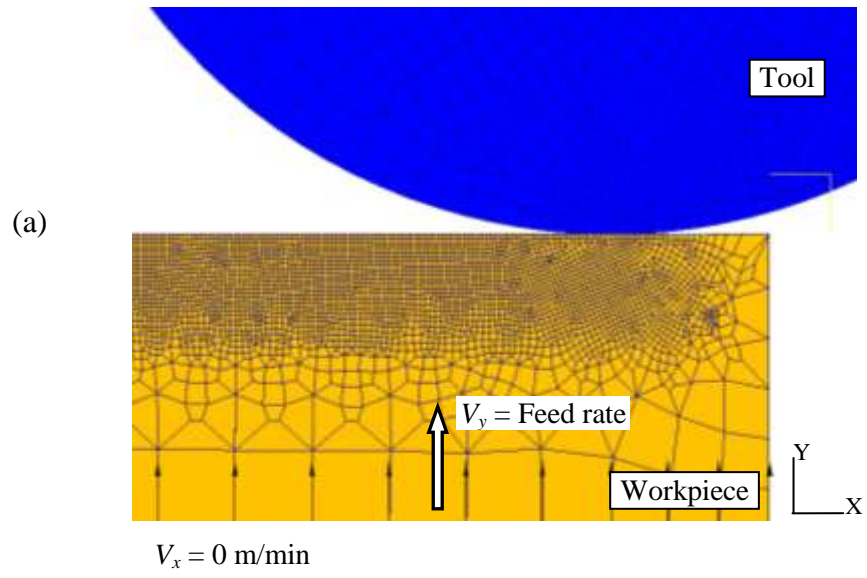


Figure 6.1: Computational domain of interest for the 2-D burnishing process and boundary conditions applied



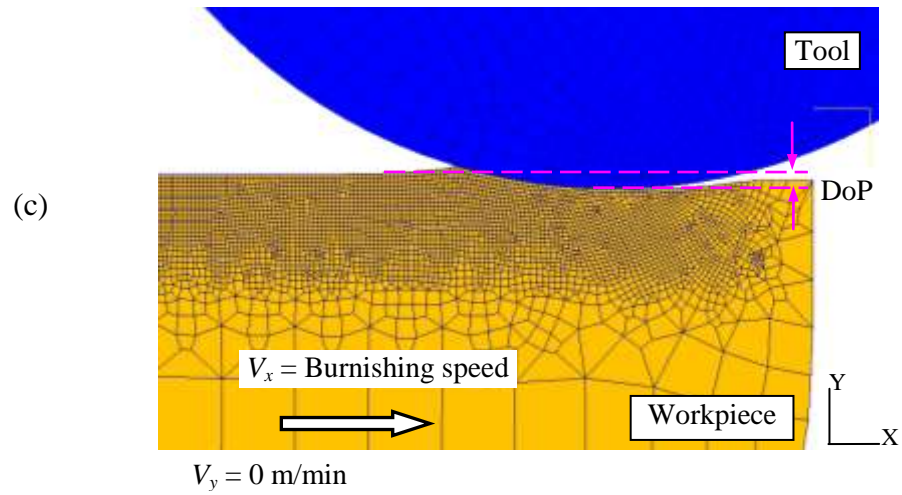


Figure 6.2: Steps for the proposed 2-D burnishing simulation: (a) roller tool starts to penetrate into workpiece, (b) roller tool reaches the predetermined DoP, (c) roller tool slides against the surface under the predetermined burnishing speed

#### 6.4 Material properties

The thermal and mechanical properties of the *Co-Cr-Mo* alloy used in the FE model are listed in Table 6.1. The default thermal and mechanical properties for the simulated uncoated carbide tool in DEFORM-2D was used and also listed in Table 6.1.



Table 6.1: Thermal and mechanical properties of uncoated carbide and BioDur CCM alloy (CRS Holdings Inc. 2007)

Material	Uncoated carbide (Tool)	BioDur <sup>®</sup> Carpenter CCM <sup>®</sup> (Workpiece)
Young's Modulus	N/A	241.3 GPa
Poisson's Ratio	0.23	0.3
Modulus of Rigidity		92.4 GPa
Density		8.276 mg/mm <sup>3</sup>
Thermal Conductivity	82.24 W/(m K)	0.0191 $T+12.9$ (N/sec °C)
Specific heat capacity	5.79 J/(kg K)	0.0017 $T+3.8$ (N/mm <sup>2</sup> °C)
Thermal expansion coefficient	$6.3 \times 10^{-6} \text{ K}^{-1}$	0.0003 $T+1.3$ ( $10^{-5}/^\circ\text{C}$ )

In order to relieve residual stresses during previous manufacturing steps, BioDur Carpenter CCM alloy is typically annealed at 1093 to 1121 °C for 1 to 2 hours followed by air cooling. Larger grain size will be created through the use of higher annealing temperatures with corresponding reductions in annealed hardness (CRS Holdings Inc. 2007). In the current study, the *Co-Cr-Mo* alloys were fully annealed at 1100 °C for 1.5 hours followed by air cooling. The measured hardness value for the annealed sample was around 30 HRC, as shown in Table 6.2 the annealed *Co-Cr-Mo* alloy with an average hardness of 30 HRC possesses a yield strength of about 585 MPa, which was used as the starting value for calibrating the constant *A* in the modified Johnson-Cook (J-C) constitutive model which will be described in the next section.

Table 6.2: Typical room temperature mechanical properties (CRS Holdings Inc. 2007)

Condition	0.2% Yield Strength		Ultimate Tensile Strength		% Elongation in 4D	% Reduction of Area	HRC Hardness
	ksi	MPa	ksi	MPa			
Annealed	85	585	150	1035	25	23	30
Warm Worked	135	930	190	1310	26	23	40
Hot Worked	110	760	160	1100	25	23	33

As shown in Figure 6.3, the proposed FE model comprised two predicting steps. In the first step, the burnishing conditions in terms of roller size, cooling method, burnishing speed and depth of penetration (DoP) were used as the input parameters for the model. The model was calibrated (parameters determined) by comparing the prediction results with the force and temperature data obtained from experiments as reported earlier in this dissertation. The strain, strain-rate and temperature values from the first step in Figure 6.3 were collected and used as the inputs for the second step of the model: which was the grain size prediction.

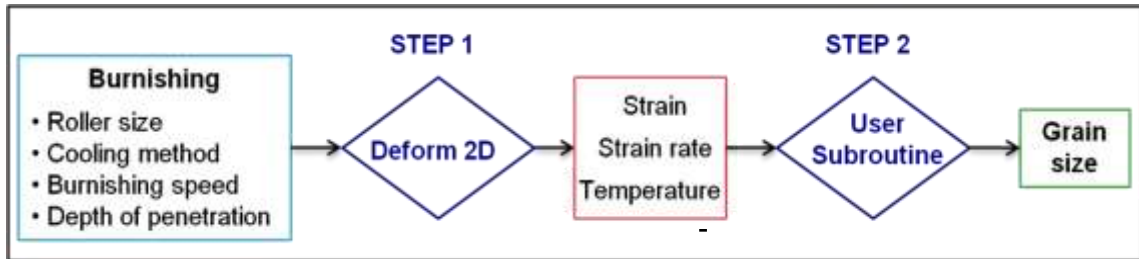


Figure 6.3: Burnishing simulation flow

## 6.5 Material flow stress development incorporating DRX effects

In any FEM analysis, accurate and robust flow stress models are considered to be highly necessary to represent work material constitutive behavior under high strain/strain-rate deformation conditions. During inhomogeneous plastic deformation, strain energy is stored in the deformed volume as residual stresses. The restoration process that occurs

dynamically (i.e., during plastic straining) tends to compromise the effect of work hardening. In dynamic recovery (DRV), the generation and accumulation of dislocation due to work hardening is continuously offset by dislocation rearrangement and annihilation, a general flow curve of this type behavior is depicted in Figure 6.4 (marked DRV). The flow stress at large strain reaches a saturated ( $\sigma_{sat}$ ) value which results from a balance between work softening and hardening. When DRX is the dominant restoration process, the flow curve (marked DRX in Figure 6.4) initially rises as a continued result of work hardening and recovery process eventually reaching a peak value ( $\sigma_p$ ). It has been shown that a critical value of strain ( $\epsilon_{cr}$ ) is required for the initiation of the DRX process in the grain boundaries, which initiates the DRX process and this occurs before the strain ( $\epsilon_p$ ) at peak stress ( $\sigma_p$ ) (Dehghan-Manshadi et al. 2008). The dislocations then congregate very near the thin grain boundaries. Subsequently, the flow stress drops with increasing straining to a steady state value ( $\sigma_{ss}$ ) at large strains. The flow stress softening beyond peak stress reflects the reduction of dislocations density in the grain interior and adding them to the grain boundaries (Sarkar et al. 2011). In general the strain required for reaching the steady state ( $\sigma_{ss}$ ) in DRV is much greater than  $\epsilon_{cr}$  for DRX initiation. It is also reported that, compared to the slow processing methods, the high flow stress during machining of steels experiences a sudden drop as the material element exits the tool contact after the actual strain exceeds the critical value, which is attributed to the very high strain-rates that occurs in machining (Umbrello 2004).

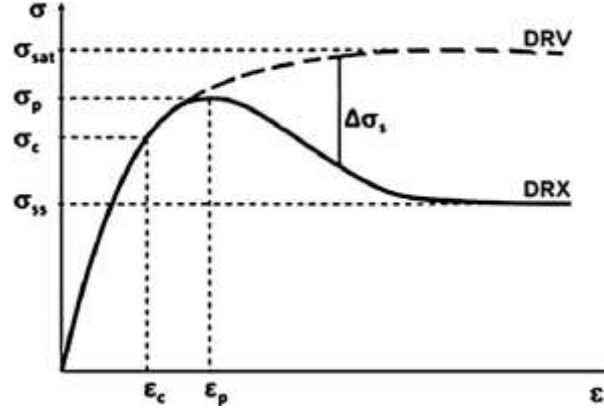


Figure 6.4: Schematic representation of flow curves during DRV and DRX defining various stress and strain parameters (Sarkar et al. 2011)

The modified Johnson-Cook (J-C) constitutive model proposed by Ee et al. (2005) describes the flow stress of a material incorporating the effects of strain, strain-rate, and temperature (Equation 6.1) was used for describing the flow stress behavior of the DRV process (expected stress-strain behavior if recovery were the only operative restoration processes) in the current study:

$$\sigma_{DRV} = [A + B \cdot (\varepsilon)^n] \left\{ 1 + C \cdot \ln \left[ \frac{\dot{\varepsilon}}{\dot{\varepsilon}_0} + 0.0001 \cdot \exp \left( -100 \cdot \frac{\dot{\varepsilon}}{\dot{\varepsilon}_0} \right) \right] \right\} \left[ 1 - \left( \frac{T - T_{ref}}{T_{melt} - T_{ref}} \right)^m \right] \quad (6.1)$$

In the modified J-C model,  $\sigma_{DRV}$  is the equivalent DRV flow stress; the constant  $A$  is the initial yield strength of the material at room temperature and a reference strain-rate of  $1 \text{ s}^{-1}$  (MPa);  $B$  is the hardening modulus (MPa);  $C$  is the strain-rate sensitivity coefficient;  $n$  is the hardening coefficient and  $m$  is the thermal softening exponent;  $\varepsilon$  represents the plastic equivalent strain. The effective strain-rate  $\dot{\varepsilon}$  ( $\text{s}^{-1}$ ) is normalized with a reference strain-rate  $\dot{\varepsilon}_0$ .  $T$  is the temperature of the work material ( $^{\circ}\text{C}$ );  $T_m$  is the melting temperature of the work material ( $1350 \text{ }^{\circ}\text{C}$ ) and  $T_{ref}$  is the initial reference temperature

(20 °C). The temperature term in the J-C model reduces the flow stress to zero at the melting temperature of the work material, leaving the constitutive model with no temperature effect ( $m = 1$ ), thus, it is not recommended to use this formula when the temperature is close to the melting temperature. The maximum temperature from burnishing experiments was less than 800 °C, which is much less than the 1350 °C melting temperature of *Co-Cr-Mo* alloy. In this study, burnishing of *Co-Cr-Mo* alloy under dry and cryogenic conditions was investigated and the J-C material model was further modified to incorporate the DRX effect to do so. Predicting the process of manufacturing *Co-Cr-Mo* alloys under very high strain and strain-rate conditions is a novel topic, and there is almost no prior research conducted on this area. Thus, there is no directly available literature providing the material constants in the J-C constitutive equation of the *Co-Cr-Mo* alloy for high strain/strain-rate manufacturing processes.

DRX is considered to be an important restoration mechanism during thermo-mechanical processing of a wide variety of materials (Belyakov et al. 2003; Hatherly et al. 1986; Le Gall and Jonas 1999). It is the grain size change mechanism. Extensive research work has been carried out during the past decades not only for academic interest but also for the immense influence in industrial processing. For example, in hot working processes such as rolling, extrusion and swaging, DRX offers powerful means for microstructure control and provides a suitable microstructure for the secondary processing which may involve cold working, annealing and phase transformation. The details of DRX characteristics affect the overall microstructural development brought about by interaction of both static and dynamic structural changes and hence control the final mechanical properties of the product (Hameda and Blaz 1998; Yamagata et al.

2001). Among the dynamic events during processing, work hardening and dynamic recovery always occur within the deforming workpiece. In some materials, if the amount of total existing localized dislocations (strain) exceeds a critical value (critical strain), DRX occurs in the deforming workpiece which leads to the drastic changes of microstructure. When it occurs, this is one of the most important microstructural evolution processes.

For improved accuracy of the model, the flow stress was therefore modified to include the DRX softening effect within the DEFORM program, because it can greatly change the material behavior during deformation processing as well as the subsequent properties. Grain size is used as the parameter that quantifies the DRX process. Following (Jonas et al. 2009), this was carried out by separating the flow stress into three stages. Before reaching the peak strain  $\varepsilon_p$ , the material flow stress followed a further modified J-C constitutive model by multiplying an extra term proposed by Subramanian et al. (2002):

$$\sigma = \sigma_{DRV} \cdot \left\{ D + (1 - D) \left( \tanh \left( \frac{1}{(\varepsilon + p)^r} \right) \right)^s \right\} \quad (6.2)$$

where  $\sigma$  is the equivalent flow stress, the parameters  $D$ ,  $p$ ,  $r$ ,  $s$  were derived from the experimental data given by Chiba et al. (2009b) and Yamanaka et al. (2009), their values were found to be  $D = 0.1$ ,  $p = 0$ ,  $r = 1$ ,  $s = 5$ .

When the peak strain value ( $\varepsilon_p$ ) is reached, the flow stress (Equation (6.2)) was replaced by a newly developed model based on the Avrami relation. The peak strain ( $\varepsilon_p$ ) is determined when  $d\sigma/d\varepsilon = 0$ . The Avrami relation (Avrami 1939; Johnson and Mehl 1939), originally developed to study static recrystallization (SRX) in metallic systems, is being increasingly adopted by researchers to model the progress of DRX in a wide

variety of metals and alloys (El Wahabi et al. 2005; Jonas et al. 2009; Queleñec et al. 2011; Sarkar et al. 2011; Zahiri et al. 2005). The application of the Avrami relation to DRX kinetics was originally proposed as a so-called flow curve analysis method by Medina and Hernandez (1996) and modified recently by Jonas et al. (2009) using a different functional form to evaluate the work hardening characteristics. The idea of using the Avrami relation for DRX stems from the physically observed similarities between SRX and DRX. The model is expressed as:

$$\sigma_{DRX} = \sigma_{DRV} - X \cdot (\sigma_{sat} - \sigma_{ss}) \quad (6.3)$$

$$X = 1 - \exp(-k(\varepsilon - \varepsilon_{cr})^t) = (\sigma_{DRV} - \sigma_{DRX})/(\sigma_{sat} - \sigma_{ss}) \quad (6.4)$$

$$\sigma_{ss} = constant \cdot \sigma_p \quad (6.5)$$

where  $\sigma_{DRX}$  is the DRX flow stress;  $\sigma_{DRV}$  is the DRV stress predicted by the J-C model;  $X$  represents the volume fraction of the recrystallized grains;  $\sigma_{sat}$  is the saturated stress during DRV and determined when  $d\sigma_{DRV}/d\varepsilon = 0$ ;  $\sigma_p$  is the peak stress and determined when the peak strain  $\varepsilon_p$  is reached;  $\sigma_{ss}$  is the steady state stress when DRX is complete. The parameters  $k$  and  $t$  are material constants. When DRX is finished, the flow stress will reach its steady state (less than  $\sigma_p$ ) and will not be changed by further straining. Sometimes the steady state is only reached at very large strains. The steady state stress  $\sigma_{ss}$  is found to be linearly proportional to  $\sigma_p$  for cobalt as shown in Equation (6.5) (Sarkar et al. 2011), similar relations have been found in many other materials and the value of the constant typical ranges from 0.7 to 0.95 (Dehghan-Manshadi and Hodgson 2007; Jonas et al. 2009; Ryan and Mcqueen 1990). This constant is determined by experiments. Unfortunately, there is no flow stress data available for the *Co-Cr-Mo* alloy under high strain (4-5) and strain-rate ( $10^4$ - $10^5$  s<sup>-1</sup>) conditions which are very common in machining

and burnishing. The predicted strain and strain-rate results from the current study will be discussed in the later part of this chapter. Thus, the constants in Equation (6.5) reflecting the reduction of flow stress due to DRX softening can only be approximated. Figure 6.5 shows a borrowed example of the influences of strain-rate and temperature on the flow stress behavior of *Co-28Cr-6Mo-0.16N* alloy (Chiba et al. 2009a) which is very similar to the currently studied BioDur CCM alloy. The stress-strain data was extracted from the plots in Figure 6.5, an average reduction value of 0.8 was found by analyzing the limited data points, which fell into the range found by other researchers (0.7 to 0.95) and was used as the constant value in Equation (6.5) in the current study. Very recently, it is reported that the steady stress ( $\sigma_{ss}$ ) was approximately equal to the critical stress ( $\sigma_c$ ) during the simulation of high temperature austenite flow curves based on the Avrami kinetics of DRX (Quelellennec et al. 2011). However, this study was done for slow hot compression tests; the strain-rates involved ( $\leq 0.5 \text{ s}^{-1}$ ) were much lower than the ones in burnishing ( $10^4$ - $10^5 \text{ s}^{-1}$ ), and the testing temperatures were high ( $\geq 1000 \text{ }^\circ\text{C}$ ). The findings from this study should be carefully evaluated as a potential approach for determining the steady state stresses in the future.



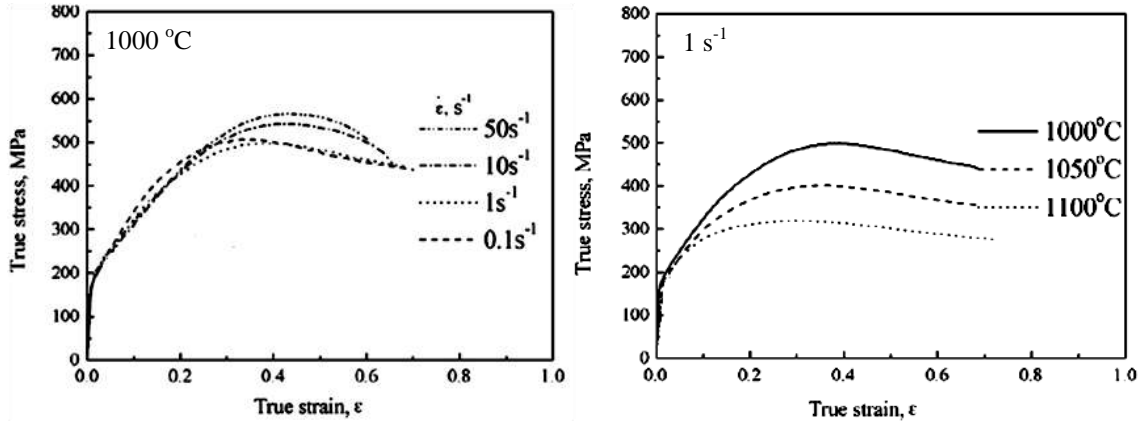


Figure 6.5: True stress-true strain curves of *Co-28Cr-6Mo-0.16N* (adapted) (Chiba et al. 2009a)

In the present work, we demonstrate applicability of this model to study the progress of DRX in the *Co-Cr-Mo* alloy during burnishing. This will be done by comparing previously published hot compression flow behavior data (Chiba et al. 2009a; Yamanaka et al. 2009) with the predictions from the new model (Figure 6.6). However, it should be noted that due to the annealing of the materials before burnishing, the material constants used for FE model were different from the values used for evaluating the applicability of this proposed methodology. The material constants for the FE model were adjusted and calibrated by comparing with the collected experimental data on force and temperature during burnishing.

As shown in Figure 6.6, the testing temperatures used in these compression tests were very close to the annealing temperature (1100 °C) used in the current study, which is likely to be the reason for the  $A$  values (500 MPa) in the J-C material model obtained from the compression tests similar to the proposed yield stress (585 MPa) after annealing (Table 6.2). Thus, the  $A$  value in the material model (Equation (6.1)) was set to 500 MPa, the strain-rate sensitivity coefficient  $C$  was 0.054 and the hardening coefficient  $n$  was 0.5.

The material constants in Equation (6.4) were found to be  $k = -1$  and  $t = 4$ .

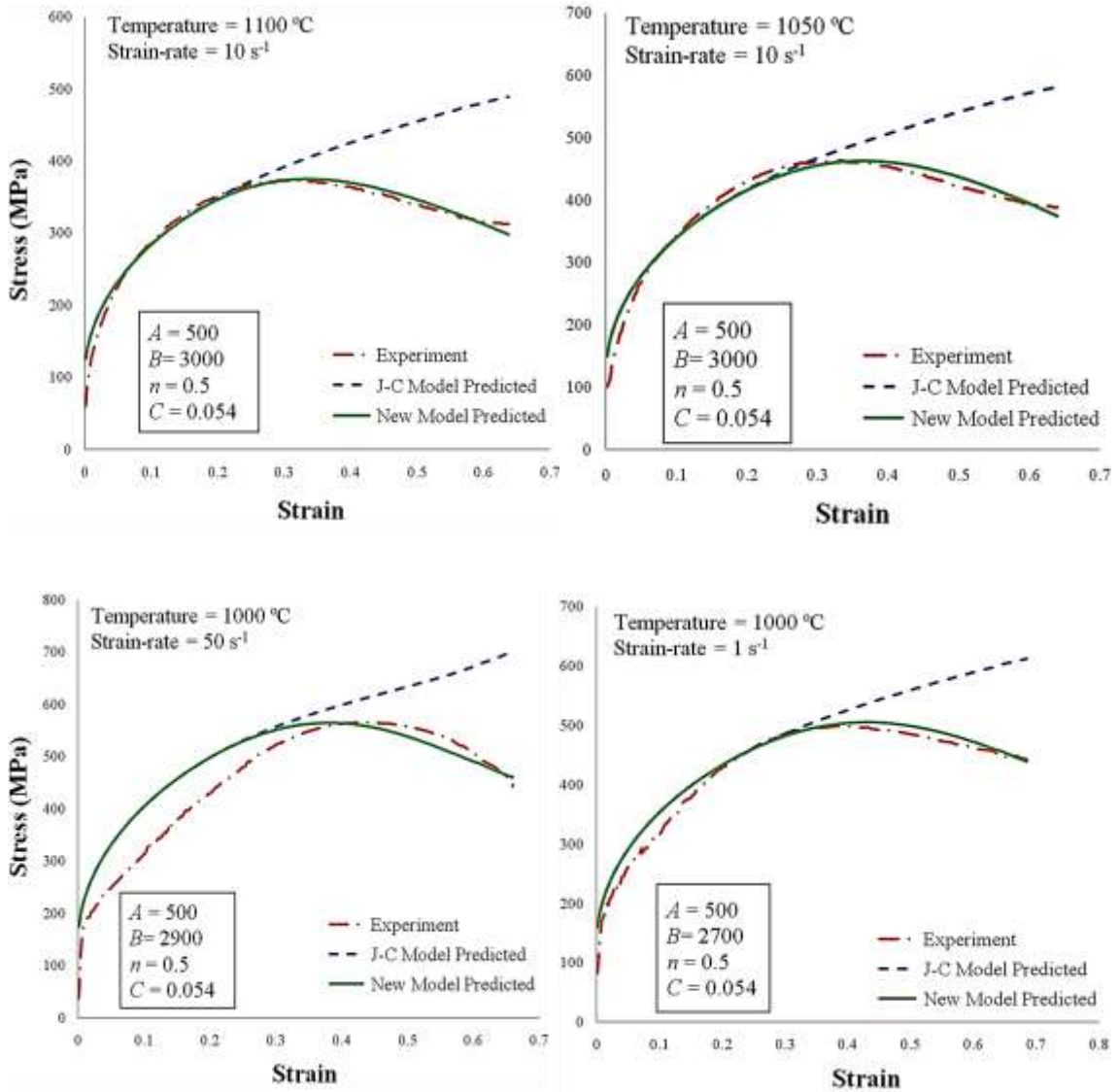


Figure 6.6: Comparison between measured and predicted stress-strain curves for the *Co-Cr-Mo* alloy, experimental data from (Chiba et al. 2009a; Yamanaka et al. 2009)

The grain sizes obtained from the Zener-Holloman equation (Equations (6.6)-(6.8) below) was updated in this model during each iteration, which is demonstrated in the following section. This iterative process was continued during the whole simulation for improved accuracy of grain size prediction. This permits one to consider "unstable

materials" which as noted earlier are not commonly done in FEM programs. The details of the changing grain size model are given in the section 6.9.

## 6.6 User subroutine for predicting grain size

In designing the simulation processing steps, an accurate understanding of the DRX characteristics is of paramount importance. Research has been reported in the hot rolling process by Fruehan (1998). Strain, strain-rate and temperature are the most critical factors for the occurrence of DRX; many attempts have been made to simulate the microstructural evolution and grain size changes caused by DRX (Busso et al. 1998; Sellars and Zhu 2000) in tension or compression tests where the strains are nearly uniform. We now propose to extend these ideas to the complex deformation field created when the specimens are burnished as well as being cooled differently.

The grain size prediction was incorporated into the proposed FEM-based thermo-mechanical burnishing model as indicated in Figure 6.3. Many studies have shown that one can predict the grain sizes after complete DRX by using the Zener-Holloman ( $Z$ ) parameter (Shekhar et al. 2012; Torrente et al. 2011; Yamanaka et al. 2009):

$$Z = \dot{\epsilon} \cdot \exp(Q/RT) \quad (6.6)$$

where  $Q$  is the activation energy of lattice diffusion of the material,  $R$  is the gas constant,  $\dot{\epsilon}$  is the effective strain-rate and  $T$  is the local temperature. The  $Z$  parameter combines the two effects of temperature and strain-rate into a single parameter which has been shown to be successful in correlating grain size data obtained for drastically different conditions.

The critical strain ( $\epsilon_{cr}$ ) for the onset of DRX was determined by the material and expressed as a function of the  $Z$  value. This data is used in simulated burnishing by first

obtaining values of  $Z$  from the FEM calculations. DRX can be triggered only when the strain was larger than this critical strain. The relationship between  $\varepsilon_{cr}$  and  $Z$  shown in Figure 6.7 was derived by the author using the experimental data from series studies of Chiba group on *Co-Cr-Mo* alloys (Chiba et al. 2009a; Kurosu et al. 2010b; Yamanaka et al. 2009). The critical strains were often found to be 80% of the peak strain values. The  $Z$  value corresponding to each critical strain was calculated by using Equation (6.6) and the given strain-rate and temperature in the Chiba group publications. The used critical strain for the *Co-Cr-Mo* alloy is expressed in Equation (6.7) as:

$$\varepsilon_{cr} = a \cdot \ln(Z) - b \quad (6.7)$$

where  $Z$  is the Zener-Hollomon parameter;  $a$  and  $b$  are the material constants and found to be  $a = 0.0167$  and  $b = 0.652$  for the *Co-Cr-Mo* alloy from the above mentioned experimental data from the Chiba group.

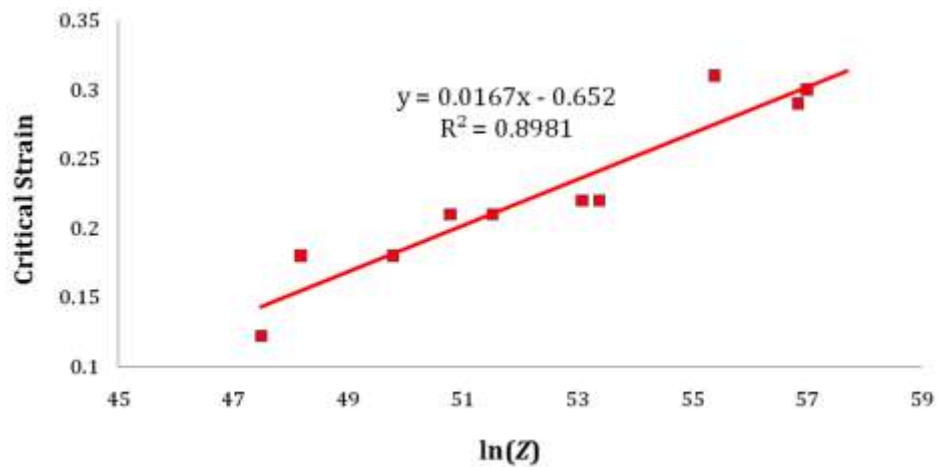


Figure 6.7: Critical strain of *Co-Cr-Mo* alloy as a function of  $Z$  values

Once DRX is completed, the recrystallized grain size  $d$  can be calculated as:

$$d = d_0 \cdot \alpha \cdot (Z^{m'}) \quad (6.8)$$

where  $d_0$  is the initial grain size in microns, an average measured grain size of 80  $\mu\text{m}$  was used in the current model for *Co-Cr-Mo* alloy. The parameters  $\alpha$  and  $m'$  are the material constants, which need to be obtained for good grain size prediction. Yanagimoto et al. (1998) and Di Renzo (2010) have shown that Equation (6.8) represents experimental data on steels. A new grain size after DRX was calculated using Equation (6.8). In the user subroutine, this calculation was carried out continuously for every element in the workpiece for each step. This methodology has been successfully used by Yanagimoto et al. (1998) for predicting the microstructure changes during hot forming of *50CrV4* steel. The effectiveness of this methodology has recently been demonstrated by one of our collaborators in the University of Calabria to predict the grain size changes during machining of *AISI 52100* steel (Di Renzo 2010). It should be noted that, due to the high strain and strain-rate involved during burnishing, DRX occurs very rapidly and is assumed to be fully complete, in addition, the grains are assumed to be fully recrystallized as long as the DRX process starts (the strain exceeds the critical strain). The partial recrystallization due to incomplete DRX is not taken into consideration in the user subroutine for predicting grain size.

It can be observed from Equation (6.8) that in addition to the  $Z$  value, the DRXed grain size is also influenced by the material constants  $\alpha$  and  $m'$ . For accurate grain size prediction, these two constants were obtained from curve fitting Equation 6.8 to the data in Figure 3.16.

## 6.7 Variable friction modeling

The tool-chip/workpiece friction has long been recognized as an unsolved bottleneck problem in fundamental machining research. Much research has shown that metallic materials with nano-/ultrafine microstructure often possess appealing friction properties due to the large volume fraction of hard grain boundaries within the material structures after DRX has occurred (Dao et al. 2007; Shi and Han 2008). For predicting the effect of DRX during the burnishing process, a friction model with a friction coefficient value that changes due to DRX was developed. As shown in Figure 6.8, before the strain reached the critical strain  $\epsilon_{cr}$ , a friction coefficient value of 0.4 was used (this was described and the calibration process is shown in section 6.8). The choice of the initial friction coefficient value 0.4 was supported by a study on friction properties of cobalt-base alloys (Buckley 1968). After the critical strain was reached, DRX occurred, which led to a significant drop of the friction coefficient due to the formation of refined grains on the burnished surface. Unfortunately, there is no friction data directly available in the literature for *Co-Cr-Mo* alloy with nano-/ultra-fine microstructure. However, it is reported that the friction coefficient of *Co-Cr-Mo* alloy in the steady state wear regime was less than 0.1 during pin-on-ball wear tests (Wimmer et al. 2001), which is often associated with the formation of a nanostructured surface layer during the wear process (Buscher and Fischer 2005; Wimmer et al. 2003). Thus, a very small value,  $\mu = 0.05$ , was chosen for the friction coefficient after DRX for predicting the improved tribological behavior of the nano-/ultrafine-structured surface layer induced by burnishing process.

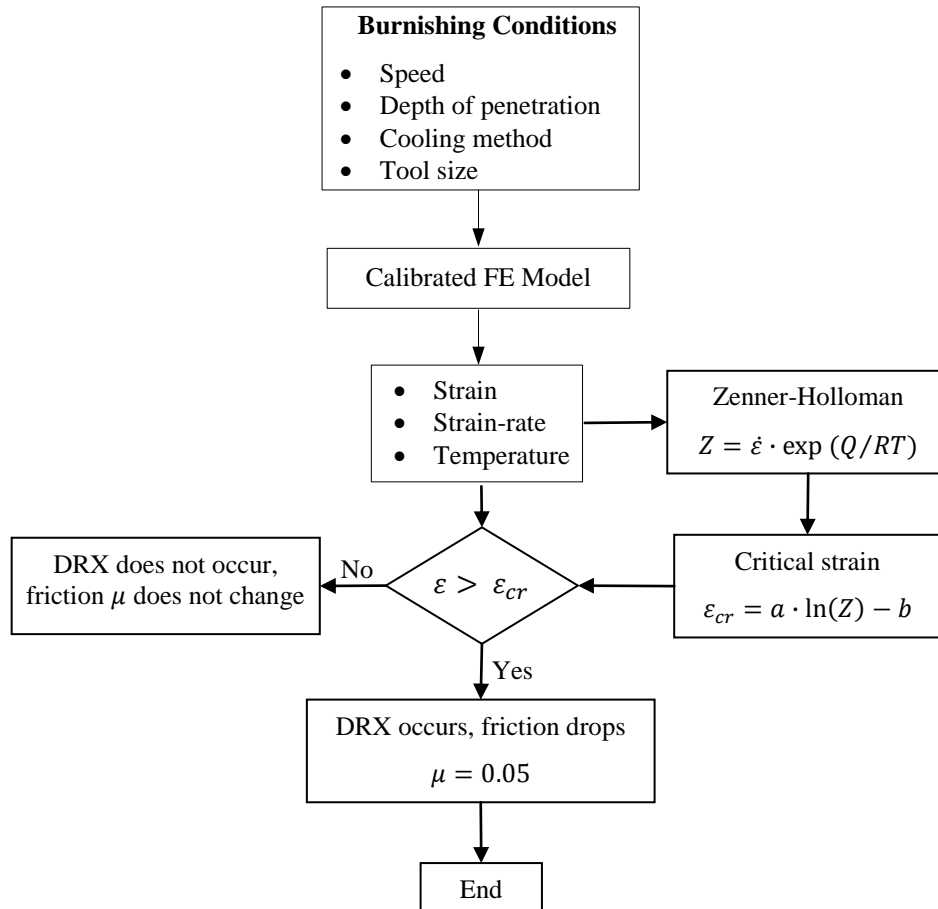


Figure 6.8: Variable friction model due to DRX

## 6.8 Calibration and validation of burnishing model for force and temperature

The calibration procedure for step 1 of the burnishing model is shown in Figure 6.9. The values of J-C constants  $A$  and  $B$  as well as the one used for the friction coefficient  $\mu$  were determined through an iterative calibration process using the experimental data as described in Section 6.3. All were based on the experimental burnishing radial force data from dry burnishing under the conditions of DoP = 0.254 mm, burnishing speed = 100 m/min, tool diameter = 14.3 mm.

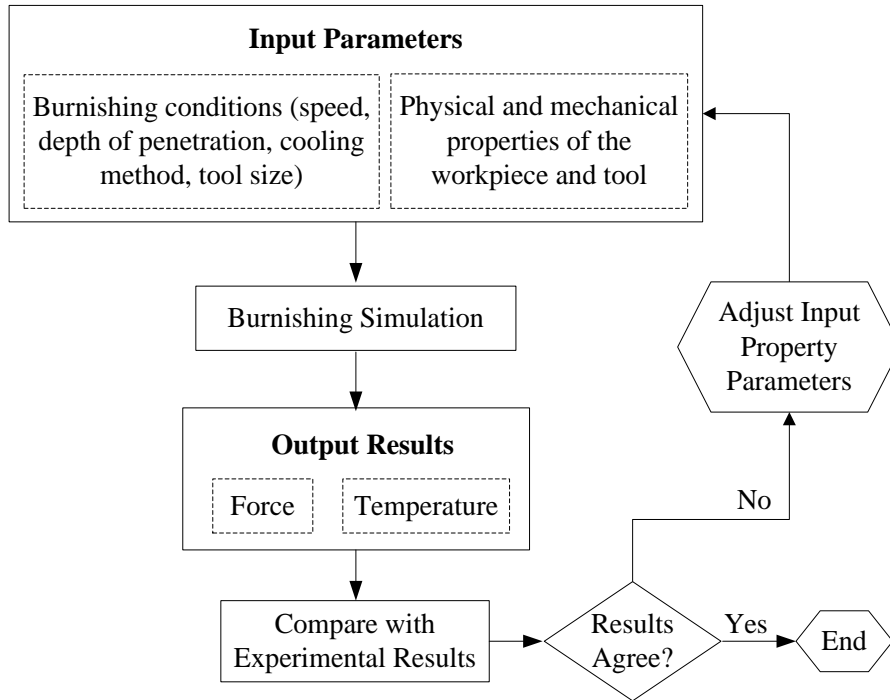


Figure 6.9: Calibration procedure for burnishing model

Figure 6.10 shows the effect of variation of the J-C constants  $A$  and  $B$  on radial force predictions as determined by the FE model. It was found that agreement in radial burnishing force was achieved (2.2% difference between the experiment and predicted values) when the values of  $A$  and  $B$  were taken to be 500 and 100, respectively. As mentioned in Chapter 4, the phase transformation of this *Co-Cr-Mo* alloy is very complicated. The main effect of this metastable material behavior (mainly DRX at low temperatures) in the FEM modeling of the burnishing process is its role in determining the proper value of the parameter  $B$  in the J-C material model to be used. For example, this variation in  $B$  subsequently affects the value of the "critical strain" where DRX begins. Since part of the purpose of this project is to determine the grain size of the burnished surface layer, the proposed methodology is less accurate than one would like to achieve. At this time, we consider it more important to develop an inclusive and robust



model for the burnishing process rather than to generate precise knowledge about the values of  $B$ . It is our current view, that  $B$  is not a constant but, in effect, varies with material "internal variables" such as grain size or stacking fault energy (related to twinning) value. The value of  $B$  used in the FE simulation is a forced number in order to approximate the measured forces.

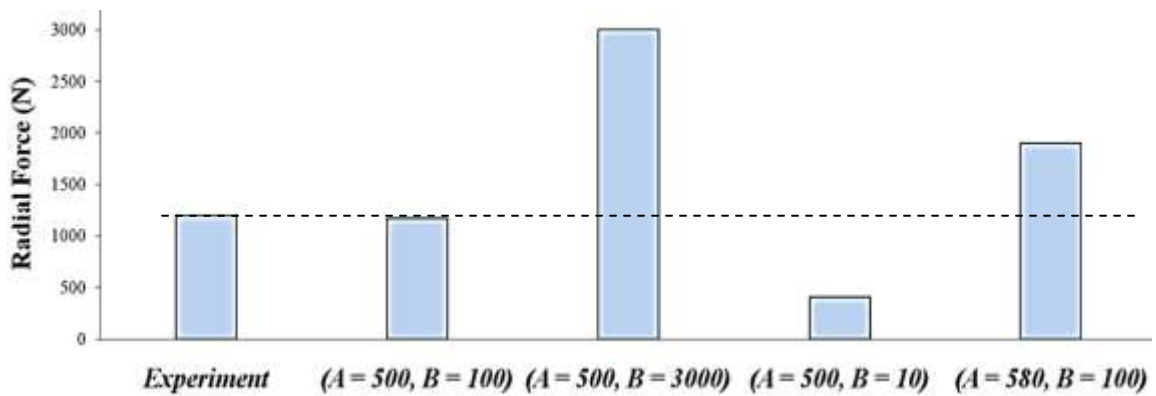


Figure 6.10: Examples of the effect of J-C constants  $A$  and  $B$  on radial force predictions (Dry, DoP = 0.254 mm, burnishing speed = 100 m/min, tool diameter = 14.3 mm)

The same calibration process was used for finding a reasonable friction coefficient  $\mu$  by comparing force predictions with corresponding measured data. Figure 6.11 shows the effect of friction coefficient  $\mu$  on radial forces predicted by the FE model using  $A = 500$  MPa,  $B = 100$  MPa. It was reported that the value of  $\mu$  is an influencing factor for the cutting forces in machining (Umbrello 2008). In the current study, increasing the  $\mu$  value from 0.2 to 0.8 can lead to an increase of the radical force by a factor of 1.3. A decent agreement between the predicted force and the experimental value was found when  $\mu$  was set to be 0.4 before the strain exceeds the critical strain value.

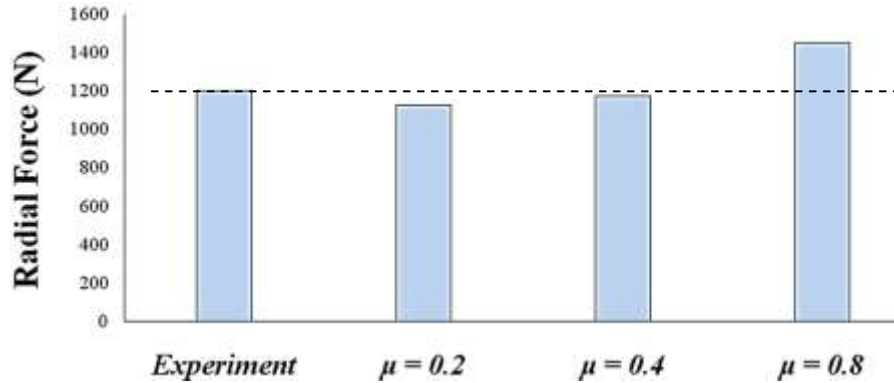


Figure 6.11: The effect of friction coefficient  $\mu$  on the calculated radial force predictions (Dry, DoP = 0.254 mm, burnishing speed = 100 m/min, tool diameter = 14.3 mm)

Temperature is an important factor influencing the material behavior during burnishing process as has been proved by the experimental observations reported in previous chapters. As described in Chapter 3, due to the design of the burnishing tool, the experimental tool-workpiece temperature cannot be captured by the used infrared camera. For dry burnishing, the measured temperature on the workpiece around the tool-workpiece interface was considered as the maximum workpiece temperature and was used for the calibration process. The predicted maximum temperature can no longer be used as a comparison parameter. Figure 6.12 shows the predicted temperature distribution on the workpiece for dry burnishing with 0.08 mm DoP and 100 m/min burnishing speed. As shown in Figure 6.12, the temperature right behind the tool-workpiece interface (where the arrow is pointing) was defined as the exit temperature and used for calibration and validation purposes.

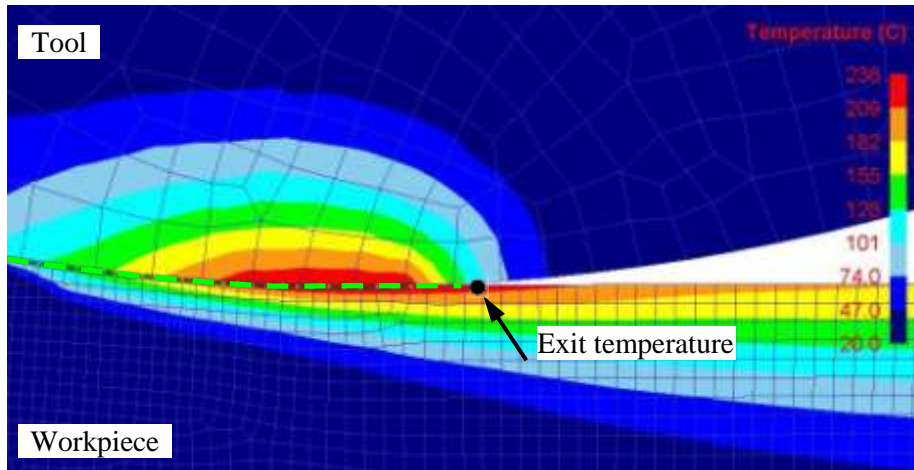


Figure 6.12: Tool-workpiece interface and the exit temperature position (Dry, DoP = 0.08 mm, burnishing speed = 100 m/min, tool diameter = 14.3 mm)

The heat transfer coefficient at the tool-chip interface  $h_l$  was determined through an iterative process using the measured temperature data from dry burnishing experiment with DoP = 0.254 mm, burnishing speed = 100 m/min, tool diameter = 14.3 mm. As shown in Figure 6.13, when the  $h_l$  value was larger than 1000 kW/(m<sup>2</sup> K), the workpiece exit temperature did not change much with further increases of the  $h_l$  value. Large heat transfer coefficient values on the order 10<sup>3</sup> to 10<sup>4</sup> are commonly used for simulation of machining process (Filice et al. 2007; Umbrello et al. 2007); this is due to the fact that the simulation time (10<sup>-3</sup> s to 10<sup>-4</sup> s) is significantly shorter than the time for running a real experiment (10 s to 20 s). In order to reach the thermally stable status quickly during simulation, the heat transfer coefficient was often set to very large numbers. A good agreement between the predicted and measured temperature was achieved in dry burnishing when  $h_l = 10,000$  kW/(m<sup>2</sup> K) was used.

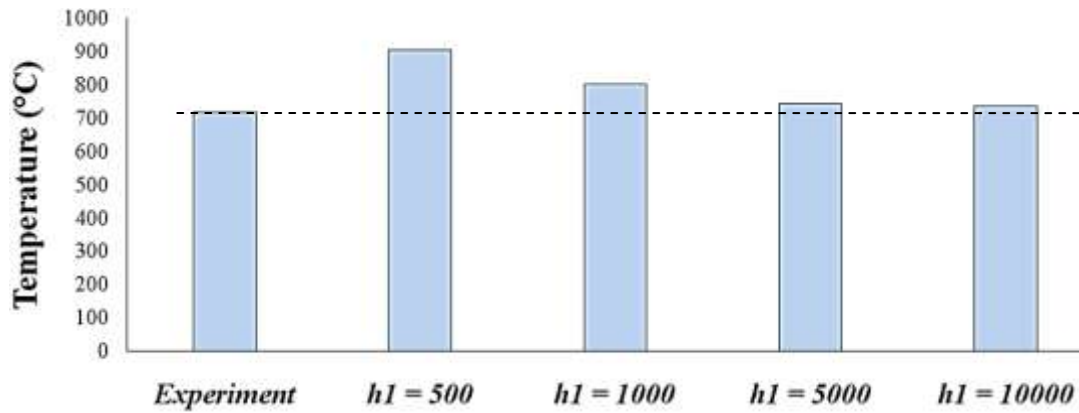


Figure 6.13: The effect of tool-workpiece heat transfer coefficient  $h_1$  on workpiece exit temperature predictions (Dry, DoP = 0.254 mm, burnishing speed = 100 m/min, tool diameter = 14.3 mm)

To simulate the cryogenic cooling effects, a local heat exchange window was used in DEFORM-2D to allow one to impose different thermal boundary conditions on a portion of the boundary as shown in Figure 6.1. The size of the used window is 3 mm  $\times$  1 mm which is assumed to be the liquid nitrogen (spray) influencing area. The convection coefficient  $h_2$  for the local heat exchange in the window domain was set to 10000 kW/(m<sup>2</sup>K), the same as the tool-workpiece heat exchange coefficient. This local heat exchange window only changes the convection coefficient within the area covered by the window. Figure 6.15 (a) shows the predicted temperature distributions during cryogenic burnishing with 0.254 mm DoP, 100 m/min burnishing speed and 14.3 mm tool diameter. Figure 6.15 (b) shows the predicted exit temperatures for both dry and cryogenic conditions. Good agreements between measured and predicted temperatures were achieved for dry burnishing with 0.15 mm DoP (5.3% higher) and cryogenic burnishing with 0.254 mm DoP (2.5% higher). However, the predicted exit temperature for dry burnishing under 0.08 mm DoP was 29.4% higher than the measured value.

This discrepancy is likely caused by the overlooking of the phase structure changes of the *Co-Cr-Mo* alloy due to the strain-induced fcc => hcp transformation during processing. The standard (stress = 0) phase diagram for the *Co-Cr-Mo* alloy is shown below:

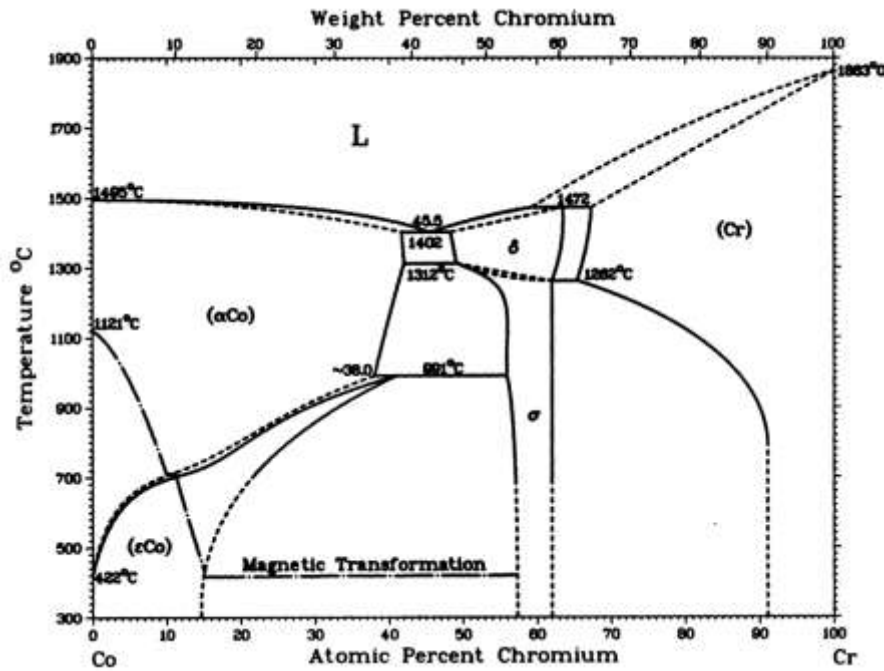


Figure 6.14: Equilibrium phase diagram of the binary *Co-Cr* system (ASM 1986)

It indicates that no phase transformation occurs at room temperature and zero stress conditions below 900 °C. However, when this material is deformed to large strains/stresses, the phase transformation picture is very complicated because of the nature of plastic deformations combined with phase changes. It is claimed by some authors that a phase transformation even occurs at room temperature. Ramesh and Melkote (2008) found that both the hydrostatic and deviatoric components of stress modified the standard phase transformation temperature dramatically in *AISI 52100* steel. Unfortunately, similar data is not available for the *Co-Cr-Mo* materials. Even worse, the data needed to determine these numbers does not exist (to our knowledge). The basic

reason for the lack of data in the literature appears to be the metastable material behavior that occurs in this cobalt alloy in which local microstructural parameter variations appreciably influences the transformation temperature. Depending on the precise prior preparation history, the plastic deformation of the *Co-Cr-Mo* alloy being burnished always involves both "slip" via dislocation motion and "twinning". Which of these deformation types dominate varies dramatically and changes as the deformation proceeds. For example, the local grain size can (and does) change the dominant type of deformation. Meng et al. (2002) calculated the stable phase type of *Co* in the nano-grain domain and found that it undergoes a phase transformation from the fcc to hcp that is controlled by very small differences in the grain size.

As described in Chapter 5, the phase structure of the *Co-Cr-Mo* alloy significantly affects its mechanical properties in terms of hardness, friction, etc. The used material model was calibrated by using the experimental data from dry a burnishing with 0.254 mm DoP, 100 m/min burnishing speed and 14.3 mm tool diameter. The sample from this condition showed no fcc => hcp transformation after burnishing (Figure 3.20), however, grain refinement due to DRX was detected in the surface layer (Figure 3.15). Among the three burnished samples used for temperature validation shown in Figure 6.15 (b), the sample from dry burnishing with 0.08 mm DoP underwent the most significant (observable) phase structure changes of the strain-induced fcc => hcp transformation type (Figure 4.9). In comparison, the predictions for the other two samples which had very little fcc => hcp transformation during burnishing gave much better temperature predictions.

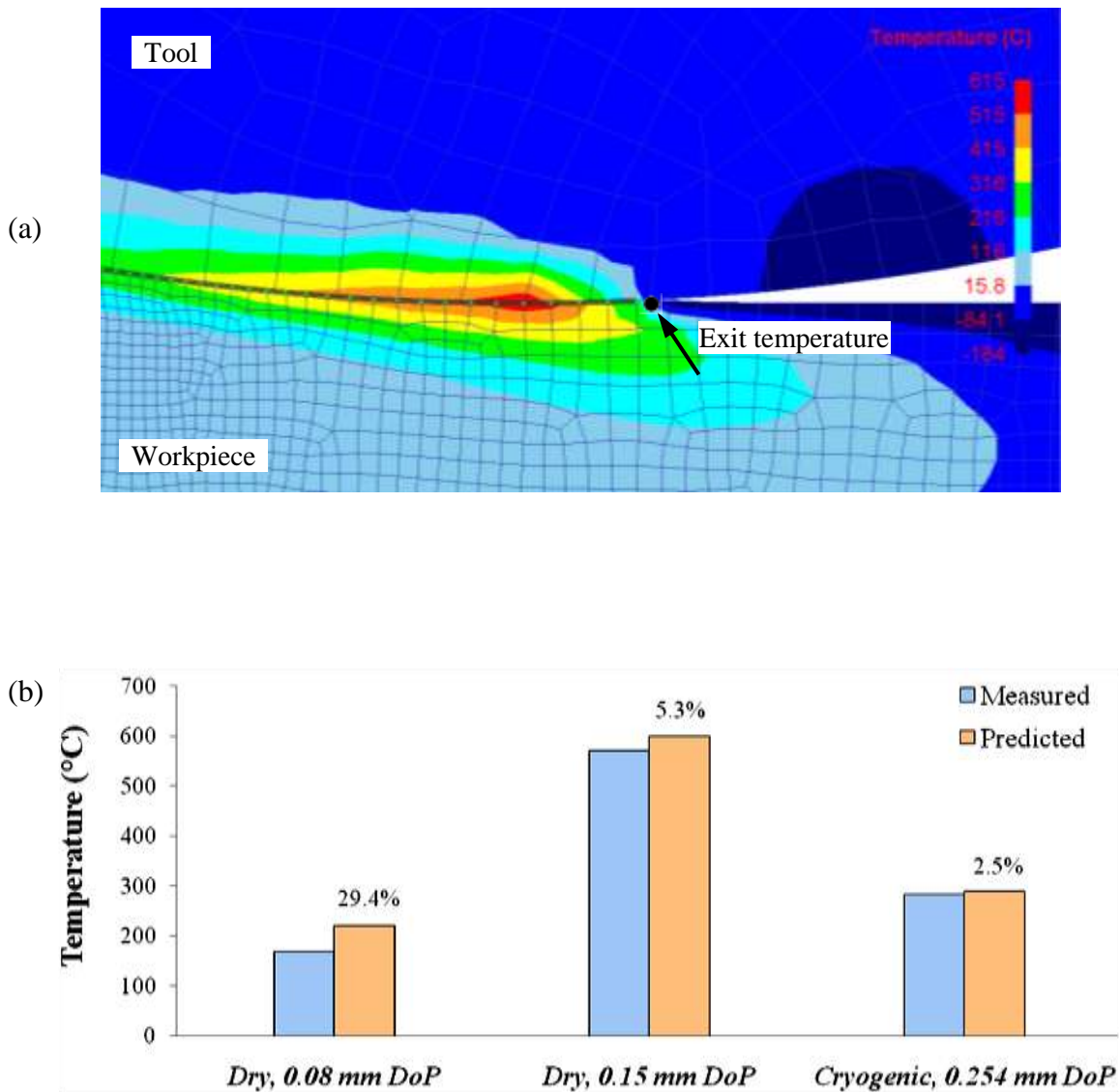


Figure 6.15: (a) The exit temperature for cryogenic conditions (Cryogenic, DoP = 0.254 mm, burnishing speed = 100 m/min, tool diameter = 14.3 mm); (b) predicted exit temperature from different burnishing conditions (burnishing speed = 100 m/min, tool diameter = 14.3 mm)

After the model calibration process, the values of the important parameters used for the FE model were determined and are listed in Table 6.3.

Table 6.3: Important used material parameters for the FE model

Modified Johnson-Cook constants	$A = 500 \text{ MPa}, B = 100 \text{ MPa}, C = 0.054, n = 0.5, m = 1, D = 0.1, p = 0, r = 1, s = 5$
Avrami constants	$k = -1$ and $t = 4$
Critical strain constants	$a = 0.0167$ and $b = 0.652$
Friction coefficient	$\mu = 0.4$ (before $\varepsilon_{cr}$ ), $\mu = 0.05$ (after $\varepsilon_{cr}$ )
Heat transfer coefficient at the tool-workpiece interface	$h1 = 10,000 \text{ kW}/(\text{m}^2 \text{ K})$
Convection coefficient for cryogenic condition	$h2 = 10,000 \text{ kW}/(\text{m}^2 \text{ K})$

Figure 6.16 shows the comparison of measured and predicted radial forces under different burnishing conditions (14.3 mm tool diameter). Except for the case of dry burnishing with 0.08 mm DoP and 100 m/min burnishing speed, good agreements were achieved between the measured and predicted radial forces for the three conditions used for model validation. The large difference on the predicted force (26.5% higher than the measured one) from dry burnishing (0.08 mm DoP, 100 m/min burnishing speed) is again likely attributed to the strain-induced fcc => hcp transformation. In the current model, DRX is the only microstructural evolution mechanism studied; the model does not consider that the phase transformation might occur during burnishing. The large difference between a crude prediction and only one experiment indicates the need for a more robust predicting model including both the mechanisms of DRX and phase transformation which might occur simultaneously at the same conditions.



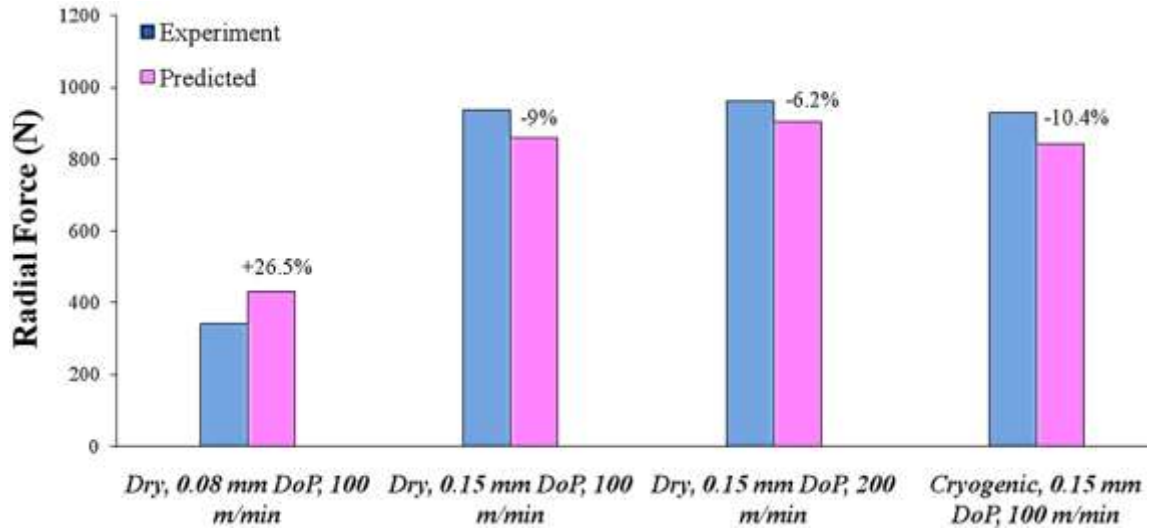


Figure 6.16: Comparison of measured and predicted radial forces under different burnishing conditions (14.3 mm tool diameter)

Figure 6.17 shows the contour plots of predicted effective stress in the workpieces during dry and cryogenic burnishing with 0.254 mm DoP, 100 m/min burnishing speed and 14.3 mm diameter tool. The maximum stress (~ 450 MPa) was observed at a distance (~ 0.5 mm) beneath the workpiece surface for both dry and cryogenic conditions. This is in qualitative agreement with the results reported from the fundamental study on contact mechanics based on analytical methods (Johnson 1985). It should be noted that with or without the application of cryogenic cooling, the predicted effective stresses were similar in terms of values and distributions.

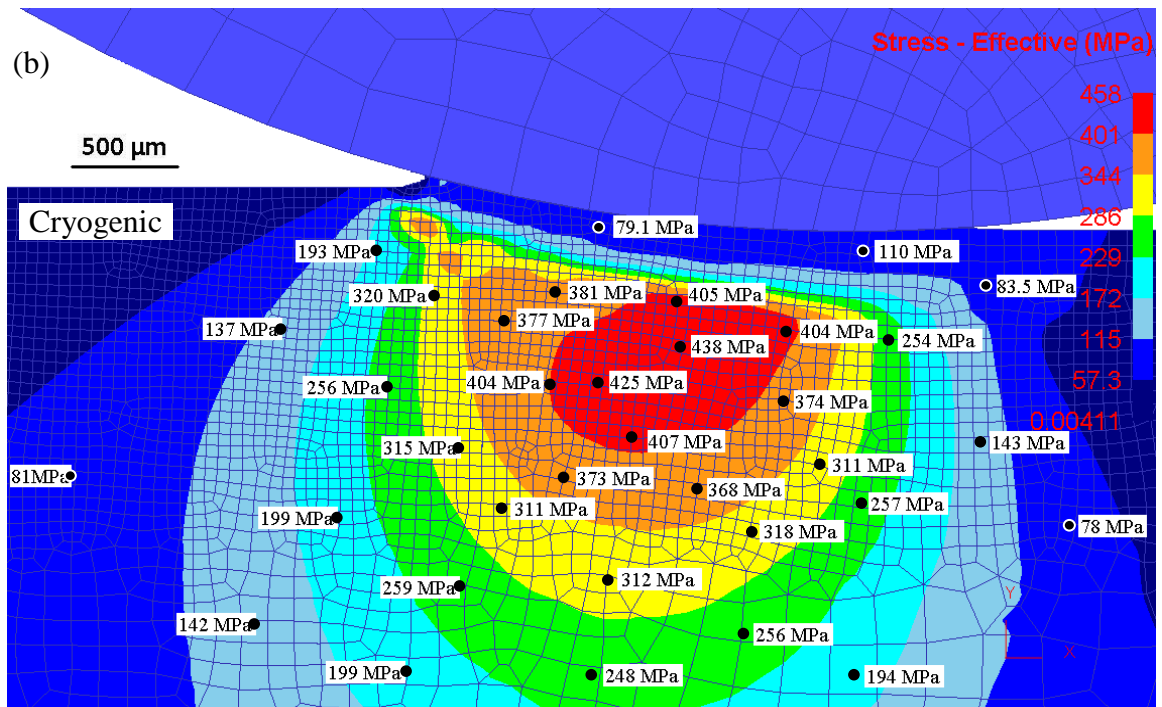
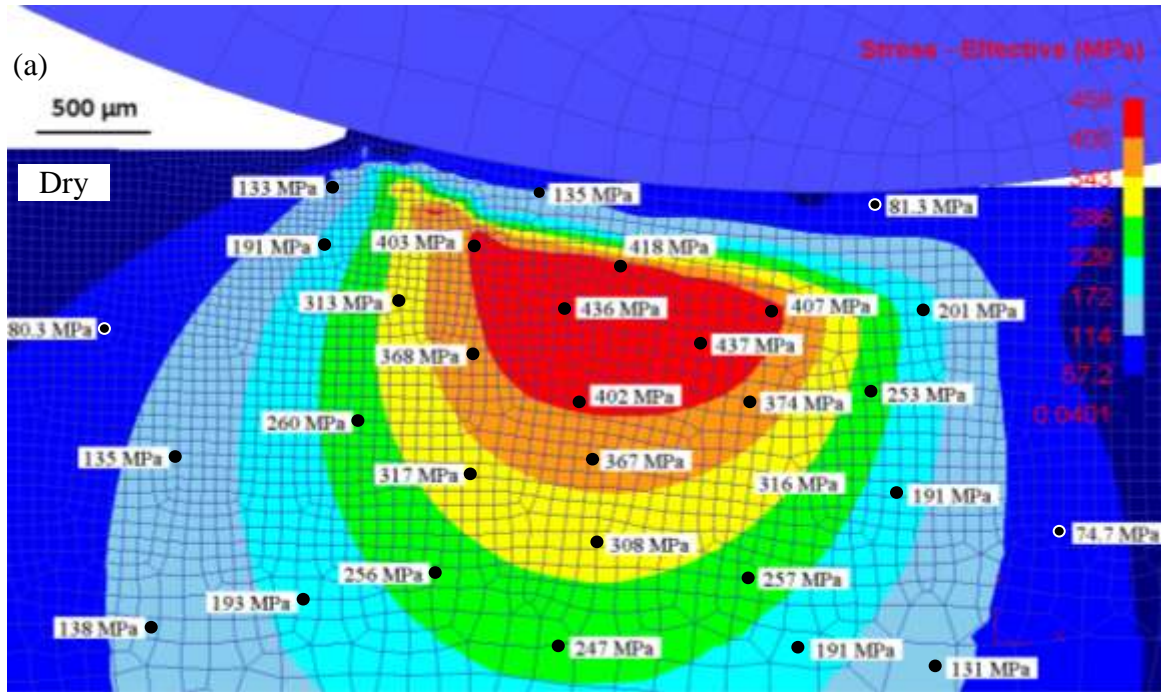


Figure 6.17: Distribution of effective stresses: (a) dry burnishing, (b) cryogenic burnishing. (0.254 mm DoP, 100 m/min speed, 14.3 mm tool)

## 6.9 Calibration and validation of user subroutine for grain size prediction

The calibration procedure used for the Zener-Hollomon constants  $\alpha$  and  $m'$  in Equation 6.7 is different from the calibration procedure described in section 6.8 for the J-C constants as well as the one used for the heat and friction coefficients. The flow chart for the calibration of the Zener-Hollomon constants is shown in Figure 6.18.

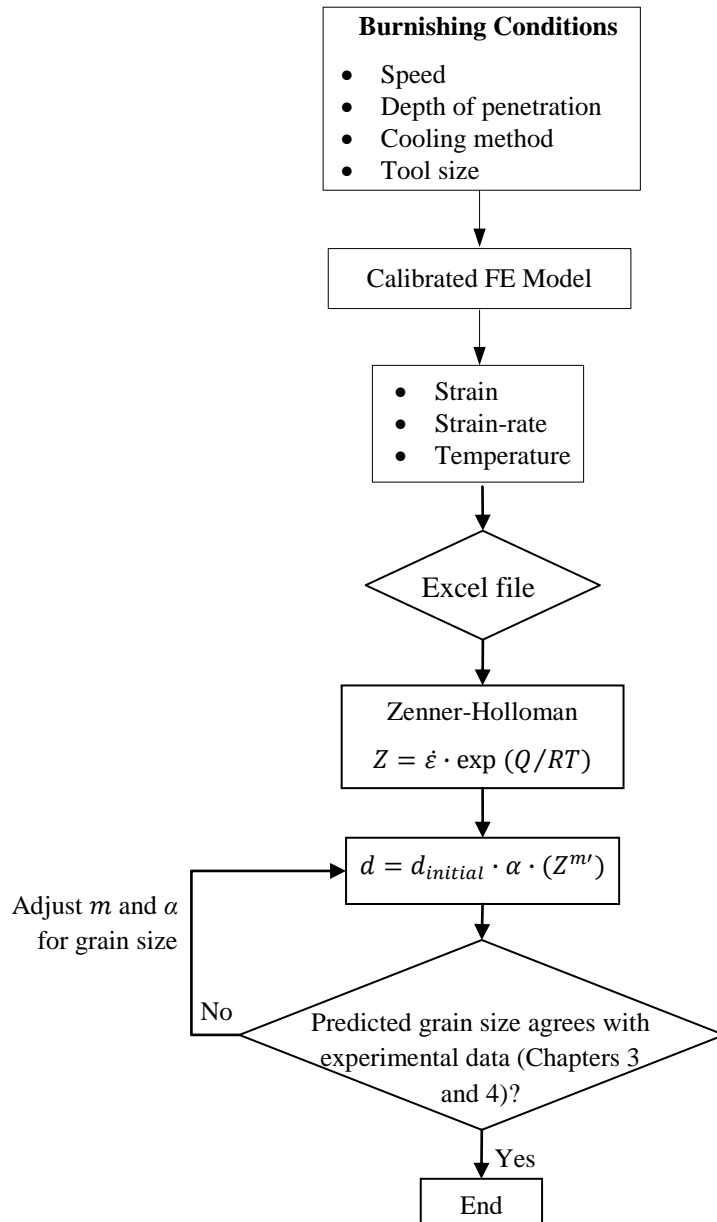
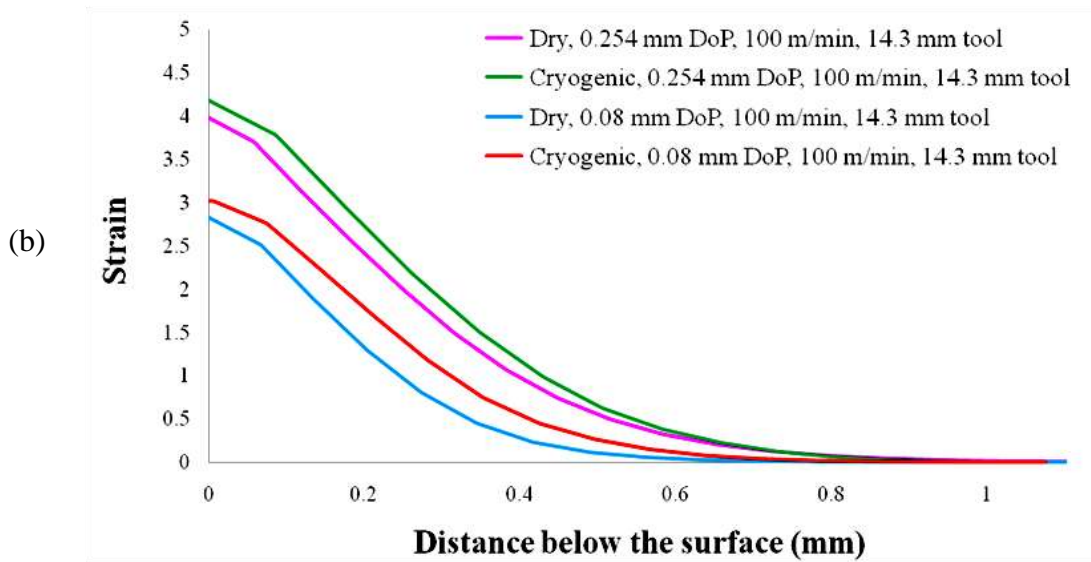
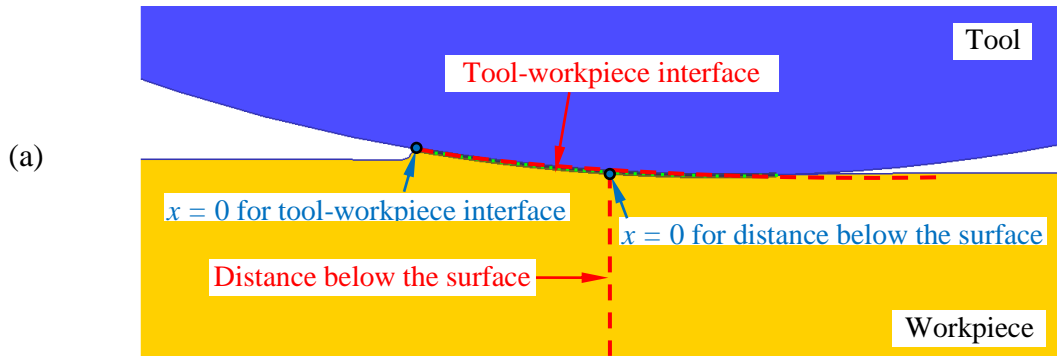
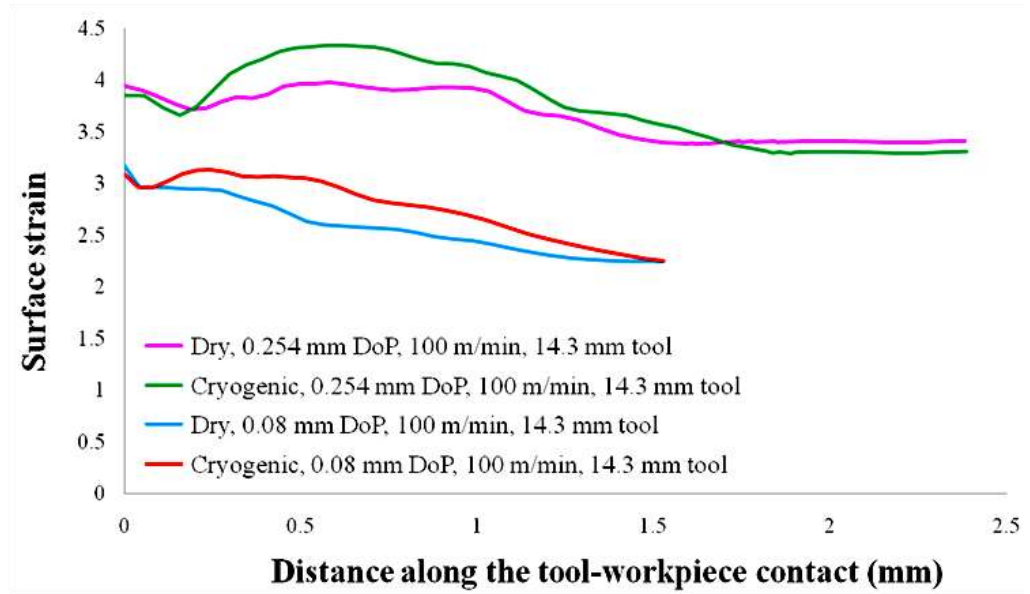


Figure 6.18: Calibration procedure for grain size prediction

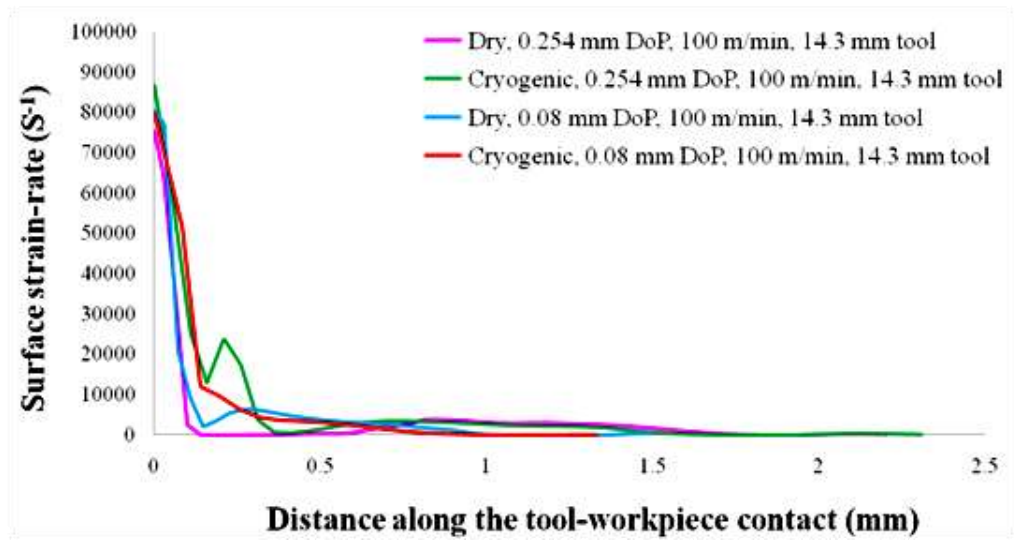
Instead of running the FE model and comparing the predicted results with the experimental data, the calculation procedure for grain size was done within an Excel file. The strain, strain-rate and temperature data were extracted from the standard DEFORM FE simulation data and used as the inputs for the Excel file to calculate the DRXed grain size after the critical strain (Equation (6.7)) was reached. The strain, strain-rate and temperature data used were collected from the simulation run for dry burnishing with 0.254 mm DoP, 100 m/min burnishing speed and 14.3 mm tool diameter. Figure 6.19 (a) indicates the locations of the tool-workpiece interface and the distance below the surface profile for collecting the corresponding strain, strain-rate and temperature data obtained under different burnishing conditions. The predicted strain distribution along the distance below the surface is shown in Figure 6.19 (b). Figures 6.19 (c-e) show the predicted strain, strain-rate and temperature distributions along the tool-workpiece interface. It can be observed from Figure 6.19 (b) and (c) that larger DoP (0.254 mm) settings resulted in higher predicted surface strains for both dry and cryogenic conditions compared to the values from 0.08 mm DoP. This is due to the greater SPD effect under larger DoP conditions. In addition, as shown in Figure 6.19 (c), the application of cryogenic cooling led to small “humps” of surface strains along the tool-workpiece interfaces for both DoPs used. Compared to the relatively smooth surface strains under dry conditions, the “humps” under cryogenic conditions are likely caused by the higher burnishing force due to the increase of material strength under lower temperature and the more inhomogeneous initial state of the material caused by the liquid nitrogen spray as well (Figure 6.19 (e)).



(c)



(d)



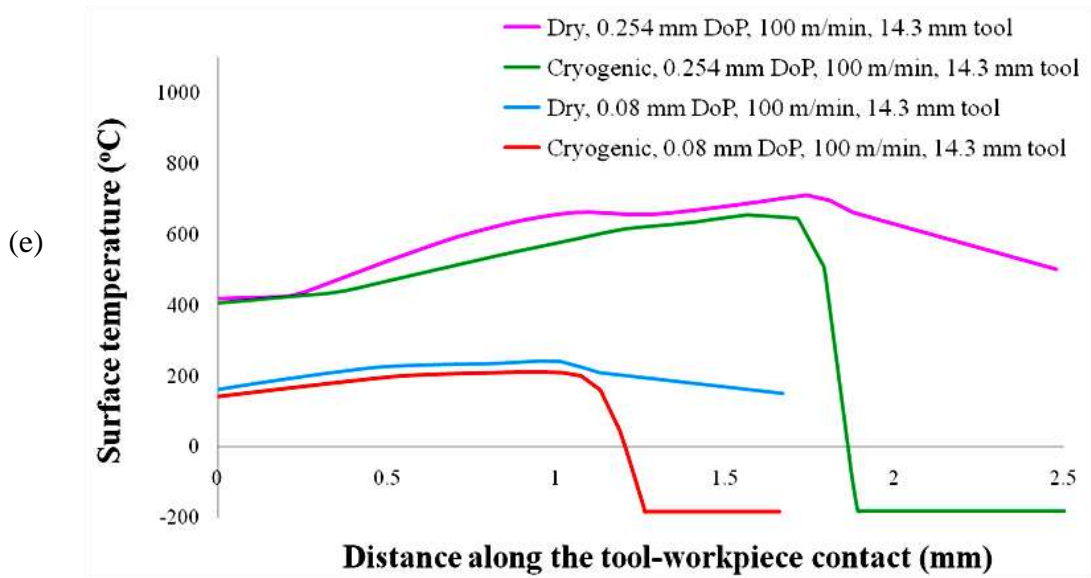


Figure 6.19: (a) Tool-workpiece interface; (b) strain, (c) strain-rate and (d) temperature distributions along the tool-workpiece interface; (e) strain distribution along the distance below the surface

Figure 6.20 shows the calculated grain size for the case of dry burnishing (0.254 mm DoP, 100 m/min burnishing speed, 14.3 mm tool diameter) using Equation (6.7) and the Excel file for determining the  $\alpha$  and  $m'$  values. It can be observed that the calculated grain size is very sensitive to the values of the two constants  $\alpha$  and  $m'$  in Equation (6.7), especially for the constant  $m'$ , whose value can significantly influence the calculated grain size after DRX. This finding is in agreement with the study by Di Renzo (2010) for predicting the grain size changes during machining of *AISI 52100* steel when following similar methodology. Agreement between the calculated grain size and the measured one was found when using  $\alpha = 10$  and  $m' = -0.08$  in Equation 6.7.

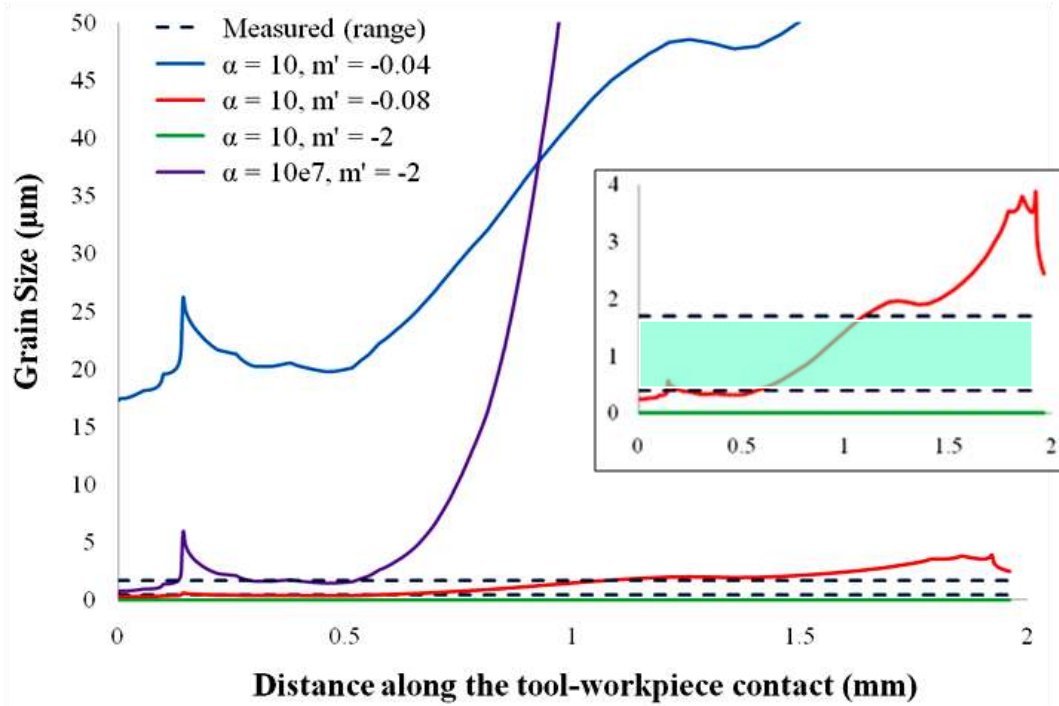
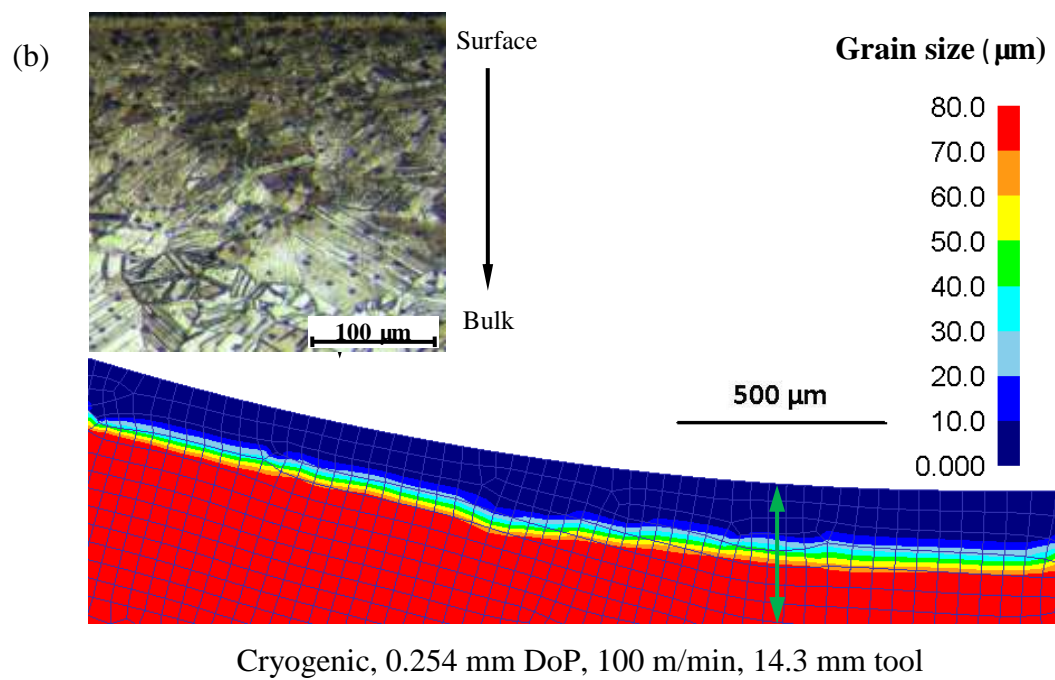
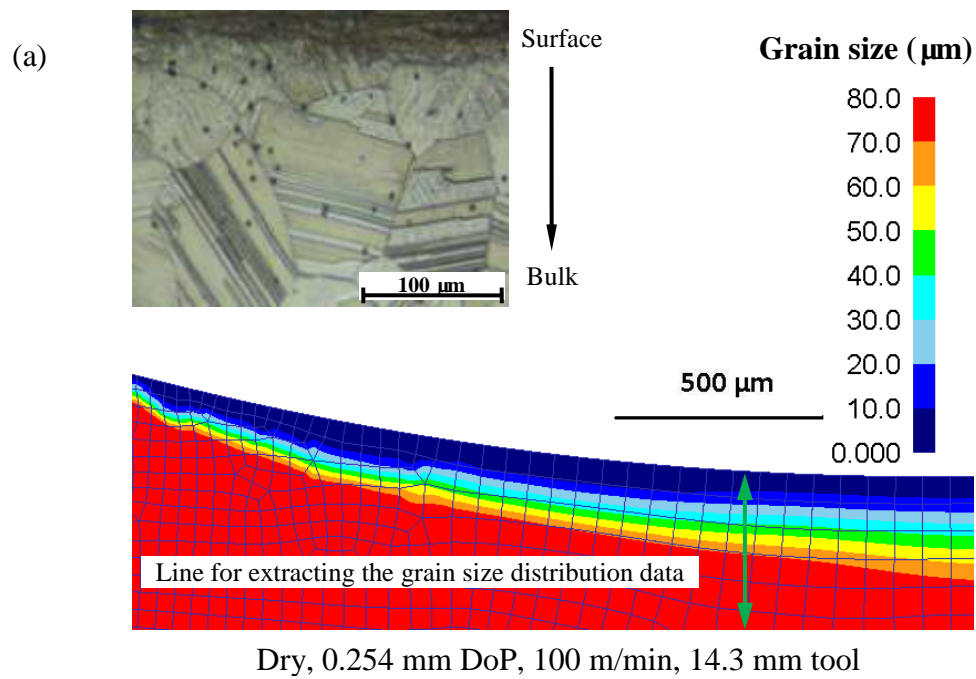
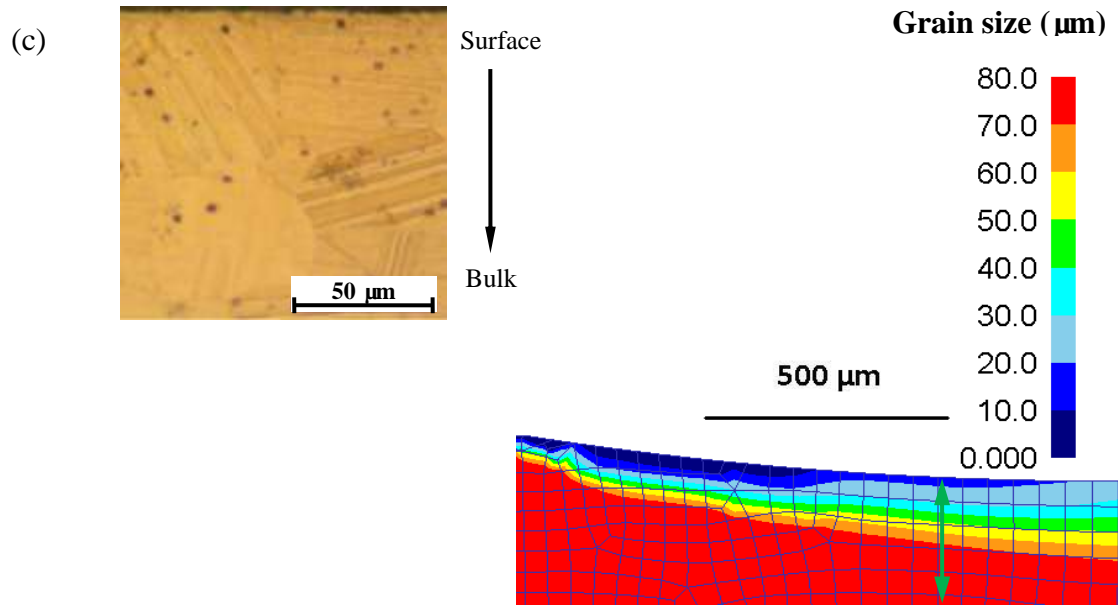


Figure 6.20: The effect of Zener-Hollomon constants  $\alpha$  and  $m'$  on grain size

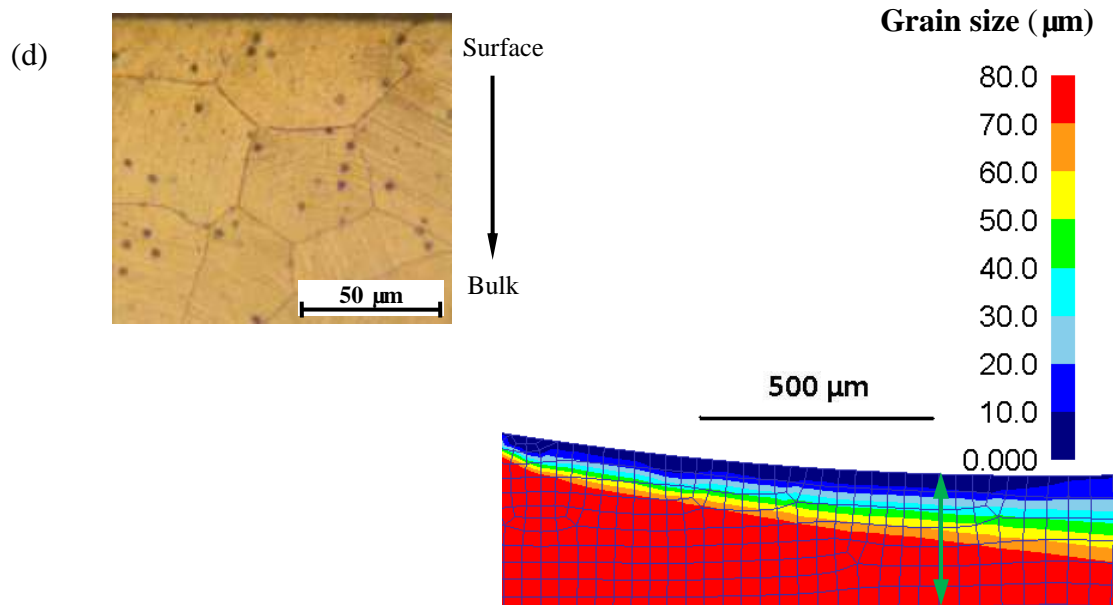
The predicted spatial grain size distributions for different burnishing conditions are shown in Figure 6.21. The experiment data from dry burnishing with 0.254 mm DoP, 100 m/min burnishing speed and 14.3 mm tool diameter was used for finding the Zener-Hollomon constants. The predictions from this condition along with another three conditions were used for model validation. As shown in Figure 6.21, the cross-sectional microstructure images from the four burnishing experiments are embedded into the figures. The lines for extracting the grain size data along the depth from surface are shown in Figure 6.21 also. For all the conditions studied, the application of liquid nitrogen led to thicker burnishing-influenced layers. Grain refinement on the surface and sub-surface was successfully predicted by the user subroutine.







Dry, 0.08 mm DoP, 100 m/min, 14.3 mm tool



Cryogenic, 0.08 mm DoP, 100 m/min, 14.3 mm tool

Figure 6.21: Predicted grain size distributions after burnishing from different conditions

Figure 6.22 (a) and (b) show the variation of grain size with depth below the burnished surface under different burnishing conditions. The predicted grain sizes on the burnished surface were around 20  $\mu\text{m}$  after dry burnishing and 7  $\mu\text{m}$  after cryogenic burnishing when using a 0.08 mm DoP. The predicted grain size distribution in Figure 6.16 (b) from cryogenic burnishing with 0.254 mm DoP was very similar to the experimentally observed microstructure in the surface layer, where the evolution of microstructure from DRXed small grains, elongated subgrains to bulk grains was shown with increasing distance from the surface. However, as shown in Figure 6.21 (c), the predicted thickness of the burnishing-influenced layers was generally larger than the observed ones, for example, the measured layer thicknesses for cryogenic and dry burnishing with 0.254 mm DoP are around 140  $\mu\text{m}$  and 45  $\mu\text{m}$  respectively; in contrast, the predicted layer thickness where an average grain size of 80  $\mu\text{m}$  occurs at about 200  $\mu\text{m}$  for cryogenic condition and 140 for the dry condition, which are 1.4 and 3.1 times larger than experimental measurements. It can be observed that, with smaller DoP (0.08 mm), the effect of cryogenic cooling on increasing the burnishing-influence layer thickness is not as significant as when using larger DoP (0.254 mm), which is consistent with the experimental observation (Figure 3.14).

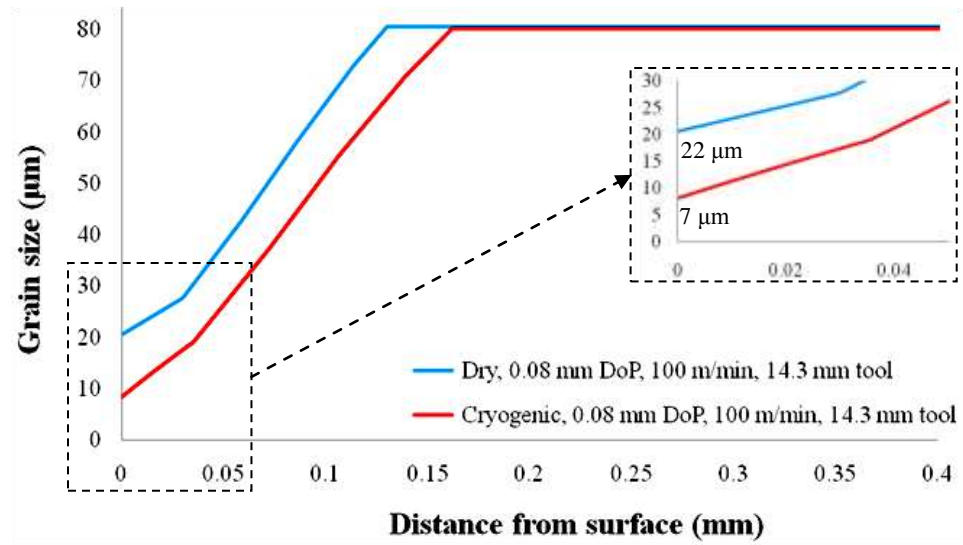
In addition, all the predicted surface layers showed a similar microstructural evolution as the one shown in Figure 6.21 (b); in contrast, the evolutions of the observed surface layer microstructures from DRXed small grains to bulk grains were much faster than the predictions, the transition regions which in the observed layers contain elongated subgrains and heavy twinings were not so obvious in the simulations. The discrepancies on the measured and predicted burnishing-influenced layer thickness and microstructural

evolution may be caused by four reasons. The first reason is that the user subroutine for DRX does not consider grain growth after DRX. Referring to Figure 3.10, the workpiece temperature did not drop significantly after the material left the tool-workpiece interface and kept almost unchanged along the disc perimeter. Thus, during the burnishing test, the recrystallized grains tended to grow after DRX occurred and the thickness of the burnishing-influenced layer was reduced. This claim was supported by the findings from the study on machining of *Mg* alloys (Pu 2012). Grain growth was observed on the surface/subsurface region of *Mg* alloys after machining, which is attributed to be the reason for the thicker predicted machining-influenced layer compared to the measured value. In the DEFORM program this is called "metadynamic" recrystallization and we have not considered that in our model. The second reason for the difference between the predicted and measured burnishing-influenced layers may be due to the overlooking of the phase transformation effect. As described in Chapters 4 and 5, the strain-induced phase transformation of *Co-Cr-Mo* alloy was observed along with DRX after burnishing. This transformation can change the properties of the materials and may also influence the DRX behavior of the material. However, the actual effect of strain-induced phase transformation on DRX properties of *Co-Cr-Mo* alloy is still unclear. The third reason for this difference could be due to the constants used in the critical strain expression (Equation (6.7)). The generally larger predicted burnishing-influenced layer thickness suggested a relatively smaller critical strain used for triggering DRX. The critical strain constants were derived by using the stress-strain data from hot compression tests provided by the Chiba group (Chiba et al. 2009a; Kurosu et al. 2010b; Yamanaka et al. 2009), the testing conditions in terms of strain, strain-rate and temperature (especially the

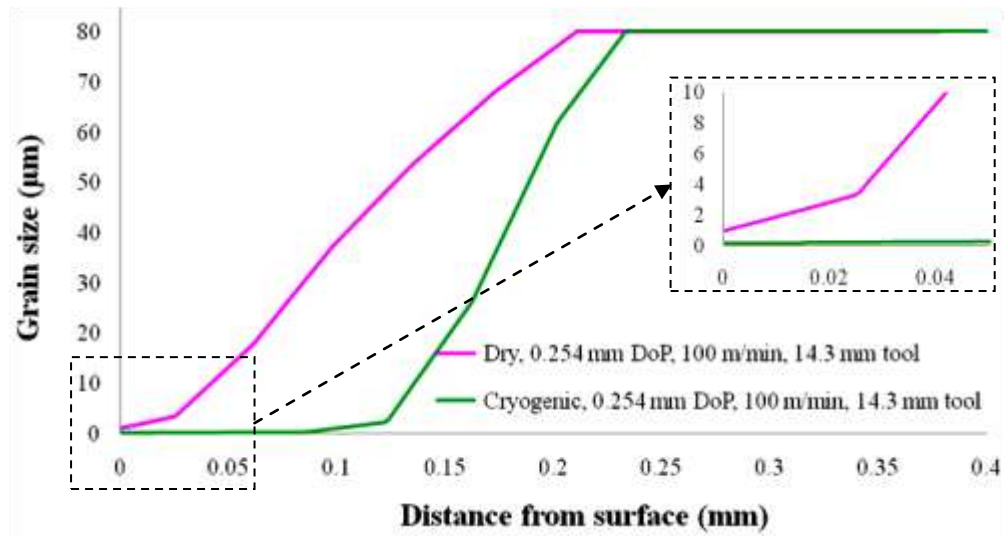
strain-rate) were very different from the existing conditions in burnishing. A further calibration on the critical strain constants may therefore be helpful for improving the accurate prediction of the burnishing-influenced layer thickness. Lastly, the differences are also attributed to the element size used. When the tool traveled along the workpiece surface, the mesh densities of the workpiece ahead and below the tool were remeshed to be much higher than the one behind the tool; in other words, for a fixed point on the workpiece, its corresponding element size firstly became smaller as the tool approached this specific point, then became larger again as the tool passed the point due to continuous remeshing. All of these effects are in addition to the fact that the changing surface layer thickness and grain size are occurring over small distances relative to the mesh sizes. The change of element size led to interpolation errors during remeshing, which further led to the over estimation of the influenced layer thickness towards the downstream of the tool-workpiece interface. Similar phenomenon was reported on numerically simulating the white and dark layer formation during machining of hardened *AISI 52100* steel by using the same DEFORM-2D software as used here (Attanasio et al. 2012).

Figure 6.22 (d) shows the comparison of the measured and predicted surface grain sizes from dry and cryogenic burnishing with 0.254 mm DoP, 100 m/min and 14.3 mm tool diameter. The surface grain sizes for dry conditions are  $1 \pm 0.5 \mu\text{m}$  (measured) and 814 nm (predicted); the surface grain sizes for cryogenic condition are  $500 \pm 300 \text{ nm}$  (measured in average) and 350 nm (predicted). The predicted values are in good agreement with the measured ones. The slightly larger grain size from measurements may possibly also due to the grain growth after burnishing.

(a)



(b)



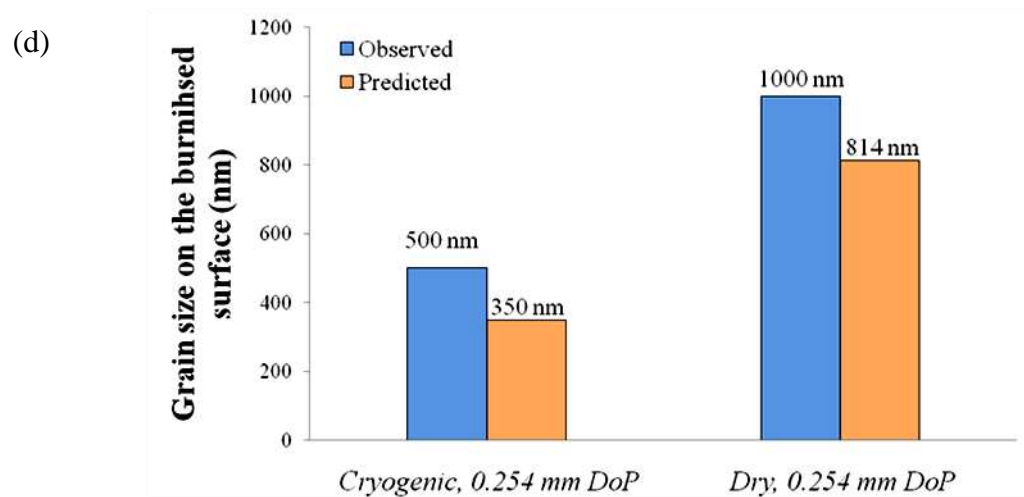
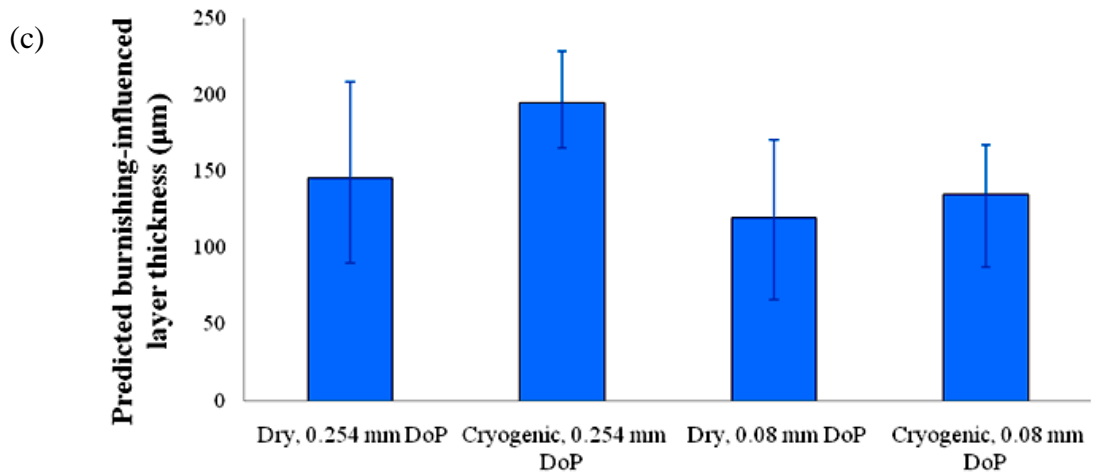


Figure 6.22: Predicted grain size variation below the burnished surface: (a) dry and cryogenic burnishing under 0.08 mm DoP, (b) dry and cryogenic burnishing under 0.254 mm DoP; (c) predicted burnishing-influenced layer thicknesses; (d) comparison of the observed and predicted grain size on the burnished surface (burnishing speed = 100 m/min, tool diameter = 14.3 mm)

It should be noted that during the burnishing experiments, the roller tool passed over the workpiece surface more than one time, however, the effect of subsequent

burnishing passes was not considered in the FE simulation. In the current FE model, the prediction results were all from first-pass simulation runs. The influence of number of burnishing passes has been reported on the resulting surface integrity properties of many materials. Hassan and AlBsharat (1996) studied the effect of the number of tool passes during burnishing process. It is found that increasing the number of tool passes from 1 to 5 increased the surface hardnesses of *Al* by 26% and brass by 14% respectively. The surface roughness decreased with an increase in the number of tool passes to a certain limit, and then started to increase with further increasing of pass number. This is attributed to repeated plastic deformation induced surface fatigue. Similar findings were reported by El-Axir and El-Khabeery (2003). It is found that the increase of burnishing passes firstly increased the microhardness until it reaches a maximum value. With a further increase in number of burnishing passes, the microhardness increasing rate gradually decreased, which is due to the over hardening and consequently flaking of the surface layers. Yeldose and Ramamoorthy (2008) studied the surface roughness of burnished *EN24* steel from 1 to 3 passes. Their results showed that increasing the tool pass number from 1 to 3 reduced the surface roughness of *EN24* steel from 0.26  $\mu\text{m}$  to 0.15  $\mu\text{m}$ . Extensive effort has been made on investigating the number of tool passes effect during rolling process, whose mechanism is very similar to the studied burnishing process. The method of accumulative roll-bonding (ARB) has been used successfully on a number of materials (Tsuji et al. 2003). During ARB process, plastic deformation was accumulated by repetition of tool passes. The material was severely strained after several passes and the grain size was significantly refined (Saito et al. 1999). In addition, the need for modelling the pass-by-pass development of microstructure during multipass



rolling operations was considered and discussed (Sellars 1990). It is claimed that the strain of one pass can contribute to the total stored energy after a second pass when there is no recrystallization, or only partial recrystallization between passes. When no recrystallization took place, there may still be some softening by static recovery, but its effects were soon eliminated during the subsequent pass. Simple addition of the pass strains was assumed in their model for isothermal deformations. In another study for simulating of orthogonal cutting process, Ee (2002) found that the simulated surface residual stresses changed with two cutting passes, as compared to one, but changed little with more passes. In the current FE model, the influence due to number of tool passes was not considered, which is likely to be another factor affecting the accuracy of the predicted results for grain size and burnishing-influenced layer thickness.

## **6.10 Chapter concluding remarks**

An FEM-based model was built using the commercial software program DEFORM-2D<sup>TM</sup> to simulate the burnishing of *Co-Cr-Mo* alloy. A new material model was developed for incorporating flow stress softening and associated grain size refinement caused by DRX. This is the major contribution since one normally cannot use DEFORM when  $d\sigma/d\varepsilon < 0$ . The force and temperature data from one experimental condition were used to calibrate the FE model by updating the model parameters ( $A$ ,  $B$ ,  $\mu$ ,  $h_I$ ). A heat exchange window was added for simulating the cryogenic cooling effect. The calibrated FE model was validated by using different sets of experimental data. A user subroutine was developed to predict the grain size changes during burnishing based on the DRX mechanism of *Co-Cr-Mo* alloys. The predicted grain size was evaluated by comparing with the experimental data; good agreements were achieved between

predictive and experimental results. However, the predicted burnishing-influenced layer thicknesses were generally larger than the corresponding experimental values. In this author's view, there is a major need for a complete predictive model incorporating DRX and strain-induced phase transformation, as well as considering number of tool passes during burnishing in order to manufacture products with superior surface parameters such as hip implants. The present model is a first step in fulfilling this need. Its accuracy can be improved with experience (finer grids) and improved input data. Similar remarks appear to be justified with regard to increased use of cryogenic cooling during burnishing (and machining) when superior surface conditions are desired.

## CHAPTER 7: CONCLUSIONS AND FUTURE WORK

In this Chapter, the findings and results of the current research are summarized with final remarks and conclusions. The concluding remarks are given in order of appearance in the chapters. The directions and recommendations of the future work are discussed briefly based on the results and observations presented in this dissertation.

### 7.1 Conclusions

Burnishing experiments with the application of liquid nitrogen were conducted on an annealed *Co-Cr-Mo* alloy using a custom-made burnishing tool. Surface integrity modifications on this *Co-Cr-Mo* alloy were achieved from cryogenic burnishing processing. Pin-on-disk wear tests were conducted to explore the influence of burnished-induced surface integrity modifications on the wear performance of the studied *Co-Cr-Mo* alloy. The specific surface integrity parameters studied are microstructure (grain size and processing influenced layer), phase transformation, residual stresses, hardness and surface roughness. The major findings from this research are summarized below:

- (1) The experimental temperature study using the infrared-thermal camera showed that the application of liquid nitrogen during burnishing significantly suppresses the temperature rise within and outside the tool-workpiece contact zone. The liquid nitrogen can largely sustain the effect of SPD during burnishing as well as keeping the DRX refined grains from growing after leaving the tool.
- (2) Microstructure refinement, especially in the surface layer was observed under both dry and cryogenic conditions. With the application of liquid nitrogen, the

created burnishing-influenced layer thickness can be increased by up to a factor of 3 compared to the one from dry conditions. In addition to the cooling method, the thickness of the burnishing-influenced layer with microstructure refinement was also dependent on depth of penetration of the used tool and the burnishing speed. The results on microstructural changes also suggest that optical microscopy may not be adequate to accurately characterize the resulting microstructures obtained using different burnishing conditions. Advanced characterization techniques, such as SEM, TEM or AFM, are needed.

- (3) The residual stresses became more tensile after burnishing at large DoP (0.15 mm), when compared with the initial data, and became compressive under smaller DoP (0.08 mm). However, the application of liquid nitrogen during burnishing generally led to the formation of more compressive residual stresses in both directions. In addition, larger differences of up to 1400 MPa were found in residual stresses between tangential and axial directions. The large difference in residual stress values in the two directions could be caused by the different deformation directions (geometry and loading conditions). Severe flow of the material in the axial direction was evident during the burnishing process. Further studies are needed to investigate the causes for the different distribution of residual stresses in the two directions. Without the application of liquid nitrogen, the surface residual stresses became more tensile under all conditions when compared with the virgin material as well as the ones with cryogenic cooling.
- (4) A remarkable increase in the relative intensity of the hcp  $(10\bar{1}1)_e$  peak was achieved on the cryogenically burnished surface, which should significantly

enhance the wear performance of the *Co-Cr-Mo* alloy. However, increasing of DoP and burnishing speed all led to a decrease of the amount of the hcp phase present. This can be due to the complicated phase transformation mechanisms of the *Co-Cr-Mo* alloy especially when DRX is also included.

- (5) Microhardness measurements indicated that the hardness close to the surface in the burnishing-influenced layer was increased to varying extents. The most significant hardness increase was achieved when using cryogenic burnishing with 0.254 mm DoP, 100 m/min burnishing speed, an increase of up to 87% relative to the bulk value. However, the hardness was not only dependent on the microstructures, but also on the phase composition and residual stress values.
- (6) Compared to dry burnishing, application of liquid nitrogen reduced the surface roughness by about 40% for both burnishing conditions with 0.127 mm and 0.254 mm DoP. However, burnishing with larger DoP increased the surface roughness due to more severe plastic deformation and higher processing temperature. Due to the severe plastic deformation involved in the process, it should be noted that the application of cryogenic burnishing is limited for creating super-smooth bearing surfaces as the final finishing process. However, better surface finish created under cryogenic conditions will be favorable for retaining the process-enhanced surface layer by minimizing the material loss during the final polishing, thus improving the functional performance of the processed components.
- (7) Pin-on-disk wear tests were conducted to evaluate the wear performance of the burnished *Co-Cr-Mo* alloy under different conditions. Cryogenic burnishing can

significantly improve the wear performance of the *Co-Cr-Mo* alloy, which was attributed to the burnishing-induced surface integrity enhancements.

- (8) The major wear mechanism was identified as surface fatigue leading to fractured or torn-off metallic or oxide particles, which became interfacial media. This further led to abrasion or surface fatigue depending on whether the particles stick to one surface and scratch the other or act as rolling particles bringing about indentations.
- (9) It was found that minimal wear volume losses were achieved in pins with the highest hcp amount. In contrast, the highest values of mass losses corresponded to fcc pins. Intermediate wear values were found in pins with lower hcp amounts for the wear conditions used in this work. Moreover, it was found that the exhibited wear volume losses do not follow a single linear trend with the phase structure differences. Apparently, the phase structures of the contacting surfaces play an important role in the tribological response. Under the wear conditions employed (metal-metal pin-on-disk), the dominant mechanism involved some plastic deformation on the contacting surfaces, and included some oxidation of the wear debris.
- (10) It is also found that the presence of the hcp structure exceeded the effect of grain size on the wear performance of the *Co-Cr-Mo* alloy. However, the comparison between cryogenic and dry burnishing with 0.254 mm DoP showed that when there was no hcp structure presenting in the crystal matrix, the better wear performance of the cryogenically burnished pin was likely due to the thicker burnishing-induced refinement layer and compressive residual stresses. Thus, it is

fair to conclude that the surface layer properties in terms of phase structure, microstructure and residual stresses were concurrently influencing the pin-on-disk wear behavior of this *Co-Cr-Mo* alloy. Further studies are needed for systematically identifying the relative importance of each of these properties on the wear performance of the *Co-Cr-Mo* alloy.

- (11) Based on the above results, it is suggested that future developments in *Co-Cr-Mo* hip implants should consider material prototypes that have high percentages of hcp structure, fine-grained microstructure as well as thick compressive residual stress layers as these properties tend to represent superior wear performance in metal-on-metal contact. Manufacturing these products can benefit from using cryogenic cooling to enhance the microstructure.
- (12) An FEM-based model was built using the commercial software program DEFORM-2D<sup>TM</sup> to simulate the burnishing of the *Co-Cr-Mo* alloy. A new material model was developed for incorporating flow stress softening and associated grain size refinement caused by DRX. The force and temperature data from one experimental condition were used to calibrate the FE model by updating the model parameters ( $A$ ,  $B$ ,  $\mu$ ,  $h_i$ ). A heat exchange window was added for simulating the cryogenic cooling effect. The calibrated FE model was validated by using different sets of experimental data. A user subroutine was developed to predict the grain size changes during burnishing based on the DRX mechanism of *Co-Cr-Mo* alloys. The predicted grain size was evaluated by comparing with the experimental data; good agreements were achieved between predictive and experimental results. However, the predicted burnishing-influenced layer

thicknesses were generally larger than the corresponding experimental values. In this author's view, there is a major need for a complete predictive model of the burnishing process which incorporates simultaneous DRX and strain-induced phase transformation, as well as considering number of tool passes made during burnishing in order to manufacture products with superior surface parameters such as hip implants. The present model is a first step in fulfilling this need. Its accuracy can be improved with experience (finer grids) and improved input data. Similar remarks appear to be justified with regard to increased use of cryogenic cooling during burnishing (and machining) when superior surface conditions are desired.

Overall, the results suggest that cryogenic burnishing can significantly modify the surface/subsurface properties of *Co-Cr-Mo* alloy, leading to potential performance improvement of critical components in various applications, including biomedical implants.

## **7.2 Future Research Directions**

- (1) Better temperature measurements need to be conducted by using an infrared camera with higher resolution and magnification than the one used in the current study. The measured temperature distribution near the tool-workpiece interface will help the researcher to better understand the mechanism of DRX, and will also provide valuable data for modeling.
- (2) In addition, a better design of the burnishing tool is needed to enable a clear view of the tool-workpiece interface by the thermal camera.



- (3) The results on microstructural changes suggest that optical microscopy is not adequate to accurately characterize the resulting surface microstructures from different burnishing conditions.
- (4) Only spraying of liquid nitrogen on the flank side of the tool at one fixed flow rate was used herein for the burnishing process study. It is strongly recommended that the influences of flow rate, number of nozzles, precooling, nozzle position for applying cryogenic cooling, etc., on surface integrity of burnished *Co-Cr-Mo* alloys to be studied.
- (5) Data for an optimization process is needed in order to find the optimal combination of surface integrity properties for achieving the most desirable wear performance of the *Co-Cr-Mo* alloy.
- (6) Designing of different burnishing tools is encouraged in order to create the desirable surface integrity properties on real hip implants as well as other components/products with complex geometries.
- (7) A complete predictive model incorporating DRX and strain-induced phase transformation, as well as considering number of tool passes during burnishing is needed in order to manufacture products with superior surface parameters such as hip implants
- (8) The used material constitutive equation for *Co-Cr-Mo* alloy in the finite element (FE) model was calibrated by the experimental data from hot compression tests. The processing conditions in terms of strain, strain-rate and temperature involved were very different from the ones in burnishing. Moreover, the quantity of available property data at the needed conditions was very limited. A better

material model should be developed based on the material property data which was obtained under conditions close to the burnishing process. By doing so, the model should achieve much better accuracy in predicting the very valuable grain size change of *Co-Cr-Mo* alloy in burnishing.

## REFERENCES

- Abbas, G. and West, D. R. F. (1991). "Laser surface cladding of stellite and stellite-sic composite deposits for enhanced hardness and wear." *Wear* 143(2): 353-363.
- Affatato, S., Bersaglia, G., Yin, J. Q., Traina, F., Toni, A. and Viceconti, M. (2006). "The predictive power of surface profile parameters on the amount of wear measured in vitro on metal-on-polyethylene artificial hip joints." *Proceedings of the Institution of Mechanical Engineers Part H-Journal of Engineering in Medicine* 220(H3): 457-464.
- Alghamdi, A., Lavigne, M. and Vendittoli, P. A. (2012). "Metal on metal bearing in total hip arthroplasty." *Minerva Ortopedica E Traumatologica* 63(2): 85-99.
- Altenberger, I., Scholtes, B., Martin, U. and Oettel, H. (1999). "Cyclic deformation and near surface microstructures of shot peened or deep rolled austenitic stainless steel AISI 304,." *Materials Science and Engineering A* 264: 1-16.
- Anissian, H. L., Stark, A., Gustafson, A., Good, V. and Clark, I. C. (1999). "Metal-on-metal bearing in hip prosthesis generates 100-fold less wear debris than metal-on-polyethylene." *Acta Orthop. Scand.* 70(6): 578-582.
- Arzt, E. (1998). "Overview no. 130 - Size effects in materials due to microstructural and dimensional constraints: A comparative review." *Acta Materialia* 46(16): 5611-5626.
- ASM (1986). *Binary alloy phase diagrams*. Metals Park, OH.
- ASTM-F75. (2011). "Standard test method for wear testing of polymeric materials used in total joint prostheses."
- ASTM F2033-12 "Standard specification for total hip joint prosthesis and hip endoprosthesis bearing surfaces made of metallic, ceramic, and polymeric materials, 2005."
- Attanasio, A., Umbrello, D., Cappellini, C., Rotella, G. and M'Saoubi, R. (2012). "Tool wear effects on white and dark layer formation in hard turning of AISI 52100 steel." *Wear* 286: 98-107.
- Avrami, M. (1939). "Kinetics of phase change I - General theory." *Journal of Chemical Physics* 7(12): 1103-1112.
- Belyakov, A., Tsuzaki, K., Miura, H. and Sakai, T. (2003). "Effect of initial microstructures on grain refinement in a stainless steel by large strain deformation." *Acta Materialia* 51(3): 847-861.
- Ben Fredj, N. and Sidhom, H. (2006). "Effects of the cryogenic cooling on the fatigue strength of the AISI 304 stainless steel ground components." *Cryogenics* 46(6): 439-448.
- Berlin, R. M., Gustavson, L. J. and Wang, K. K. (1999). *Influence of post processing on the mechanical properties of investment cast and wrought Co-Cr-Mo alloys*. West Conshohocken, PA.

- Berry, G., Bolton, J. D., B., B. J. and McQualde, S. (1999). The production and properties of wrought high carbon Co-Cr-Mo alloys. West Conshohocken, PA, American Society for Testing and Materials.
- Bhattacharyya, D., Allen, M. N. and Mander, S. J. (1993). "Cryogenic machining of Kevlar composites." *Materials and Manufacturing Processes* 8(6): 631–651.
- Black, A. J., Kopalinsky, E. M. and Oxley, P. L. B. (1997). "Analysis and experimental investigation of a simplified burnishing process." *International Journal of Mechanical Sciences* 39(6): 629-&.
- Bougharriou, A., Sai, W. B. and Sai, K. (2010). "Prediction of surface characteristics obtained by burnishing." *International Journal of Advanced Manufacturing Technology* 51(1-4): 205-215.
- Bouزيد, W., Tsoumarev, O. and Sai, K. (2004). "An investigation of surface roughness of burnished AISI 1042 steel." *International Journal of Advanced Manufacturing Technology* 24(1-2): 120-125.
- Brown, R. (2001). "Powder metallurgical processing improves high-carbon Co-Cr-Mo alloy for orthopaedic implants." *Cobalt News* 1/4: 9–14.
- Brown, T. L., Swaminathan, S., Chandrasekar, S., Compton, W. D., King, A. H. and Trumble, K. P. (2002). "Low-cost manufacturing process for nanostructured metals and alloys." *Journal of Materials Research* 17(10): 2484-2488.
- Buckley, H. (1968). "Adhesion, friction and wear of cobalt and cobalt-base alloys." *Cobalt*(38): 20-28.
- Buford, A. and Goswami, T. (2004). "Review of wear mechanisms in hip implants: Paper I - General." *Materials & Design* 25(5): 385-393.
- Buscher, R. and Fischer, A. (2003). "Metallurgical aspects of sliding wear of fcc materials for medical applications." *Materialwissenschaft Und Werkstofftechnik* 34(10-11): 966-975.
- Buscher, R. and Fischer, A. (2005). "The pathways of dynamic recrystallization in all-metal hip joints." *Wear* 259: 887-897.
- Buscher, R., Tager, G., Dudzinski, W., Gleising, B., Wimmer, M. A. and Fischer, A. (2005). "Subsurface microstructure of metal-on-metal hip joints and its relationship to wear particle generation." *Journal of Biomedical Materials Research Part B-Applied Biomaterials* 72B(1): 206-214.
- Busso, E. P., Meissonnier, F., O'Dowd, N. P. and Nouailhas, D. (1998). "Length scale effects on the geometric softening of precipitated single crystals." *Journal De Physique Iv* 8(P8): 55-61.
- Byrne, G., Dornfeld, D. and Denkena, B. (2003). "Advancing cutting technology." *Cirp Annals-Manufacturing Technology* 52(2): 483-507.
- Campbell, P., McKellop, H., Adim, R., Mirra, J., Nutt, S., Dorr, L. and Amstutz, H. C. (1999). Metal-on-metal hip replacements: Wear performance and cellular

- response to wear particles. West Conshohocken, PA, American Society for Testing and Materials.
- Carter, W. A. (1956). Metal machining, part VI, cutting fluids, Machinery Lloyd.
- Cavaleiro, A. and De Hosson, J. T. M. (2006). Nanostructured coatings, New York: Springer-Verlag.
- Chan, C. L. and Villar, R. N. (1996). "Obesity and quality of life after primary hip arthroplasty." *The Journal of bone and joint surgery. British* volume 78(1): 78-81.
- Chiba, A., Kumagai, K., Nomura, N. and Miyakawa, S. (2007). "Pin-on-disk wear behavior in a like-on-like configuration in a biological environment of high carbon cast and low carbon forged Co-29Cr-6Mo alloys." *Acta Materialia* 55(4): 1309-1318.
- Chiba, A., Lee, S. H., Matsumoto, H. and Nakamura, M. (2009a). "Construction of processing map for biomedical Co-28Cr-6Mo-0.16N alloy by studying its hot deformation behavior using compression tests." *Materials Science and Engineering A* 513-14: 286-293.
- Chiba, A., Lee, S. H., Matsumoto, H. and Nakamura, M. (2009b). "Construction of processing map for biomedical Co-28Cr-6Mo-0.16N alloy by studying its hot deformation behavior using compression tests." *Materials Science and Engineering a-Structural Materials Properties Microstructure and Processing* 513-14: 286-293.
- Crook, P. and Li, C. C. (1983). "The elevated temperature metal to metal wear behavior of selected hardfacing alloys." *Wear Mater* 272-279.
- CRS Holdings Inc. (2007). "BioDur® Carpenter CCM® Alloy, <http://cartech.ides.com/datasheet.aspx?i=101&e=8&c=TechArt>."
- Cuckler, J. M. (2005). "The rationale for metal-on-metal total hip arthroplasty." *Clinical Orthopaedics and Related Research*(441): 132-136.
- Czichos, H. (1986). Introduction to friction and wear, *Friction and Wear of Polymer Composites, Composite Material Series*. Amsterdam, Elsevier.
- Dao, M., Lu, L., Asaro, R. J., De Hosson, J. T. M. and Ma, E. (2007). "Toward a quantitative understanding of mechanical behavior of nanocrystalline metals." *Acta Materialia* 55(12): 4041-4065.
- Dehghan-Manshadi, A., Barnett, M. and Hodgson, P. D. (2008). "Hot deformation and recrystallization of austenitic stainless steel: Part I. Dynamic recrystallization." *Metallurgical and Materials Transactions a-Physical Metallurgy and Materials Science* 39A(6): 1359-1370.
- Dehghan-Manshadi, A. and Hodgson, P. D. (2007). "Dynamic recrystallization of austenitic stainless steel under multiple peak flow behaviours." *Isij International* 47(12): 1799-1803.

- Denkena, B. and Lucas, A. (2007). "Biocompatible magnesium alloys as absorbable implant materials - Adjusted surface and subsurface properties by machining processes." *Cirp Annals-Manufacturing Technology* 56(1): 113-116.
- Deshpande, A., Yang, S., Dillon, J., O.W. , Puleo, D. A., Pienkowski, D., Outeiro, J. C. and Jawahir, I. S. (2012). Minimized wear and debris generation through optimized machining of Co-Cr-Mo alloys used in metal-on-metal hip implants. ASME Manufacturing Science and Engineering Conference, Notre Dame, IN.
- Dhar, N. R. and Kamruzzaman, M. (2007). "Cutting temperature, tool wear, surface roughness and dimensional deviation in turning AISI-4037 steel under cryogenic condition." *International Journal of Machine Tools & Manufacture* 47(5): 754-759.
- Di Renzo, S. (2010). Modelling and experimental validation of surface integrity in hard machining of AISI 52100 steel. MS, University of Calabria, Italy.
- DIN50320. (1979). *Wear, Terms, System Analysis, Classification of Wear*. Beuth, Berlin, Germany,: 1-8.
- Doorn, P. F., Campbell, P. A., Worrall, J., Benya, P. D., McKellop, H. A. and Amstutz, H. C. (1998). "Metal wear particle characterization from metal on metal total hip replacements: transmission electron microscopy study of periprosthetic tissues and isolated particles." *Journal of Biomedical Materials Research* 42(1): 103-111.
- Dowson, D., Hardaker, C., Flett, M. and Isaac, G. H. (2004). "A hip joint simulator study of the performance of metal-on-metal joints - Part I: The role of materials." *Journal of Arthroplasty* 19(8): 118-123.
- Dudzinski, D., Devillez, A., Moufki, A., Larrouquere, D., Zerrouki, V. and Vigneau, J. (2004). "A review of developments towards dry and high speed machining of Inconel 718 alloy." *International Journal of Machine Tools & Manufacture* 44(4): 439-456.
- Ee, K. C. (2002). Finite element modeling and analysis of residual stresses in 2-D machining PhD., University of Kentucky.
- Ee, K. C., Dillon, O. W. and Jawahir, I. S. (2005). "Finite element modeling of residual stresses in machining induced by cutting using a tool with finite edge radius." *International Journal of Mechanical Sciences* 47(10): 1611-1628.
- El-Axir, M. H. and El-Khabeery, M. M. (2003). "Influence of orthogonal burnishing parameters on surface characteristics for various materials." *Journal of Materials Processing Technology* 132(1-3): 82-89.
- El-Tayeb, N. S. M. (1993). The mechanical wear behaviour of burnishing surfaces. Proc. 4th Intern. Conf. on Production Eng. and Des. for Develop., Cairo.
- El-Tayeb, N. S. M. (1994). Frictional behaviour of burnished copper surfaces under dry contact conditions. *Engin. Research Bulletin. HU, Cairo*: 171–184.

- El-Tayeb, N. S. M., Low, K. O. and Brevern, P. V. (2008). "Enhancement of surface quality and tribological properties using ball burnishing process." *Machining Science and Technology* 12(2): 234-248.
- El Wahabi, M., Gavard, L., Montheillet, F., Cabrera, J. M. and Prado, J. M. (2005). "Effect of initial grain size on dynamic recrystallization in high purity austenitic stainless steels." *Acta Materialia* 53(17): 4605-4612.
- Fatemi-Varzaneh, S. M., Zarei-Hanzaki, A. and Beladi, H. (2007). "Dynamic recrystallization in AZ31 magnesium alloy." *Materials Science and Engineering a-Structural Materials Properties Microstructure and Processing* 456(1-2): 52-57.
- Fattouh, M. and Elkhabeery, M. M. (1989). "Residual-stress distribution in burnishing solution treated and Aged 7075 aluminum-alloy." *International Journal of Machine Tools & Manufacture* 29(1): 153-160.
- Filice, L., Micari, F., Rizzuti, S. and Umbrello, D. (2007). "A critical analysis on the friction modelling in orthogonal machining." *International Journal of Machine Tools & Manufacture* 47(3-4): 709-714.
- Fischer, A. (1996). "Well-founded selection of materials for improved wear resistance." *Wear* 194(1-2): 238-245.
- Fischer, A. (2009). "Subsurface microstructural alterations during sliding wear of biomedical metals. Modelling and experimental results." *Computational Materials Science* 46(3): 586-590.
- Fisher, D. A. (2011). "Joint Replacement: <http://www.davidafishermd.com/patients/patienteducation/joint.shtml>."
- Fontana, M. G. and Greene, N. D. (1978). *Corrosion Engineering*. New York, McGraw-Hill.
- Fruehan, R. J. (1998). *The making, shaping and treating of steel (steel making and refining)*, The AISE Steel Foundation.
- Furukawa, M., Horita, Z., Nemoto, M., Valiev, R. Z. and Langdon, T. G. (1996). "Microhardness measurements and the Hall-Petch relationship in an Al-Mg alloy with submicrometer grain size." *Acta Materialia* 44(11): 4619-4629.
- Galvan, D., Pei, Y. T. and De Hosson, J. T. M. (2005). "TEM characterization of a Cr/Ti/TiC graded interlayer for magnetron-sputtered TiC/a-C : H nanocomposite coatings." *Acta Materialia* 53(14): 3925-3934.
- Gardin, C., Courtin, S., Bertheau, D., Bezine, G. and Hamouda, H. B. H. (2007). "The influence of roller burnishing on the fatigue crack propagation in notched round bars - Experimental observations under three-point bending." *Fatigue & Fracture of Engineering Materials & Structures* 30(4): 342-350.
- Germain, M. A., Hatton, A., Williams, S., Matthews, J. B., Stone, M. H., Fisher, J. and Ingham, E. (2003). "Comparison of the cytotoxicity of clinically relevant cobalt-chromium and alumina ceramic wear particles in vitro." *Biomaterials* 24(3): 469-479.

- Gharbi, F., Sghaier, S., Al-Fadhlah, K. J. and Benameur, T. (2011). "Effect of ball burnishing process on the surface quality and microstructure properties of AISI 1010 steel plates." *Journal of Materials Engineering and Performance* 20(6): 903-910.
- Ghosh, R. (2005). Interrupted hard turning with cryogenically cooled ceramic tools ceramic tools *Transactions of the North American Manufacturing Research Institute of SME* 33.
- Graham, A. H. and Youngblo, J. I. (1970). "Work strengthening by a deformation-induced phase transformation in Mp-alloys." *Metallurgical Transactions* 1(2): 423-&.
- Greenwald, A. S., Garino, J. P. and Comm, C. B. E. (2001). "Alternative bearing surfaces: The good, the bad, and the ugly." *Journal of Bone and Joint Surgery-American Volume* 83A: 68-72.
- Grzesik, W. and Zak, K. (2012). "Modification of surface finish produced by hard turning using superfinishing and burnishing operations." *Journal of Materials Processing Technology* 212(1): 315-322.
- Hall, E. O. (1951). "The deformation and ageing of mild steel .3. Discussion of results." *Proceedings of the Physical Society of London Section B* 64(381): 747-753.
- Hallab, N. J. and Jacobs, J. J. (2009). "Biologic effects of implant debris." *Bulletin of the NYU hospital for joint diseases* 67(2): 182-188.
- Hallab, N. J., Jacobs, J. J., Skipor, A., Black, J., Mikecz, K. and Galante, J. O. (1999). Serum protein carriers of chromium in patients with cobalt-base alloy total joint replacement components. West Conshohocken, PA, American Society for Testing and Materials.
- Hamadache, H., Laouar, L., Zeghib, N. E. and Chaoui, K. (2006). "Characteristics of Rb40 steel superficial layer under ball and roller burnishing." *Journal of Materials Processing Technology* 180(1-3): 130-136.
- Hameda, A. A. and Blaz, L. (1998). "Microstructure of hot-deformed Cu-3.45 wt% Ti alloy." *Materials Science and Engineering a-Structural Materials Properties Microstructure and Processing* 254(1-2): 83-89.
- Han, S. I., Melkote, S. N., Haluska, M. S. and Watkins, T. R. (2008). "White layer formation due to phase transformation in orthogonal machining of AISI 1045 annealed steel." *Materials Science and Engineering a-Structural Materials Properties Microstructure and Processing* 488(1-2): 195-204.
- Han, Z., Lu, L. and Lu, K. (2006). "Dry sliding tribological behavior of nanocrystalline and conventional polycrystalline copper." *Tribology Letters* 21(1): 47-52.
- Hashimoto, F., Melkote, S. N., Singh, R. and Kalil, R. (2009). "Effect of finishing methods on surface characteristics and performance of precision components in rolling/sliding contact." *International Journal of Machining and Machinability of Materials* 6: 3-15.



- Hassan, A. M. and AlBsharat, A. S. (1996). "Influence of burnishing process on surface roughness, hardness, and microstructure of some non-ferrous metals." *Wear* 199(1): 1-8.
- Hassan, A. M. and Momani, A. M. S. (2000). "Further improvements in some properties of shot peened components using the burnishing process." *International Journal of Machine Tools & Manufacture* 40(12): 1775-1786.
- Hatherly, M., Malin, A. S., Carmichael, C. M., Humphreys, F. J. and Hirsch, J. (1986). "Deformation processes in hot worked copper and alpha-brass." *Acta Metallurgica* 34(11): 2247-2257.
- Heisel, C., Silva, M. and Schmalzried, T. P. (2003). "Bearing surface options for total hip replacement in young patients." *Journal of Bone and Joint Surgery-American* Volume 85A(7): 1366-1379.
- Ho, J. W., Noyan, C., Cohen, J. B., Khanna, V. D. and Eliezer, Z. (1983). "Residual-stresses and sliding wear." *Wear* 84(2): 183-202.
- Hong, S. Y. and Zhao, Z. (1999). "Thermal aspects, material considerations and cooling strategies in cryogenic machining." *Clean Products and Processes* 1: 107-116.
- Howie, D. W., McCalden, R. W., Nawana, N. S., Costi, K., Pearcy, M. J. and Subramanian, C. (2005). "The long-term wear of retrieved McKee-Farrar metal-on-metal total hip prostheses." *Journal of Arthroplasty* 20(3): 350-357.
- Huang, J. Y., Wu, Y. K. and Ye, H. Q. (1995). "Phase-transformation of cobalt-induced by ball-milling." *Applied Physics Letters* 66(3): 308-310.
- Huang, P. and Lopez, H. F. (1999). "Effects of grain size on development of athermal and strain induced epsilon martensite in Co-Cr-Mo implant alloy." *Materials Science and Technology* 15(2): 157-164.
- Iglesias, P., Bermudez, M. D., Moscoso, W., Rao, B. C., Shankar, M. R. and Chandrasekar, S. (2007). "Friction and wear of nanostructured metals created by large strain extrusion machining." *Wear* 263: 636-642.
- Immarigeon, J. P., Rajan, K. and Wallace, W. (1984). "Microstructural changes during isothermal forging of a Co-Cr-Mo alloy." *Metallurgical Transactions a-Physical Metallurgy and Materials Science* 15(2): 339-345.
- Ingham, E. and Fisher, J. (2000). "Biological reactions to wear debris in total joint replacement." *Proceedings of the Institution of Mechanical Engineers Part H- Journal of Engineering in Medicine* 214(H1): 21-37.
- James, M. N., Hughes, D. J., Chen, Z., Lombard, H., Hattingh, D. G., Asquith, D., Yates, J. R. and Webster, P. J. (2007). "Residual stresses and fatigue performance." *Engineering Failure Analysis* 14(2): 384-395.
- Jang, D. Y., Watkins, T. R., Kozaczek, K. J., Hubbard, C. R. and Cavin, O. B. (1996). "Surface residual stresses in machined austenitic stainless steel." *Wear* 194(1-2): 168-173.

- Jawahir, I. S., Brinksmeier, E., M'Saoubi, R., Aspinwall, D. K., Outeiro, J. C., Meyer, D., Umbrello, D. and Jayal, A. D. (2011). "Surface integrity in material removal processes: Recent advances." *Cirp Annals-Manufacturing Technology* 60(2): 603-626.
- Jawahir, I. S., Dillon, O. W., Rouch, K. E., Joshi, K. J., Venkatachalam, A. and Jaafar, I. H. (2006). Total Life-cycle considerations in product design for sustainability: A framework for comprehensive evaluation. 10th Int. Research/Expert Conf., Barcelona, Spain.
- Jayal, A. D., Umbrello, D., Dillon, O. W., Jr. and Jawahir, I. S. (2010). "An investigation of the effects of cutting conditions, tool edge geometry and workpiece hardness on surface integrity in orthogonal machining of AISI 52100 steel." *Transactions of NAMRI/SME* 38: 57–64.
- Jayaraman, N., Hornbach, D. and Prevey, P. S. (2007). Mitigation of fatigue and pre-cracking damage in aircraft structures through low plasticity burnishing. Proc. ASIP. Palm Springs, CA.
- Jiang, X. P., Wang, X. Y., Lia, J. X., Li, D. Y., Man, C. S., Shepard, M. J. and Zhai, T. (2006). "Enhancement of fatigue and corrosion properties of pure Ti by sandblasting." *Materials Science and Engineering a-Structural Materials Properties Microstructure and Processing* 429(1-2): 30-35.
- Johnson, K. L. (1985). *Contact Mechanics*, Cambridge University Press.
- Johnson, W. A. and Mehl, R. F. (1939). "Reaction kinetics in processes of nucleation and growth." *Transactions of the American Institute of Mining and Metallurgical Engineers* 135: 416-442.
- Jonas, J. J., Quelennec, X., Jiang, L. and Martin, E. (2009). "The Avrami kinetics of dynamic recrystallization." *Acta Materialia* 57(9): 2748-2756.
- Kamikawa, N., Sakai, T. and Tsuji, N. (2007). "Effect of redundant shear strain on microstructure and texture evolution during accumulative roll-bonding in ultralow carbon IF steel." *Acta Materialia* 55(17): 5873-5888.
- Karch, J., Birringer, R. and Gleiter, H. (1987). "Ceramics ductile at low-temperature." *Nature* 330(6148): 556-558.
- Karimpoor, A. A., Erb, U., Aust, K. T. and Palumbo, G. (2003). "High strength nanocrystalline cobalt with high tensile ductility." *Scripta Materialia* 49(7): 651-656.
- Kenda, J., Pusavec, F. and Kopac, J. (2011). "Analysis of residual stresses in sustainable cryogenic machining of nickel based alloy -Inconel 718." *Journal of Manufacturing Science and Engineering-Transactions of the Asme* 133(4).
- Khan, A. A. and Ahmed, M. I. (2008). "Improving tool life using cryogenic cooling." *Journal of Materials Processing Technology* 196(1-3): 149-154.
- Klocke, F. and Krieg, T. (1999). "Coated tools for metal cutting - Features and Applications." *Annals of the CIRP* 42(2): 515-525.

- Korzynski, M. (2007). Smoothing slide burnishing. Warszawa.
- Korzynski, M. (2009). "A model of smoothing slide ball-burnishing and an analysis of the parameter interaction." *Journal of Materials Processing Technology* 209(1): 625-633.
- Korzynski, M., Lubas, J., Swirad, S. and Dudek, K. (2011). "Surface layer characteristics due to slide diamond burnishing with a cylindrical-ended tool." *Journal of Materials Processing Technology* 211(1): 84-94.
- Kumar, K. V. B. S. K. and Choudhury, S. K. (2008). "Investigation of tool wear and cutting force in cryogenic machining using design of experiments." *Journal of Materials Processing Technology* 203(1-3): 95-101.
- Kurosu, S., Li, Y. P., Matsumoto, H. and Chiba, A. (2010a). "Grain refining technique and mechanical properties of the biomedical Co-Cr-Mo alloy." *Materials Science Forum* 654-656: 2184-2187.
- Kurosu, S., Matsumoto, H. and Chiba, A. (2010b). "Grain refinement of biomedical Co-27Cr-5Mo-0.16N alloy by reverse transformation." *Materials Letters* 64(1): 49-52.
- Kustas, F. M., Fehrenbacher, L. L. and Komanduri, R. (1997). "Nanocoatings on cutting tools for dry machining." *Annals of the CIRP* 46(1): 39-42.
- Langford, G. and Cohen, M. (1969). "Strain hardening of iron by severe plastic deformation." *Asm Transactions Quarterly* 62(3): 623-&.
- Lawsuits & Legal News (2012).  
["http://www.lawyersandsettlements.com/case/hip\\_and\\_knee\\_replacement\\_implant\\_failure.html."](http://www.lawyersandsettlements.com/case/hip_and_knee_replacement_implant_failure.html)
- Le Gall, R. and Jonas, J. J. (1999). "Solute drag effects during the dynamic recrystallization of nickel." *Acta Materialia* 47(17): 4365-4374.
- Lee, R. Y. and Eliezer, Z. (1984). "On the critical film thickness of protective films at sliding interfaces." *Wear* 95: 165-175.
- Lee, S. H., Saito, Y., Tsuji, N., Utsunomiya, H. and Sakai, T. (2002). "Role of shear strain in ultragrain refinement by accumulative roll-bonding (ARB) process." *Scripta Materialia* 46(4): 281-285.
- Leskovar, P. and Peklenik, J. (1981). "Influence affecting surface integrity in the cutting process." *Ann. CIRP* 245-248.
- Li, B. Y., Mukasyan, A. and Varma, A. (2003). "Combustion synthesis of CoCrMo orthopedic implant alloys: microstructure and properties." *Materials Research Innovations* 7(4): 245-252.
- Li, W. L., Tao, N. R. and Lu, K. (2008). "Fabrication of a gradient nano-micro-structured surface layer on bulk copper by means of a surface mechanical grinding treatment." *Scripta Materialia* 59(5): 546-549.
- Liang, G. L. and Yuan, S. Q. (2008). "Study on the temperature measurement of AZ31B Magnesium Alloy in Gas Tungsten Arc Welding." *Materials Letters* 62(16): 2282-2284.

- Lippard, H. E. and Kennedy, R. L. (1999). Process metallurgy of wrought Co-Cr-Mo alloy. West Conshohocken, PA, American Society for Testing and Materials.
- Loh, N. H., Tam, S. C. and Miyazawa, S. (1989a). "Statistical-Analyses of the Effects of Ball Burnishing Parameters on Surface Hardness." *Wear* 129(2): 235-243.
- Loh, N. H., Tam, S. C. and Miyazawa, S. (1989b). "A Study of the Effects of Ball-Burnishing Parameters on Surface-Roughness Using Factorial Design." *Journal of Mechanical Working Technology* 18(1): 53-61.
- Lopez, L. N., Lamikiz, A., Sanchez, J. A. and Arana, J. L. (2007). "The effect of ball burnishing on heat-treated steel and Inconel 718 milled surfaces." *International Journal of Advanced Manufacturing Technology* 32(9-10): 958-968.
- Lu, Z., Xu, Y. B. and Hu, Z. Q. (1997). "Low cycle fatigue behaviour of a DZX40M directionally solidified co-base superalloy." *Acta Metall. Sin.* A33: 1239-1245.
- Lu, Z., Xu, Y. B. and Hu, Z. Q. (1999). "Evolution of dislocation structure induced by cyclic deformation in a directionally solidified cobalt base superalloy." *Materials Science and Technology* 15(2): 165-168.
- Luca, L., Neagu-Ventzel, S. and Marinescu, I. (2005). "Effects of working parameters on surface finish in ball-burnishing of hardened steels." *Precision Engineering-Journal of the International Societies for Precision Engineering and Nanotechnology* 29(2): 253-256.
- Luo, H. Y., Liu, J. Y., Wang, L. J. and Zhong, Q. P. (2006). "The effect of burnishing parameters on burnishing force and surface microhardness." *International Journal of Advanced Manufacturing Technology* 28(7-8): 707-713.
- M'Saoubi, R., Outeiro, J. C., Chandrasekaran, H., Dillon Jr., O. W. and Jawahir, I. S. (2008). "A review of surface integrity in machining and its impact on functional performance and life of machined products." *Int. J. Sustainable Manufacturing* 1: 203-236.
- Majzoobia, G. H., Azadikhahb, K. and Nematia, J. (2009). "The effects of deep rolling and shot penning on fretting fatigue resistance of Aluminum-7075-T6." *Mater. Sci. Eng.* 516: 235-247.
- Marshall, A., Ries, M. D., Paprosky, W. and Clinic, I. W. S. (2008). "How prevalent are implant wear and osteolysis, and how has the scope of osteolysis changed since 2000?" *Journal of the American Academy of Orthopaedic Surgeons* 16: S1-S6.
- Martin, J. W. (2006). *Concise encyclopedia of the structure of materials*, Elsevier Science.
- Maximov, J. T., Kuzmanov, T. V., Duncheva, G. V. and Ganev, N. (2009). "Spherical motion burnishing implemented on lathes." *International Journal of Machine Tools & Manufacture* 49(11): 824-831.
- Medina, J. (2012). "Structure of the hip joint, [http://www.ehow.com/facts\\_5180731\\_structure-hip-joint.html](http://www.ehow.com/facts_5180731_structure-hip-joint.html)."
- Medina, S. F. and Hernandez, C. A. (1996). "Modelling of the dynamic recrystallization of austenite in low alloy and microalloyed steels." *Acta Materialia* 44(1): 165-171.

- Meng, Q. P., Rong, Y. H. and Hsu, T. Y. (2002). "The structural stability in nano-sized crystals of metals." *Science in China* 5(5): 485-494.
- Mishra, A. K., Hamby, M. A. and Kaiser, W. B. (1999). *Metallurgy, microstructure, chemistry and mechanical properties of a new grade of cobalt-chromium alloy before and after porous-coating*. West Conshohocken, PA.
- Nalla, R. K., Altenberger, I., Noster, U., Liu, G. Y., Scholtes, B. and Ritchie, R. O. (2003). "On the influence of mechanical surface treatments - deep rolling and laser shock peening - on the fatigue behavior of Ti-6Al-4V at ambient and elevated temperatures." *Materials Science and Engineering a-Structural Materials Properties Microstructure and Processing* 355(1-2): 216-230.
- National Council for Advanced Manufacturing (2009). "Sustainable Manufacturing, <http://nacfam02.dev.web.sba.com/PolicyInitiatives/SustainableManufacturing/tabid/64/Default.aspx>".
- Nevelos, J., Shelton, J. C. and Fisher, J. (2004). "Metallurgical considerations in the wear of metal-on-metal hip bearings." *Hip International* 14(1): 1-10.
- Ni, H., Elmadagli, M. and Alpas, A. T. (2004). "Mechanical properties and microstructures of 1100 aluminum subjected to dry machining." *Materials Science and Engineering a-Structural Materials Properties Microstructure and Processing* 385(1-2): 267-278.
- NIAMS (2011). "National institute of arthritis and musculoskeletal and skin diseases, [http://www.niams.nih.gov/news\\_and\\_events/Press\\_Releases/2011/12\\_22.asp](http://www.niams.nih.gov/news_and_events/Press_Releases/2011/12_22.asp)."
- Niberg, A. N. (1987). "Wear resistance of sideways strengthened by burnishing." *Soviet Engineering Research* 7(5).
- Nieh, T. G. and Wadsworth, J. (1991). "Hall-Petch relation in nanocrystalline solids." *Scripta Metallurgica Et Materialia* 25(4): 955-958.
- Nieh, T. G., Wadsworth, J. and Wakai, F. (1991). "Recent Advances in Superplastic Ceramics and Ceramic Composites." *International Materials Reviews* 36(4): 146-161.
- Nikitin, I., Altenberger, I., Maier, H. J. and Scholtes, B. (2005). "Mechanical and thermal stability of mechanically induced near-surface nanostructures." *Materials Science and Engineering A* 403(1-2): 318-327.
- Noyan, I. C. and Cohen, J. B. (1987). *Residual stress: measurement by diffraction and interpretation*. New York, N.Y., Springer.
- O'Sullivan, D. and Cotterell, M. (2002). *Workpiece temperature measurement in machining*. Proc. of the Institution of Mechanical Engineers. Part B. J. Engi. Manuf.
- Olson, G. B. and Cohen, M. (1975). "Kinetics of strain-induced martensitic nucleation." *Metallurgical Transactions A* 6(4): 791-795.

- Outeiro, J. C., Pina, J. C., M'Saoubi, R., Pusavec, F. and Jawahir, I. S. (2008). "Analysis of residual stresses induced by dry turning of difficult-to-machine materials." *Cirp Annals-Manufacturing Technology* 57(1): 77-80.
- Palka, K., Weronki, A. and Zaleski, K. (2006). "Mechanical properties and corrosion resistance of burnished X5CrNi 18-9 stainless steel." *Journal of Achievements in Materials and Manufacturing Engineering*: 57–62.
- Papsev, D. D. (1978). *Finishing & hardening with cold working*. Moskva.
- Park, J. B. and Kim, B. K. (2003). *Metallic biomaterials, ceramic biomaterials. Biomaterials principles and applications*, Boca Raton, CRC Press.
- Petch, N. J. (1953). "The cleavage strength of polycrystals." *Journal of the Iron and Steel Institute* 174(1): 25-28.
- Pezzotti, G., Takahashi, Y., Zhu, W. and Sugano, N. (2012). "In-depth profiling of elastic residual stress and the in vivo wear mechanism of self-mating alumina hip joints." *Wear*.
- Pickering, F. B. (1978). *Physical metallurgy and the design of steels*. Essex, Applied Science.
- Prev éy, P. S. (2000). The effect of cold work on the thermal stability of residual compression in surface enhanced. The effect of cold work on the thermal stability of residual compression in surface enhanced, St. Louis, Missouri.
- Prev éy, P. S., Shepard, M. J. and Smith, P. R. (2001). The effect of low plasticity burnishing (LPB) on the HCF performance and fod resistance of Ti-6Al-4V. Sixth National Turbine Engine High Cycle Fatigue (HCF) Conference, Jacksonville, FL.
- Prev éy, P. S., Telesman, J., Kantzos, P. and Gabb, T. (2000). Fod resistance and fatigue crack arrest in low plasticity burnished IN718. Fifth National Turbine Engine High Cycle Fatigue Conference Chandler, AZ.
- Prevey, P., Hornbach, D., Maston, P., Jacobs, T. and Commett, J. (2001). Low cost surface enhancement method for improved fatigue life of superalloys at engine temperature. NAS3-99116 SBIR, NASA Final Report.
- Prevey, P., Telesman, J., Gabb, T. and Kantzos, P. (2000). FOD resistance and fatigue crack arrest in low plasticity burnished IN718. Proceedings of the 5th Nat. Turbine Eng. HCF Conf.
- Przybylski, W. (1987). *Burnishing Technology*. Warszawa.
- Pu, Z. (2012). Cryogenic machining and burnishing of AZ31B magnesium alloy for enhanced surface integrity and functional performance. PhD, University of Kentucky.
- Pu, Z., Outeiro, J. C., Batista, A. C., Dillon Jr, O. W., Puleo, D. A. and Jawahir, I. S. (2012a). "Enhanced surface integrity of AZ31B Mg alloy by cryogenic machining towards improved functional performance of machined components." *International Journal of Machine Tools and Manufacture* 56: 17–27.

- Pu, Z., Puleo, D. A., Dillon, J., O.W. and Jawahir, I. S. (2011a). Controlling the biodegradation rate of magnesium-based implants through surface nanocrystallization induced by cryogenic machining. *Proc. of Magnesium Tech.* 2011.
- Pu, Z., Song, G. L., Yang, S., Outeiro, J. C., Dillon, O. W., Puleo, D. A. and Jawahir, I. S. (2012b). "Grain refined and basal textured surface produced by burnishing for improved corrosion performance of AZ31B Mg alloy." *Corrosion Science* 57: 192-201.
- Pu, Z., Yang, S., Song, G. L., Dillon, O. W., Puleo, D. A. and Jawahir, I. S. (2011b). "Ultrafine-grained surface layer on Mg-Al-Zn alloy produced by cryogenic burnishing for enhanced corrosion resistance." *Scripta Materialia* 65(6): 520-523.
- Pusavec, F., Deshpande, A., Yang, S., M'Saoubi, R., Kopac, J., Dillon, J., O.W. and Jawahir, I. S. Sustainable machining of high temperature nickel alloy – Inconel 718: predictive performance models and optimization.
- Qi, Z. Q., Jiang, J. C. and Meletis, E. I. (2009). "Wear mechanism of nanocrystalline metals." *Journal of Nanoscience and Nanotechnology* 9(7): 4227-4232.
- Quelebec, X., Bozzolo, N., Jonas, J. J. and Loge, R. (2011). "A new approach to modeling the flow curve of hot deformed austenite." *Isij International* 51(6): 945-950.
- Röttger, K. (2002). *Walzen hartgedrehter Oberflächen*. Ph.D Dissertation, Technical University of Aachen.
- Rabinowicz, E. (1995). *Friction and wear of materials*. New York, John Wiley and Sons.
- Radziejewska BN, J. and Kalita, W. (2005). "Hybrid method for modification of surface layer." *Trnava, Slovakia*: 111–116.
- Radziejewska, J., Nowicki, B. and Kalita, W. (2005). Hybrid method for modification of surface layer. *Proc. 13th International Scientific Conference CO-MAT-TECH*, Trnava, Slovakia.
- Radziejewska, J. and Skrzypek, S. J. (2009). "Microstructure and residual stresses in surface layer of simultaneously laser alloyed and burnished steel." *Journal of Materials Processing Technology* 209(4): 2047-2056.
- Rajan, K. (1982). "Phase-transformations in a wrought Co-Cr-Mo-C alloy." *Metallurgical Transactions a-Physical Metallurgy and Materials Science* 13(7): 1161-1166.
- Rajan, K. and Vandersande, J. B. (1982). "Room-Temperature Strengthening Mechanisms in a Co-Cr-Mo-C Alloy." *Journal of Materials Science* 17(3): 769-778.
- Ramesh, A. and Melkote, S. N. (2008). "Modeling of white layer formation under thermally dominant conditions in orthogonal machining of hardened AISI 52100 steel." *International Journal of Machine Tools & Manufacture* 48(3-4): 402-414.
- Rao, D. S., Hebbar, H. S., Komaraiah, M. and Kempaiah, U. N. (2008). "Investigations on the effect of ball burnishing parameters on surface hardness and wear

- resistance of HSLA dual-phase steels." *Materials and Manufacturing Processes* 23(3-4): 295-302.
- Ratner, B. D., Hoffman, A. S., Schoen, F. J. and Lemons, J. E. (1996). *Biomaterials science - An introduction to materials in medicine*. Toronto, Academic Press.
- Ray, A. E., Smith, S. R. and Scofield, I. D. (1991). "Study of the phase transformation of cobalt." *Journal of Phase Equilibria* 12(6).
- Rodriguez, A., de Lacalle, L. N. L., Celaya, A., Lamikiz, A. and Albizuri, J. (2012). "Surface improvement of shafts by the deep ball-burnishing technique." *Surface & Coatings Technology* 206(11-12): 2817-2824.
- Ryan, N. D. and McQueen, H. J. (1990). "Dynamic softening mechanisms in 304 austenitic stainless-steel." *Canadian Metallurgical Quarterly* 29(2): 147-162.
- Sage, M. and Guillaud, C. (1950). "Relation entre la structure cristalline et les propriétés magnétiques des ferrites mixtes de nickel et de zinc." *Comptes Rendus Hebdomadaires Des Séances De L Academie Des Sciences* 230(20): 1751-1753.
- Saito, Y., Utsunomiya, H., Tsuji, N. and Sakai, T. (1999). "Novel ultra-high straining process for bulk materials - Development of the accumulative roll-bonding (ARB) process." *Acta Materialia* 47(2): 579-583.
- Salahshoor, M. and Guo, Y. B. (2011). "Surface integrity of biodegradable Magnesium-Calcium orthopedic implant by burnishing." *Journal of the Mechanical Behavior of Biomedical Materials* 4(8): 1888-1904.
- Saldívar-García, A. J. and López, H. F. (2005). "Microstructural effects on the wear resistance of wrought and as-cast Co-Cr-Mo-C implant alloys." *Journal of Biomedical Materials Research Part A* 74A(2): 269-274.
- Saleski, W. J., Fisher, R. M., Ritchie, R. O. and Thomas, G. (1983). *The nature and origin of sliding wear debris from steels*. Proceedings of the Conference on Wear of Materials, Reston, VA, USA, ASME.
- Salinas-Rodríguez, A. (1999). *The role of the FCC-HCP phase transformation during the plastic deformation of Co-Cr-Mo-C alloys for biomedical applications*. Cobalt-Base Alloys for Biomedical Applications, ASTM STP 1365. J. A. Disegi, R. L. K., R. Piiliar. West Conshohocken, PA, American Society for Testing and Materials.
- Sarkar, A., Chakravarty, J. K., Paul, B. and Suri, A. K. (2011). "Kinetics of dynamic recrystallization in cobalt: A study using the Avrami relation." *Physica Status Solidi a-Applications and Materials Science* 208(4): 814-818.
- Sarkar, A. D. (1976). *Wear of Metals*. Oxford, Pergamon Press.
- Sasahara, H. (2005). "The effect on fatigue life of residual stress and surface hardness resulting from different cutting conditions of 0.45% C steel." *International Journal of Machine Tools & Manufacture* 45(2): 131-136.
- Sato, M., Tsuji, N., Minamino, Y. and Koizumi, Y. (2004). "Formation of nanocrystalline surface layers in various metallic materials by near surface severe plastic deformation." *Science and Technology of Advanced Materials* 5(1-2): 145-152.



- Seemikeri, C. Y., Brahmankar, P. K. and Mahagaonkar, S. B. (2008). "Investigations on surface integrity of AISI 1045 using LPB tool." *Tribology International* 41(8): 724-734.
- Segawa, T., Sasahara, H. and Tsutsumi, M. (2004). "Development of a new tool to generate compressive residual stress within a machined surface." *International Journal of Machine Tools & Manufacture* 44(11): 1215-1221.
- Sellars, C. M. (1990). "Modeling microstructural development during hot-rolling." *Materials Science and Technology* 6(11): 1072-1081.
- Sellars, C. M. and Zhu, Q. (2000). "Microstructural modelling of aluminium alloys during thermomechanical processing." *Materials Science and Engineering A-Structural Materials Properties Microstructure and Processing* 280(1): 1-7.
- Senthilkumar, D., Rajendran, I., Pellizzari, M. and Siirainen, J. (2011). "Influence of shallow and deep cryogenic treatment on the residual state of stress of 4140 steel." *Journal of Materials Processing Technology* 211(3): 396-401.
- Shekhar, S., Abolghasem, S., Basu, S., Cai, J. and Shankar, M. R. (2012). "Effect of severe plastic deformation in machining elucidated via rate-strain-microstructure mappings." *Journal of Manufacturing Science and Engineering-Transactions of the Asme* 134(3).
- Sherby, O. D. and Wadsworth, J. (1989). "Superplasticity - Recent advances and future directions." *Progress in Materials Science* 33(3): 169-221.
- Shi, Y. N. and Han, Z. (2008). "Tribological behaviors of nanostructured surface layer processed by means of surface mechanical attrition treatment." *Key Eng. Mater.* 384: 321-334.
- Shingo Kurosu, Y. L., Hiroaki Matsumoto and Akihiko Chiba (2010). "Grain refining technique and mechanical properties of the biomedical Co-Cr-Mo alloy." *Materials Science Forum* 654-656: 2184-2187.
- Shiou, F. J. and Hsu, C. C. (2008). "Surface finish of hardened and tempered stainless tool steel using sequential ball grinding, ball burnishing and ball polishing processes on a machining centre." *Journal of Materials Processing Technology* 205: 249-258.
- Silva, M., Heisel, C. and Schmalzried, T. P. (2005). "Metal-on-metal total hip replacement." *Clinical Orthopaedics and Related Research*(430): 53-61.
- Sims, C. T. (1968). "A contemporary view of Cobalt-based alloys." *Journal of Metals* 21: 27-42.
- Skalski, K., Morawski, A. and Przybylski, W. (1995). "Analysis of contact elastic-plastic strains during the process of burnishing." *International Journal of Mechanical Sciences* 37(5): 461-472.
- Srinivasa Rao, D., Suresh Hebbar, H., Komaraiah, M. and Kempaiah, U. N. (2008). "Investigations on the effect of ball burnishing parameters on surface hardness

- and wear resistance of HSLA dual-phase steels." *Materials and Manufacturing Processes* 23: 295–302.
- St. John, K. R., Poggie, R. A., Zardiackas, L. D. and Afflitto, R. M. (1999). Comparison of two Cobalt-based alloys for use in metal-on-metal hip prostheses: evaluation of the wear properties in a simulator. *Cobalt-Base Alloys for Biomedical Applications*, ASTMSTP 1365. West Conshohocken, PA, American Society for Testing and Materials.
- Stoot, F. H., Stevenson, C. W. and Wood, G. C. (1977). "Friction and wear properties of Stellite 31 at temperatures from 293 to 1073 K." *Metals Technol.* 4: 66-74.
- Subramanian, S. V., Gekonde, H. O., Zhu, G. and Zhang, X. (2002). "Role of microstructural softening events in metal cutting." *Machining Science and Technology* 6(3): 353-364.
- Sullivan, J. L. (1987). The role of oxides in the protection of tribological surfaces. Parts I and II. *Proceedings of the Conference on Tribology — Friction, Lubrication, and Wear*, London, England, IMechE Publ. Ltd.
- Sury, P. and Semlitsch, M. (1978). "Corrosion behavior of cast and forged Cobalt-based alloys for double-alloy joint endoprostheses." *Journal of Biomedical Materials Research* 12(5): 723-741.
- Swaminathan, S., Brown, T. L., Chandrasekar, S., McNelley, T. R. and Compton, W. D. (2007a). "Severe plastic deformation of copper by machining: Microstructure refinement and nanostructure evolution with strain." *Scripta Materialia* 56(12): 1047-1050.
- Swaminathan, S., Shankar, M. R., Rao, B. C., Compton, W. D., Chandrasekar, S., King, A. H. and Trumble, K. P. (2007b). "Severe plastic deformation (SPD) and nanostructured materials by machining." *Journal of Materials Science* 42(5): 1529-1541.
- Takeuchi, S. (2001). "The mechanism of the inverse Hall-Petch relation of nanocrystals." *Scripta Materialia* 44(8-9): 1483-1487.
- Tao, N. R., Wang, Z. B., Tong, W. P., Sui, M. L., Lu, J. and Lu, K. (2002). "An investigation of surface nanocrystallization mechanism in Fe induced by surface mechanical attrition treatment." *Acta Materialia* 50(18): 4603-4616.
- Teoh, S. H. (2000). "Fatigue of biomaterials: A review." *International Journal of Fatigue* 22(10): 825-837.
- Thiele, J. D., Melkote, S. N., Peascoe, R. A. and Watkins, T. R. (2000). "Effect of cutting edge geometry and workpiece hardness on surface residual stresses in finish hard turning of AISI 2100 steel." *J. Manuf. Sci. Eng.* 122: 642–649.
- Torbilo, V. M. (1974). *Diamond Burnishing*. Moskva.
- Torrente, G., Torres, M. and Sanoja, L. (2011). "Effect of the strain rate in the dynamic recrystallization of ETP copper during its hot compression with descending temperatures." *Revista De Metalurgia* 47(6): 485-496.

- Tsuji, N. and Maki, T. (2009). "Enhanced structural refinement by combining phase transformation and plastic deformation in steels." *Scripta Materialia* 60(12): 1044-1049.
- Tsuji, N., Saito, Y., Lee, S. H. and Minamino, Y. (2003). "ARB (accumulative roll-bonding) and other new techniques to produce bulk ultrafine grained materials." *Advanced Engineering Materials* 5(5): 338-344.
- Tsuji, N., Tanaka, S. and Takasugi, T. (2008). "Evaluation of surface-modified Ti-6Al-4V alloy by combination of plasma-carburizing and deep-rolling." *Materials Science and Engineering a-Structural Materials Properties Microstructure and Processing* 488(1-2): 139-145.
- Tsuji, N., Tanaka, S. and Takasugi, T. (2009). "Effect of combined plasma-carburizing and deep-rolling on notch fatigue property of Ti-6Al-4V alloy." *Materials Science and Engineering a-Structural Materials Properties Microstructure and Processing* 499(1-2): 482-488.
- Umbrello, D. (2004). *FE – Analysis of machining processes: innovative experimental techniques for results assessing*. PhD, University of Calabria.
- Umbrello, D. (2008). "Finite element simulation of conventional and high speed machining of Ti6Al4V alloy." *Journal of Materials Processing Technology* 196(1-3): 79-87.
- Umbrello, D., M'Saoubi, R. and Outeiro, J. C. (2007). "The influence of Johnson-Cook material constants on finite element simulation of machining of AISI 316L steel." *International Journal of Machine Tools & Manufacture* 47(3-4): 462-470.
- Umbrello, D., Yang, S., Dillon, J. O. W. and Jawahir, I. S. (2012). "The effects of cryogenic cooling on surface layer alterations in machining of AISI 52100 steels." *Materials Science and Technology*, In press.
- US Department of Commerce (2009). "How does commerce define sustainable manufacturing?, [http://www.trade.gov/competitiveness/sustainablemanufacturing/how\\_doc\\_defines\\_SM.asp](http://www.trade.gov/competitiveness/sustainablemanufacturing/how_doc_defines_SM.asp)."
- Valiev, R. Z., Alexandrov, I. V., Enikeev, N. A., Murashkin, M. Y. and Semenova, I. P. (2010). "Towards enhancement of properties of UFG metals and alloys by grain boundary engineering using SPD processing." *Reviews on Advanced Materials Science* 25(1): 1-10.
- Valiev, R. Z., Krasilnikov, N. A. and Tsenev, N. K. (1991). "Plastic-deformation of alloys with submicron-grained structure." *Materials Science and Engineering a-Structural Materials Properties Microstructure and Processing* 137: 35-40.
- Vandamme, N. S. and Topoleski, L. D. T. (2005). "Control of surface morphology of carbide coating on Co-Cr-Mo implant alloy." *Journal of Materials Science-Materials in Medicine* 16(7): 647-654.

- Vander Sande, J. B., Coke, J. R., and Wulf J. (1976). "Transmission electron microscopy study of the mechanisms of strengthening in heat treated Co-Cr-Mo-C alloys." *Metallurgical Transactions A* 7A: 389-397.
- Villegas, J. C., Shaw, L. L., Dai, K., Yuan, W., Tian, J., Liaw, P. K. and Klarstrom, D. L. (2005). "Enhanced fatigue resistance of a nickel-based hastelloy induced by a surface nanocrystallization and hardening process." *Philosophical Magazine Letters* 85(8): 427-437.
- Voevodin, A. A. and Zabinski, J. S. (2000). "Supertough wear-resistant coatings with 'chameleon' surface adaptation." *Thin Solid Films* 370(1-2): 223-231.
- Wang, A., Yue, S., Boby, J. D., Chan, F. W. and Medley, J. B. (1999). "Surface characterization of metal-on-metal hip implants tested in a hip simulator." *Wear* 225: 708-715.
- Wang, Z. B., Tao, N. R., Li, S., Wang, W., Liu, G., Lu, J. and Lu, K. (2003a). "Effect of surface nanocrystallization on friction and wear properties in low carbon steel." *Materials Science and Engineering a-Structural Materials Properties Microstructure and Processing* 352(1-2): 144-149.
- Wang, Z. B., Tao, N. R., Li, S., Wang, W., Liu, G., Luc, J. and Lu, K. (2003b). "Effect of surface nanocrystallization on friction and wear properties in low carbon steel." *Materials Science and Engineering a-Structural Materials Properties Microstructure and Processing* 352(1-2): 144-149.
- Wang, Z. Y. and Rajurkar, K. P. (1997). "Wear of CBN tool in turning of silicon nitride with cryogenic cooling." *International Journal of Machine Tools & Manufacture* 37(3): 319-326.
- Wang, Z. Y. and Rajurkar, K. P. (2000). "Cryogenic machining of hard-to-cut materials." *Wear* 239(2): 168-175.
- Wang, Z. Y., Rajurkar, K. P., Fan, J., Lei, S., Shin, Y. C. and Petreanu, G. (2003c). "Hybrid machining of Inconel 718." *International Journal of Machine Tools & Manufacture* 43(13): 1391-1396.
- Weinert, K., Inasaki, I., Sutherland, J. W. and Wakabayashi, T. (2004). "Dry machining and minimum quantity lubrication." *Cirp Annals-Manufacturing Technology* 53(2): 511-537.
- Wilson, G. S., Grandt, A. F., Bucci, R. J. and Schultz, R. W. (2009). "Exploiting bulk residual stresses to improve fatigue crack growth performance of structures." *International Journal of Fatigue* 31(8-9): 1286-1299.
- Wimmer, M. A., Loos, J., Nassutt, R., Heitkemper, M. and Fischer, A. (2001). "The acting wear mechanisms on metal-on-metal hip joint bearings: in vitro results." *Wear* 250: 129-139.
- Wimmer, M. A., Sprecher, C., Hauert, R., Tager, G. and Fischer, A. (2003). "Tribochemical reaction on metal-on-metal hip joint bearings - A comparison between in-vitro and in-vivo results." *Wear* 255: 1007-1014.

- Wright, T. M. and Goodman, S. B. (1996). "Implant wear: The future of total joint replacement." American Academy of Orthopaedic Surgeons, Rosemont.
- Wu, X., Tao, N., Hong, Y., Liu, G., Xu, B., Lu, J. and Lu, K. (2005). "Strain-induced grain refinement of cobalt during surface mechanical attrition treatment." *Acta Materialia* 53(3): 681-691.
- Xiao, G. H., Tao, N. R. and Lu, K. (2008). "Effects of strain, strain rate and temperature on deformation twinning in a Cu-Zn alloy." *Scripta Materialia* 59(9): 975-978.
- Yamagata, H., Ohuchida, Y., Saito, N. and Otsuka, M. (2001). "Nucleation of new grains during discontinuous dynamic recrystallization of 99.998 mass% aluminum at 453 K." *Scripta Materialia* 45(9): 1055-1061.
- Yamanaka, K., Mori, M., Kurosu, S., Matsumoto, H. and Chiba, A. (2009). "Ultrafine grain refinement of biomedical Co-29Cr-6Mo alloy during conventional hot-compression deformation." *Metallurgical and Materials Transactions a-Physical Metallurgy and Materials Science* 40A(8): 1980-1994.
- Yanagimoto, J., Karhausen, K., Brand, A. J. and Kopp, R. (1998). "Incremental formulation for the prediction of flow stress and microstructural change in hot forming." *Journal of Manufacturing Science and Engineering-Transactions of the Asme* 120(2): 316-322.
- Yang, S., Puleo, D. A., Dillon, J., O.W. and Jawahir, I. S. (2011). "Surface layer modifications in Co-Cr-Mo biomedical alloy from cryogenic burnishing." *Procedia Engineering* 19: 383-388.
- Yeldose, B. C. and Ramamoorthy, B. (2008). "An investigation into the high performance of TiN-coated rollers in burnishing process." *Journal of Materials Processing Technology* 207(1-3): 350-355.
- Yen, Y. C., Sartkulvanich, P. and Altan, T. (2005). "Finite element modeling of roller burnishing process." *Cirp Annals-Manufacturing Technology* 54(1): 237-240.
- Zahiri, S. H., Davies, C. H. J. and Hodgson, P. D. (2005). "A mechanical approach to quantify dynamic recrystallization in polycrystalline metals." *Scripta Materialia* 52(4): 299-304.
- Zener, C. and Hollomon, J. H. (1946). "Problems in non-elastic deformation of metals." *Journal of Applied Physics* 17(2): 69-82.
- Zhang, P. and Lindemann, J. (2005). "Effect of roller burnishing on the high cycle fatigue performance of the high-strength wrought magnesium alloy AZ80." *Scripta Materialia* 52(10): 1011-1015.
- Zhao, Z. and Hong, S. Y. (1992). "Cooling strategies for cryogenic machining from a materials viewpoint." *Journal of Materials Engineering and Performance* 1(5): 669-678.
- Zhilyaev, A. P. and Langdon, T. G. (2008). "Using high-pressure torsion for metal processing: Fundamentals and applications." *Progress in Materials Science* 53(6): 893-979.

- Zhilyaev, A. P., Nurislamova, G. V., Kim, B. K., Baro, M. D., Szpunar, J. A. and Langdon, T. G. (2003). "Experimental parameters influencing grain refinement and microstructural evolution during high-pressure torsion." *Acta Materialia* 51(3): 753-765.
- Zhu, K. Y., Vassel, A., Brisset, F., Lu, K. and Lu, J. (2004). "Nanostructure formation mechanism of alpha-titanium using SMAT." *Acta Materialia* 52(14): 4101-4110.
- Zhuang, W. Z. and Halford, G. R. (2001). "Investigation of residual stress relaxation under cyclic load." *International Journal of Fatigue* 23: S31-S37.
- Zum Gahr, K. H. (1987). *Microstructure and wear of materials*. Amsterdam, Elsevier.
- Zurecki, Z., Ghosh, R. and Frey, J. H. (2003). Investigation of white layers formed in conventional and cryogenic hard turning of steels. *Proc. of ASME Manufact. Eng. Division*.
- Zurecki, Z., Ghosh, R. and Frey, J. H. (June 2003). Finish-turning of hardened powdermetallurgy steel using cryogenic cooling. *Proceedings of the International Conference on Powder Metallurgy and Particulate Materials, Las Vegas*.
- Zurecki, Z., Ghosh, R., and Frey, J.H. (2003). Investigation of white layers formed in conventional and cryogenic hard turning of steels. *Proceedings of IMECE'03, Washington, D.C.*

## VITA

### Name

Shu Yang

### Date and Place of Birth

October, 31st, 1984

Yangquan, Shanxi Province, China

### Education

B.S. in Mechanical Engineering Department, Xiamen University, Fujian, China

September, 2002 - July, 2006

### Experience

- Research Assistant (05/2008 ~ 09/2012), Machining Research Group, Institute for Sustainable Manufacturing, University of Kentucky
- Editorial Assistant (11/2010 ~ 09/2012), Journal of Machining Science & Technology, University of Kentucky.
- Visiting Scholar (01/2012 ~ 02/2012), University of Coimbra, Portugal.
- Teaching Assistant (08/2007 ~ 05/2010), Mechanical Engineering, University of Kentucky.

### Journal Papers

- S. Yang**, O. W. Dillon, Jr., D. A. Puleo, I. S. Jawahir, Effect of cryogenic burnishing on surface integrity modifications of Co-Cr-Mo alloy used in metal-on-metal joint implants, 2012, Journal of Biomedical Materials Research: Part B - Applied Biomaterials, in press.
- S. Yang**, O. W. Dillon, Jr., D. A. Puleo, J. C. Outeiro, I. S. Jawahir, Enhanced wear resistance of Co-Cr-Mo biomaterial through cryogenic burnishing, submitted to Acta Materialia.
- S. Yang**, D. Umbrello, I. S. Jawahir, An Investigation of the cryogenic cooling effect on surface microstructure modifications in burnishing of Co-Cr-Mo biomaterial, submitted to Journal of Materials Processing Technology.

- D. Umbrello, **S. Yang**, O.W. Dillon, Jr. and I.S. Jawahir, The effects of cryogenic cooling on surface layer alterations in machining of AISI 52100 steels, 2012, Journal of Material Science and Technology, in press.
- Z. Pu, G.-L. Song, **S. Yang**, J.C. Outeiro, O.W. Dillon, Jr., D.A. Puleo, I.S. Jawahir, Grain refined and basal textured surface produced by burnishing for improved corrosion performance of AZ31B Mg alloy, 2012, Corrosion Science, 57:192–201.
- Z. Pu, **S. Yang**, G.L. Song, O.W. Dillon, Jr., D.A. Puleo and I.S. Jawahir, Ultrafine-grained surface layer on Mg-Al-Zn alloy produced by cryogenic burnishing for enhanced corrosion resistance, 2011, Scripta Mater, 65:520-523.

#### Conference Papers

- I. S. Jawahir, Z. Pu, **S. Yang**, G. Rotella, Y. Kaynak, T. Lu, A. Deshpande, D. Umbrello, O.W. Dillon Jr., “Cryogenic processing of materials for enhanced product life, performance and sustainability”, 15th International Conference on Advances in Materials & Processing Technologies, Australia, 23-26 September, 2012.
- A. Deshpande, **S. Yang**, D. Puleo, D. Pienkowski, O.W. Dillon Jr., J.C. Outeiro, I.S. Jawahir, 2012, Minimized wear and debris generation through optimized machining of Co-Cr-Mo alloys for use in metal-on-metal hip implants, ASME 2012 ICTMP conference, Notre Dame, IN.
- S. Yang**, D. A. Puleo, O. W. Dillon, Jr., I.S. Jawahir, Surface layer modifications in Co-Cr-Mo biomedical alloy from cryogenic burnishing, Procedia Engineering, 2011, Vol 19, Pages 383-388.
- S. Yang**, Z. Pu, D.A. Puleo, O.W. Dillon, Jr., I.S. Jawahir, Cryogenic processing of biomaterials for improved surface integrity and product sustainability, Adv in Sust Manuf, 2011, Part 4, 177-182.
- Z. Pu, G.-L. Song, **S. Yang**, O.W. Dillon, Jr., D. A. Puleo, I.S. Jawahir, “Cryogenic Burnishing of AZ31B Mg Alloy for Enhanced Corrosion Resistance”, Proceeding of Magnesium Technology 2011, TMS Annual Meeting & Exhibition, San Diego, California, 2011.